FEASIBILITY ANALYSIS OF AN OPEN CYCLE THERMOACOUSTIC ENGINE WITH INTERNAL PULSE COMBUSTION

A Dissertation
Presented to
The Academic Faculty

By

Nathan T. Weiland

In Partial Fulfillment
of the Requirements for the Degree
Doctor of Philosophy in the
School of Mechanical Engineering

Georgia Institute of Technology

December 2004

FEASIBILITY ANALYSIS OF AN OPEN CYCLE THERMOACOUSTIC ENGINE WITH INTERNAL PULSE COMBUSTION

Approved by:

Dr. Ben T. Zinn, Advisor

Dr. Yves Berthelot

Dr. Timothy Lieuwen

Dr. Samuel Shelton

Dr. Gregory Swift

Date Approved: August 9, 2004

ACKNOWLEDGEMENT

There are many, many people to thank, who have made this work possible.

First, a huge thanks to my wife, Lisa, who has been very supportive, understanding, and accommodating during these past few years, and especially so over the final weeks of the dissertation process. And a special thanks, as well, to my little son, Jacob, who has helped me type, reorganize files, and read papers, in addition to providing good motivation to get this dissertation completed.

Also, many thanks to my parents, who have always provided love, support and encouragement in any of my undertakings. And many thanks, as well, to my siblings, extended family, and friends, for helping me out and providing much needed stress relief.

Thanks, especially, to my advisor Dr. Zinn, who has been very tolerant of my extended degree program and move to Virginia. He has also provided much appreciated research funding, encouragement, and feedback, and has allowed me the freedom to conduct research in an independent manner, for which I am very grateful.

Thanks, as well, to Dr. Swift, for his suggestions and valuable insights into this research, and to my committee members and co-workers at the combustion lab, for their feedback on the direction of my studies.

And last but not least, I give thanks to God, who has granted me many gifts, surrounded me with many good people, and made all things possible.

TABLE OF CONTENTS

LIST OF TABLES

LIST OF FIGURES

LIST OF SYMBOLS

English Symbols

A	area, m^2
a	speed of sound, m/s
b_μ	exponent for temperature dependence of viscosity
b	curve fit parameter used in determining the regenerator heat transfer coefficient
C	acoustic capacitance, $m^4 \cdot s^2/kg$
c	coefficients in the solution of the eigenvalue problem
c	curve fit coefficients
c_p	constant pressure specific heat, J/kg·K
D	diameter, m
D_{wire}	wire diameter, m
$\dot{E}$	acoustic energy flux, W
e	exponential function, 2.71828…
e	internal energy per unit mass, J/kg
F	Moody friction factor
f	frequency, Hz
f	area-averaged thermoviscous functions
g	acoustic gain factor due to thermoacoustic or pulse combustion effects
g	curve fit parameter
$\dot{H}$	total energy flux, W
h	spatial thermoviscous functions
h	convective heat transfer coefficient, $W/m^2 \cdot K$
h	enthalpy per unit mass, J/kg
h_f°	chemical enthalpy of formation at the reference state, J/kg
i	imaginary number, $\sqrt{-1}$
k	thermal conductivity, W/m·K
L	acoustic inertance, kg/m^4
L	length of the regenerator, m
M	ratio of reactant heat capacitance rate to product heat capacitance rate
$\dot{M}$	mean mass flux, kg/s
MW	molecular weight, kg/kmol
$\dot{m}$	mass flux, kg/s
N	reactant heat transfer constant
N	number of moles, mol
Nu	Nusselt number
n	number of preheat pipes
n_{mesh}	wire screen mesh number
p	pressure, Pa
$\dot{Q}$	heat release rate or heat transfer rate, W

q specific heat transfer, J/kg
$\dot{q}$ heat release rate per unit volume, W/m^3
R resistance, kg/m^4·s
R constant in eigenvalue solution
R gas constant, J/kg·K
R_u universal gas constant, 8.31434 J/kmol·K
Re Reynolds number
r resistance per unit length, kg/m^5·s
r_h hydraulic radius, m
$\dot{S}$ thermoacoustic entropy flux, W/K
s entropy per unit mass, J/kg·K
T temperature, K
t thickness, m
t time, s
U volumetric velocity, m^3/s
u velocity, m/s
V volume, m^3
v specific volume, m^3/kg
$\dot{W}$ rate of work, W
w specific work, J/kg
w fraction of available work
x axial coordinate, m
x length, m
x number of carbon atoms in a fuel molecule
Y mass fraction
y transverse coordinate, m
y number of hydrogen atoms in a fuel molecule
Z acoustic impedance, kg/m^4·s
z transverse coordinate, m
z integration variable

Greek Symbols

α regenerator pressure difference geometric factor
α oscillating heat release gain parameter
γ ratio of specific heats
Δ change in a variable across a component
δ viscous or thermal penetration depth, m
ε_k intermittent stacked screen contact factor
ε_h regenerator heat transfer coefficient parameter from Swift and Ward (1996)
η efficiency
θ phase angle, radians
θ_{pq} phase shift between acoustic pressure and oscillating heat release, radians
λ acoustic wavelength, m
λ eigenvalues in the solution to the reactant preheating problem
μ dynamic viscosity, kg/m·s
Ξ ratio of convective to conductive effects in the regenerator, 1/m

ξ acoustic gas displacement, m
Π perimeter, m
π 3.14159…
ρ density, kg/m^3
σ Prandtl number
σ' viscous stress tensor
Φ equivalence ratio
ϕ regenerator porosity
χ mole fraction
ψ coefficient of entropy flux by imperfect thermal contact, W·m/K
ω angular frequency, rad/s

Special Characters

$\langle\ \rangle$ averaged over the cross-sectional area
∂ partial derivative
∇ gradient
$\sum$ summation
$\approx$ approximately equal to
$\equiv$ defined as
$|\ |$ magnitude or absolute value

Superscript Characters

$\bar{}$ molar quantity
$\tilde{}$ complex conjugate
$'$ per unit length
$'$ shorthand derivative, d/dx
$\dot{}$ rate

Subscript Characters

$_0$ ambient
$_1$ first order oscillating component
$_{2,0}$ mean component of second order term
$_{II}$ second law
$_C$ compliance
$_c$ impedance of compliance
$_c$ cold
$_{cd}$ cold duct location
$_{chx}$ cold heat exchanger
$_{comb}$ combustion
$_{cz}$ combustion zone
$_e$ exhaust
$_{fb}$ feedback
$_{flow}$ irreversibility attached to the mean flow
$_{fuel}$ fuel
$_{gen}$ generation (entropy)

H2O	water vapor component
h	hot, hot duct location
i	individual
ideal	ideal case
in	entering the control volume
ins	insulation
int	regenerator/hot duct interface
k	conduction and imperfect entropy flux effect
κ	thermal conductivity effect (penetration depth, thermoviscous function, etc.)
L	impedance of inertance
L	acoustic load
l	inertance
lfl	lean flammability limit
lost	lost work due to irreversibility
m	mean component
max	maximum
mid	midpoint
mix	gas mixture
v	viscosity effect (penetration depth, thermoviscous function, etc.)
other	due to other modeled irreversibilities
out	exiting the control volume
pc	pulse combustion
ph	preheated
pp	parallel plate regenerator
pr	combustion products
q	combustion or heat release component
re	regenerator
re,c	cold side of the regenerator
re,h	hot side of the regenerator
ref	reference
rh	reactant header
rx	combustion reactants
s	supply
s	solid components
sat	saturation
ss	stacked wire mesh screen regenerator
ss	stainless steel
T	temperature
ta	thermoacoustic
tasfe	time average steady flow equivalent
tbt	thermal buffer tube
th	thermal
tot	total
wall	wall

SUMMARY

Thermoacoustic engines convert thermal energy into acoustic energy with few or no moving parts, thus they require little maintenance, are highly reliable, and are inexpensive to produce. These traits make them attractive for applications in remote or portable power generation, where a linear alternator converts the acoustic power into electric power. Their primary application, however, is in driving thermoacoustic refrigerators, which use acoustic power to provide cooling at potentially cryogenic temperatures, also without moving parts.

This dissertation examines the feasibility of a new type of thermoacoustic engine, where mean flow and an internal pulse combustion process replace the hot heat exchanger in a traditional closed cycle thermoacoustic engine, thereby eliminating the heat exchanger's cost, inefficiency, and thermal expansion stresses. The theory developed in this work reveals that a large temperature difference must exist between the hot face of the regenerator and the hot combustion products flowing into it, and that much of the convective thermal energy input from the combustion process is converted into conductive and thermoacoustic losses in the regenerator. The development of the Thermoacoustic Pulse Combustion Engine, as described in this study, is designed to recover most of this lost thermal energy by routing the inlet pipes through the regenerator to preheat the combustion reactants. Further, the developed theory shows that the pulse combustion process has the potential to add up to 7% to the engine's acoustic power

output for an acoustic pressure ratio of 10%, with linearly increasing contributions for increasing acoustic pressure ratios.

Computational modeling and optimization of the Thermoacoustic Pulse Combustion Engine yield thermal efficiencies of about 20% for atmospheric mean operating pressures, though higher mean engine pressures increase this efficiency considerably by increasing the acoustic power density relative to the thermal losses. However, permissible mean engine pressures are limited by the need to avoid fouling the regenerator with condensation of water vapor out of the cold combustion products. Despite lower acoustic power densities, the Thermoacoustic Pulse Combustion Engine is shown to be well suited to portable refrigeration and power generation applications, due to its reasonable efficiency and inherent simplicity and compactness.

CHAPTER 1

INTRODUCTION

Thermoacoustics, as the name might imply, is the study of interactions between thermal and acoustic processes. In the acoustics community, the term "thermoacoustic" applies specifically to a class of devices whose primary purpose is to convert thermal energy to acoustic energy, or vice versa. These devices take advantage of the fact that temperature oscillations accompany the pressure oscillations resulting from acoustic perturbations in a fluid. All that is required to take advantage of these temperature oscillations is the thermal interaction of the acoustic fluid with solid surfaces. Thus, in their simplest form, thermoacoustic devices achieve conversion between thermal and acoustic energy with few or no moving parts, yielding devices that are highly reliable, relatively inexpensive to manufacture, and require very little maintenance for continuous operation. The lack of moving parts is particularly important in a thermoacoustic refrigerator, as cold sliding friction losses that are a major source of inefficiency in many refrigeration cycles are completely eliminated. In addition, thermoacoustic devices tend to work best with inert gases such as helium, thus eliminating the need for the environmentally harmful chlorofluorocarbons used in many refrigeration cycles today.

A simple traveling wave thermoacoustic engine is shown in Figure 1.1, where hot and cold heat exchangers are positioned at either end of a regenerator, which provides

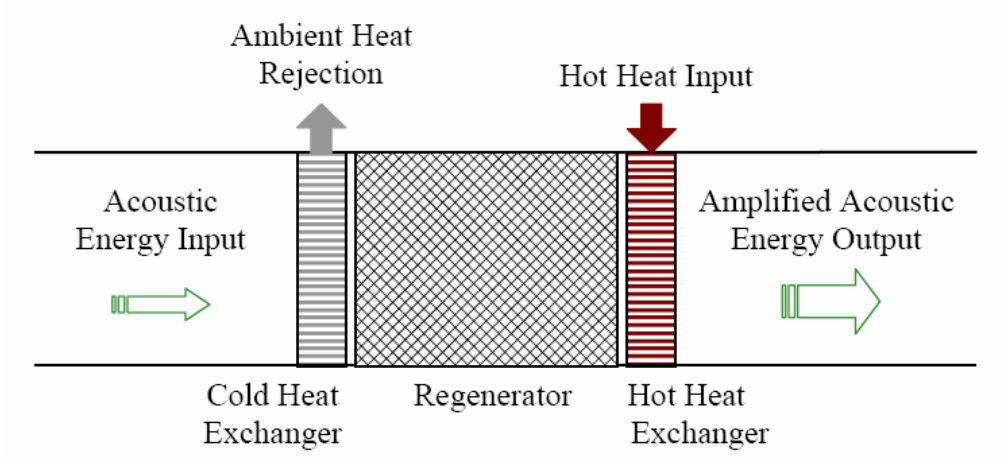

Figure 1.1: A schematic of a basic traveling wave thermoacoustic engine

ample solid-gas contact area for thermal energy exchange. This creates a temperature gradient across the stack or regenerator, which is used to amplify an acoustic traveling wave that passes from cold to hot through the regenerator [Ceperley (1978, 1979)]. The best-performing thermoacoustic engine to date is the Thermoacoustic Stirling Heat Engine (TASHE), built by Scott Backhaus and Greg Swift at Los Alamos National Lab [Backhaus and Swift (2000)]. This engine uses an electrical resistance hot heat exchanger to convert electrical energy to thermal energy, which is in turn converted into acoustic energy in the TASHE with a maximum thermal efficiency of 30%, corresponding to about 42% of the Carnot efficiency.

Another means of converting thermal energy into acoustic energy is through a pulse combustion process. Rayleigh's criterion states that unsteady heat release oscillations that are in phase with acoustic pressure oscillations will add acoustic energy to the combustion system [Zinn (1986)]. Therefore, adding a properly controlled internal

pulse combustion process to a thermoacoustic engine could, in principle, increase the acoustic power output of the engine. In such an engine, the pulse combustion process would replace the hot heat exchanger as the primary source of heat input to the engine.

Simple though it may seem, implementation of an internal combustion process in a thermoacoustic engine requires an open cycle architecture, where combustion reactants flow into the engine and combustion products flow out. To date, such an open cycle thermoacoustic engine has never been studied or built, so a degree of uncertainty exists over whether or not such a device is even possible, or how it might operate.

After considering several design options, one design has been chosen which holds a great deal of promise for producing a working thermoacoustic engine, and has been dubbed the Thermoacoustic Pulse Combustion Engine, or TAPCE for short. In addition to providing an internal pulse combustion process and the required open cycle architecture, an important feature in the design of the TAPCE is the recovery of some of the engine's natural thermal energy losses by preheating the incoming combustion reactants, thereby increasing the feasibility and potential efficiency of the engine. Indeed, as the following study indicates, the TAPCE design concept has the potential to yield the highest possible fuel energy to acoustic energy conversion efficiencies.

The following dissertation examines the feasibility and likely operation and performance of the TAPCE. In the following chapter, the various types of thermoacoustic devices are presented, and a brief review of pulse combustion is given. Chapter 3 presents the details of the TAPCE design concept, points out its inherent advantages and disadvantages over current thermoacoustic engines, and explores its potential applications. In Chapter 4, the thermoacoustic and combustion theory necessary

for understanding and evaluating the operation and performance of the TAPCE is developed. Using these theories, a computer model of the TAPCE has been developed, the details of which are presented in Chapter 5. Chapter 6 describes the optimization of the TAPCE design, presents details on the likely operation of the device, and compares the TAPCE to other thermoacoustic engine designs using various performance parameters. The dissertation is concluded in Chapter 7, and is followed by an Appendix for the computer code used to model the Thermoacoustic Pulse Combustion Engine.

CHAPTER 2

BACKGROUND

2.1 Traveling Wave Thermoacoustics

Thermoacoustic devices are divided into two classes, depending on which type of acoustics they employ: standing wave or traveling wave acoustics. Effective use of either standing or traveling wave acoustics depends critically on a thermoacoustic length scale referred to as the thermal penetration depth, defined in Swift's (2002) text as:

$$\delta_\kappa = \sqrt{\frac{2k}{\omega\rho c_p}}, \tag{2.1}$$

where k is the thermal conductivity of the gas, ω is the angular frequency of acoustic oscillation, ρ is the gas density and c_p is the constant pressure specific heat of the gas. This length scale approximately expresses the distance that thermal energy is conducted through the gas during one fourth of an acoustic cycle.

Note that another closely related quantity is the viscous penetration depth,

$$\delta_\nu = \sqrt{\frac{2\mu}{\omega\rho}}, \tag{2.2}$$

where μ is the dynamic viscosity of the gas. These two length scales are roughly of the same order of magnitude, and are related by the Prandtl number, σ:

$$\sigma = \frac{\mu c_p}{k} = \frac{\delta_\nu^2}{\delta_\kappa^2}\,. \tag{2.3}$$

For most gases employed in thermoacoustic devices, $0.66 < \sigma < 0.8$, though the Prandtl number can be much smaller for certain types of gas mixtures [Belcher et. al. (1999)].

The thermal and viscous penetration depths essentially describe the thickness of the boundary layer in which axial acoustic gas motions interact laterally with the surrounding walls. From this perspective, the degree of interaction that acoustic waves have with their local solid boundaries can be measured by comparing the thermal and viscous penetration depths with the average distance between the gas and solid in a closed channel. This convenient measure is known as the hydraulic radius:

$$r_h = \frac{A}{\Pi}, \tag{2.4}$$

where A is the cross-sectional area in the channel, and Π is its perimeter.

In open channels and ducts, where the boundary layers are small compared to the size of the duct (i.e., $\delta_{\kappa,\nu} << r_h$), the acoustic gas oscillations are approximately adiabatic and reversible, and acoustic pressure oscillations are accompanied by temperature and density oscillations that are in phase with the pressure oscillations. As the size of the duct decreases, however, thermal interactions with the walls begin to distort the relationships between the acoustic pressure, temperature and density. In the limit where the average distance to the walls is much smaller than a thermal penetration depth (i.e., $\delta_{\kappa,\nu} >> r_h$), very good thermal contact between the gas and the solid creates an approximately isothermal environment, where the gas temperature is always the same as the local temperature of the surrounding solid material. Thermodynamically, isothermal

heat transfer between the gas and solid is a reversible process, and contributes to the excellent efficiency of traveling wave thermoacoustic devices.

The apparatus used to attain these near-isothermal conditions in a traveling wave thermoacoustic device is commonly referred to as a regenerator. There are several regenerator designs that achieve the desired degree of solid-gas thermal contact, including thinly-spaced stacks of parallel plates [Backhaus and Swift (2001)], stacked wire mesh screens [Backhaus and Swift (2000), Kays and London (1984)], etc., each with their own particular advantages and disadvantages. Fortunately, since regenerators play a critical role in Stirling cycle devices, they have been extensively studied, and experimental data on the heat exchange effectiveness and viscous dissipation within the various types regenerators is readily available [Kays and London (1984)].

In typical traveling wave thermoacoustic devices, the regenerator is bracketed by a hot heat exchanger and a cold heat exchanger, which effectively create a temperature gradient across the regenerator. Due to this temperature gradient and the good solid/gas thermal contact within the regenerator, the temperature of the gas is primarily a function of its acoustically oscillating position in the regenerator. As will be seen below, the acoustic phasing between the oscillating pressure and displacement causes the gas in the regenerator to undergo a thermodynamic cycle that can either produce work or pump heat up the temperature gradient. The direction of the temperature gradient relative to the direction of the traveling acoustic wave, as well as the particular choice for the ambient temperature heat exchanger, dictates whether the thermoacoustic device will function as a heat engine or a heat pump.

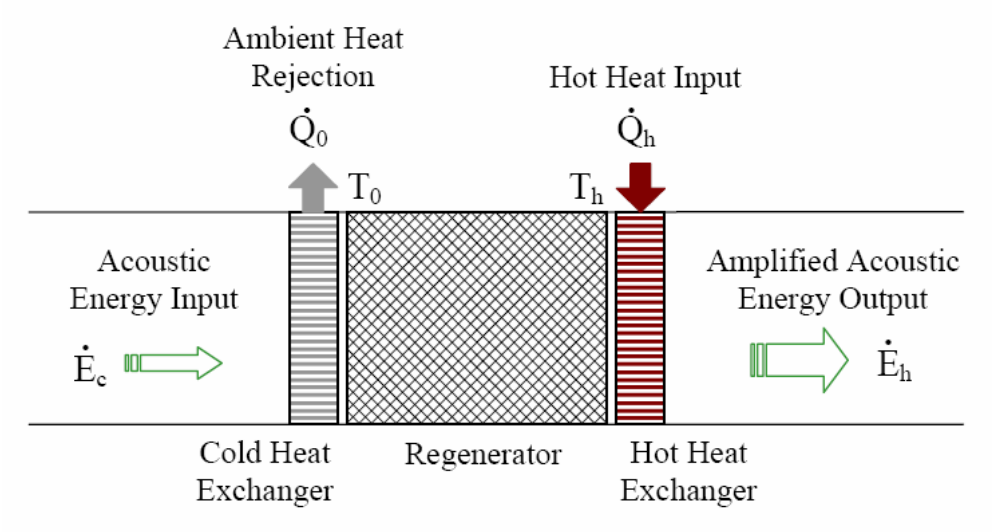

Figure 2.1: A detailed schematic of a basic traveling wave thermoacoustic engine.

2.1.1 The traveling wave engine

A schematic of a basic traveling wave thermoacoustic engine is shown in Figure 2.1. In this simplified engine configuration, the regenerator is situated between an ambient temperature heat exchanger on the left, and a hot heat exchanger on the right. The hot heat exchanger transfers heat into the engine at a rate $\dot{Q}_h$ at the hot temperature T_h, while the cold heat exchanger exhausts heat at a rate $\dot{Q}_0$ to the environment at the ambient temperature T_0. In this configuration, a temperature gradient develops across the regenerator, ideally between the ambient temperature T_0 on the left and the hot temperature T_h on the right.

An acoustic traveling wave passes through the cold heat exchanger and enters the regenerator from the left, carrying with it an acoustic power $\dot{E}_c$. Upon passing through the temperature gradient in the regenerator, its acoustic power is amplified, and it exits the regenerator's right side with an acoustic power $\dot{E}_h$. Note that in the most ideal case,

where there is perfect gas-solid heat transfer in the regenerator and viscous losses and other irreversibilities are ignored, the acoustic power exiting the regenerator is proportional to the absolute temperature ratio across the regenerator [Backhaus and Swift (2000)], i.e.:

$$\dot{E}_h = \dot{E}_c \frac{T_h}{T_0}. \tag{2.5}$$

2.1.1.1 Traveling wave engine thermodynamics

The mechanism causing this acoustic power amplification is depicted schematically in Figure 2.2. The regenerator is portrayed in Figure 2.2a as consisting of a stack of thin, parallel plates, where the hydraulic radius, equal to half of the separation distance between each plate in this case, is much less than one thermal penetration depth in the acoustically oscillating gas. As a result, the solid-gas thermal contact is very good, and the temperature of the "parcels" of gas that acoustically oscillate back and forth between the plates, is, to a good approximation, equal to the temperature of the solid plates at any axial location.

In Figure 2.2b, attention is focused on one representative gas parcel within the regenerator, which begins the acoustic cycle at its left-most position. To simplify the cycle description, we'll approximate the sinusoidally oscillating quantities in this figure as four separate processes. In an acoustic traveling wave, acoustic pressure and acoustic velocity oscillations are in phase, which allows for the transmission of acoustic energy in the direction of the acoustic traveling wave [Kinsler et. al. (1982), Pierce (1989)].

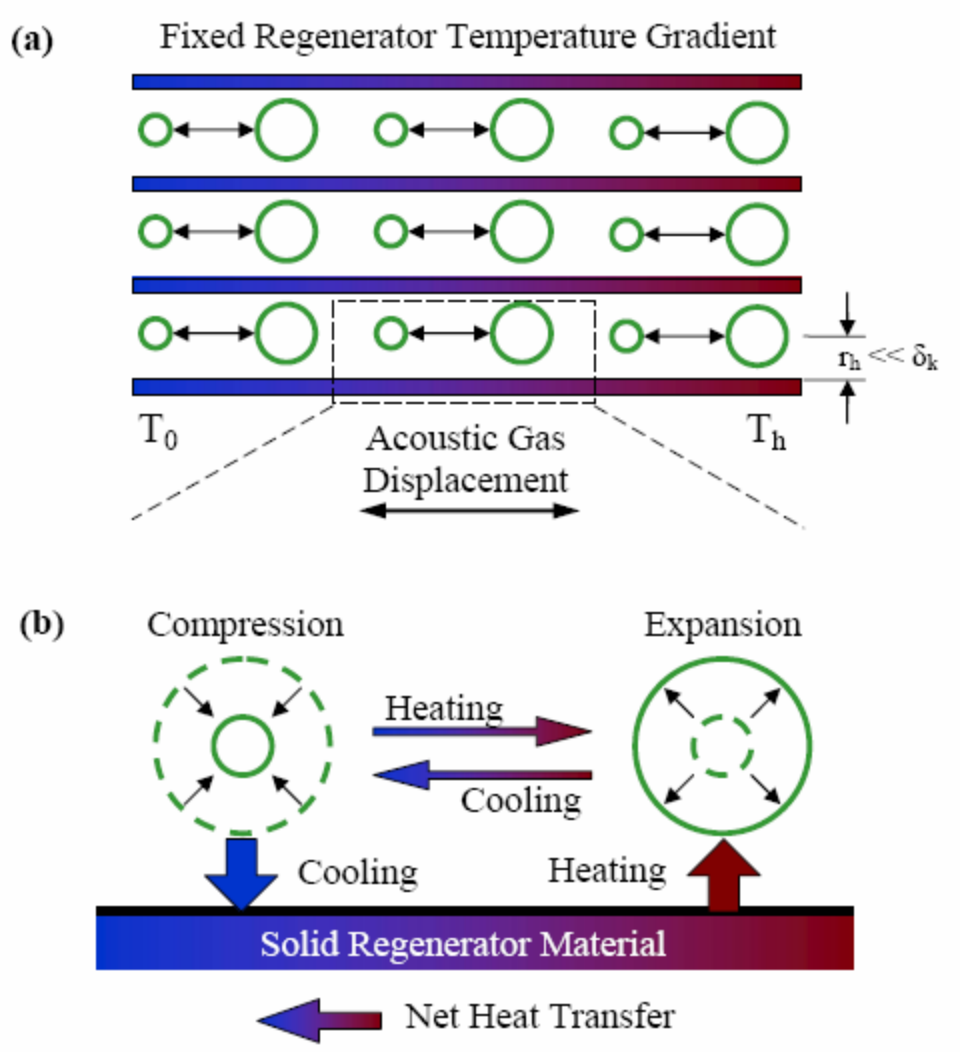

Figure 2.2: a) A magnified view of a parallel plate regenerator, b) thermodynamic processes of an acoustically oscillating gas parcel within the regenerator of a thermoacoustic engine

Therefore, for an acoustic wave traveling to the right in a medium with no mean gas velocity, the acoustic velocity is positive while the pressure is high, so the gas parcel moves to the right along the regenerator, increasing in temperature along with the solid temperature gradient. At the gas parcel's right-most position, the gas temperature equals the temperature of the regenerator while its pressure decreases, thereby causing the gas parcel to expand at high temperature. After attaining its low pressure, the gas parcel translates back to the left, decreasing in temperature along with the solid temperature gradient as it does so. Finally, at the left-most position, the pressure increases and the gas parcel is compressed at low temperature.

An understanding of how these gas motions and property changes create acoustic power is aided by plots of the oscillating gas properties as a function of time in Figure 2.3a. For a sinusoidally oscillating acoustic velocity (e.g., $u_1 = \sin t$), the acoustic gas displacement, ξ_1, is simply the integral of the acoustic velocity (e.g., $\xi_1 = -\cos t$). Since the acoustic pressure and velocity are both in phase for an acoustic wave traveling to the right, the acoustic gas displacement lags the acoustic pressure by 90°. Also, assuming perfect solid-gas thermal contact in the regenerator, the acoustic displacement is proportional to the gas temperature, due to the temperature gradient along the regenerator's solid. Thus, knowing the gas pressure and temperature at all points in the acoustic cycle, the other gas properties can be calculated. For instance, for an ideal gas, the change in the specific volume of the gas, v, follows the ideal gas law, i.e.:

$$\frac{dv}{v} = \frac{dT}{T} - \frac{dp}{p}, \tag{2.6}$$

while the change in the gas's entropy, is related to the change in pressure and temperature by:

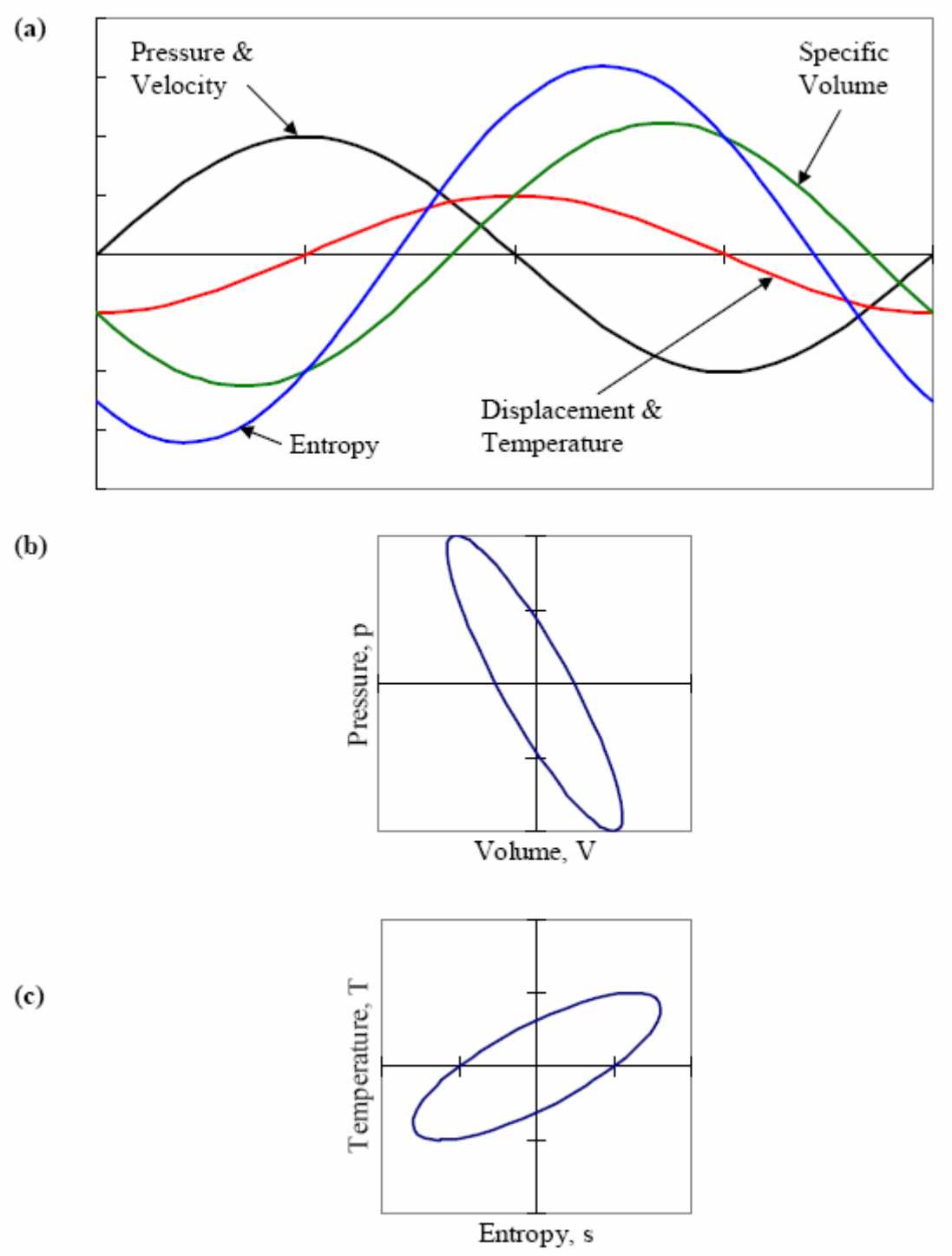

Figure 2.3: a) Gas parcel properties as a function of time for one acoustic cycle in the thermoacoustic engine of Figure 2.2, b) Gas parcel P-V diagram (PdV Work Output), c) Gas parcel T-s diagram (T-ds Heat Input)

$$ds = c_p \frac{dT}{T} - R\frac{dp}{p}, \tag{2.7}$$

where R is the gas constant. Note that an increase in the entropy of the gas, s, indicates heat transfer from the solid to the gas, q, according one definition of entropy: $dq = T\,ds$. Finally, noting that $c_p \approx (5/2)R$ for monatomic gases, which are frequently used in thermoacoustic engines, the gas specific volume and entropy can be plotted for changes in temperature and pressure over the course of an acoustic cycle in Figure 2.3a.

Using these results, we can now show that each gas parcel produces a net work output during each acoustic cycle by examining the cycle on a pressure vs. the specific volume diagram, since:

$$w = \oint dw = \oint p dv, \tag{2.8}$$

where w is the work output per unit mass of fluid, per acoustic cycle. The p-v diagram is plotted in Figure 2.3b, where the area enclosed by the ellipse is the specific work output, w, since integration over an acoustic cycle occurs in a clockwise fashion in this case. This work output is realized as an increase in acoustic power traveling to the right through the regenerator.

Similarly, the heat absorbed by the gas in order to produce this work output can be calculated from:

$$q = \oint dq = \oint T ds, \tag{2.9}$$

where q is the heat absorbed per unit mass of fluid, per acoustic cycle. The amount of heat absorbed is equal to the area inside the ellipse of the T-s diagram in Figure 2.3c, since this, too, is integrated in a clockwise fashion around the ellipse over the course of an acoustic cycle.

The physical realization of this heat absorption is slightly more difficult to perceive, but is aided by referring back to the gas parcel schematic of Figure 2.2b. Note that at the gas parcel's right-most position, expansion is accompanied by heat transfer from the solid to the gas in order to keep the gas at constant temperature, while at its left-most position, compression is accompanied by heat transfer from the gas to the solid, again to maintain a constant gas temperature. In this manner, one can envision a "bucket brigade" of gas parcels that pick up heat at the right and drop it off on the left, thereby "shuttling" heat down the regenerator [Swift (1988)]. The heat absorbed over the course of an acoustic cycle is realized as a decrease in the amount of heat "shuttled" from right to left down the regenerator's temperature gradient. This heat, q, is converted to work, w, in the form of acoustic energy gain in the regenerator, thus the area enclosed by ellipse of Figure 2.3b is equal to that of Figure 2.3c (i.e., $w = q$).

Finally, note that the heat transfer between the gas and the solid in the regenerator is a reversible process, since the temperature of the gas and solid is approximately the same at any axial location in the regenerator due to the good solid-gas thermal contact achieved in the regenerator. The reversible, isothermal heat transfer and the compression and expansion due to pressure changes are traits shared by another thermodynamic cycle – the Stirling cycle. As a result, traveling wave thermoacoustic devices are frequently viewed as acoustic realizations of the Stirling cycle, where acoustic gas motions replace the pistons in a Stirling engine or refrigerator.

2.1.1.2 History of the traveling wave thermoacoustic engine

The first to realize the connection between the Stirling cycle and traveling wave thermoacoustics was Peter Ceperley, who performed the first experiments on traveling

wave thermoacoustic engines. His attempts to create a working engine failed, however, as viscous losses in the regenerator destroyed any acoustic amplification that might have occurred [Ceperley (1978, 1979)]. Realizing this, Ceperley went on to design and analyze other traveling wave thermoacoustic engine concepts in which a standing wave acoustic field was superimposed on the traveling wave acoustic field in order to increase the specific acoustic impedance in the regenerator [Ceperley (1982, 1985)]. By locating the regenerator at the acoustic velocity node of the standing wave, the acoustic pressure in the regenerator, and hence, the acoustic energy gain, could be increased without increasing the acoustic velocity, which is responsible for the viscous dissipation in the regenerator.

Although the superposition of a standing wave on the traveling wave acoustic field was a step in the right direction, Ceperley's (1982) use of full wavelength and half-wavelength resonators to generate the standing wave acoustic field introduce additional viscous losses at the walls of the resonator, and also open up a path for mean mass flux to circulate through the engine, which generally convects heat input away from the regenerator. Following up on one of Ceperley's design ideas, Yazaki et. al. (1998) successfully built and demonstrated a thermoacoustic engine in which acoustic traveling waves circulate around a looped tube containing a regenerator bracketed by hot and cold heat exchangers. Though the engine performs well as an experimental apparatus, it is of little practical value, as all of the acoustic energy gain in the regenerator is used to sustain the viscous dissipation losses along the walls of the looped tube, which is about two acoustic wavelengths long.

2.1.1.3 The Thermoacoustic Stirling Heat Engine (TASHE)

The development of traveling wave thermoacoustic engines took a giant leap forward with Backhaus and Swift's (2000) invention of the Thermoacoustic Stirling Heat Engine (TASHE). Incorporating their innovations on pulse tube refrigerators [Swift et. al. (1999)], this device employs an acoustically compact network that allows the TASHE to convert thermal energy to acoustic energy with a thermal efficiency of 30%. In addition to producing the needed acoustic traveling wave phasing at the regenerator, this network increases the specific acoustic impedance at the regenerator, thus limiting its viscous losses, while also providing a feedback path that supplies the input acoustic energy to the regenerator.

As shown in Figure 2.4a, the TASHE device is comprised of a resonator, a variable acoustic load, and a thermoacoustic driving section. The entire device is filled with helium compressed to approximately thirty atmospheres. The use of high-pressure helium increases the acoustic power density of the TASHE, thus increasing the importance of the thermoacoustic effects compared to the heat conduction losses in the regenerator, which are not a function of the mean pressure [Backhaus and Swift (2000)]. The full engine functions as a quarter-wavelength standing wave resonator, though the standing wave acoustic phasing in the driver section at the left end of the engine is modified by its compact acoustic network.

Figure 2.4b provides a more detailed description of the thermoacoustic driver of the TASHE in Figure 2.4a. The thermoacoustic driver contains a toroidal acoustic feedback loop (or torus), in which a regenerator is bracketed by a primary cold heat exchanger and a hot heat exchanger. As described with reference to Figure 2.1, the

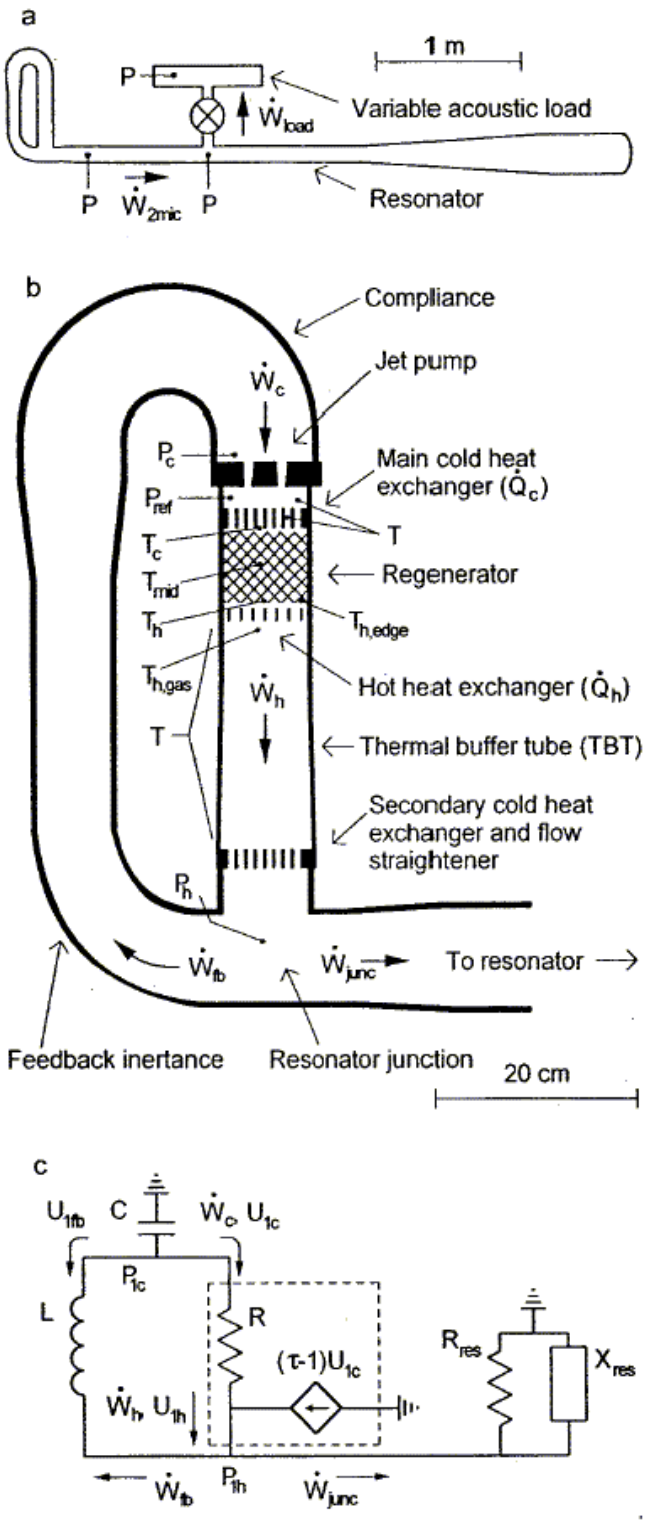

Figure 2.4: a) The full Thermoacoustic Stirling Heat Engine (TASHE), b) the detail of the driver section of the TASHE, and c) a basic electrical circuit representation of the TASHE. (Reprinted with permission from [Backhaus and Swift (2000)])

primary cold heat exchanger, the regenerator, and the hot heat exchanger are configured to amplify traveling acoustic waves that propagate clockwise around the torus. At the resonator junction, a portion of the amplified acoustic energy, $\dot{W}_{junc}$, travels to the right towards the resonator and the acoustic load, while the remainder, $\dot{W}_{fb}$, is fed back through the torus to provide acoustic power, $\dot{W}_c$, to the cold end of the regenerator. The latter is amplified within the regenerator to $\dot{W}_h$, and exits the hot side of the regenerator. Below the hot heat exchanger is a thermal buffer tube and a secondary cold heat exchanger, which thermally isolate the hot heat exchanger from the rest of the TASHE beyond the cold heat exchangers.

The torus of the TASHE consists of an inertance, which functions as a mass-like acoustic element, a compliance, which functions as a spring-like acoustic element, and the regenerator, which functions as a viscous resistance and acoustic amplifier [Backhaus and Swift (2000)]. Since each of these components are much shorter than an acoustic wavelength, they can be modeled as acoustically compact lumped parameter elements, much like a mechanical mass-spring-damper system or an electrical L-R-C network [Kinsler et. al. (1982), Pierce (1989)]. A basic electrical circuit representation of the TASHE is shown in Figure 2.4c, where the compliance and inertance are represented by the capacitance, C, and the inductance, L, respectively. The regenerator is represented by the combination of the resistance, R, and the current source below it, while the resonator of the TASHE is represented by a parallel combination of a resistance, R_{res}, and a reactance, X_{res}.

The key to the successful operation of the TASHE is that the acoustic impedance of the inertance branch is much smaller than the resistance of the regenerator branch (i.e.

$\omega L/R << 1$) [Backhaus and Swift (2000)]. As a result, the acoustic velocity in the inertance section is much larger than that in the regenerator branch, which serves two purposes. First, the inertance and the compliance shift the phase of the acoustic velocity so that it is approximately in phase with the acoustic pressure in the regenerator, as in an acoustic traveling wave. Second, the larger impedance in the regenerator means that the impedance of the traveling wave in the regenerator is much larger than that of a pure traveling wave. Therefore, although the acoustic phasing is such that the gas is forced to undergo a Stirling cycle within the regenerator, the acoustic velocities and resulting viscous losses are much smaller than those experienced by a thermoacoustic engine employing a pure traveling acoustic wave in the regenerator, as depicted in Figure 2.1.

Ceperley's original engine (1978, 1979) was unable to produce any net acoustic energy gain for this reason, although his later, untested designs (1982), were meant to remedy this problem by superimposing a standing wave on the traveling wave acoustic field. The invention of De Blok and Van Rijt (2001) also describes a similar arrangement to the acoustically compact network, which is meant to reduce the acoustic velocities and to create traveling wave acoustic phasing within the regenerator, though their designs include annular feedback paths as opposed to the toroidal feedback path in the TASHE.

One drawback of traveling wave thermoacoustic engines is that acoustic energy flux through the regenerator results in either a second order mean pressure gradient across the regenerator, or a mean mass flux, traveling in the same direction as the acoustic energy flux, due acoustic streaming in the regenerator [Gedeon (1997)]. In the TASHE, this results in a convection current that travels clockwise around the torus of the thermoacoustic driver, carrying thermal energy from the hot heat exchanger away from

the regenerator and out the secondary cold heat exchanger [Backhaus and Swift (2000)]. Since this degrades the performance of the engine, it is desirable to eliminate or minimize any clockwise mean flow around the torus and through the regenerator. To counteract this effect, the thermoacoustic driver of the TASHE includes a hydrodynamic mass-flux suppressor (or jet pump) that can be adjusted to minimize or eliminate any net flow of the compressible fluid around the torus. Since the operation of the mass-flux suppressor relies on turbulence and viscous dissipation of kinetic energy, its use in suppressing the clockwise convection current is also accompanied by some dissipation of acoustic energy.

Also, in the TASHE, conduction of heat through the walls of the torus can result in significant energy losses. These energy losses are due to heat conduction radially through the walls into the insulation or atmosphere surrounding the torus, and also due to axial heat conduction along the walls of the torus between the hot and cold heat exchangers, essentially bypassing the regenerator. To safely contain the high pressure gas in the TASHE, greater wall thickness is required, which results in greater axial conduction losses. In addition, the strength of the pipe wall is reduced at high temperatures, therefore limiting the maximum temperature, and hence the thermal efficiency, that the TASHE can attain [(Petach et. al. (2004)]. Furthermore, cross-flow heat exchangers, which are typically used due to geometric constraints, result in sub-optimal heat extraction and potentially enormous thermal stresses, especially in the hot heat exchanger, as will be discussed in Chapter 7. Given these inefficiencies, a need exists for more efficient traveling wave thermoacoustic devices.

2.1.2 *Traveling wave heat pumps*

In contrast to a thermoacoustic engine, which absorbs thermal energy in order to create acoustic energy, a traveling wave thermoacoustic heat pump absorbs work in the form of acoustic energy for the purposes of providing heating or cooling power. The primary difference which distinguishes the two types of devices is the direction of the acoustic energy flux in relation to the temperature gradient in the regenerator. In the engine, the acoustic wave travels in the same direction as the increasing temperature gradient, whereas the acoustic energy travels in the direction of decreasing temperature gradient in a traveling wave thermoacoustic heat pump.

Depending on where the ambient temperature heat exchanger is located, a traveling wave thermoacoustic heat pump can operate either as a refrigerator or a heater. In the traveling wave refrigerator of Figure 2.5a, a fraction of the acoustic power entering the regenerator on the left, $\dot{E}_h$, is absorbed in passing through the regenerator, resulting in a lower acoustic power, $\dot{E}_c$, exiting the right side of the regenerator. This work input produces heat pumping action up the regenerator's temperature gradient, which draws a cooling heat load, $\dot{Q}_c$, from the cold heat exchanger at the temperature T_c, and exhausts heat at a rate $\dot{Q}_0$ to the environment at the ambient temperature T_0. Likewise, the acoustic energy absorbed in the heat pump of Figure 2.5b draws heat at a rate $\dot{Q}_0$ from the environment through the ambient temperature heat exchanger, and delivers a heating power $\dot{Q}_h$ to the hot heat exchanger at the hot temperature T_h.

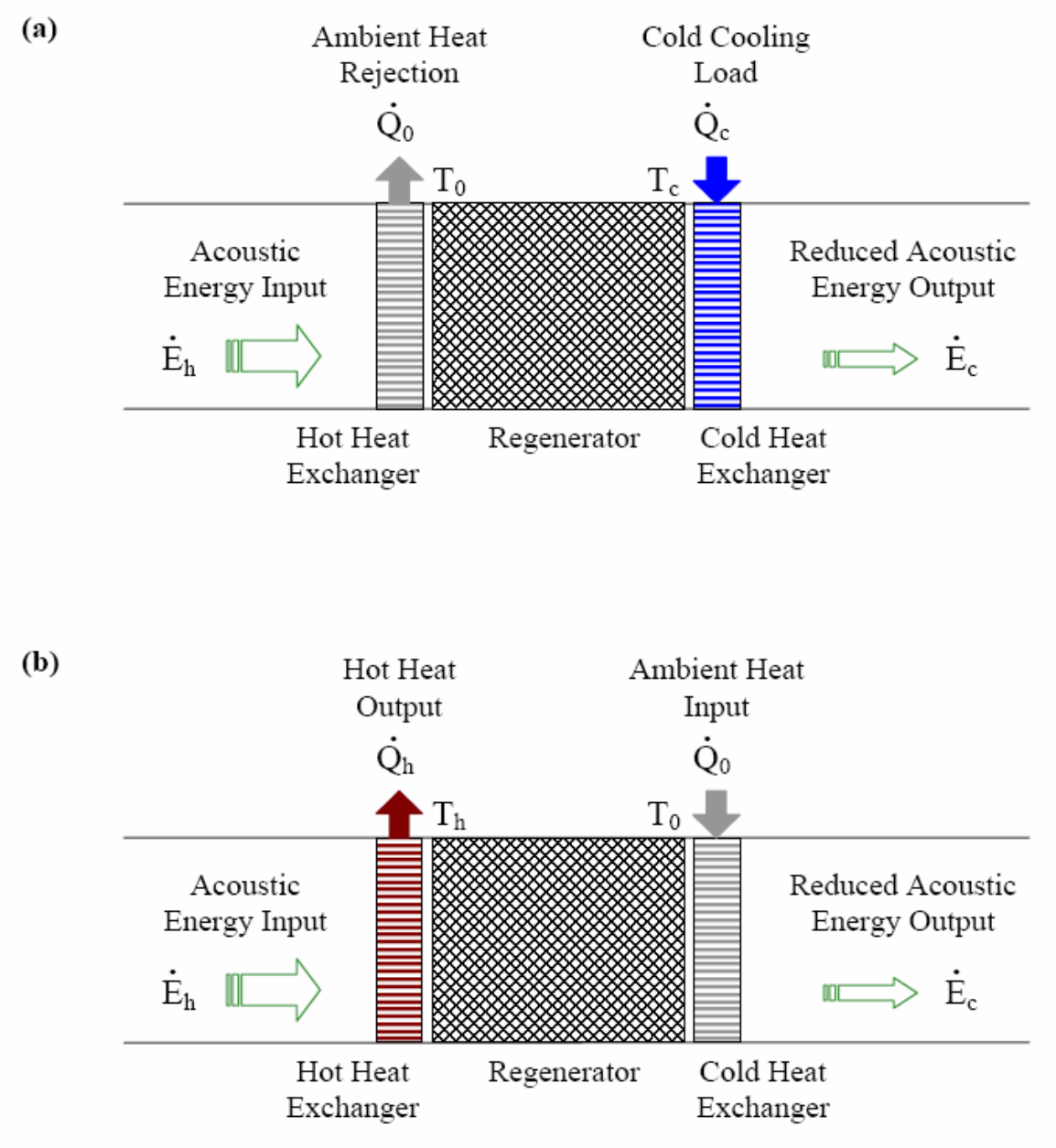

Figure 2.5: a) Traveling wave thermoacoustic refrigerator, b) Traveling wave thermoacoustic heater

2.1.2.1 Traveling wave heat pump thermodynamics

Central to the operation of either of the devices in Figure 2.5 is the fact that, as with the traveling wave engine, acoustic gas motions and pressure changes cause heat to be pumped through the regenerator in a direction opposite to that of the acoustic traveling wave. These processes are shown in greater detail in Figure 2.6a, which tracks a representative gas parcel through an acoustic cycle as was done above for the thermoacoustic engine. This cycle is identical to that for the thermoacoustic engine, as shown in Figure 2.2b, with the exception that the temperature gradient in the regenerator solid is reversed so that compression of the gas parcel occurs at high temperature and its expansion occurs at low temperature. As these compression and expansion processes are accompanied by heat transfer to and from the regenerator solid, respectively, the gas parcels "shuttle" heat from cold to hot, up the regenerator's temperature gradient.

Accounting for the oscillatory fluctuations in the gas properties and the reversed temperature gradient, Eqs. 2.6 and 2.7 are again used to calculate the gas properties throughout an acoustic cycle, and the results are plotted in Figure 2.6b. Using this data, the *p*-*v* and *T*-*s* diagrams can again be obtained for the cycle, though they look exactly the same as those for the traveling wave engine in Figures 2.3b and 2.3c, respectively. The only difference between this case and the engine case is that the cyclic integrals for work output, Eq. 2.8, and heat input, Eq. 2.9, traverse the ellipses in a counter-clockwise fashion over the course of an acoustic cycle. As a result, the work output, w, and the heat input, q, are both negative for the case of the thermoacoustic heat pump, as the above description of the device would imply.

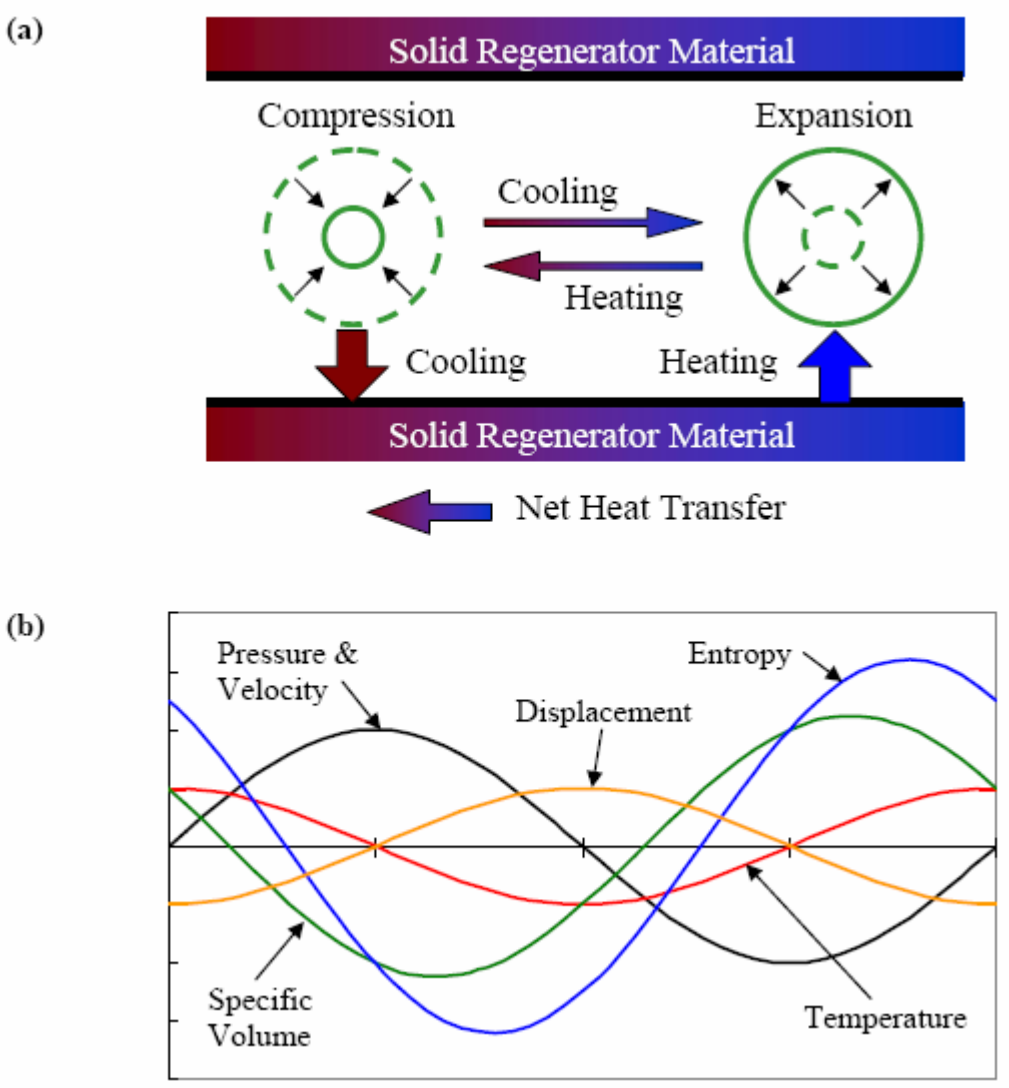

Figure 2.6: a) thermodynamic processes of an acoustically oscillating gas parcel within the regenerator of a thermoacoustic heat pump, b) Gas parcel properties as a function of time for one acoustic cycle in the thermoacoustic heat pump

2.1.2.2 History and applications of the traveling wave thermoacoustic refrigerator

Conventional traveling wave thermoacoustic refrigerators evolved out of the field of pulse tube refrigeration [Radebaugh (1990), Popescu et. al. (2001), Swift (2002)], which was accidentally discovered and exploited for cryogenic refrigeration applications. These devices used the interactions of acoustic pressure oscillations with the walls of a "pulse tube" to produce refrigeration, though it wasn't until later that the stacks and regenerators of conventional thermoacoustic refrigerators were added. With the addition of an orifice at one end of the pulse tube, traveling wave acoustic phasing was attained in the regenerator, and traveling wave thermoacoustic refrigeration was born. While these devices were able to attain low refrigeration temperatures, much of the input acoustic power was dissipated in the orifice for the purposes of creating the required traveling wave acoustic phasing.

The recent innovation of the acoustic feedback loop by Swift et. al. (1999) has increased the efficiency of the pulse tube refrigeration process by recycling the previously dissipated acoustic power. The pulse tube refrigerator of Swift et. al. (1999) is very similar to the TASHE of Figure 2.4, except that the acoustic traveling waves propagate in a counter-clockwise direction through the torus. These acoustic traveling waves are attenuated in the regenerator, and result in a refrigerator configuration in which heat is pumped from the cold heat exchanger to the hot heat exchanger, in a manner similar to that shown in Figure 2.5a.

The inherent simplicity of the traveling wave thermoacoustic process represents a substantial improvement over Stirling and other types of refrigeration cycles, simply due to the reduction in the number of moving parts. This is particularly true in regards to the

Stirling refrigeration cycle, since the moving component that has been removed is the cold displacer piston, which accounted for much of the irreversibility in the cycle due to the cold friction losses on the piston seal. However, note that the thermoacoustic refrigerator still requires an acoustic power input in order to produce refrigeration, and many designers have opted to use electrodynamic drivers, such as those produced by CFIC Inc. [Yarr and Corey (1995)], to generate this acoustic power. Although this type of design is appropriate for some applications, these components still contain moving parts that require maintenance and increase the complexity and production cost of these refrigerators. In addition, these transducers require an electrical energy input, which increases the complexity involved in using these devices in remote or portable cooling applications. In contrast, traveling wave thermoacoustic engines could provide this acoustic energy input without the addition of moving parts or the use of electric power, thereby increasing the reliability and portability of the thermoacoustic refrigeration process.

The ability of traveling wave refrigerators to achieve cooling temperatures as low as 30 K in a single stage, and 3.6 K in multiple stages [Popescu et. al. (2001)], has made them very popular in the field of cryogenics, particularly since they have eliminated the cold piston seal problem of Stirling refrigerators. In these applications, they are frequently used for liquefaction of gases such as methane, which are more easily contained and transported in a liquid state. Additionally, the fact that thermoacoustic refrigerators work best with inert gases such as helium makes them attractive for more widespread refrigeration applications, as they do not require exotic or environmentally toxic refrigerants to produce cooling power. Despite the fact that pulse-tube

thermoacoustic refrigeration has found widespread use in the industrial sector, there is currently very little interest in applying traveling wave thermoacoustics in heat pump applications, although Swift (2002) has mentioned the possibility of using them in industrial drying and commercial or residential water heating applications.

2.2 Standing Wave Thermoacoustics

Another method by which thermal energy can be converted into acoustic energy, and vice versa, is through the use of standing wave thermoacoustics [Swift (1988, 2002)]. Though similar in many ways to traveling wave thermoacoustics, the basic thermodynamic cycle that is used in standing wave thermoacoustics is fundamentally different, as is some of the hardware required to achieve the thermoacoustic energy conversion. As the name implies, these devices employ standing wave acoustic phasing in which acoustic pressure and velocity oscillations are 90° out of phase. A pure standing wave cannot transmit any acoustic energy because of this, and as a result, a heat transfer time delay is required in order to produce or absorb any acoustic energy in a standing wave thermoacoustic cycle.

To achieve this time delay, the regenerator in the traveling wave thermoacoustic device is replaced by a "stack," which is simply a stack of thin parallel plates, separated by gaps that are on the order of 1-4 times the thermal penetration depth, δ_k. The larger plate separation yields imperfect thermal contact between the solid and the gas, where heat transfer between the two is approximately proportional to the temperature difference between the gas and the solid. Unfortunately, heat transfer across a finite temperature difference is an inherently irreversible process, though it is required for proper operation of the standing wave thermoacoustic device.

In spite of this inherent loss mechanism, standing wave thermoacoustic systems have been extensively studied in the literature, probably because of the relative ease with which an acoustic standing wave can be created. However, the thermal efficiency difference between the two types of thermoacoustic engines is fairly substantial. Specifically, the most efficient standing wave thermoacoustic engine to date has achieved a thermal efficiency of about 20%, while its traveling wave counterpart has achieved thermal efficiencies of about 30% [Backhaus and Swift (2000)]. Therefore, since we are interested in creating an engine with a high fuel energy to acoustic energy conversion efficiency, and the reversible traveling wave engine possesses an inherent thermal efficiency advantage over the standing wave engine, standing wave thermoacoustic engines will not be considered further in this work.

2.3 Open vs. Closed Cycle Thermoacoustics

2.3.1 The open cycle standing wave refrigerator

Research in the field of thermoacoustics has been limited mostly to closed cycle designs in recent years, although there is a potential for significant improvements in efficiency for open cycle thermoacoustic devices. Recognizing this potential, the first open cycle thermoacoustic refrigerator was built and tested by Reid et. al. (1998) at Los Alamos in 1997. This device, shown in Figure 2.7, is composed of a loop, one acoustic wavelength long, with inlet and exhaust ports at the top and bottom of the loop, respectively. Loudspeakers drive an acoustic standing wave in this loop, with the pressure nodes at the inlet and exhaust ports to minimize the acoustic losses through these ports. By driving the speakers 180˚ out of phase with one another, the working fluid

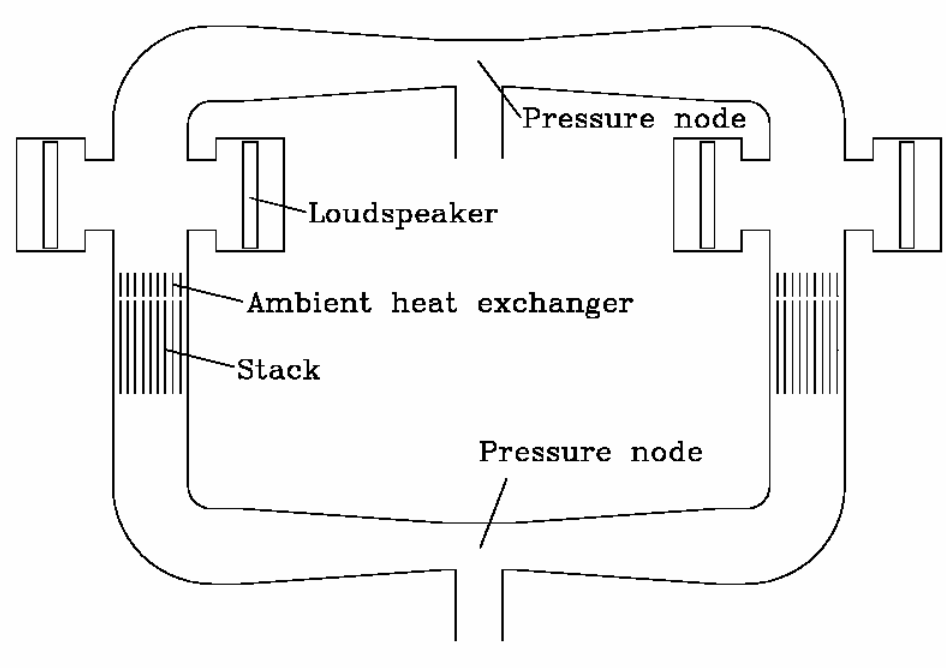

Figure 2.7: Schematic of the open cycle standing wave thermoacoustic refrigerator. (Reprinted with permission from [Swift (2002)])

oscillates back and forth between the two halves of the device, forming a full wavelength standing wave in the loop.

Standing wave thermoacoustic processes create a temperature difference across the stacks in each half of the refrigerator, from ambient temperature at the heat exchanger above the stack to some cold temperature at the cold heat exchanger below the stack. A slow mean flow is imposed on standing wave thermoacoustic oscillations, entering at the pressure node at the upper inlet port. The steady flow is cooled in passing through the stack on each side of the device, and exits at the pressure node at the lower exhaust port.

In this arrangement, a thermodynamic advantage is gained in that refrigeration occurs over the full range of gas temperatures in the stack, which is more efficient than providing cooling power only at the temperature of the cold heat exchanger [Reid et. al.

(1998), Reid and Swift (2000)]. Furthermore, it was also found that the addition of a mean flow eliminates the need for the cold heat exchanger, provided that the mean flow velocity is an order of magnitude smaller than the acoustic velocity amplitude in order to keep thermal convection effects from overwhelming the thermoacoustic effects in the device.

2.3.2 Open cycle thermoacoustic engines

So long as the slow mean flow condition is met, it is expected that the superposition of a steady flow can be used to eliminate one of the two heat exchangers in thermoacoustic heat pumps and engines as well [Reid (1999)]. In a thermoacoustic engine, this open cycle configuration would enable a flow of hot gas, created either by combustion or some other means, to replace the hot heat exchanger for a more direct conversion of fuel energy to acoustic energy, thereby eliminating the heat exchanger's cost, complexity and inefficiency. Furthermore, allowing for the passage of a fluid through a thermoacoustic engine opens up the possibility of creating an engine that employs a combustion process, either inside or outside the engine, to generate a stream of hot combustion products that pass through the stack or regenerator to provide the engine's thermal energy input.

In designing an open cycle thermoacoustic device, the utilization of standing wave thermoacoustics is appealing because the inlet and exhaust ports can be located at the pressure nodes in order to minimize the loss of acoustic energy through these ports [Reid and Swift (2000)]. However, standing wave thermoacoustic systems rely on irreversible processes for their operation, thus they are inherently less efficient than their traveling wave counterparts, as mentioned above [Backhaus and Swift (2000)]. It would

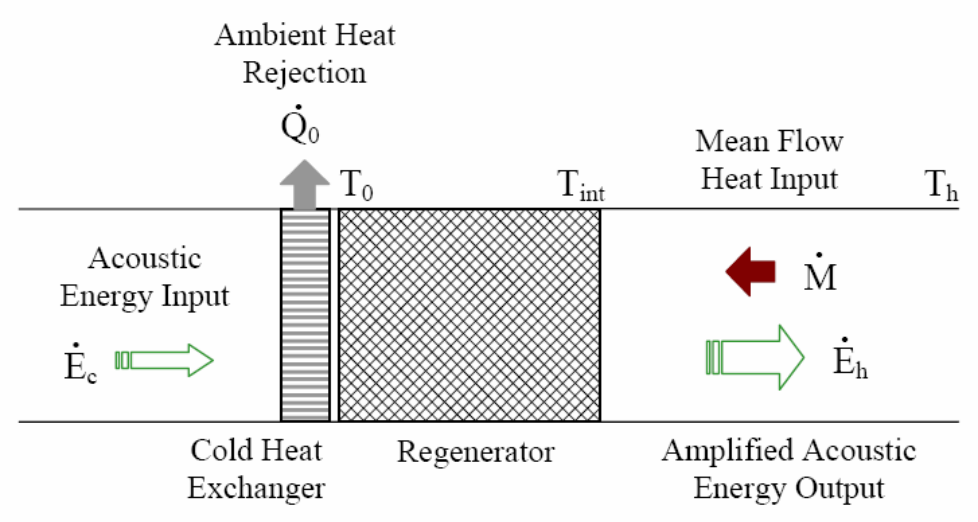

Figure 2.8: Schematic of a simple open cycle traveling wave thermoacoustic engine

therefore be desirable to combine the inherent efficiency advantages of traveling wave thermoacoustics with the benefits of an open cycle architecture. Such a combination offers, in principle, the most efficient means of converting the thermal energy in a stream of gas into acoustic energy. However, the implementation of such an engine is more challenging due to the lack of true acoustic pressure nodes in a traveling wave acoustic field, which minimize the escape of acoustic energy from the system, as with the open cycle standing wave refrigerator.

A schematic of a simple open cycle traveling wave thermoacoustic engine is shown in Figure 2.8 [Weiland and Zinn (2003)]. A slow mean flow of hot gas is superimposed on the acoustic field in the device, and approaches the regenerator from an open duct on the right. The origin of this hot gas is not important for the purposes of this example, but could be supplied by a combustion process, for instance, occurring either inside or outside the thermoacoustic device. A cold heat exchanger at the other end of the regenerator rejects heat to the surroundings at the ambient temperature, T_0, and

creates a temperature gradient across the regenerator. As the mean flow passes through the regenerator, some of its thermal energy is converted into acoustic energy, thus amplifying a traveling acoustic wave as it moves from the cold side to the hot side of the regenerator [Ceperley (1978, 1985)].

Note, however, that by replacing the hot heat exchanger in such a device by a mean flow of hot gas, an unusual heat transfer situation at regenerator's hot-side interface is created [Weiland and Zinn (2003)]. As will be shown in Chapter 4, steady-state operation of this engine requires that a mean temperature difference exist between the incoming mean flow and the regenerator's solid material at this interface. This temperature difference is not necessarily small, and may profoundly affect the acoustics, thermodynamics and overall performance of the engine.

2.4 Pulse Combustion

Pulse combustion devices come in many shapes and sizes, though they all share a common trait in that they each take advantage of the interaction between combustion and acoustic processes. To drive acoustic oscillations, the oscillating combustion must satisfy Rayleigh's criterion, which states that a periodic heat addition process amplifies/damps acoustic energy if it is in/out of phase with acoustic pressure oscillations [Zinn (1986)].

Although the Rayleigh criterion is fairly general and can be used to help describe many oscillating combustion processes, a distinction is generally made between beneficial and detrimental oscillations. The latter are usually referred to as combustion instabilities, which range in severity from a simple nuisance, in the case of a noisy, "buzzing" flame, to very damaging or even catastrophic instabilities in rocket motors and jet engines. Due to the wide range of problems that these combustion oscillations can

cause, there is a great body of research that is aimed at understanding and suppressing these oscillations.

At the other extreme, the study of beneficial combustion oscillations are considered to be part of the general field of pulse combustion. In these systems, the acoustic oscillations are used for a variety of purposes such as increasing heat transfer rates, pumping combustion reactants and products through the system, generating thrust, or simply enhancing the combustion process by improving fuel/air mixing or decreasing pollutant emissions [Zinn (1986)].

The operation of a general air-breathing pulse combustor is depicted in Figure 2.9, where the physical processes occurring in the combustor are shown at four different times during the combustion cycle [Zinn (1986)]. On the left side of the device is the combustion chamber and the flapper valves, which open when the pressure in the combustion chamber is low, and close when the pressure is high. The right side of the device is comprised of the exhaust pipe, which is generally tailored to best suit the particular application of the pulse combustor.

In the steady state operation of a pulse combustor, a typical cycle begins with the ignition of a combustible fuel/air mixture within the combustion chamber, as shown in Figure 2.9a. The combustion process increases the temperature and pressure of the gas mixture, causing the flapper valves to close. This also causes the gas to expand, initiating the flow of combustion products towards the exhaust. In the next stage, the inertia of the flowing combustion products creates a region of low pressure in the combustion chamber. As a result, the flapper valves open and admit a fresh charge of fuel and air into the combustion chamber as shown in Figure 2.9b. The fuel and air generally enter

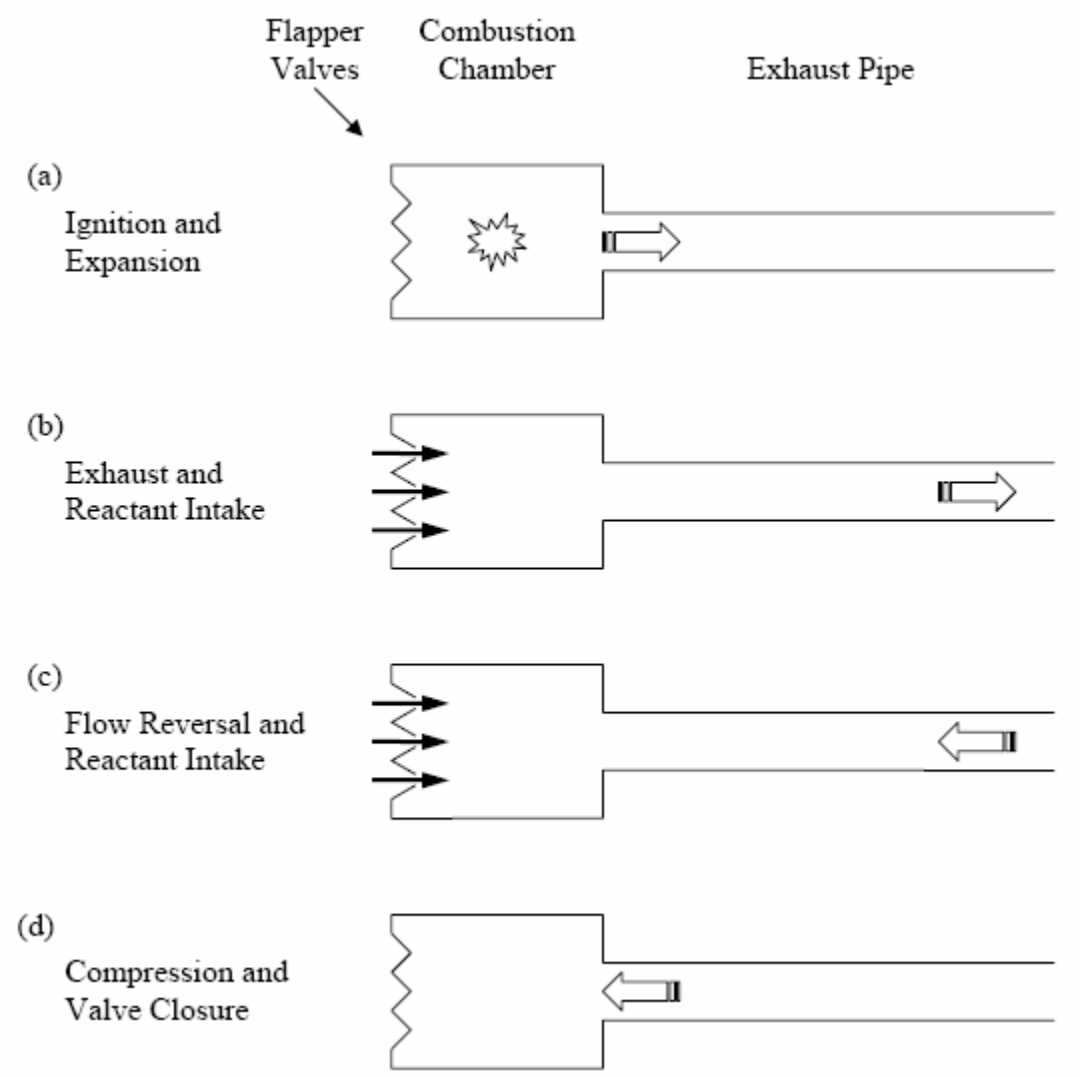

Figure 2.9: Operation of a simple air-breathing pulse combustor

the device through separate inlet ports, and mix upon entering the combustion chamber. As shown in Figure 2.9c, the low pressure in the combustion chamber eventually causes the product gases in the exhaust pipe to reverse direction and flow back towards the combustion chamber during the third stage of the pulse combustion cycle. In the final stage of Figure 2.9d, the influx of combustion reactants and the return flow of the combustion products increases the pressure in the combustion chamber, causing the fuel/air mixture to be compressed. Through a combination of several effects, including compression of the reactants, contact with hot surfaces in the combustion chamber and mixing of the reactants with hot combustion products and the reactive combustion radicals that they contain, the combustible mixture ignites in the combustion chamber, and the pulse combustion cycle begins again from Figure 2.9a. This process is self-sustaining, and will continue indefinitely until the flow of fuel to the pulse combustor is turned off.

Using the acoustic processes described above, the pulse combustor can be made to resemble a Helmholtz resonator, where the combustion chamber forms the compliance and the exhaust pipe forms the inertance, both of which are much shorter than an acoustic wavelength. For larger or higher frequency devices, the acoustics of the pulse combustor resemble a 1/4 wavelength standing wave pipe, with a closed end at the flapper valves and an open end at the far side of the exhaust pipe. In either case, the operating frequency of the device is generally the lowest resonant frequency determined by the geometry of the pulse combustor, although tunable pulse combustors have been designed that can operate over a range of frequencies [Zinn (1996)].

One of the first successful applications of pulse combustion was in the German-made V-1 "Buzz Bomb," where the pulse combustion process was used to generate thrust for propelling rockets during World War II [Zinn (1986)]. The Lennox pulse combustion furnace represents a more recent success of pulse combustion, where the oscillating gas flow in the exhaust pipe of the pulse combustor enhances the rate of heat transfer out of the exhaust pipe, thus providing a very efficient means for residential heating [Zinn (1996)]. Another promising application is the tunable pulse combustor, which provides acoustic and thermal energy to a large vessel for the purposes of accelerating a range of industrial processes occurring in the vessel, including waste incineration, spray drying, or metal heating processes [Zinn (1996)].

CHAPTER 3

THE THERMOACOUSTIC PULSE COMBUSTION ENGINE

The Thermoacoustic Pulse Combustion Engine (TAPCE), as described below, ameliorates several of the problems associated with the TASHE or other known thermoacoustic devices [Weiland and Zinn, (2003b), Weiland et. al. (2004)]. Unlike the conventional thermoacoustic driver of the TASHE, which seeks to eliminate any mean flow, the TAPCE introduces a mean flow across the regenerator. This mean flow is superimposed on the acoustic motions of the fluid and, for small mean flow velocities relative to the acoustic velocities, the mean flow and the acoustic motions can be considered to act independently of one another. The use of an applied mean flow facilitates the addition of an internal combustion process in the device, as the mean flow can supply the combustion process with fresh reactants and carry away combustion products. Adding inlet and exhaust ports to bring in combustion reactants and carry away combustion products signifies an important shift from a traditional closed cycle thermoacoustic engine such as the TASHE, to an open cycle engine configuration. Thermodynamically, an open cycle thermoacoustic engine can be more efficient than a closed cycle thermoacoustic engine in converting fuel energy to acoustic energy, as the inefficiencies of the hot heat exchanger have been eliminated in an open cycle configuration.

Thus, as a result of the mean flow, the hot heat exchanger may be replaced by a mean flow of hot gas, where the heat in the hot gas is obtained from a combustion zone inside the device. The absence of the hot heat exchanger can drastically reduce thermal stresses that are present in the TASHE and other thermoacoustic engines, particularly if the heat exchanger being replaced is a cross-flow hot heat exchanger. Additionally, by concentrically disposing a thermoacoustic driver within an outer shell, the thickness of the walls of the thermoacoustic driver may be significantly reduced. Consequently, axial heat conduction losses through these walls may be reduced as a result of the reduced wall thickness, and higher combustion temperatures can be attained without reducing the strength of the pressure vessel design. Furthermore, radial heat transfer from the thermoacoustic driver may be used to further increase the efficiency of the thermoacoustic device in some configurations.

3.1 The TAPCE Design

As shown in Figure 3.1, the complete thermoacoustic device is composed of the TAPCE and a resonator, which includes a wave guide attached to an acoustic load. Specific forms of the acoustic load will be presented at a later point in this chapter, when the various applications of the TAPCE are discussed. The entire device is filled with air and combustion products that can be pressurized to increase its acoustic power density, which reduces the impact of thermal conduction losses within the thermoacoustic device. Unlike the conventional thermoacoustic driver of Figure 2.1 or the TASHE of Figure 2.4, the TAPCE of Figure 3.1 generates acoustic energy by supplying heat to a regenerator with a mean flow of hot combustion products.

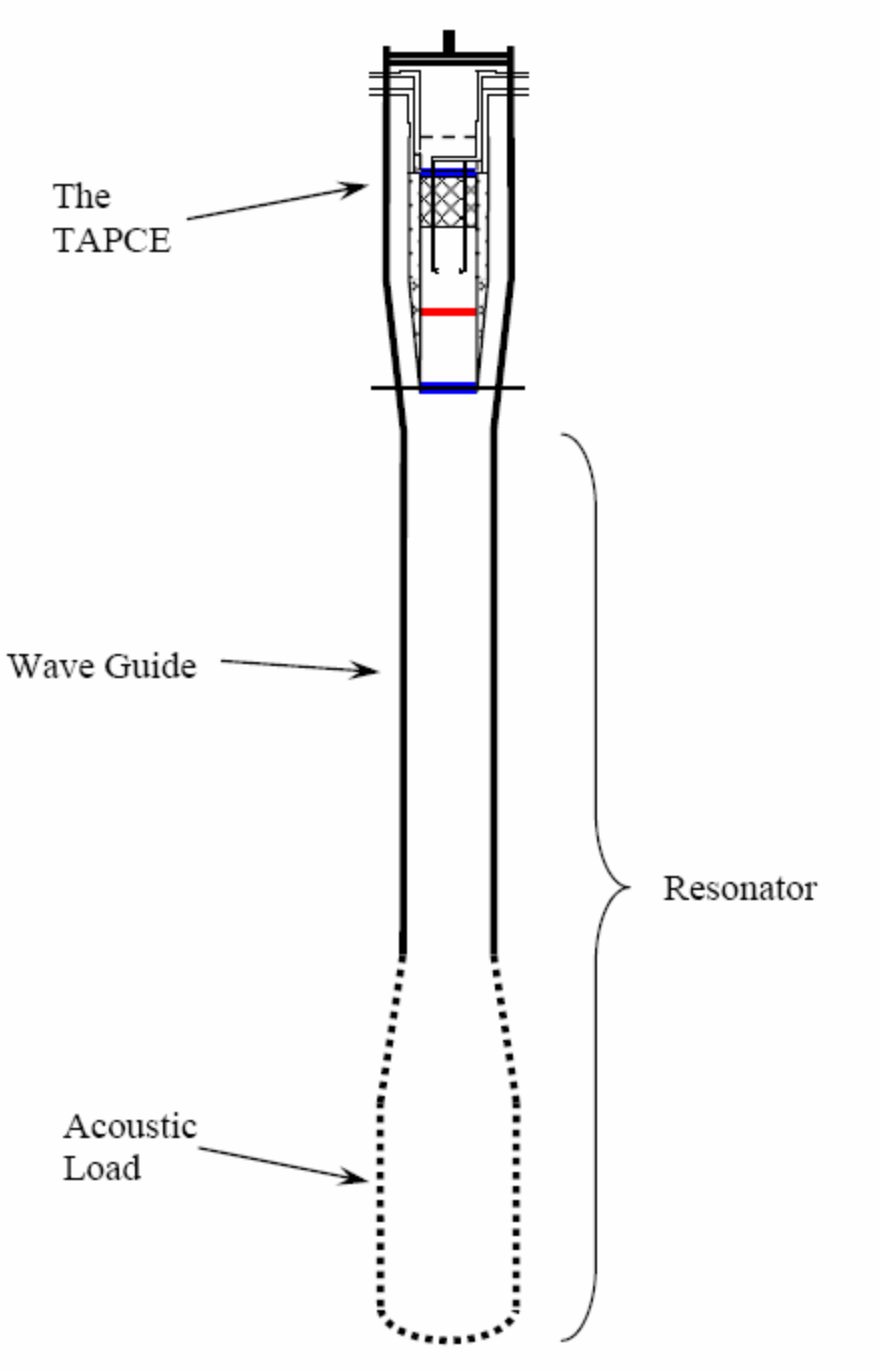

Figure 3.1: Schematic of the TAPCE and resonator portions of a thermoacoustic device

3.1.1 The acoustically compact network

The Thermoacoustic Pulse Combustion Engine is shown in greater detail in Figure 3.2, and is primarily composed of a cylindrical shell and a thermoacoustic driver, which is located inside an inner pipe concentrically disposed within the shell. By locating the thermoacoustic driver within the shell, the burden of containing the potentially high pressures inside the device is shifted from the thermoacoustic driver to the shell. Thus, the thickness of the walls of the thermoacoustic driver may be significantly reduced as compared to the TASHE. Consequently, axial conduction losses through these walls may be greatly reduced due to the reduced wall thickness. In addition, higher temperatures than those used in the TASHE can be used without fear of pressure vessel failure, which in turn should result in higher thermal efficiencies. Furthermore, this configuration promises to be easier to construct, in many regards, than the toroidal architecture of the TASHE [Backhaus and Swift (2000)].

The size and positioning of the thermoacoustic driver within the shell creates a compliance section and an inertance section, which permit the feedback of acoustic energy from the hot end of the thermoacoustic driver to the cold end. The inertance is formed by the annular region between the thermoacoustic driver and the shell, while the compliance is formed by the open volume in the shell, above the thermoacoustic driver and the inertance.

To retain the acoustic characteristics of the highly successful TASHE engine, the geometries of the inertance and compliance are designed to mimic the acoustically compact network of the TASHE [Backhaus and Swift (2000)]. This is achieved by computing the acoustic impedance ratios between of various components in the TASHE,

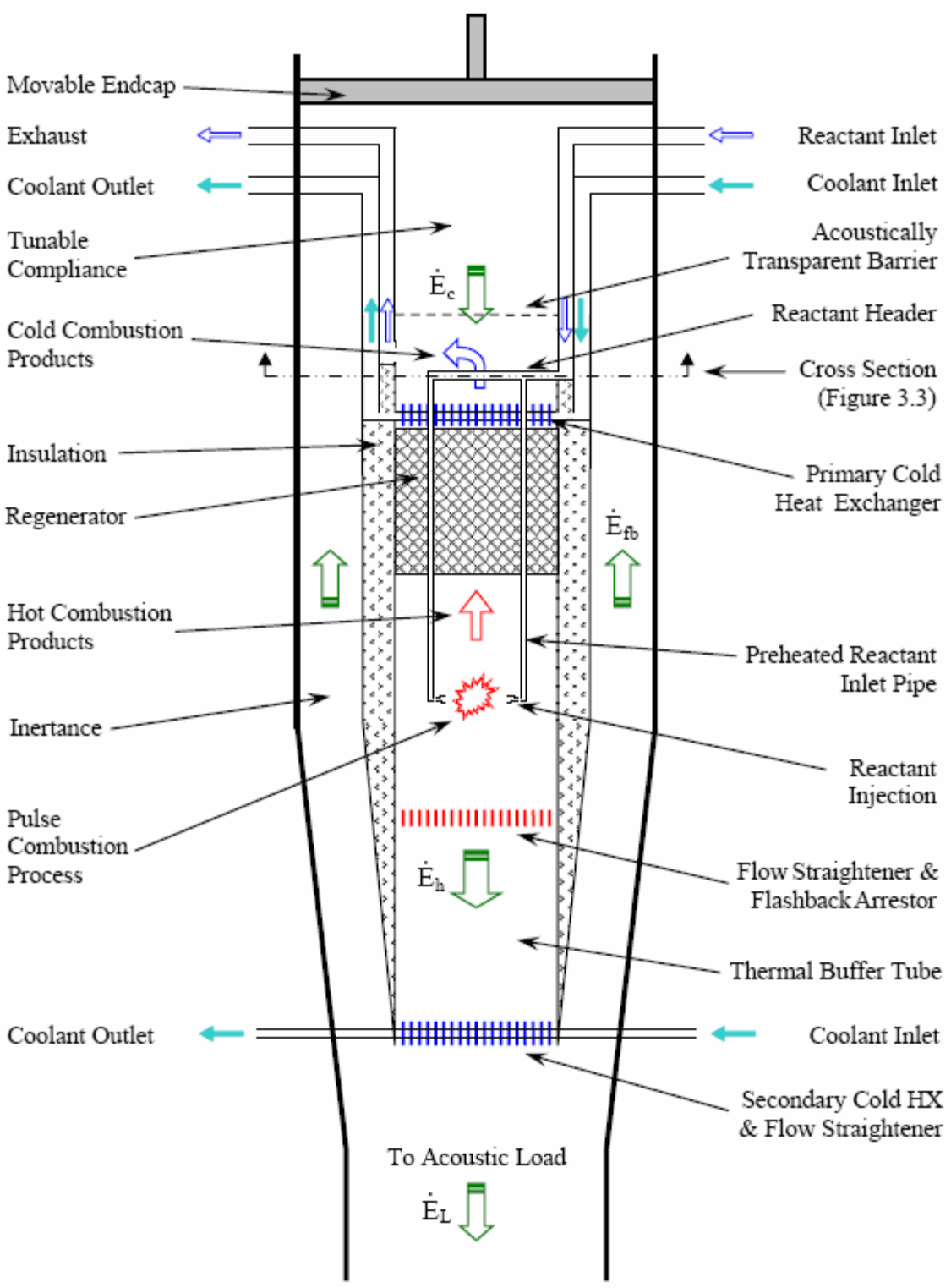

Figure 3.2: A schematic of the detailed TAPCE design.

and designing the TAPCE geometry to match these impedance ratios. In this manner, the starting design of the geometry of the TAPCE retains the acoustic character of the TASHE, although this geometry can be further optimized once a full model of the TAPCE is created. This process is discussed in further detail in Chapter 5.

The compliance section, the inertance section, and the regenerator make up the basic components of the acoustically compact network in the TAPCE, which sets up a traveling wave acoustic phasing at the regenerator, thereby constructively providing the feedback acoustic energy for amplification at the regenerator. Additionally, these components are geometrically configured to establish a region of relatively low acoustic velocity across the regenerator, thereby decreasing viscous losses within the regenerator.

Depending on the internal pressure chosen, the TAPCE may have a movable end-cap positioned at the top of the shell in order to tune the volume of the compliance section. Since an impedance matching condition between the compliance and the resonator primarily determines the resonant frequency of the device [Backhaus and Swift (2000)], adjustment of the volume of the compliance permits one to make small adjustments to the resonant frequency of the thermoacoustic device. In addition to providing a tunable compliance, the end-cap permits easy access to the thermoacoustic driver in the event that maintenance is required on the thermoacoustic driver.

Finally, note that the density of the gas in the inertance is important in determining the mass-like properties of this component in the acoustically compact network. In order for this component to operate as designed, it is important that the density of the gas in the inertance, and hence its temperature, remain constant. This is accomplished by thermally insulating the thermoacoustic driver from the rest of the

device by insulating its walls and positioning a cold heat exchanger at either end of the thermoacoustic driver, as shown in Figure 3.2.

Insulating the inner pipe from the annulus surrounding it would be most effectively accomplished by constructing the inner surface of the annulus with pipes that are attached to either end of the inner pipe, thereby creating an enclosed, annular insulating space around the inner pipe, as shown in Figure 3.2. Pipes entering and exiting the inner pipe can be routed through this annular region without interfering with the acoustics of the engine, and the insulation properties of this annular region can be enhanced by either evacuating the insulating space or filling it with a highly insulating material.

3.1.2 The thermoacoustic driver

As shown in Figure 3.2, the interior of the thermoacoustic driver contains a primary cold heat exchanger, a regenerator, a combustion zone, a flow straightener, a thermal buffer tube, and a secondary cold heat exchanger. The heat exchangers are typically crossflow heat exchangers of the shell and tube variety, as are commonly used in thermoacoustic devices [Backhaus and Swift (2000), Swift (2002)]. The regenerator has a cold side, which is coupled to the primary cold heat exchanger, and a hot side, which is coupled to the combustion zone, thus establishing a temperature gradient across the regenerator. The temperature gradient amplifies acoustic traveling waves as the combustion products expand and contract within the regenerator due to the pressure oscillations of the acoustic traveling wave. This process is identical to that described for a general traveling wave thermoacoustic engine in the previous chapter.

The regenerator consists of packing material that is fine enough to force the combustion products in the regenerator to essentially be in thermal equilibrium with the packing around it, but not so fine as to prevent the passage of acoustic waves through the regenerator. As mentioned above, many regenerator geometries have been used, including stacks of parallel plates [Backhaus and Swift (2001)], stacks of wire mesh screens [Backhaus and Swift (2000), Kays and London (1984)], and packed steel wool [Ceperley (1979)].

The stacked wire mesh screen regenerator is the ideal choice for this application, as it is easy and inexpensive to produce, and offers the desired thermal conduction characteristics. As the individual stainless steel screens are stacked together in the axial direction, the intermittent surface contact between adjacent screens drastically reduces the axial thermal conduction losses down the regenerator's temperature gradient. In addition, the wires in the screen provide good lateral thermal conduction, which is important in providing a more uniform lateral temperature profile in the regenerator. This is especially true in the somewhat non-uniform conditions in the case described below, where heat is transferred laterally to the reactant inlet pipes to preheat the combustion reactants as they pass through the regenerator. In this case, it may even be helpful to enhance the lateral heat conduction characteristics of the regenerator by using high-conductivity wire mesh screens (e.g., copper screens). However, in order to reduce the increased axial heat conduction losses that would accompany the use of high-conductivity screens, these screens should be alternated with screens of lower thermal conductivity (e.g., plastic, fiberglass screens) in the stack of wire mesh screens so as to interrupt the axial conduction of thermal energy.

The combustion zone below the regenerator is configured to burn a combustible mixture, which generates heat and the combustion products that are conveyed to the hot side of the regenerator by the mean flow. Specific designs for the combustion zone are considered below, though in some configurations, radiative heat transfer from the combustion zone to the regenerator may be used to augment the transfer of heat by convective means.

As shown in Figure 3.2, a flow straightener is located between the combustion zone and the thermal buffer tube to preserve thermal stratification in the thermal buffer tube. Since the combustion zone contains a pulse combustion process, a fairly turbulent environment may exist within the combustion zone, which in turn may introduce undesired turbulence into the thermal buffer tube through axial acoustic gas motions. The flow straightener reduces the encroachment of turbulence from the combustion zone to the thermal buffer tube, although it may also serve a secondary role as a flashback arrestor.

Through gas diffusion and the axial acoustic motions that occur across the flow straightener between the combustion zone and the thermal buffer tube, it is possible that the thermal buffer tube may contain some quantity of unburned combustible mixture. Through thermal and chemical interactions with the walls of the flow straightener, the flames that burn the combustible mixture in the combustion zone should not be able to propagate beyond the flow straightener/flashback arrestor [Turns (1996)]. Thus, the combustible mixture in the thermal buffer tube should not explosively ignite and burn, thereby avoiding a potentially hazardous situation. Another way to avoid this problem is to coat the flow straightener with a catalyst, which would promote combustion of any

fuel attempting to flow downward into the thermal buffer tube, thereby limiting combustion processes to the combustion zone and keeping the remainder of the device free of potentially explosive mixtures. In addition, note that the upward direction of the mean flow and the natural buoyancy of the preheated combustion reactants and hot combustion products should help confine the combustion process to regions close to the regenerator.

The thermal buffer tube is used to help thermally isolate the combustion zone from the remaining portion of the interior of the shell. The gas within the thermal buffer tube sustains a mean temperature gradient from its hot side, which is coupled to the combustion zone, to its cold side, which is coupled to a secondary cold heat exchanger. Ideally, the gas in the thermal buffer tube will remain thermally stratified along its length, and the stability of this configuration is enhanced by orienting the thermal buffer tube with its hot end on top to take advantage of thermal buoyancy effects. To effectively sustain such a temperature gradient, net convective heat transfer in the thermal buffer tube must be minimized so that the primary method of heat transfer down the thermal buffer tube is either through thermal conduction in the gas, or through axial thermal conduction in the portion of the insulated wall that surrounds the thermal buffer tube, depending on the thickness and axial thermal conductivity of this wall. For efficient operation, the thermal buffer tube should preferably be at least six times as long as the acoustic displacement amplitude [Swift (2002)], and may be tapered to reduce the effects of Rayleigh streaming in the thermal buffer tube [Olson and Swift (1997), Swift and Olson (1999), Swift (2002)].

In conjunction with the primary cold heat exchanger and the insulated wall, the secondary cold heat exchanger thermally insulates the thermoacoustic driver from the remaining portion of the interior of the shell. The secondary cold heat exchanger helps generate the temperature gradient along the length of the thermal buffer tube, and removes any heat that is transferred down this temperature gradient from the combustion zone. Also, in the event that the flow straightener between the combustion zone and the pulse tube fails to operate effectively as a flame arrestor, the removal of heat at the secondary cold heat exchanger ensures that flames will not propagate out of the thermoacoustic driver and into the remainder of the device.

While not shown in Figure 3.2, an additional flow straightener may be coupled to the secondary cold heat exchanger at the end of the thermal buffer tube to help preserve the thermal stratification in the thermal buffer tube. This flow straightener would serve to suppress the non-axial flow movements that will be generated due to turbulent acoustic gas motions at the junction between the inertance and the lower end of the thermoacoustic driver.

3.1.3 Flow paths in the TAPCE

Both the primary and secondary cold heat exchangers require connecting pipes for the inlet and outlet flow of the coolant, which is generally cold tap water. The coolant inlet and outlet pipes for each of the heat exchangers, in addition to the reactant inlet and exhaust pipes, also serve the dual purpose of acting as the suspension system that holds the thermoacoustic driver concentrically within the outer shell. Since they pass through the high velocity region of the inertance, efforts should be made to reshape or locate these pipes within the inertance to reduce the viscous losses that they might produce. Towards

the top of the engine, this may best be achieved by routing the pipes through the lower velocity regions of the compliance.

As shown in Figure 3.2, a reactant inlet header carries combustion reactants from outside the engine to the space above the primary cold heat exchanger. To reduce viscous losses in the high velocity region of the inertance, it would be preferable if the reactant header entered the thermoacoustic driver through the compliance as shown. Inside the thermoacoustic driver, several individual reactant inlet pipes branch off of the reactant header, pass through the cold heat exchanger and the regenerator, and admit the combustion reactants directly to the combustion zone. This is done to preheat the combustion reactants before they enter the combustion zone.

As the theory of the following chapter shows, the heat transferred to preheat the combustion reactants is essentially waste heat that is not used by the thermoacoustic processes to amplify the acoustic traveling wave, thus it is advantageous to preheat the combustion reactants as much as possible. Later analysis shows that numerous small diameter reactant inlet pipes would accomplish this task most effectively, though there are practical constraints as to how many and how small these pipes can be. In particular, the number of preheat pipes is limited by the complexity of the reactant header design, the desire to reduce axial thermal conduction losses down the reactant pipe walls and viscous acoustic energy losses on the outer surfaces of the pipes. As a good balance between preheating effectiveness, complexity, and reduced loss mechanisms, the configuration of seven reactant inlet pipes as shown in Figure 3.3 should work well as a starting point.

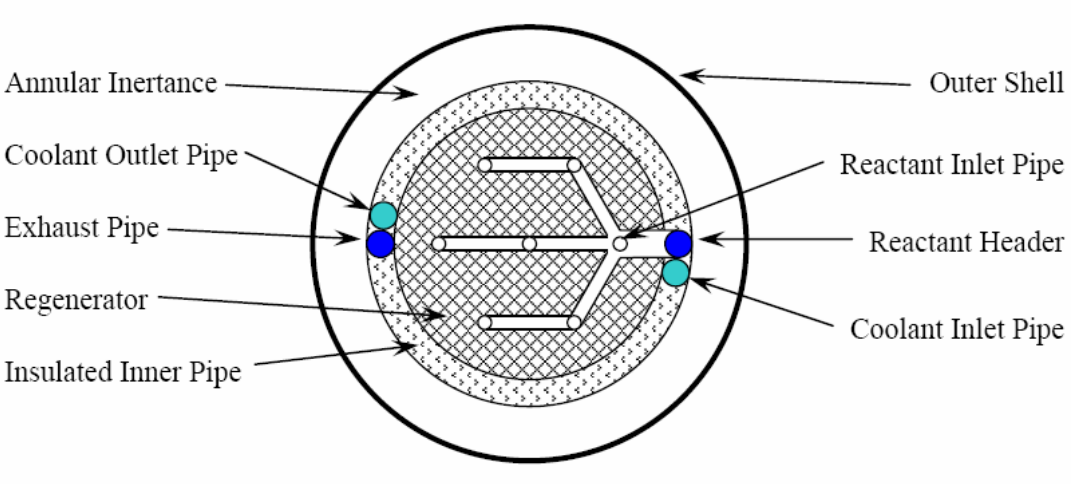

Figure 3.3: Top view schematic of the cross section from Figure 3.2, showing the reactant header and reactant inlet pipe configuration.

In some cases, it may also be advantageous to configure a portion of the reactant inlet as a thin annulus that surrounds the regenerator and the combustion zone in order to help thermally insulate the regenerator and the combustion zone from the rest of the device, and to increase the amount of heat transferred to the combustion reactants. In other cases, it may also help to add fins or ridges to those portions of the interior of the reactant inlet pipes or annulus that are in thermal contact with the regenerator, in order to enhance the rate of radial heat transfer out of the regenerator [Incropera and DeWitt (1996)].

Note that if the combustion reactants are premixed, that a significant amount of reactant preheating could cause combustion of the reactants to occur within the inlet pipes. So long as heat release from combustion begins outside the regenerator, after the reactant preheating, this situation may not be overly problematic. The primary problem with premature combustion of premixed reactants is flashback, where a flame propagates

upstream through the inlet pipes, creating a potentially explosive situation. In this case, flashback can be avoided by either using small diameter inlet pipes than act as flame inhibitors and flashback arrestors [Turns (1996)], or by using separate fuel and air inlet pipes. Furthermore, since the reactant inlet pipes pass through the cold heat exchanger in the current TAPCE configuration, any flames that propagate upstream through the regenerator should be quenched by heat removal at the cold heat exchanger, virtually eliminating the possibility of flashback beyond this location.

To increase the efficiency of the device, the reactant inlet pipes and header may be configured to suppress the escape of acoustic energy from the thermoacoustic device. In one configuration, the use of quarter- or half-wavelength inlet pipes would reflect most of the acoustic energy entering these pipes back to the interior of the thermoacoustic driver, essentially setting up a standing acoustic wave in these pipes. Another option is to admit the combustion reactants to the combustion zone through choked nozzles, which will not allow acoustic perturbations to propagate upstream into these inlet pipes and out of the device. However, to create choking conditions at the nozzle exit, the supply pressure of the combustion reactants in the inlet header and pipes must be over twice that of the interior of the TAPCE [Fox and McDonald (1992)], which may be impractical for a highly pressurized engine. In addition, some acoustic oscillations may be desired in the reactant inlet pipes, since acoustic gas motions could increase the preheating heat transfer rate in these pipes.

Once inside the combustion zone, the reactants burn in a pulse combustion process to create hot combustion products, which are carried to the hot side of the regenerator by the mean flow as shown in Figure 3.2. Due to the close thermal contact

between the gas and the solid within the regenerator, the mean flow of combustion products from the hot side of the regenerator to the cold side of the regenerator causes the combustion products to be cooled and to exit the cold side of the regenerator at approximately the same temperature as the cold side of the regenerator. From there, the cold combustion products are carried out of the engine through the exhaust port. To minimize the escape of acoustic energy out this exhaust port, the pipe itself must either be very small in diameter, or should be configured to reflect acoustic energy back into the engine.

The TAPCE also contains an acoustically transparent barrier, located at the top of the thermoacoustic driver, which sustains a small mean pressure difference in order to direct the mean flow in the device from the inlet port, through the combustion zone and the regenerator, and out the exhaust port. In the absence of the acoustically transparent barrier, the regenerator presents a significant resistance to the mean flow in the device. Thus, the path of least resistance for the mean flow is from the inlet port, through the thermal buffer tube, inertance and compliance to the exhaust port, effectively bypassing the regenerator. The acoustically transparent barrier also prevents the introduction of mean flow from the thermoacoustic driver into the shell, separating the cold combustion products from the gas within the compliance.

Furthermore, the acoustically transparent barrier must allow the passage of the feedback acoustic energy from the inertance and compliance to the regenerator with minimal attenuation of acoustic energy. Ideally, the acoustically transparent barrier is simply a vibrating membrane that is impermeable to the mean flow in the device. In experimental devices, a rubber balloon [Swift et. al. (1999)] or a latex membrane

[Keolian and Bastyr (2004)] has worked adequately, though these are not appropriate solutions for commercial applications. In these situations, the mass and stiffness of a more durable membrane could be chosen (or constructed by lamination) to assure that its resonant frequency and displacement matches the acoustic frequency and acoustic particle displacement at that location in the engine. Under these conditions, the barrier is expected to be transparent to the acoustics of the system, although small acoustic losses will likely occur.

Note, however, that the acoustically transparent barrier is the only moving part in the engine, and will therefore require the most maintenance. Consequently, its placement in the TAPCE coincides with the location of lowest acoustic velocity and temperature within the engine, which helps ensure that this component does not sustain any undue stress. Furthermore, its location is readily accessible for maintenance purposes by removing the end cap at the top of the compliance.

During proper operation, acoustic energy passes through the acoustically transparent barrier with minimal attenuation, and is directed down through the regenerator where it is amplified by the temperature gradient across the regenerator. Thereafter, the acoustic energy passes through the combustion zone, where it may be further amplified by a pulse combustion process. As the acoustic energy exits the thermoacoustic driver, a portion of the acoustic energy is directed to the resonator for use by the acoustic load, while the remaining portion of the acoustic energy is directed back to the regenerator through the feedback inertance section, thus sustaining the process.

3.1.4 The combustion zone

Burning fuel in the strong acoustic environment inside the thermoacoustic engine necessarily implies that unsteady combustion processes will be present. In order to best utilize this unsteady combustion process, it is desirable to have heat release oscillations that are in phase with the acoustic pressure oscillations to further increase the acoustic power output of the engine according to Rayleigh's Criterion [Zinn (1986)]. An analysis of the acoustic energy flux through the combustion zone in Chapter 4 shows that pulse combustion can add, at most, 7% to the acoustic power output of an engine operating at 10% acoustic pressure amplitude. However, an improperly phased pulse combustion process can also absorb 7% of the engine's power output, thus some effort must be made to control the phase difference between the unsteady heat addition and the unsteady pressure oscillations in the combustion zone, in accordance with Rayleigh's Criterion.

To maximize the acoustic gain provided by the pulse combustion process, we desire a pulse combustion process in which the ratio of the oscillating to mean heat release is as large as possible. Ideally, this means that the combustion process is extinguished from one acoustic cycle to the next, so that the amplitude of the oscillating heat release is approximately equal to the mean heat release, which is simply the time average of the heat release over an acoustic cycle. Note, however, that this would require re-ignition of the combustion reactants during each acoustic cycle, thus limiting the ability to maintain the desired self-sustaining pulse combustion process in the thermoacoustic engine. Therefore, the chosen design must strike a fine balance between maximizing the heat release oscillations without causing extinction of the flame, while also providing some flexibility in seeking to achieve this goal once the engine is built. In

addition, a great deal of flexibility will be required in attempting to create heat release oscillations that are in phase with the pressure oscillations of the combustion chamber, since the time delay between the reactant injection and the heat release will be very difficult, if not impossible, to determine a priori.

Another important feature of the TAPCE that must be considered in the design of the pulse combustion process is the presence of significant flow reversal. The modeling efforts below reveal that the ratio of mean to acoustic axial velocities is on the order of 0.01 in the combustion region of the engine, a far smaller ratio than is likely to be found in most devices featuring unsteady combustion. This will yield significant axial mixing, both between the reactants, if they enter the engine unmixed, and between the reactants and the hot combustion products. As such, the strong degree of mixing and flow reversal somewhat inhibits the ability to achieve large heat release oscillations, thus reinforcing the requirement that some flexibility be built into the design of the pulse combustion process in order to maximize its effect on the acoustic power output of the engine once it is constructed.

The flexibility needed to control the pulse combustion process can be achieved through either active or passive control methods [McManus et. al. (1993)]. Passive methods generally involve simple changes to the geometry of the combustion chamber, the reactant inlet configuration, etc., in order to achieve the desired pulse combustion performance. This is generally an iterative process which may never attain the optimum pulse combustion performance, but is the preferred control strategy in devices that are designed to operate in steady state at a fixed operating frequency, since a satisfactory geometry that gives the desired combustion characteristics should, in principle, continue

to do so for the life of the device. The use of active combustion control would include an actuator that changes the dynamics of the pulse combustion process during operation of the engine. A well-designed active control system would provide the desired degree of flexibility in attempting to increase the heat release oscillations and to match its phase to that of the unsteady pressure fluctuations, however, the addition of an actuator to the TACPE may be difficult or detrimental to its operation. Note also that the TAPCE will require an ignition source in the engine in order to initiate the combustion process, thus the design of the pulse combustion control system, whether active or passive, should proceed with the knowledge that it may be feasible to use this ignition source to help control the pulse combustion process.

3.1.4.1 Passive control of pulse combustion

There are many standard methods for providing passive control of unsteady combustion processes, though not all of these methods are applicable to the control of pulse combustion within the TAPCE. For instance, one popular method of passively controlling combustion instabilities involves alteration of vortex shedding patterns in the combustion chamber (see, for example, [Schadow and Gutmark (1992)]). Although the basic design of the combustion zone does not contain any discontinuities that would promote vortex shedding, the addition of one or more flameholders would provide recirculation zones that serve as anchors for the combustion process. Some control over the pulse combustion process could be gained, for instance, by altering the geometry of the flameholder to produce vortices for one direction of acoustic gas motions, but not the other. In fact, the size and shape of the flameholder can be most anything, from a few

wire mesh screens to various shapes of flow obstructions to the reactant inlet pipes themselves.

In general, however, generation of vortices occurs through viscous dissipation of the acoustic gas motions, and may therefore damp the acoustic energy flux passing through the combustion zone to some degree. In addition, these flameholders may induce detrimental combustion oscillations at frequencies other than the operating frequency of the engine. For these reasons, it would be preferable to avoid the use of flameholders in the TACPE, though fixing the location of the combustion process within the combustion zone may be difficult or impossible without their use.

Another standard passive control strategy that should be avoided in the TAPCE is the alteration of the geometry of the combustion chamber. Since the fundamental frequency of the TAPCE is primarily controlled by the resonance condition between the thermoacoustic engine and the acoustic load [Backhaus and Swift (2000)], the desired frequency of the pulse combustion process cannot be changed by changing the geometry of the combustion chamber, though the tunable compliance may be used to good effect for this purpose. In fact, the geometry of the combustion chamber is primarily governed by the constraints of the acoustically compact network, thus its geometry cannot be altered without changing the acoustic character of the engine.

Although some passive control methods are not well suited to the thermoacoustic engine application, those that incorporate changes to the reactant inlet and reactant mixing processes are directly applicable to the pulse combustion control in the TAPCE. There are several types of reactant inlet configurations to consider, including choked injection nozzles, unchoked injection nozzles, and flapper valves. As noted above,

choking the reactant injection nozzle prohibits acoustic energy from propagating up the inlet ports and leaving the engine, though this may be impractical at elevated mean pressures with which the TAPCE may operate. In addition, choked nozzles provide constant mass flow input, which provides little opportunity for implementing combustion control measures.

In unchoked injection nozzles, on the other hand, acoustic pressure changes at the exit plane of the nozzle result in fluctuations of the reactant injection velocity that may be used to help control the pulse combustion process. One of the ways in which these reactant injection pulsations can be used is to create fluctuations in the fuel to air ratio by bringing the fuel and air into the device through different inlet ports. These oscillations in the fuel to air ratio can create large heat release oscillations, particularly for very lean fuel/air mixtures [Lieuwen and Zinn (1998)]. For premixed reactant injection, significant pulsations in the reactant inlet pipes can lead to periodic reactant injection and oscillating heat release, especially if the combustion process occurs relatively close to the reactant inlet nozzle.

Unchoked reactant injection nozzles hold a great deal of promise for combustion control, since the nature of the injection can be altered considerably by changing the geometry of the reactant inlet pipes. In particular, a large measure of control over the ratio of mean to acoustic mass fluxes in the reactant inlet pipes can be attained, since the acoustic mass fluxes in the inlet pipes are largely controlled by the length and diameter of these pipes. Although the ratio of mean to acoustic mass fluxes is very small in the combustion zone, this ratio can be made to approach and even exceed unity in the reactant inlet pipes by altering their geometry. Therefore the designer has some measure

of control over the degree of flow reversal in the reactant inlet pipes, where having a small degree of flow reversal or periods of no reactant injection should help maximize the magnitude of the unsteady heat release.

The primary drawback to using unchoked reactant inlet pipes is that they allow acoustic energy to propagate upstream and out of the engine. This can be mitigated to some degree by designing quarter- or half-wavelength inlet pipes that reflect this acoustic energy back into the engine, though this method would generate resonant acoustic oscillations in these reactant inlet pipes. An alternative method of preventing acoustic energy leakage out the inlet pipes and creating unsteady reactant injection is to use flapper valves at the ends of the pipes. Although this method is fairly common in typical pulse combustors [Zinn (1986)], these valves would introduce moving parts to a system that seeks to eliminate as many moving parts as possible in order to reduce its cost and maintenance and increase its reliability.

In addition to altering the reactant injection properties, moving the position of the flameholder and/or combustion process within the combustion chamber provides some measure of passive combustion control, based on the specific acoustic characteristics in this region of the TAPCE. While the acoustic pressure is primarily constant with respect to position within the combustion chamber, the compliance of the combustion chamber causes the magnitude and phase of the acoustic velocity to vary significantly along its length. Initial modeling efforts indicate that the acoustic velocity lags the acoustic pressure by about 25˚ at the hot face of the regenerator, and by about 48˚ at the other end of the combustion chamber (i.e., the flow straightener situated above the thermal buffer tube, as depicted in Figure 3.2). The compliance of the combustion zone also causes the

magnitude of the acoustic velocity to increase by about 60% from the hot end of the regenerator to the flow straightener. As a result, if the pulse combustion process is linked to the acoustic velocity in the engine, then it can be passively controlled to some extent by moving it along the axis of the combustion zone to find the acoustic velocity conditions that maximize the acoustic power gain.

3.1.4.2 Active control of pulse combustion

As noted above, active control of the pulse combustion process requires the use of an actuator, which in itself can create problems for the thermoacoustic engine. For instance, great care is taken in the design of thermoacoustic devices to eliminate viscous dissipation of the acoustic wave motions, and adding hardware to the combustion chamber can only increase the viscous dissipation of acoustic energy within the combustion chamber. In addition, since acoustic velocities can be an order of magnitude larger in the annular inertance region than in the combustion chamber, further viscous dissipation will occur with the inclusion of additional pipes and/or wires that must pass through this region to gain access to the actuator in the combustion chamber. Furthermore, the use of an actuator in an active control process may include one or more moving components, which could be a detriment in a system where one of the selling points is the inherent reliability and low maintenance of a system with few or no moving parts.

As a result, the designer must ensure that the benefits of adding an active control system to the thermoacoustic engine outweigh the additional losses and complexity that are incurred by its presence. Given that the pulse combustion process is only capable of adding, at most, 7% to the acoustic power output of the engine, the incorporation of an

active control system to the engine may not be worth the additional complexity that it introduces to an already complex process.

That said, a few minimally intrusive options exist for active control of pulse combustion within the TAPCE. One of the most promising options involves modulation of the magnitude and phase of the reactant flow rate from the upstream end of the inlet pipes, as the actuator can then reside outside the engine where it will not cause viscous dissipation losses in the combustion chamber [McManus et. al. (1993)]. Control of pulsating reactant injection is not absolute in this case, however, as acoustic pressure oscillations at the exit plane of the reactant inlet pipes will have an additional effect on the reactant injection oscillations, as mentioned above.

Another active control option that is minimally intrusive and does not require any moving parts is to use periodic spark ignition of the combustion process, where the timing of the spark is adjusted to produce optimal heat release phasing with respect to the acoustic temperature oscillations. To its detriment, this method is somewhat energy intensive, requires the presence of an electric power source, and may be difficult to implement for a distributed combustion zone.

Other, more intrusive active control strategies may involve actuation to move the flameholder or combustion site along the length of the regenerator, movement of the reaction injection point or direction of the injection, and the use of synthetic jets embedded in the walls of the combustion chamber to alter the dynamics of the combustion process.

Given the above active and passive pulse combustion control options, and the desire to limit the number of moving parts and viscous losses in the engine, active control

of the reactant flow rate from outside the engine is probably the most attractive option for a first generation thermoacoustic pulse combustion engine. Extensive experimentation with this system should reveal a great deal of information about the effects of the reactant injection oscillations on the combustion process and the acoustic power output of the engine. This information can then be used to design reactant inlet pipes of the proper length and diameter so as to provide effective passive control of the reactant injection and pulse combustion process for a second generation of the thermoacoustic engine.

3.2 TAPCE Operating Conditions

3.2.1 Size and frequency

The combination of the TAPCE and the acoustic load, as shown in Figure 3.1, essentially forms a half wavelength resonator. Consequently, the size and frequency of the device are approximately governed by the basic relation: $a = \lambda f$, where a is the speed of sound in the fluid, λ is the acoustic wavelength, and f is the resonant frequency of the device. The fluid utilized in the engine affects its overall size or frequency through the speed of sound in that fluid. For a fixed temperature and fluid composition (and hence, speed of sound), a larger device would yield a lower resonant frequency, and vice versa. Thus, thermoacoustic devices can be as large as several stories tall [Wollan et. al. (2002)], to a few centimeters in length [Chen et. al. (2002)], depending on the acoustic power requirements.

Since the acoustic power is also proportional to the cross-sectional area of the duct that the acoustic energy is passing through, the choice of this scale has a large effect on the acoustic power output of the device. However, it is important that the cross

sectional area is small enough to prevent alteration of the acoustic field by radial or tangential resonant acoustic modes of the pipe.

The size for the TAPCE model below is chosen to reflect a device appropriately sized for experimentation. The only size constraint that affects the operation of the device is that the pore size of the regenerator must always smaller than the thermal penetration depth, which is a function of the frequency of the device, as shown in Eq. (2.1). For a fixed device size, a change in the fluid composition or mean temperature could change the acoustic frequency of the device, which makes the tunable compliance a valuable control mechanism for fine-tuning the operating frequency of the TAPCE.

3.2.2 Working fluids

The working fluid in the thermoacoustic driving section of the TAPCE will primarily be composed of combustion reactants or products, which will be discussed in further detail in the following section. The exact composition of the working fluid in the remainder of the engine is a little more difficult to determine, however, since air, fuel, and/or combustion products may diffuse or convect down through the thermal buffer tube and mix with this working fluid. In any case, a gas analyzer will be required in an experimental setup to determine the exact content of the fluid in the device as it slowly changes over the continual operation of the engine.

One option for separating the contents of the thermoacoustic driver from the working fluid in the rest of the device is to place another acoustically transparent barrier at the bottom of the driver, just below the secondary cold heat exchanger. Since almost any working fluid could be used in the remainder of the device in this situation, a significant attempt should be made to match the characteristic impedances of the fluids

on either side of the acoustically transparent barriers in order to minimize the acoustic reflections and loss of acoustic energy transmission through these barriers [Kinsler et. al (1982)]. In this case, air or nitrogen would make good choices for the working fluid outside the thermoacoustic driver.

Finally, while most thermoacoustic engines use helium for a working fluid, the proposed TAPCE must use combustion reactants and products, which will reduce the acoustic power density in the device. A high acoustic power density is desirable in a thermoacoustic engine to reduce the effect of thermal conduction dissipation of the input heat supplied to the engine. The acoustic power density is directly proportional to the speed of sound [Swift (2002)], so replacing helium with combustion reactants and products reduces the acoustic power density by about a factor three. However, careful selection of the regenerator materials and the use of smaller regenerator pipe wall thickness will significantly reduce thermal conduction dissipation, effectively offsetting the effect of reduced acoustic power density to some degree.

3.2.3 Combustion reactants

The types of combustion reactants that can be used in the TAPCE are primarily limited by the desire to keep the regenerator free of any obstructions. While air will be used as the oxidizer, the mode of combustion may dictate the choice of fuel that is used. Non-premixed combustion, where the fuel and oxidizer enter the combustion zone separately, is more likely to result in unburned hydrocarbons (soot) that would clog the pores of the regenerator [Turns (1996)]. Therefore, it would be preferable to premix the combustion reactants before they are brought into the engine in order to reduce the

possibility of soot fouling the regenerator. This limits the TAPCE to burning mostly gaseous hydrocarbons such as methane, ethane, propane, etc.,

Another concern is that the combustion of hydrocarbons primarily generates carbon dioxide and water, the latter of which may condense at the cold heat exchanger, thereby fouling the regenerator with liquid. Fortunately, air carries a lot of atmospheric nitrogen along with it, which is generally unaffected by the combustion process. This effectively dilutes the water content of the combustion products. In addition, if more air is used than is needed for complete combustion of the fuel, then the water content of the combustion products is even further reduced.

The amount of excess air in the combustion process is quantified by the use of the equivalence ratio, Φ, which can be defined as the ratio of the oxidizer required for complete combustion of the fuel, to the total amount of oxidizer actually used [Turns (1996)]. Thus, for stoichiometric combustion, in which the exact amount of oxidizer is used, $\Phi = 1$, and when excess oxidizer is used, $\Phi < 1$. For rich fuel/air mixtures ($\Phi > 1$), there is not enough oxidizer to burn all of the fuel. Not only is this wasteful of the fuel, but this situation is also more likely to result in unburned hydrocarbons, even for premixed combustion, thus the reactant mixtures in the TAPCE should be limited to lean mixtures ($\Phi < 1$).

The desire to avoid condensation of the water vapor in the combustion products affects the mean pressure and cold temperature in the engine, in addition to the type of fuel used. For the water vapor in the combustion products to condense, the partial pressure of the water vapor, p_{H2O}, must exceed the saturation pressure of water, $p_{sat,}$ at the local cold temperature, T_c [Turns (1996)]. The ratio of the partial pressure of the water

vapor to the total pressure in the engine, p, is equal to the mole fraction of water vapor in the combustion products, $\chi_{H2O} = p_{H2O}/p$. It can be shown that the mole fraction of water vapor is related to the equivalence ratio, Φ, and the choice of hydrocarbon fuel by the following equation [Turns (1996)]:

$$\chi_{H2O} = \frac{\Phi\, y/2}{\Phi + 4.76(x + y/4)}, \tag{3.1}$$

where x and y are the number of carbon and hydrogen atoms in the fuel molecule, C_xH_y, respectively. Therefore, the condition at which the water in the combustion products begins to condense can be expressed as:

$$p_{H2O} = p\chi_{H2O} = p_{sat}(T_c). \tag{3.2}$$

Given a hydrocarbon fuel and a cold temperature, this equation can be used to choose an equivalence ratio and mean pressure that does not yield condensation at the cold heat exchanger, i.e.,

$$p \le p_{sat}(T_c)\frac{\Phi + 4.76(x + y/4)}{\Phi\, y/2} \tag{3.3}$$

Note that p in Eqs. (3.2) and (3.3) is the total pressure, equal to the sum of the mean and oscillating acoustic pressures. Therefore, an appropriate mean pressure must be chosen with some knowledge of the desired acoustic pressure amplitude, such that the sum of the mean and acoustic pressures does not exceed the total pressure p of Eq. (3.3), thereby avoiding condensation.

The estimated maximum pressure relationship of Eq. (3.3) is plotted in Figure 3.4 for various fuels at a cold temperature of 325 K, which is the approximate cold temperature attained in the TASHE. As a general trend, the hydrocarbon fuels with higher ratios of carbon atoms to hydrogen atoms yield higher non-condensing pressures,

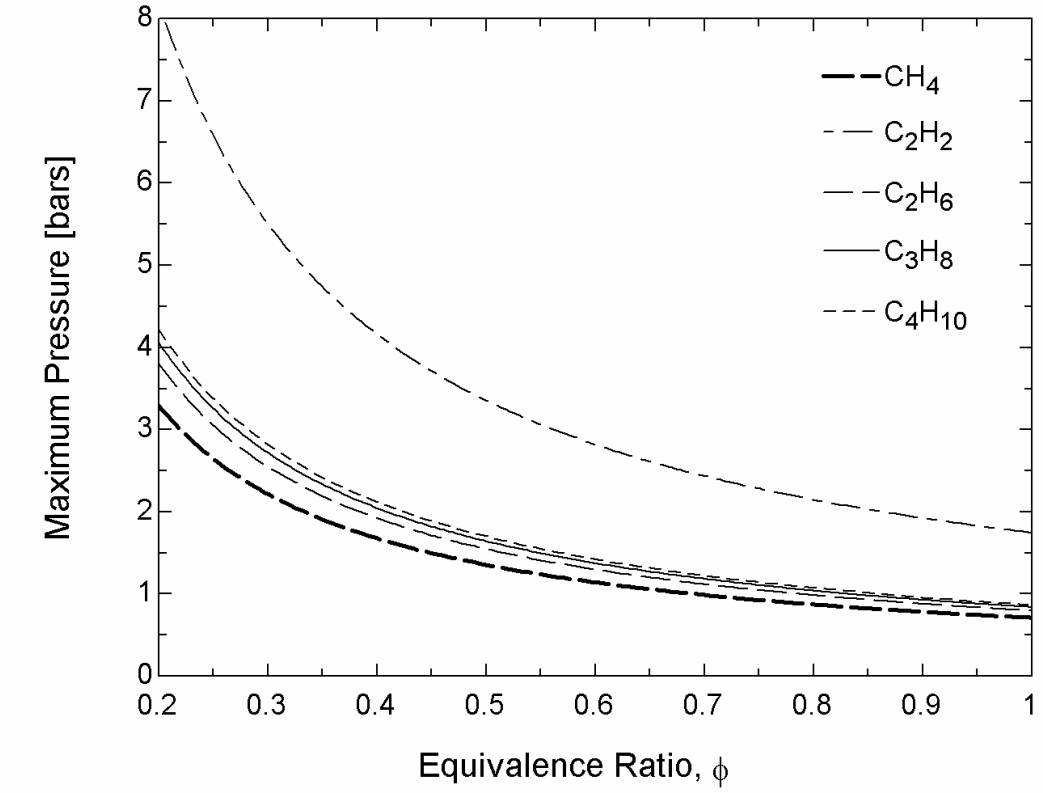

Figure 3.4: The maximum non-condensing total pressure for various fuels and equivalence ratios, at T_c = 325 K.

as these fuels result in lower water vapor mole fractions. In particular, note that methane (CH_4) has a large mole fraction of water vapor in the combustion products, and thus a low non-condensing pressure, while the opposite is true of acetylene (C_2H_2).

It turns out that the maximum non-condensing pressure is very sensitive to the temperature at the cold heat exchanger, as shown in Figure 3.5 for methane. For example, at $\Phi \approx 0.5$, increasing the cold temperature from 330 K to 340 K allows one to increase the total pressure in the engine by about an atmosphere, which may be a very useful means of increasing the acoustic power density in the engine, as explained in the following section.

Another means of increasing the maximum non-condensing pressure in the engine is to reduce the equivalence ratio, as shown in both Figures 3.4 and 3.5. This occurs because decreasing the equivalence ratio dilutes the combustion product mixture, which also serves to reduce the combustion temperature, as the heat released by the combustion of the fuel must now heat a larger mass of fluid. This can be desirable from the standpoint of pollutant emission control, as lower combustion temperatures generally result in lower emissions of nitrous oxides that create atmospheric smog and acid rain [Turns (1996)]. However, note that reducing the equivalence ratio also increases the mean mass flux in the engine, and reduces the effectiveness of the counterflow reactant preheating process between the regenerator and the reactant inlet pipes.

Note that there is a limit to how lean a combustible mixture can be before it loses the ability to ignite and combust, though preheating the lean reactant mixture lowers this low equivalence ratio limit for combustion. According to one study, this lean

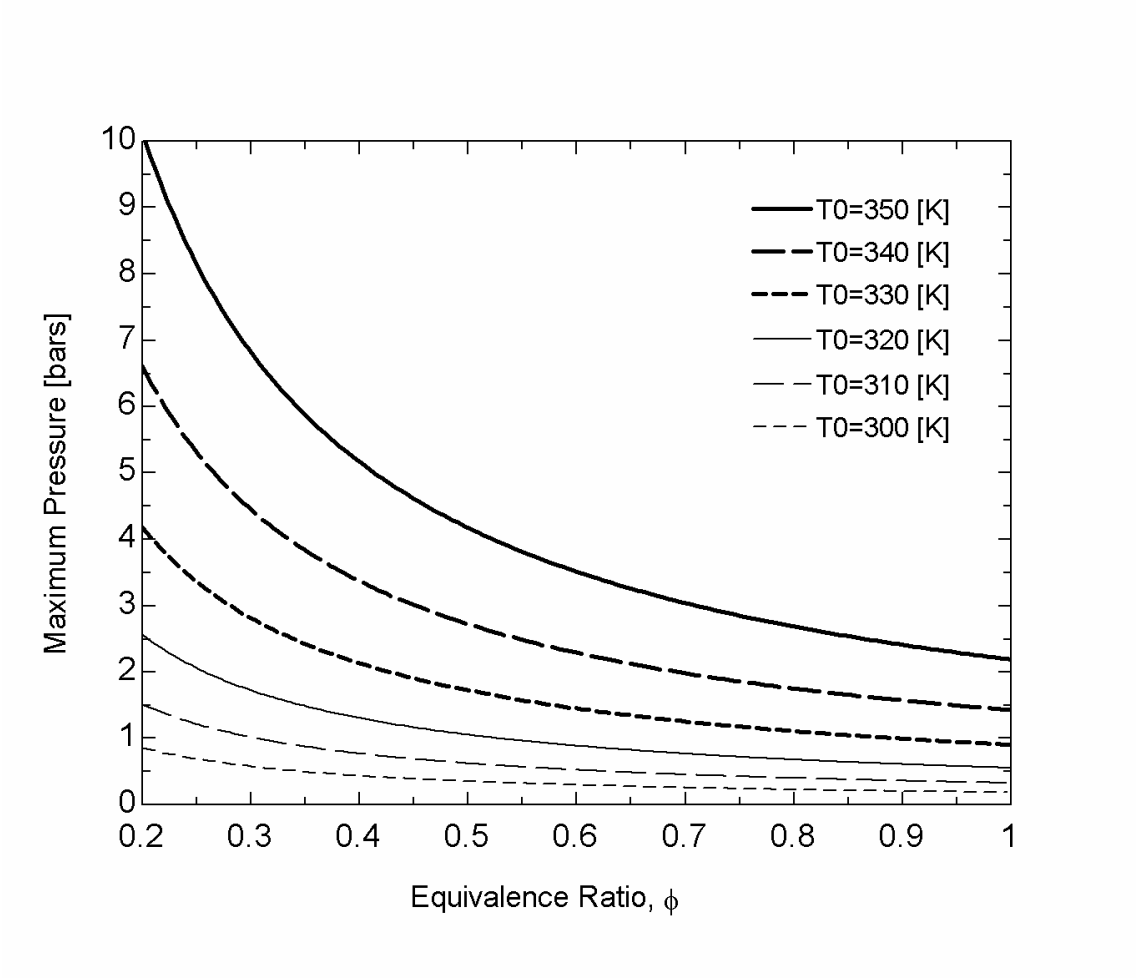

Figure 3.5: The maximum non-condensing total pressure for methane (CH_4) vs. equivalence ratio for various cold heat exchanger temperatures, T_0.

equivalence ratio flammability limit for methane has the following preheat temperature dependence [Hustad and Sonju (1988)]:

$$\Phi_{lfl} \approx 0.53\left[1 - 0.00088\left(T_{ph} - 298\,\mathrm{K}\right)\right], \tag{3.4}$$

which is valid for 298 K < T_{ph} < 725 K at atmospheric pressure. This correlation was obtained for the propagation of a flame through a premixed methane/air mixture in an open tube. It should also be noted that catalysts have the ability to burn combustible mixtures with much lower equivalence ratios, suggesting that they might be suitable for use in the TAPCE.

3.2.4 Pressure

In addition to affecting the condensation of water vapor from the combustion products, the mean pressure also affects other aspects of the engine's operation. For instance, the acoustic power density in the device is proportional to the acoustic pressure magnitude, which is in turn a function of the mean pressure in the device. Acoustic pressure amplitudes are limited to about 10% of the mean pressure in most thermoacoustic devices, since several nonlinear loss mechanisms become prevalent at higher acoustic amplitudes [Swift (2002)]. However, operation of a thermoacoustic engine at higher acoustic pressure ratios offers a simple means of increasing the acoustic power output of the engine, though at reduced thermal efficiency. If the designer wishes to avoid nonlinear effects or increase efficiency by limiting the acoustic pressure amplitude to 10% or less of the mean pressure, then increasing the mean pressure is generally the only way to increase the acoustic power density in the device.

Many thermoacoustic devices operate at higher mean pressures in order to increase the acoustic power density relative to the thermal conduction losses in the

device, which do not scale with the mean pressure. Since the design of the TAPCE reduces many of the thermal losses present in other thermoacoustic engines, the TAPCE may be able to operate at much lower pressures, though the reductions in the thermal losses may not be enough to allow efficient operation at atmospheric conditions.

In addition, the changing frequency of the device could affect the ratio of the hydraulic radius to the thermal penetration depth in the engine, resulting in a reduced gas-solid thermal contact in the regenerator. Fortunately, this ratio can be altered by changing the mean pressure within the device, as the thermal penetration depth is a function of the mean gas density in the device, as shown in Eq. (2.1). Therefore, the TAPCE should be somewhat pressurized to provide a small degree of flexibility in attaining the operating conditions that the TACPE was designed for. This brings up a slight problem with the open cycle architecture of the device, since now the inlet needs to be pressurized, and the exhaust of the device will exit the engine highly pressurized.

Two options for dealing with this problem exist. In the first option, the reactants are supplied by a large, pressurized vessel or vessels, and the supply pressure is controlled through variable resistance valves. The exhaust can then be vented to the atmosphere or, perhaps can be routed through an expansion turbine to generate mechanical or electrical power for the other peripheral devices in the TAPCE, such as the coolant water pumps.

In the second option, the pressurized exhaust is routed through a turbocharger that is used to help drive the inlet reactant compressor, though a small amount of additional energy will be required to attain the desired reactant supply pressure. If this additional power is supplied by a small gas turbine, and some of this shaft power is also used to

drive the coolant pumps, then the entire device can be powered by natural gas, without the use of any electrical power.

Note that this solution to the pressurization problem is fairly complex, and adds many moving parts to the engine. Ideally, then, we'd like to operate at or near atmospheric pressure, although even in this case some pressurization of the reactants must occur in order to force the mean flow of gas through the engine.

3.2.5 Temperature limits

As noted above, shifting from a toroidal architecture like that of the TASHE, to the concentric pipe architecture, the burden of containing the potentially elevated pressures in the device are shifted from the wall of the thermoacoustic driver to the outer shell. The highest attainable safe temperature in the TASHE was about 1000 K, due to concerns over the tensile strength of the walls of the thermoacoustic driver, which were made of 4 millimeter thick Inconel 625 [Backhaus and Swift (2000)]. In particular, the thermal cycling of the device, coupled with the 30 atmospheres of mean pressure it contained, weakened the walls over time, and resulted in a noticeable increase in diameter after several thermal cycles.

As a result of shifting the pressure vessel to the shell of the TAPCE, the walls of the thermoacoustic driver can be much thinner, as they will only have to experience pressure differences due to changes in the acoustics between the inertance and the interior of the thermoacoustic driver. Modeling efforts show that the phase and magnitude of the acoustic pressure do not change by a significant amount throughout the driver section of the TAPCE, and that the pressure difference between the inertance and the inside of the thermoacoustic driver would be, at most, about 1-2% of the mean pressure. Thus, even

for high mean pressures, the wall of the thermoacoustic driver can be much thinner than that of the TASHE, and can be designed to handle higher temperatures without fear of failure.

Since we're not concerned about the integrity of the wall of the thermoacoustic driver, the high temperature in the thermoacoustic driver is therefore limited by other material constraints, and by the combustion process. Note that, by preheating the reactants, very high combustion temperatures are possible, perhaps even exceeding 2500K for stoichiometric mixtures of the combustion reactants.

The low temperature in the engine is limited by the inlet temperature of the coolant supplied to the cold heat exchangers, and by the effectiveness of these heat exchangers. As noted above, this temperature has a strong influence on the condensation of the water vapor in the combustion products, which must be avoided if at all possible. Therefore, it may be advantageous, from an acoustic power density perspective, to raise the temperature of the cold heat exchanger to allow higher pressures to be used without initiating condensation of the combustion products.

In an experimental setting, the fuel and mean pressure of the engine are generally fixed, and the equivalence ratio is chosen to yield a desired combustion temperature and/or water vapor mole fraction in the combustion products. In this case, the flow rate of coolant to the primary cold heat exchanger could be slowly increased in order to lower the temperature of the cold heat exchanger until it reaches a point where condensation begins to appear in the exhaust, thus yielding the maximum temperature difference, and maximum acoustic gain, across the regenerator.

Finally, it should be noted that if a solution can be found for the condensation problem, that the restrictions on the mean pressure, equivalence ratio and cold heat exchanger temperature can be lifted, yielding higher acoustic power outputs and thermal efficiencies for the TAPCE device. In these cases, condensation of the water vapor will undoubtedly occur, but some means is then devised to keep the liquid water from fouling the regenerator, for instance, by wicking the water away or turning the device on its side or upside down to drain the water away. This last solution seems fairly promising, though it may lead to buoyancy-driven instabilities in the thermal buffer tube and combustion zone.

3.3 Applications for the TAPCE

As one might imagine, applications that require large amounts of acoustic power input are relatively scarce, although the inherent simplicity of the traveling wave thermoacoustic engine would be very appealing in several scenarios. Below, several applications for the TAPCE are considered, each of which could be placed at the position of the acoustic load, as shown in Figure 3.1.

3.3.1 Electric power generation

Note that the TAPCE has only one moving part, the acoustically transparent barrier, which simply vibrates back and forth. As a result, the TAPCE would have a relatively low manufacturing cost, very low maintenance requirements, and should be highly reliable. All of these traits make the TAPCE attractive for applications in remote power generation, where, for instance, its acoustic power output could be used to drive a linear alternator, which in turn produces electric power. Such a system is currently under

development for providing reliable electric power generation on deep space missions [Petach et. al. (2004)]. In this device, the heat would be supplied by the radioactive decay of Plutonium-238, a standard heat source that is used in many long term space applications. A first prototype of the device converts thermal energy to electric energy with an overall thermal efficiency of 18%, which represents a significant increase over the 8% thermal efficiency of electric power generators currently employed in satellites. Given that the linear alternator in this device is 89% efficient in converting acoustic energy to AC electric energy, a great deal of promise exists for using the TAPCE for electrical power generation in remote environments or in situations where reliability is a key factor.

One likely use for this application is as a portable power source for military personnel. The Department of Defense has been looking for a way to replace batteries with a more lightweight power source. Since the TAPCE is mostly made of pipes, a small scale version of the engine could be very lightweight in comparison to competing technologies. This device could use small, replaceable canisters of a pressurized liquid fuel such as propane or butane to power the engine. These fuels have a much higher energy density than batteries, and vaporize quickly to allow premixing with air before entering the engine for combustion.

3.3.2 Pulse tube refrigeration driver

A more natural application for the TAPCE is as a source of acoustic power for driving traveling wave thermoacoustic refrigerators. This configuration is capable of turning thermal energy at high temperatures into cooling power at cryogenic temperatures without the use of moving parts. Such a device has been developed by Los Alamos

National Lab and Praxair, Inc., for the purposes of liquefying natural gas [Swift (1995)]. Since natural gas is much easier to transport in its liquefied form, such a device could make the processing, transport and sale of associated natural gas from off-shore oil production sites a financially feasible venture [Van Wijingaarden (1999)].

A small-scale, 350 gallon per day natural gas liquefier is shown in Figure 3.6 [Arman et. al. (2004)]. This device burns part of the input natural gas stream in the combustor at the top of the device, and the hot combustion gases flow through a hot heat exchanger to deliver the input thermal energy to a circulating helium heat transfer loop which delivers the heat, in turn, to a thermoacoustic engine situated just below the combustor. This thermoacoustic engine is similar to the TASHE, except that it employs a concentric pipe architecture similar to the TAPCE. The acoustic energy that is generated travels down the device to three traveling wave thermoacoustic refrigerators, where the remainder of the natural gas is liquefied in stages at a rate of up to 350 gallons per day, thus far. The device currently burns about 55% of the natural gas to liquefy the remaining 45%, although it is expected that the addition of a flue gas recuperator will allow the engine to only burn 30% of the gas to liquefy the rest. A larger, 10,000 gallon per day device, shown in Figure 3.7, is expected to consume only 15% of the input stream of gas to liquefy the remaining gas [Wollan et. al. (2002)].

The primary problem with the 350 gallon per day natural gas liquefier is the hot heat exchanger, which is fairly inefficient at transferring heat from the combustion products to the engine. More importantly, this component introduces some very large thermal stresses into the engine, which has resulted in two broken welds requiring lengthy repair times [Wollan et. al. (2002)]. In switching to a design similar to the

Figure 3.6: The 350 gallon per day natural gas liquefier. (Photo courtesy of Greg Swift)

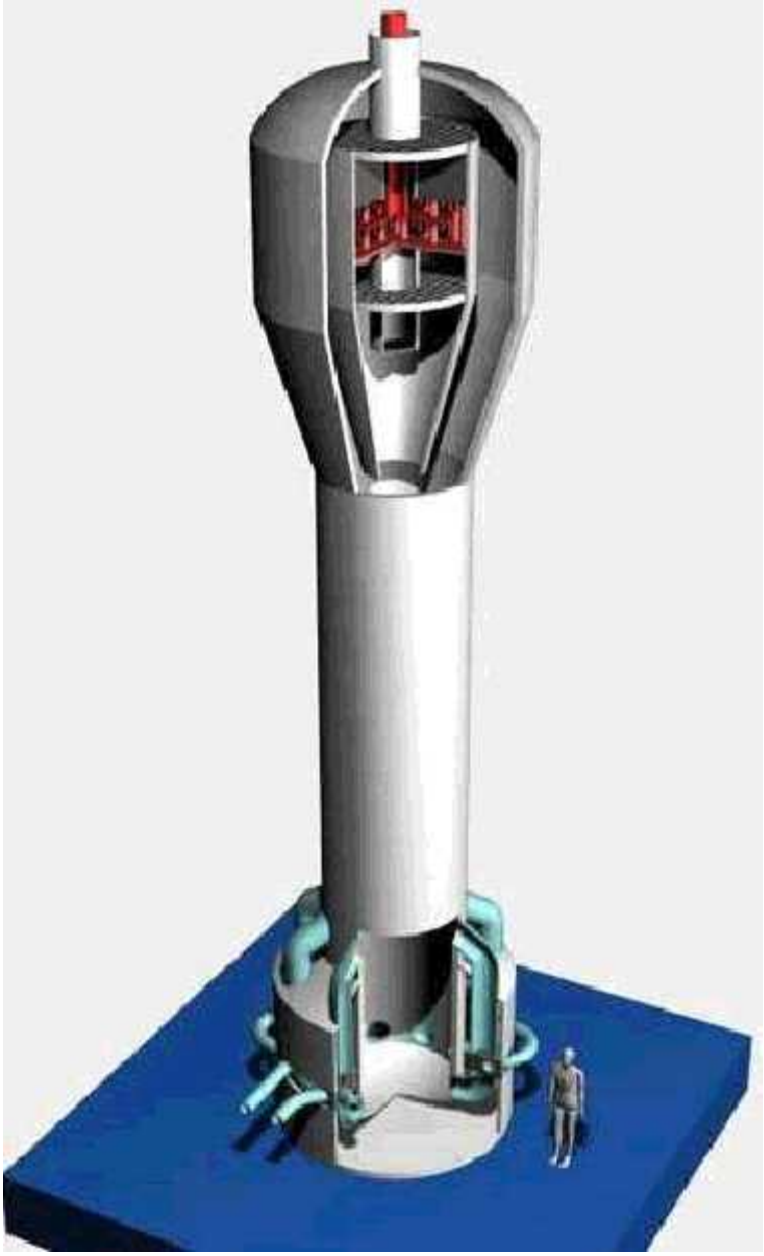

Figure 3.7: A drawing of the 10,000 gallon per day natural gas liquefier. (Reprinted with permission from [Wollan et. al. (2002)])

TAPCE, the natural gas that is burned to power the liquefier could be routed directly through the thermoacoustic engine in an open cycle configuration, thereby eliminating the hot heat exchanger and providing a simpler and possibly more efficient means of converting fuel energy into acoustic energy. A device of this type has application beyond the liquefaction of offshore natural gas, and could be used in many industrial cryogenic refrigeration systems, portable refrigeration systems, gas liquefaction and separation systems, and liquefied natural gas production from oil wells, landfills and coal mines.

3.3.3 Ultra-efficient water heater

Similar to the thermoacoustic refrigeration application, the TAPCE could also be used to drive a traveling wave thermoacoustic heat pump. Swift (2002) notes that this has potential application as an ultra-efficient water heater, where the heat pump draws heat from the atmosphere to heat the water. By further "cooling" the engine with this same water, it is possible to create a water heater that has a thermal efficiency that is greater than 100%. As Swift notes, several types of these ultra-efficient water heaters have been built, though at costs that are commercially unattractive to the consumer. Given the inherent simplicity and high potential efficiency of the TAPCE, this may be a plausible application for this engine.

3.3.4 Industrial processes

As noted by Zinn (1996), there are many large scale industrial processes that would benefit from the addition of acoustic oscillations. It is well known that the rates of thermal or fluid transport processes can be increased in the presence of acoustic oscillations, primarily because the oscillating flow field increases the rates of convective

processes in the system. Increasing these transport process rates generally leads to an increase in the efficiency of the industrial process, which manifests itself as either an increase in the throughput of the process, or a reduction in the energy input required to achieve the same process throughput.

For instance, in a boiler, the addition of an acoustic field would increase the heat transfer from the hot combustion gases to the tubes of the boiler, since the oscillating hot gas comes into thermal contact with the boiler tubes more often than it does in the absence of an acoustic field. As a result, the size of the boiler or fuel input could be reduced while maintaining the desired steam output, or the steam production of the boiler could be increased for the same fuel input and boiler size.

The acoustic oscillations used to enhance the industrial process are generated by placing an acoustic energy source at the wall of the process vessel. Ideally, the acoustic energy source should be tuned to one of the natural resonant acoustic modes of the process vessel, thereby producing large amplitude, resonant acoustic gas oscillations. By using a tunable pulse combustor, this process has been successfully applied to solid and hazardous waste incineration, cement calcining, metal heating and spray drying processes [Zinn (1996)]. The TAPCE can be used as the acoustic energy source in these and other applications, such as lumber drying.

While the tunable pulse combustors add heat input as well as acoustic energy input to the industrial process chamber, the goal of the TAPCE is to convert as much of the heat of combustion as possible into acoustic energy. As a result, a much smaller fuel input would be required to achieve the same level of acoustic field forcing by using the TAPCE as opposed to a tunable pulse combustor. In addition, the TAPCE could also be

used to supply acoustic energy to industrial processes that do not require an additional thermal energy input, thereby increasing the efficiency of devices such as steam condensers, heat exchangers, and catalytic chemical reactors.

CHAPTER 4

THEORY OF TRAVELING WAVE THERMOACOUSTICS WITH MEAN FLOW AND COMBUSTION

The operation of the Thermoacoustic Pulse Combustion Engine includes a few novel processes that have not been adequately described in the literature to date. Namely, the use of mean flow in a traveling wave thermoacoustic device and the inclusion of a pulse combustion process in a thermoacoustic environment require that some underlying theory be developed to better understand how these processes affect the performance of the thermoacoustic engine.

This chapter develops the pertinent first and second order thermoacoustics equations that account for the presence of mean flow and combustion. Additionally, a simple model describing the reactant preheating process is proposed, and the irreversibilities in various components of the TAPCE are explored. The theory developed in this chapter will be applied to the development of a computational model of the TAPCE, as described in Chapter 5, which can be used to help optimize the design and performance of the engine, as described in Chapter 6.

4.1 Basic Equations with Mean Flow and Combustion

The basic thermoacoustic equations for open cycle thermoacoustics have already been developed [Reid (1999), Swift (2002)], though these equations need to be modified

somewhat to account for volumetric heat addition, as produced, for example, by a combustion process. The notation followed here is primarily that used by Swift (2002).

4.1.1 Relevant orders of magnitude

Before proceeding, we should address the nature of the order of magnitude analysis presented here. In a standard ordered analysis, any variable is assumed to be composed of a mean component and a perturbed component. In this analysis, the perturbed component is assumed to oscillate in time at the acoustic frequency of the engine. As a result, a general variable can be expressed as:

$$\alpha(\mathbf{x},t) = \alpha_m(\mathbf{x}) + \mathrm{Re}\left[\alpha_1(\mathbf{x})e^{i\omega t}\right], \tag{4.1}$$

where the subscript "*m*" represents the mean component of the variable, the subscript "1" represents the perturbation quantity, which is typically a complex number, and ω is the angular frequency of the acoustic oscillations.

In most ordered analyses, the acoustic quantity is considered to be much smaller than the mean quantity, i.e. $|p_1|/p_m << 1$. This also applies to the other state variables, T_1, s_1, and ρ_1, but it does not apply to all variables in this analysis. For instance, the magnitude of the acoustic velocity is assumed to be small compared to the speed of sound, a, rather than the mean velocity, i.e. $|u_1|/a << 1$. Insofar as the mean velocity is concerned, it is shown below to be a second order quantity, rather than a zeroth order quantity as with the state variables.

Consider that the purpose of the TAPCE, and any other open cycle thermoacoustic engine, is to produce acoustic energy from thermal energy. In the TAPCE, this thermal energy is generated from the mean heat of combustion at a rate,

$\dot{Q}_m$, and is converted to acoustic power to be supplied to the acoustic load, $\dot{E}_L$, with an efficiency:

$$\eta_{th} = \frac{\dot{E}_L}{\dot{Q}_m}. \tag{4.2}$$

Next, note that the acoustic power is derived from the product of that acoustic pressure, p_1, and acoustic volumetric velocity, $U_1 = \int u_1 dA$, i.e. [Swift (2002)]:

$$\dot{E} = \tfrac{1}{2}\mathrm{Re}\left[p_1 \widetilde{U}_1\right], \tag{4.3}$$

where the tilde (~) denotes the complex conjugate. The acoustic energy flux, being a product of two first order oscillating quantities, is a time averaged second order quantity. Since the thermal efficiency of the TAPCE, η_{th}, should be at least 20%, Eq. (4.2) states that the magnitude of $\dot{Q}_m$ should also be a second order quantity.

If we also consider that the heat of combustion is primarily converted into a mean convective energy flux,

$$\dot{Q}_m \approx \dot{M} c_p \left(T_h - T_0\right) \approx \rho_m u_m A c_p \left(T_h - T_0\right), \tag{4.4}$$

it then follows that the magnitudes of the mean mass flux, $\dot{M}$, and the mean velocity, u_m, are also second order quantities, since all of the other quantities on the right side of Eq. (4.4) are of zeroth order. Therefore, it is assumed, throughout the remainder of the analysis, that $u_m/|u_1| << 1$ and $\dot{M}/|\dot{m}_1| << 1$ [Reid (1999), Reid and Swift (2000)].

In addition, we'll need to make a few simplifying assumptions about the nature of the processes occurring in the thermoacoustic engine. Namely, we'll assume that the geometry is quasi-one dimensional, where the fluid moves only in the axial direction, along the x-axis, though with variations in the lateral direction. Similarly, the mean state

variables are assumed to only be functions of the axial direction, and their derivatives in this direction can be of zeroth order.

In contrast, the x-derivatives of the acoustic variables can generally be neglected by invoking an assumption commonly made in thermoacoustic studies [Rott (1969), Swift (2002)], that the axial derivative of an acoustic variable scales with $1/\lambda$, whereas the lateral derivatives scale with $1/\delta$. Since $\delta << \lambda$, the x derivatives of the acoustic variables are negligible in comparison to the y and z derivatives, i.e. $\partial\alpha_1/\partial x << \partial\alpha_1/\partial y$, $\partial\alpha_1/\partial z$.

Given the above assumptions, the pertinent variables can be expressed as:

$$p = p_m(x) + \mathrm{Re}\left[p_1(x)e^{i\omega t}\right], \tag{4.5}$$

$$T = T_m(x) + \mathrm{Re}\left[T_1(x,y,z)e^{i\omega t}\right], \tag{4.6}$$

$$\rho = \rho_m(x) + \mathrm{Re}\left[\rho_1(x,y,z)e^{i\omega t}\right], \tag{4.7}$$

$$s = s_m(x) + \mathrm{Re}\left[s_1(x,y,z)e^{i\omega t}\right], \tag{4.8}$$

$$u = u_m(x,y,z) + \mathrm{Re}\left[u_1(x,y,z)e^{i\omega t}\right] + u_{2,0}(x,y,z). \tag{4.9}$$

Note that a second order mean velocity, $u_{2,0}$, appears in Eq. (4.9). Ordinarily, if all of the variables above were expanded to second order in a perturbation series, mean, second order terms such as $u_{2,0}$ would appear, though Swift (2002) shows that these terms are negligible when compared to their zeroth order mean terms in the ordinary thermoacoustic equations. An exception must be made for the velocity, however, as the applied mean velocity, u_m, is of second order in magnitude, like $u_{2,0}$. As will be shown below, $u_{2,0}$ is a very useful term that helps describe the effects of acoustic streaming in a thermoacoustic device [Gusev et. al. (2000), Waxler (2001)].

4.1.2 The mean continuity equation

To better understand the distinction between the second order velocity terms, we'll first take a look at the time averaged conservation of mass equation, following the derivation of Swift (2002). The basic continuity equation is [Landau and Lifshitz (1987)]:

$$\frac{\partial \rho}{\partial t} + \nabla \cdot (\rho \mathbf{u}) = 0 . \tag{4.10}$$

Invoking the quasi-one dimensional assumption, substituting Eqs. (4.7) and (4.9) into Eq. (4.10), neglecting all terms of third and higher order, integrating over the cross sectional area, and time averaging results in:

$$\frac{d}{dx}\int \left(\rho_m u_m + \rho_m u_{2,0} + \tfrac{1}{2}\mathrm{Re}[\rho_1 \tilde{u}_1]\right) dA = 0 . \tag{4.11}$$

Integration of Eq. (4.11) with respect to x results in a constant, the mean mass flux, $\dot{M}$, i.e.:

$$\dot{M} = \int \left(\rho_m u_m + \rho_m u_{2,0} + \tfrac{1}{2}\mathrm{Re}[\rho_1 \tilde{u}_1]\right) dA , \tag{4.12}$$

that satisfies $d\dot{M}/dx = 0$ in the device.

In closed cycle thermoacoustic devices, the u_m term is not present, but a mean mass flux may still develop, depending on the relative magnitudes of the second and third terms on the right side of Eq. (4.12). For instance, in a traveling wave thermoacoustic device with a feedback path, $u_{2,0}$ is generally small or non-existent, and a mean mass flux due to acoustic streaming, the last term on the right side of Eq. (4.12), travels through the feedback path. The work of Gedeon (1997) implies that in the regenerator of such a device:

$$\dot{M}_{fb} \approx \int \tfrac{1}{2}\mathrm{Re}[\rho_1 \tilde{u}_1]dA \approx \rho_m \dot{E}_c / p_m \,, \tag{4.13}$$

where the density and acoustic energy flux are evaluated at the ambient temperature location. Thus, the acoustic streaming mass flux is proportional to, and travels around the feedback loop in the same direction as, the acoustic energy flux. This case has recently received more detailed theoretical [Gusev et. al. (2000)] and experimental [Job et. al. (2003), Ueda et. al. (2004)] treatments, though these studies do not consider effects that might counter the mass flux due to acoustic streaming.

In many closed cycle thermoacoustic devices, $\dot{M}$ is forced to be zero, either by utilizing a geometry that does not include a feedback path [Bailliet et. al. (2001), Gardner and Swift (2003)], or by incorporating other means to suppress this mass flux [Charles et. al. (1999), Swift et. al. (1999)]. For instance, as discussed in Chapter 2, the TASHE employs a hydrodynamic jet pump in order to suppress the mean mass flux around its toroidal feedback path [Backhaus and Swift (2000)]. In these cases, a second order mean pressure difference develops across the regenerator, which is caused by the boundary conditions in a linear device, or, in a device with a feedback path, by the mass flux suppressor (e.g. the jet pump of the TASHE). As will be seen in the following section, this small pressure difference generates the second order mean velocity, $u_{2,0}$, that balances the effect of the acoustic streaming term, $\rho_1 u_1$. In this case, mean mass flux in the device is suppressed, and Eq. (4.12) yields:

$$\rho_m \int u_{2,0} dA + \int \tfrac{1}{2}\mathrm{Re}[\rho_1 \tilde{u}_1]dA = 0 \,. \tag{4.14}$$

In an open cycle thermoacoustic device with a feedback path, such as the TAPCE, the mean mass flux at any location in the device could include components from applied mean flow velocities, u_m, as well as acoustic streaming mass fluxes that circulate around

the feedback path, as described by the last term in Eq. (4.12). In the TAPCE, the inclusion of the acoustically transparent barrier is designed to stop these circulating mass fluxes due to acoustic streaming, thereby enforcing the condition in Eq. (4.14) to hold as discussed above for closed cycle configurations. Consequently, the mean mass flux can be set equal to $\dot{M} = \rho_m U_m$, where $U_m = \int u_m dA$, since the last two terms in Eq. (4.12) must cancel one another out according to Eq. (4.14).

4.1.3 The mean pressure equation

To derive an equation for the mean pressure gradient in a thermoacoustic engine, we'll start with the *x*-component of the Navier-Stokes equations, assuming bulk viscosity is negligible [Landau and Lifshitz (1987)]:

$$\rho\left[\frac{\partial u}{\partial t} + u\frac{\partial u}{\partial x}\right] = -\frac{\partial p}{\partial x} + \mu\nabla^2 u\,. \tag{4.15}$$

Applying Eqs. (4.5), (4.7) and (4.9), invoking the above assumptions, and taking the time average yields, to second order in magnitude:

$$\frac{dp_m}{dx} = \mu\nabla^2_{y,z}\left(u_m + u_{2,0}\right). \tag{4.16}$$

As noted by Swift (2002), this equation means that the axial mean pressure gradient in the thermoacoustic device is a second order term, due to viscous drag on the second order mean velocities.

In closed cycle thermoacoustic devices, where $u_m = 0$, the second order mean pressure gradient can be thought of as causing a viscous flow with mean velocity $u_{2,0}$. In devices where the mean mass flux is suppressed, this pressure gradient develops across the regenerator so that the resulting $u_{2,0}$ cancels the acoustic streaming mass flux in the

regenerator, as discussed above. In a traveling wave thermoacoustic device with a feedback path, however, where no attempt is made to mitigate the development of a mean mass flux, the feedback path causes the pressure gradient across the regenerator to be essentially zero, thus allowing $\dot{M}_{fb}$ to flow through the feedback path, as expressed in Eq. (4.13).

As noted Figure 3.2, the mean mass flux in the TAPCE travels in the opposite direction as the acoustic energy flux, thus an external force is required to cause mass to flow in the desired direction. This external force is provided by imposing a mean pressure gradient across the regenerator, and the magnitude of the mean mass flux is controlled by adjusting the inlet and outlet gas pressures on either side of the regenerator.

An equation relating $\dot{M}$ to the pressure difference across a parallel plate regenerator, Δp_m, is given by Waxler (2001). Bailliet et. al. (2001) and Backhaus and Swift (2003) note that Waxler's analysis does not include effects of temperature dependence of viscosity and thermal conductivity, though their analyses also point out that these effects are not important for regenerators in the small plate spacing approximation, $r_h << \delta_\kappa$, which applies to the regenerator in a traveling wave thermoacoustic device.

A generalized version of Waxler's regenerator pressure difference equation is [Waxler (2001)]:

$$\Delta p_m = -\frac{\alpha \mu_m L}{\rho_m} \dot{M} + \Delta p_{\dot{M}=0}, \tag{4.17}$$

where μ_m is the gas viscosity evaluated at the regenerator's mean temperature, the factor α accounts for the geometry of the regenerator (e.g., $\alpha = 1.5/Ar_h^2$ for a parallel plate

geometry), L is the length of the regenerator, and $\Delta p_{\dot{M}=0}$ is the pressure difference that results when $\dot{M} = 0$. Comparing this equation with an integrated version of Eq. (4.16), and noting that $\dot{M} = \rho_m U_m$ in the TAPCE, we can see that $\Delta p_{\dot{M}=0}$ is due to the viscous drag on $u_{2,0}$, where $u_{2,0}$ is determined by the acoustic streaming effects through Eq. (4.14).

Waxler (2001) derives an expression for $\Delta p_{\dot{M}=0}$ in a parallel plate regenerator, but for the order of magnitude calculation presented here it is sufficient to use the more general result of Eq. (4.13), which applies when $\Delta p_m \approx 0$ across the regenerator. Setting Eq. (4.17) equal to zero, and using the ideal gas law and Eq. (4.13), a rough estimate for $\Delta p_{\dot{M}=0}$ is obtained:

$$\Delta p_{\dot{M}=0} = \frac{\alpha \mu_m L}{\rho_m} \dot{M} \approx \frac{\alpha \mu_m L}{\rho_m} \frac{\dot{E}_c}{R T_0}. \tag{4.18}$$

Substituting this equation back into Eq. (4.17), the required pressure difference across the regenerator is approximated by:

$$\Delta p_m \approx \frac{\alpha \mu_m L}{\rho_m} \left[\frac{\dot{E}_c}{R T_0} - \dot{M} \right]. \tag{4.19}$$

Since $\dot{E}_c$ and $\dot{M}$ are both second order quantities and all the other terms are of order zero, this equation verifies that the mean pressure difference across the regenerator is a second order quantity. Note that the first term in brackets on the right hand side of Eq. (4.19) is the pressure gradient required to counteract the effects of acoustic streaming in the regenerator, while the second term is the additional pressure required to force mass to flow at the desired rate from hot to cold through the regenerator. According to the sign convention adopted here, $\dot{M} < 0$, as it travels in the opposite direction as the acoustic

energy flux, thus the higher pressure must be applied to the hot side of the regenerator, as logic would dictate.

4.1.4 The first order momentum equation

Noting that the volumetric heat addition does not appear in the momentum equation, Eq. (4.15), the first order momentum equation has already been derived by Swift (2002). The basic derivation will be repeated here to demonstrate the solution procedure followed in thermoacoustic analyses. This thermoacoustic formulation was pioneered by Rott, (1969), although the derivation here follows Swift (2002). Expanding the variables in Eq. (4.15), applying the above assumptions, and neglecting all terms of second order and higher yields the first order momentum equation:

$$i\omega\rho_m u_1 = -\frac{dp_1}{dx} + \mu\left[\frac{\partial^2 u_1}{\partial y^2} + \frac{\partial^2 u_1}{\partial z^2}\right]. \tag{4.20}$$

Considering the pressure gradient to be an inhomogeneous forcing function, Eq. (4.20) is a second order, inhomogeneous partial differential equation for the spatial variation of the acoustic velocity. Solving Eq. (4.20) for $u_1(y, z)$, and applying the no-slip boundary condition at the solid surfaces yields [Swift (2002)]:

$$u_1(y,z) = -\frac{1 - h_v(y,z)}{i\omega\rho_m}\frac{dp_1}{dx}, \tag{4.21}$$

where the complex spatial function $h_v(y, z)$ depends on the specific cross-sectional geometry of the system.

Integration of Eq. (4.21) over the cross sectional area and rearrangement yields an expression for the axial change in the acoustic pressure, as a function of the acoustic volumetric velocity:

$$\frac{dp_1}{dx} = \frac{-i\omega\rho_m}{A(1-f_v)}U_1, \tag{4.22}$$

where the function f_v is a spatial average of the function $h_v(y, z)$. These functions have been computed for many geometries, including parallel plates, circular pores, rectangular channels, and pin arrays, and can be found in Swift's book (2002). As an example, the spatial functions h and f for the boundary layer of an open duct, generally valid when the radius of the duct is larger than the thermal and viscous penetration depths ($y/\delta >> 1$), are [Swift (2002)]:

$$h = e^{-(1+i)y/\delta}, \tag{4.23}$$

$$f = \frac{(1-i)\delta}{2r_h}, \tag{4.24}$$

where $y = 0$ at the wall of the duct.

4.1.5 The first order temperature equation

Following the derivation procedure set forth in the example for the momentum equation, we'll now derive the basic first order heat equation for thermoacoustics. This is similar to previous derivations [Swift (2002)], although the rate of heat addition per unit volume, $\dot{q}$, must be included in the general heat equation [Landau and Lifshitz (1987)], i.e.:

$$\rho T\left(\frac{\partial s}{\partial t} + \mathbf{u}\cdot\nabla s\right) = \nabla\cdot k\nabla T + (\sigma'\cdot\nabla)\cdot\mathbf{u} + \dot{q}, \tag{4.25}$$

where σ' is the viscous stress tensor. Applying the equation of state in Eq. (2.7) yields:

$$\rho c_p\left(\frac{\partial T}{\partial t} + \mathbf{u}\cdot\nabla T\right) - \left(\frac{\partial p}{\partial t} + \mathbf{u}\cdot\nabla p\right) = \nabla\cdot k\nabla T + (\sigma'\cdot\nabla)\cdot\mathbf{u} + \dot{q}. \tag{4.26}$$

Perturbing this equation, applying the above assumptions in addition to assuming that the thermal conductivity, k, is constant, and retaining the first order terms yields:

$$k\left[\frac{\partial^2 T_1}{\partial y^2}+\frac{\partial^2 T_1}{\partial z^2}\right]-i\omega\rho_m c_p T_1=\rho_m c_p\frac{dT_m}{dx}u_1-i\omega p_1-\dot{q}_1. \tag{4.27}$$

This equation is identical to those derived by Swift (2002) and Rott (1969), with the addition of the oscillating heat release term, $\dot{q}_1$, due to combustion.

Equation (4.27) is an inhomogeneous PDE for T_1, where the homogeneous equation has a general solution and each of the inhomogeneous terms can be solved for independently with particular solutions. Similar to the solution of the momentum equation, the solution of Eq. (4.27) is subject to the boundary condition $T_1 = 0$ at the solid surfaces, which is approximately true when the specific heat of the solid is much larger than that of the gas. After some manipulation and the use of Eqs. (4.21) and (4.22), the resulting solution of Eq. (4.27) for T_1 can be shown to be similar in form to those derived by Swift (2002) and Rott (1969, 1975):

$$T_1=\frac{1-h_\kappa}{\rho_m c_p}p_1-\frac{1}{i\omega A}\left[\frac{(1-h_\kappa)-\sigma(1-h_\nu)}{(1-f_\nu)(1-\sigma)}\right]\frac{dT_m}{dx}U_1+T_{1,q} \tag{4.28}$$

The new term, $T_{1,q}$, is obtained by solving the following inhomogeneous PDE, given a specific form for $\dot{q}_1(y,z)$ and applying the appropriate boundary conditions:

$$k\left[\frac{\partial^2 T_{1,q}}{\partial y^2}+\frac{\partial^2 T_{1,q}}{\partial z^2}\right]-i\omega\rho_m c_p T_{1,q}=-\dot{q}_1. \tag{4.29}$$

Since the specific form of $\dot{q}_1(y,z)$ depends greatly on the characteristics of the pulse combustion process, it will suffice to assume a simple form for $\dot{q}_1$ that is uniform in the lateral direction, and hence independent y and z. In this case, the solution of Eq. (4.29) is:

$$T_{1,q} = \frac{1-h_\kappa}{i\omega\rho_m c_p}\dot{q}_1 . \tag{4.30}$$

Substituting this expression into Eq. (4.28) and averaging the resulting equation over the cross sectional area of the channel yields [Swift (2002)]:

$$\langle T_1 \rangle = \frac{1-f_\kappa}{\rho_m c_p} p_1 - \frac{1}{i\omega A}\left[\frac{(1-f_\kappa)-\sigma(1-f_\nu)}{(1-f_\nu)(1-\sigma)}\right]\frac{dT_m}{dx}U_1 + \frac{1-f_\kappa}{i\omega\rho_m c_p}\dot{q}_1 , \tag{4.31}$$

where $\langle\ \rangle$ denotes spatial averaging. This equation can be used in conjunction with the first order continuity equation to derive a differential equation for dU_1/dx.

4.1.6 The first order continuity equation

The first order, spatially averaged continuity equation, subject to the assumptions made above, is [Swift (2002)]:

$$i\omega\langle\rho_1\rangle + \frac{d}{dx}\left(\rho_m\langle u_1\rangle\right) = 0 . \tag{4.32}$$

Note that, with the use of the ideal gas equation of state, the spatially averaged acoustic density is:

$$\langle\rho_1\rangle = -\frac{\rho_m}{T_m}\langle T_1\rangle + \frac{\rho_m}{p_m}p_1 . \tag{4.33}$$

Substituting this equation and Eq. (4.31) into Eq. (4.32) for the first order continuity equation yields, after rearrangement:

$$\frac{dU_1}{dx} = -\frac{i\omega A\left[1-f_\kappa(\gamma-1)\right]}{\gamma p_m}p_1 + \frac{f_\kappa - f_\nu}{(1-f_\nu)(1-\sigma)}\frac{dT_m}{dx}\frac{U_1}{T_m} + \frac{A(\gamma-1)(1-f_\kappa)}{\gamma p_m}\dot{q}_1 . \tag{4.34}$$

This equation is the same as that of Swift (2002), with the addition of the last term that describes the effect of the oscillating heat release. In this form, the effect of the oscillating heat release is shown to be a source of acoustic volumetric velocity. Its effect

on the acoustics of the thermoacoustic system is more clearly ascertained by examining its influence on the acoustic energy flux equation.

4.1.7 The acoustic energy flux equation

Following the development of Swift (2002), the differential equation for the axial change in the acoustic energy flux can be expressed, with the help of Eq. (4.3), as:

$$\frac{d\dot{E}}{dx} = \frac{1}{2}\mathrm{Re}\left[\widetilde{U}_1 \frac{dp_1}{dx} + \widetilde{p}_1 \frac{dU_1}{dx}\right]. \tag{4.35}$$

Substituting Eqs. (4.22) and (4.34) for dp_1/dx and dU_1/dx, respectively, and taking the real component of this equation yields:

$$\frac{d\dot{E}}{dx} = -\frac{r_\nu}{2}|U_1|^2 - \frac{1}{2r_\kappa}|p_1|^2 + \frac{1}{2}\mathrm{Re}\left[g_T \widetilde{p}_1 U_1\right] + \frac{1}{2}\mathrm{Re}\left[g_q \widetilde{p}_1 \dot{q}_1\right], \tag{4.36}$$

where the viscous resistance per unit length, r_ν, thermal relaxation resistance per unit length, $1/r_\kappa$, thermal gain factor, g_T, and heat release gain factor, g_q, are defined as:

$$r_\nu = \frac{\omega\rho_m}{A}\frac{\mathrm{Im}\left[-f_\nu\right]}{\left|1-f_\nu\right|^2}, \tag{4.37}$$

$$\frac{1}{r_\kappa} = \frac{\gamma-1}{\gamma}\frac{\omega A\,\mathrm{Im}\left[-f_\kappa\right]}{p_m}, \tag{4.38}$$

$$g_T = \frac{f_\kappa - f_\nu}{(1-f_\nu)(1-\sigma)}\frac{1}{T_m}\frac{dT_m}{dx}, \tag{4.39}$$

$$g_q = \frac{\gamma-1}{\gamma}\frac{A(1-f_\kappa)}{p_m}. \tag{4.40}$$

Again, Eq. (4.36) is similar to Swift's acoustic energy flux equation (2002), with the addition of the last term that accounts for the effect of the oscillating heat release on the

acoustic energy flux. In effect, this term is a form of the Rayleigh Criterion for thermoacoustics.

To this point in the analysis, all of the equations derived above are relevant to general thermoacoustics with uniform volumetric heat addition, in both open and closed cycle systems. For the specific case of the TAPCE, the combustion process occurs in an open duct as shown in Figure 3.2, where $\delta/r_h << 1$, and the spatial functions f_v and f_κ are approximately zero according to Eq. (4.24). In this case, Eqs. (4.36) – (4.40) reduce to:

$$\frac{d\dot{E}}{dx} \approx \frac{1}{2}\frac{\gamma-1}{\gamma} A \,\mathrm{Re}\left[\frac{\tilde{p}_1 \dot{q}_1}{p_m}\right], \tag{4.41}$$

which is a more familiar form of the Rayleigh Criterion [Zinn (1986)].

4.1.8 Maximum effect of pulse combustion on acoustic energy gain

To estimate the effect of the pulse combustion process on the acoustic power output of the engine, $\dot{E}_L$, we'll assume that $\dot{E}_L = \dot{E}_{ta} + \dot{E}_{pc}$, where the power output contribution from the thermoacoustic process is $\dot{E}_{ta}$, and that of the pulse combustion process is $\dot{E}_{pc}$. Using Eq. (4.2), we can write the thermoacoustic energy gain as: $\dot{E}_{ta} = \eta_{th,ta}\dot{Q}_m$, where $\eta_{th,ta}$ is the thermal efficiency of the thermoacoustic process. The acoustic energy gain from the pulse combustion process can be attained by integrating Eq. (4.41) across the length of the combustion zone, i.e.:

$$\dot{E}_{pc} = \frac{\gamma-1}{2\gamma} A \int_{x_{cz}} \frac{|p_1||\dot{q}_1|}{p_m}\cos\theta_{pq}\, dx\,, \tag{4.42}$$

where x_{cz} is the length of the combustion zone, and θ_{pq} is the phase difference between p_1 and $\dot{q}_1$. Dividing this result by the thermoacoustic power gain and recognizing that $\dot{Q}_m = Ax_{cz}\dot{q}_m$ yields:

$$\frac{\dot{E}_{pc}}{\dot{E}_{ta}} = \frac{\gamma - 1}{2\gamma\eta_{th,ta}} \frac{1}{x_{cz}} \int_{x_{cz}} \frac{|p_1|}{p_m} \frac{|\dot{q}_1|}{\dot{q}_m} \cos\theta_{pq} dx . \tag{4.43}$$

If it is assumed that $|p_1|/p_m << 1$ and $|\dot{q}_1|/\dot{q}_m << 1$, then Eq. (4.43) indicates that the acoustic energy addition by unsteady combustion is very small, approximately fourth order in comparison to the second order thermoacoustic power output. However, steps can be taken during the design process to ensure that the effect of pulse combustion is maximized for the purposes of increasing the acoustic energy output of the engine. For instance, to make the ratio $|\dot{q}_1|/\dot{q}_m$ as large as possible, an ideal situation would call for extinction of the combustion process to occur once per acoustic cycle. This case could be represented by:

$$\dot{q} = \dot{q}_m + |\dot{q}_1| \cos\omega t = \dot{q}_m (1 + \cos\omega t) \tag{4.44}$$

where $|\dot{q}_1| = \dot{q}_m$, ω is the angular frequency of acoustic oscillations, and extinction of the combustion process would occur during each acoustic cycle at $\omega t = \pi + 2\pi n$, where n is a positive integer. In addition, it would be advantageous to use large acoustic amplitudes in the thermoacoustic engine to maximize $|p_1|/p_m$. Acoustic pressure oscillations up to 10% of the mean are not uncommon in thermoacoustic devices [Backhaus and Swift (2000)], though it should be noted that significant nonlinear loss mechanisms develop for larger acoustic amplitudes [Backhaus and Swift (2000), Swift (2002)]. Finally, maximizing the effect of the Rayleigh Criterion requires that p_1 and $\dot{q}_1$ be in phase with one another, i.e., $\theta_{pq} = 0$. As unsteady combustion systems can sometimes be

unpredictable, active or passive control systems will be necessary to ensure that this criterion is met.

If the above conditions are satisfied, then the contribution of the pulse combustion process to driving the acoustic oscillations in a thermoacoustic engine is greatly increased. To estimate the maximum acoustic energy gain from the pulse combustion process, we'll assume that $|\dot{q}_1| = \dot{q}_m$ as in Eq. (4.44) above, and that the oscillating pressure and heat release are both in phase ($\theta_{pq} = 0$) and uniform over the length of the combustion zone. Applying these assumptions to Eq. (4.42) yields:

$$\dot{E}_{pc,\max} = \dot{Q}_m \frac{\gamma - 1}{2\gamma} \frac{|p_1|}{p_m}. \tag{4.45}$$

Dividing by the thermoacoustic power gain and assuming that γ =1.4 and $\eta_{th,ta} \approx 20\%$, the maximum acoustic energy gain by pulse combustion, compared to the gain by thermoacoustic processes, is about:

$$\frac{\dot{E}_{pc,\max}}{\dot{E}_{ta}} = \frac{1}{\eta_{th,ta}} \frac{\gamma - 1}{2\gamma} \frac{|p_1|}{p_m} \approx 0.7 \frac{|p_1|}{p_m}. \tag{4.46}$$

For an acoustic pressure ratio of $|p_1|/p_m \approx 0.10$, this means that the pulse combustion process can add, at most, 7% to the acoustic power output of the engine. Given that this is a fairly low number, and an optimistic one at that, design efforts to improve the efficiency of the TAPCE would probably be better directed elsewhere. However, since pulse combustion will be inevitable in a device such as the TAPCE, this calculation shows that improper phasing between p_1 and $\dot{q}_1$ (i.e. $\theta_{pq} = 180^\circ$) could lead to a 7% reduction in acoustic power output, so some effort must at least be made to control the phase between the acoustic pressure and unsteady heat release.

Finally, note from Eq. (4.46) that the pulse combustion process becomes more important at higher acoustic pressure ratios, and could potentially contribute as much as 21% to the acoustic power output of the engine for an acoustic pressure ratio of $|p_1|/p_m = 0.3$. Most thermoacoustic devices today do not operate above pressure ratios of $|p_1|/p_m \approx 0.1$ due to the nonlinear loss mechanisms that arise at higher amplitudes, though the addition of a pulse combustion process to a thermoacoustic engine may become more appealing as these operating pressure amplitudes increase. For the purposes of this study, however, pressure ratios above $|p_1|/p_m = 0.10$ will not be considered so that linearized acoustic analyses can be applied.

4.2 Engine Energy Fluxes

While Eq. (4.36) describes the axial change in acoustic energy flux, this expression does not tell us how the thermal energy is converted into acoustic energy, or any details of the other thermal energy processes, such as conduction and convection. Study of these effects is accomplished by examining the total time-averaged energy flux.

Unfortunately, the volumetric heat addition by combustion complicates matters, as the total heat flux is affected by the coupling of the unsteady combustion to both the acoustic pressure oscillations, as in (4.36), and to the unsteady entropy oscillations. For example, if we look at Eqs. (4.36) - (4.40) for the case of a regenerator, where $r_h << \delta$ and $f \rightarrow 1$, we see that there is little or no acoustic energy gain by unsteady combustion in such an environment, due to the good solid/gas thermal contact within the regenerator. Instead, the pulse combustion process affects the total energy flux in the device through the oscillating entropy, which occurs in response to the acoustic pressure oscillations in

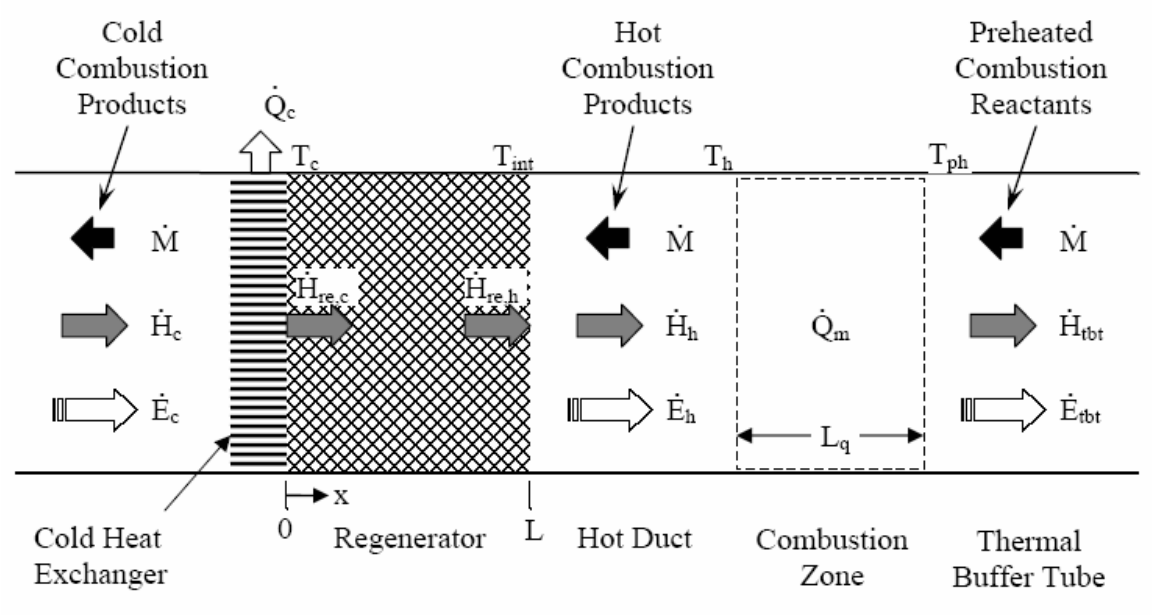

Figure 4.1: Geometry and energy fluxes in the thermoacoustic driver of the TAPCE, without reactant preheating.

the nearly isothermal regenerator. However, as other entropy effects are also present in this formulation, the total power equation and its interpretation becomes fairly complex.

Given the geometry of the TAPCE, however, these issues can be avoided by considering the combustion zone separately from the regenerator. In this case, the combustion process is assumed to be fully contained within the open duct below the regenerator, with no volumetric heat release occurring inside the regenerator. In this manner, the existing total power equations for open cycle thermoacoustics [Reid (1999), Swift (2002)] can be used in all parts of the TAPCE except the combustion zone. Inside the open duct of the combustion zone, if it assumed that boundary layer effects are small, the time averaged energy flux equations become fairly simple, as shown below.

The geometry used in the derivations below is shown in Figure 4.1. Here, the thermoacoustic driving section of the TAPCE is laid on its side, with the cold heat

exchanger on the left and the combustion zone on the right. The acoustic energy travels to the right, in the positive *x*-direction, while the mean mass flux, $\dot{M}$, travels to the left, thus $\dot{M} < 0$. In order to more clearly illustrate the basic operation of the open cycle traveling wave thermoacoustic engine, reactant preheating effects are not considered here, but will be presented later in the chapter. Instead, it is assumed that the reactants enter the combustion zone from the right, hot combustion products travel to the left out of the combustion zone and into the regenerator, and cold combustion products exit the cold heat exchanger on the left.

4.2.1 Combustion zone

As noted above, if it is assumed that the boundary layer effects are negligible in the combustion zone, then the time averaged acoustic effects are appropriately described by Eq. (4.41). These acoustic effects are not the only time averaged energy fluxes in the combustion zone, however. One must also consider the mean energy fluxes, which, when coupled with Eq. (4.41), describe the total time averaged energy flux through the combustion zone. As such, one version of the mean energy equation is [Landau and Lifshitz (1987)]:

$$\frac{\partial}{\partial t}\left[\rho_m\left(e_m + \frac{u_m^2}{2}\right)\right] + \nabla\cdot\left[\rho_m u_m\left(h_m + \frac{u_m^2}{2}\right) - \mathbf{u}_m\cdot\sigma'_m + k\nabla T_m\right] = \dot{q}_m, \tag{4.47}$$

where e_m is the mean internal energy, h_m is the mean enthalpy, and σ'_m is the mean viscous stress tensor, which is a second order quantity since it primarily contains functions of u_m. Applying the above assumptions, neglecting all terms of third order and higher in magnitude, and assuming steady state conditions, the mean energy equation becomes:

$$\frac{d}{dx}\left(\rho_m u_m h_m + k_s \frac{dT_m}{dx}\right) = \dot{q}_m . \tag{4.48}$$

Note that while the thermal conduction term usually includes both thermal conduction through the gas and the solid walls of the combustion chamber, the thermal conduction through the gas, k, has been neglected here because it is much smaller than the conduction through the solid, k_s.

Integrating Eq. (4.48) over the cross sectional area of the combustion zone, A, and applying Eqs. (4.12) and (4.14) yields:

$$\frac{d}{dx}\left(\dot{M} h_m + A_s k_s \frac{dT_m}{dx}\right) = A\dot{q}_m \tag{4.49}$$

While the mean and acoustic energy flux equations of Eqs. (4.49) and (4.41) are essentially independent of one another, the two equations should technically be combined to form one equation for the time averaged total energy flux in the combustion zone:

$$\frac{d}{dx}\left(\dot{M} h_m + \dot{E} + A_s k_s \frac{dT_m}{dx}\right) = A\dot{q}_m + \frac{1}{2}\frac{\gamma - 1}{\gamma} A \,\mathrm{Re}\left[\frac{\tilde{p}_1 \dot{q}_1}{p_m}\right] \tag{4.50}$$

This equation describes how the pulse combustion process changes the convective, conductive and acoustic energy fluxes passing through the combustion zone. Although Eq. (4.50) was derived somewhat casually, it should be noted that this same equation can also be derived by more rigorous methods [Weiland and Zinn (2004b)].

Integrating Eq. (4.50) over the length of the combustion zone, x_{cz}, yields a relationship between the input and output energy fluxes across the combustion zone. Assuming that the pressure and combustion heat release are each independent of axial position within the combustion zone, this integration yields, in the nomenclature of Figure 4.1:

$$\dot{M}\left(h_{tbt}-h_h\right)+\dot{E}_{tbt}-\dot{E}_h+\left(A_s k_s \frac{dT_m}{dx}\right)_{tbt}-\left(A_s k_s \frac{dT_m}{dx}\right)_h = \dot{Q}_m+\frac{1}{2}\frac{\gamma-1}{\gamma}\mathrm{Re}\left[\frac{\tilde{p}_1\dot{Q}_1}{p_m}\right]. \tag{4.51}$$

As noted above, in an open duct, the mean and acoustic effects in this equation can be assumed to be independent of one another. Consequently, the acoustic component of Eq. (4.51) can be expressed as:

$$\dot{E}_{tbt}-\dot{E}_h=\frac{1}{2}\frac{\gamma-1}{\gamma}\mathrm{Re}\left[\frac{\tilde{p}_1\dot{Q}_1}{p_m}\right], \tag{4.52}$$

which is basically the integrated form of Eq. (4.41) that gives the total acoustic energy gain due to uniform pulse combustion across the combustion zone. The mean component of Eq. (4.51) is:

$$\left(\dot{M}c_p\right)_{rx}T_{ph}-\left(\dot{M}c_p\right)_{pr}T_h+\left(A_s k_s \frac{dT_m}{dx}\right)_{tbt}-\left(A_s k_s \frac{dT_m}{dx}\right)_h=\dot{Q}_m, \tag{4.53}$$

where the mean mass flux and specific heat of the combustion reactants are denoted with the subscript *rx*, and those of the combustion products are denoted by the subscript *pr*. Noting that $\dot{M} < 0$ in the sign convention of Figure 4.1, Eq. (4.53) gives the temperature rise produced by the combustion process across the combustion zone. Also, since the highest temperature in the device will occur in the combustion zone, the temperature must decrease on either side, so that $(dT_m/dx)_{tbt} < 0$ and $(dT_m/dx)_h > 0$. Assuming that the reactant preheat temperature is constant, Eq. (4.53) indicates that the hot combustion product temperature exiting the combustion zone, T_h, is reduced by the presence of thermal conduction out of the combustion zone, which is indicative of non-adiabatic combustion processes [Turns (1996)].

4.2.2 *General thermoacoustic energy flux equation*

As noted above, those portions of the TAPCE that do not include heat release by combustion (e.g. everywhere but the combustion zone, as shown in Figure 3.2) can be modeled using previously derived total power equations for open cycle thermoacoustics [Reid (1999), Swift (2002)]. The following sections primarily follow the nomenclature and derivations of Swift (2002), though additional nomenclature and equations are introduced to assist in the analysis of the various energy fluxes surrounding the regenerator portion of the TAPCE. Note that although most of the developments in the rest of this section appear in the paper by Weiland and Zinn (2004a), they are fairly important to the remainder of this study, and are included here for the sake of completeness.

The analysis begins with an expression for the total energy flux in an open cycle thermoacoustic device, Swift's Equation 7.105 [Swift (2002)], which is the sum of the relevant energy fluxes in the device. In deriving this equation, Swift's assumptions are consistent with those made above concerning the relative magnitudes of the various terms and their derivatives. This equation expresses the total second-order energy flux, $\dot{H}$, as:

$$\dot{H} = \dot{M} c_p (T_m - T_0) - (Ak + A_s k_s) \frac{dT_m}{dx} + \tfrac{1}{2} \rho_m c_p \int \mathrm{Re}[T_1 \tilde{u}_1] dA . \tag{4.54}$$

The first term on the right side of Eq. (4.54) is the convective energy flux, where c_p is the constant pressure specific heat of the gas, T_m is its mean temperature, and T_0 is the ambient reference temperature. The second term on the right side of Eq. (4.54) is the conductive energy flux, generally a loss term, where A and A_s are the cross-sectional areas of the gas and solid, respectively, and k and k_s are the thermal conductivities of the gas and solid, respectively. The solid components in this term may include pipe walls,

insulation, regenerator screens, and any other solid materials that are present in the control volume. The last term on the right side of Eq. (4.54) essentially represents the thermoacoustic energy fluxes in the engine, expressed as the time average of the product of T_1 and u_1. Note that this equation forms the original basis for assuming that $\dot{M} << \dot{m}_1$ in an open cycle device, since these thermoacoustic effects must be at least as large as the convection and conduction terms in Eq. (4.54) [Swift (2002)].

Using the ideal gas relationship: $c_p T_1 = T_m s_1 + p_1/\rho_m$, the definition of the thermoacoustic entropy flux $\dot{S} \equiv \frac{1}{2}\rho_m \int \mathrm{Re}[s_1 \tilde{u}_1] dA$, where s_1 is the first order oscillating entropy, and Eq. (4.3), the thermoacoustic term in Eq. (4.54) can be written as:

$$\tfrac{1}{2}\rho_m c_p \int \mathrm{Re}[T_1 \tilde{u}_1] dA = \dot{E} + T_m \dot{S} . \tag{4.55}$$

The second order thermoacoustic entropy flux, $\dot{S}$, is sometimes referred to as a "thermoacoustic heat flux", and is frequently described as a "bucket brigade" of gas parcels shuttling heat up or down a temperature gradient [Swift (1988, 2002)].

In open channels and isentropic environments this second order entropy flux is generally negligible, and Eq. (4.55) is equal to the acoustic energy at that location. Inside a regenerator, however, the second order entropy flux can be fairly large. In an ideal regenerator, perfect solid-gas thermal contact results in an isothermal environment, where $T_1 = 0$. Applying this condition to Eq. (4.55) yields:

$$\dot{S}_{re,ideal} = -\frac{\dot{E}}{T_{re}}, \tag{4.56}$$

where T_{re} is the mean temperature at an axial location within the regenerator. This equation expresses the relationship between the ideal entropy and work fluxes in the regenerator, where at any location, a unit of acoustic power traveling to the right is

countered by a unit of thermal energy transported to the left by the ideal second order entropy flux. This entropy flux is caused by a combination of the acoustic gas movement and the heat transfer between the solid and gas that accompanies acoustic pressure changes in the regenerator, where the temperature of the gas is ideally constrained to equal the regenerator's local solid temperature, $T_{re}(x)$.

4.2.3 Entropy flux due to imperfect thermal contact in the regenerator

For imperfect thermal contact in the regenerator, $T_1 \neq 0$, and the last term in Eq. (4.54) contributes an additional thermoacoustic entropy flux to the total energy flux in the regenerator. This entropy flux is proportional to the mean temperature gradient in the regenerator, thus the last term in Eq. (4.54) can be written as:

$$\tfrac{1}{2}\rho_m c_p \int \mathrm{Re}[T_1 \tilde{u}_1] dA \approx -\psi \frac{dT_{re}}{dx}. \tag{4.57}$$

Using Swift's expression for the last term in Eq. (4.54), evaluated for a parallel plate regenerator in the limit of very small plate spacing, the coefficient ψ can be approximated to lowest order by [Swift (2002)]:

$$\psi_{pp} \equiv \frac{17}{35} \frac{\rho_m c_p}{A\omega} \frac{r_h^2}{\delta_\kappa^2} |U_1|^2. \tag{4.58}$$

A non-zero value of ψ expresses the effect of imperfect solid-gas thermal contact in a parallel plate regenerator. In contrast, perfect solid-gas thermal contact in the regenerator results when the plate spacing or pore size is very small relative to the thermal penetration depth, i.e. $r_h^2/\delta_\kappa^2 << 1$, yielding $\psi_{pp} \approx 0$ in Eq. (4.58) and $T_1 \approx 0$ in Eq. (4.57). The parameter ψ, divided by the cross-sectional area, has been referred to as an "effective" thermal conductivity in other studies on energy fluxes in closed cycle

thermoacoustic devices [Rott (1975), Xiao (1992)], although this terminology tends to de-emphasize the acoustic nature of this energy flux.

Substituting Eqs. (4.57) into Eq. (4.55) yields the following expression for the thermoacoustic entropy flux inside the regenerator:

$$\dot{S}_{re} \approx \frac{-1}{T_{re}}\left[\dot{E} + \psi \frac{dT_{re}}{dx}\right] = \dot{S}_{re,ideal} + \dot{S}_{re,loss}, \tag{4.59}$$

where the entropy flux loss has been defined as:

$$\dot{S}_{re,loss}(x) \equiv -\frac{\psi}{T_{re}}\frac{dT_{re}}{dx}. \tag{4.60}$$

As described by Eq. (4.59), the "bucket brigade" heat transfer by the second order entropy flux is composed of both perfect and imperfect regenerator thermal contact components. As will be shown below, $\dot{S}_{re,ideal}$ carries thermal energy used to amplify the acoustic wave in the regenerator, while $\dot{S}_{re,loss}$ is an unwanted entropy flux that carries thermal energy out of the system without converting it to work in the form of acoustic energy. Also, note from Eq. (4.58) that ψ is approximately third or fourth order in magnitude, although the regenerator temperature gradient, dT_{re}/dx, can become very large in the presence of mean mass flux, as will be shown below. Therefore, under certain conditions, $\dot{S}_{re,loss}$ can become a second order term like $\dot{S}_{re,ideal}$, according to Eq. (4.59).

Since the TAPCE does not contain a parallel plate architecture, but rather a stacked wire mesh screen regenerator, Eq. (4.58) must be replaced by suitable expression that characterizes the entropy flux due to imperfect thermal contact in a stacked screen regenerator. Such an expression can be obtained by manipulating the results of Swift and

Ward (1996), who investigated the equations governing thermoacoustic processes in wire mesh regenerators.

Assuming traveling wave acoustic phasing in the stacked screen regenerator, the last term in Eq. (4.54) can be expressed, to lowest order, as [Swift and Ward (1996)]:

$$\tfrac{1}{2}\rho_m c_p \int \mathrm{Re}[T_1 \tilde{u}_1]dA \approx -\frac{\rho_m c_p}{2A\omega}\mathrm{Im}\left[\frac{\varepsilon_s + \varepsilon_h(g_c - g_v)}{1+\varepsilon_s + \varepsilon_h\left(g_c - e^{2i\theta_T} g_v\right)}\right]|U_1|^2 \frac{dT_{re}}{dx}, \tag{4.61}$$

where ε_s is the ratio of the gas heat capacity to the solid heat capacity, ε_h is defined as:

$$\varepsilon_h = \frac{8ir_h^2}{b(\phi)\sigma^{1/3}\delta_\kappa^2}, \tag{4.62}$$

and g_c, g_v and $b(\phi)$ are determined by curve fits to experimental data of the heat transfer coefficient, h, for stacked screen regenerators. Swift and Ward (1996) note that denominator of the term in brackets in Eq. (4.61) is approximately equal to 1 for most regenerators. Making this assumption, and further assuming that the heat capacity of the gas is much smaller than that of the solid ($\varepsilon_s \approx 0$), substitution of (4.62) into Eq. (4.61) allows one to define an imperfect thermal contact entropy flux coefficient for a stacked screen regenerator, similar to that in Eq. (4.58), i.e.:

$$\psi_{ss} = \frac{4\rho_m c_p}{A\omega}\frac{(g_c - g_v)r_h^2}{b(\phi)\sigma^{1/3}\delta_\kappa^2}|U_1|^2 = \frac{2(g_c - g_v)}{b(\phi)\sigma^{1/3}}\frac{\left(c_p|\dot{m}_1|r_h\right)^2}{\phi A_{re} k_m}, \tag{4.63}$$

where Eq. (2.1) has been applied to obtain the last equality in Eq. (4.63), and the area occupied by the gas in the regenerator, A, is equal to ϕA_{re}, where A_{re} is the cross-sectional area of the regenerator, and ϕ is the porosity of the regenerator, defined as the ratio of the gas volume to the total volume of the regenerator.

To obtain the curve fit functions g_c, g_v and $b(\phi)$, Swift and Ward (1996) chose the data of Kays and London (1984), which present the heat transfer coefficient, h, as a

function of the porosity of the stacked screen regenerator, ϕ, and the Reynolds Number, *Re*, of the flow passing through the stacked screen regenerator. Using a curve fit of the form:

$$h(Re_1) = \frac{b(\phi)\sigma^{1/3}}{4}\frac{k}{r_h}\left(1 + Re_1^{3/5}\right), \tag{4.64}$$

where the acoustic Reynolds Number is:

$$Re_1 = \frac{4|U_1|r_h\rho_m}{A\mu_m} = \frac{4r_h|\dot{m}_1|}{A\mu_m}, \tag{4.65}$$

the curve fits to the Kays and London (1984) data can be expressed as [Swift and Ward (1996)]:

$$b(\phi) = 3.81 - 11.29\phi + 9.47\phi^2, \tag{4.66}$$

$$g_c(Re_1) = \frac{2}{\pi}\int_0^{\pi/2}\frac{dz}{1 + Re_1^{3/5}\cos^{3/5}(z)}, \tag{4.67}$$

$$g_\nu(Re_1) = -\frac{2}{\pi}\int_0^{\pi/2}\frac{\cos(2z)dz}{1 + Re_1^{3/5}\cos^{3/5}(z)}. \tag{4.68}$$

Using Eqs. (4.65) - (4.68), the coefficient ψ_{ss} can be computed from Eq. (4.63). It should be noted, however, that the curve fit functions of Eqs. (4.66) - (4.68) are specific to the data of Kays and London (1984). If more accuracy in these equations is desired, the experiments of Kays and London can be repeated on the actual TAPCE regenerator once it is constructed, and more accurate curve fit functions can be derived from the resulting experimental data.

4.2.4 Energy fluxes at the regenerator/open duct interface

Hot gas at temperature T_h flows towards the regenerator from the combustion zone through the adjoining open duct, as shown in Figure 4.1. Since the oscillations in

the open duct can be assumed to be approximately isentropic and the mean gas temperature there is nearly uniform, the conduction and entropy flux terms can be neglected in Eqs. (4.54) and (4.55), respectively, to yield the total energy flux in the open duct:

$$\dot{H}_h = \dot{M} c_p \left(T_h - T_0\right) + \dot{E}_h , \tag{4.69}$$

where the subscript "*h*" denotes conditions at the hot-side open duct.

Denoting the temperature in the regenerator near the hot side regenerator interface as T_{int}, Eqs. (4.54) and (4.57) can be used to express the total energy flux at the right side of the stacked screen regenerator of the TAPCE:

$$\dot{H}_{re,h} = \dot{M} c_p \left(T_{int} - T_0\right) - \left(\psi + Ak + A_s k_s\right) \left. \frac{dT_{re}}{dx} \right|_{int} . \tag{4.70}$$

Assuming that the periphery of the engine is well-insulated, the total energy flux remains constant everywhere in the engine except at the cold heat exchanger, where heat is transferred out of the engine at the ambient temperature, T_0. Therefore, equating the total energy fluxes of Eqs. (4.69) and (4.70) yields the following expression for the acoustic energy flux in the open duct:

$$\dot{E}_h = \dot{M} c_p \left(T_{int} - T_h\right) - \left(\psi + Ak + A_s k_s\right) \left. \frac{dT_{re}}{dx} \right|_{int} . \tag{4.71}$$

This equation states that the acoustic energy output of the regenerator is a function of the difference in the convected thermal energy across the regenerator interface, minus the conductive and entropy flux losses down the regenerator. The same relationship was derived by very different means in a previous study [Weiland and Zinn (2003)], though without the entropy flux loss term, since $\psi = 0$ in the perfect thermal contact assumption of that study.

Rearranging Eq. (4.71) with the help of Eq. (4.59) and the state relation $dh = c_p dT$, where h is the enthalpy of the gas, an alternate description of the energy balance at the regenerator interface is obtained:

$$\dot{M}h_h = \dot{M}h_{int} + T_{int}\dot{S}_{re,ideal} + T_{int}\dot{S}_{re,loss} - (Ak + A_s k_s)\left.\frac{dT_{re}}{dx}\right|_{int} . \tag{4.72}$$

This equation states that the input thermal energy convected to the regenerator interface, $\dot{M}h_h$, is split into four thermal energy fluxes upon entering the regenerator. In the open cycle thermoacoustic engine without reactant preheating, three of these thermal energy fluxes are loss mechanisms that transport heat down the regenerator's temperature gradient without converting it into acoustic energy: the conductive heat flux, the thermoacoustic entropy flux due to imperfect thermal contact in the regenerator, $\dot{S}_{re,loss}$, and the convective heat flux at lower enthalpy, $\dot{M}h_{int}$. The remaining thermal energy is transported into the regenerator by the ideal entropy flux, $\dot{S}_{re,ideal}$.

4.2.5 Temperature difference at the regenerator/open duct interface

Note from Eq. (4.71) that the acoustic energy leaving the hot side of the regenerator, $\dot{E}_h$, increases as the mean temperature difference between the hot, incoming combustion products and the hot side of the regenerator increases. This temperature difference can be fairly substantial, and is a direct result of the joining conditions between the isothermal environment of the regenerator and the isentropic environment of the open duct [Weiland and Zinn (2003)].

The physical processes responsible for creating the temperature difference at the regenerator/open duct interface are shown schematically for various gas parcels in Figure

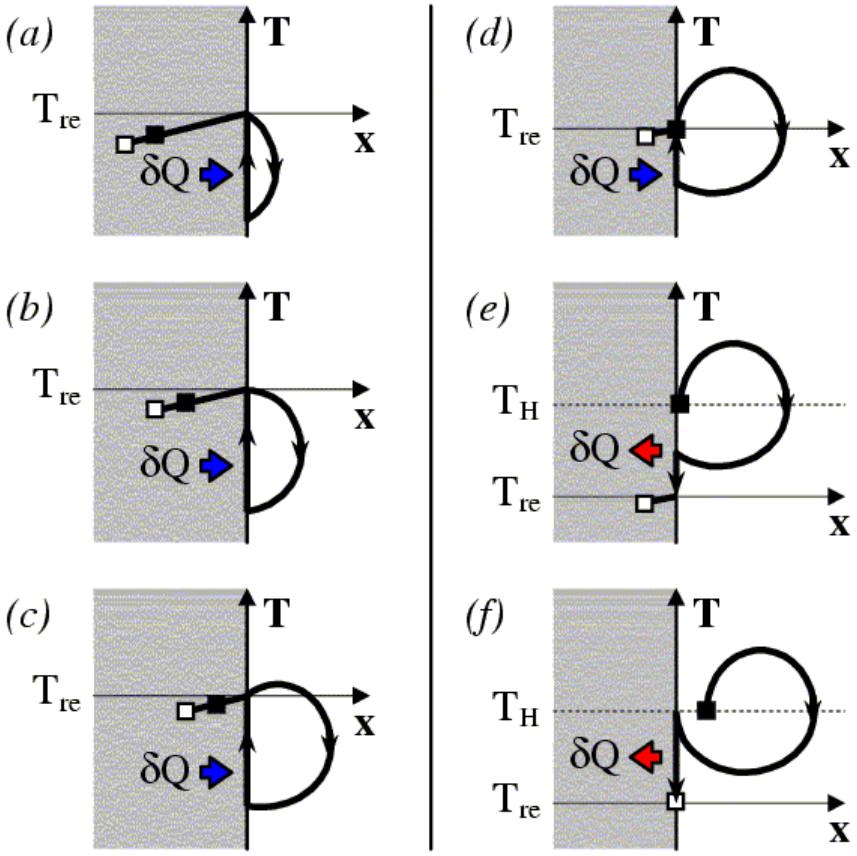

Figure 4.2: The temperature and acoustic displacement histories of various gas parcels near the regenerator/open duct interface (Reprinted with permission from [Weiland and Zinn (2003a)])

4.2, which can be viewed as a magnification of the regenerator/hot duct interface in Figure 4.1. Gas parcels that start the acoustic cycle at various locations within the regenerator are shown in Figures 4.2a through 4.2d. For good gas-solid thermal contact within the regenerator, these parcels of gas remain at the regenerator's temperature until they enter the open duct, where they undergo isentropic temperature oscillations in concert with the pressure oscillations of the traveling acoustic wave. These oscillations cause the gas parcels to re-enter the regenerator at temperatures below that of the regenerator [Smith and Romm (1992), Bauwens (1998), Kittel (1998)], where they receive heat from the regenerator solid and are rapidly heated back up to the temperature of the regenerator at the interface, T_{int}. Towards the end of the acoustic cycle, fresh gas parcels supplied by the steady mean gas flow that moves towards the regenerator, as depicted in Figures 4.2e and 4.2f, enter the regenerator for the first time. These gas parcels isentropically oscillate about their mean temperature, T_h, until they enter the regenerator, at which time they are cooled to T_{int} by contact with the regenerator's solid material.

In the absence of other sources of heat input or output, a heat balance of the regenerator solid at the interface shows [Weiland and Zinn (2003)] that the heat transferred from the solid to the cold returning gas must equal the heat transferred from the fresh gas to the regenerator solid, if the solid material is to maintain a constant mean temperature during steady-state operation. Satisfying this criterion gives rise to the mean temperature difference between the regenerator solid and the hot incoming gas, as cited above.

Through the development of an idealized theoretical model encompassing the physical processes described above [Weiland and Zinn (2003)], we can predict the dependence of the mean temperature difference upon important design and operating parameters of the TAPCE, including the acoustic pressure, mean mass flow rate, acoustic phase angles, and conductive heat losses. The results of this model show that the ratio of hot gas temperature to the regenerator interface temperature can be approximately expressed as [Weiland and Zinn (2003)]:

$$\frac{T_h}{T_{int}} \approx 1 - \frac{\gamma - 1}{\gamma} \frac{|p_1|}{p_m} \frac{|\dot{m}_1|}{\dot{M}} \frac{\cos\theta}{2} - \frac{A_s k_s \left(dT_{re}/dx\right)_{int}}{\dot{M} c_p T_{int}}, \tag{4.73}$$

where θ is the phase difference between the acoustic pressure and the acoustic mass flux, and $(dT_{re}/dx)_{int}$ is the mean temperature gradient of the regenerator solid at the open duct interface. Note that, since $\dot{M}$ is negative, $T_h > T_{int}$ for $-\pi/2 \le \theta \le \pi/2$, which corresponds to a positive acoustic energy flux (i.e. $\dot{E}$ travels to the right). Also, since the model used to derive Eq. (4.73) assumes perfect thermal contact within the regenerator, this equation does not account for the effects of the entropy flux due to the imperfect thermal contact in the regenerator.

The parameter with the largest impact on the temperature difference is $\dot{M}$, according to Eq. (4.73). As the mean mass flux decreases relative to the acoustic mass flux, the temperature difference increases considerably, and T_h can easily be 2-3 times larger than T_{int}, which is useful in yielding an appreciable acoustic power output according to Eq. (4.71).

4.2.6 *The acoustic energy gain in the regenerator*

The interface energy balance of Eq. (4.72) shows that acoustic energy is neither created nor destroyed at the regenerator interface. Instead, this equation shows that the ideal entropy flux carries thermal energy that is converted into acoustic energy as it travels down the regenerator's temperature gradient. To demonstrate this point, note first that $\dot{S}_{re,ideal}$ is a constant if viscous effects are neglected in the regenerator. Although this proof is somewhat tedious and will not be shown here, a constant ideal entropy flux can be used with Eq. (4.56) to show that the acoustic gain across the regenerator is:

$$\dot{E}_h - \dot{E}_c = -\left(T_{int}\dot{S}_{re,ideal} - T_c\dot{S}_{re,ideal}\right), \tag{4.74}$$

where T_c is the temperature at the cold side of the regenerator near the cold heat exchanger, which is not necessarily the same as the ambient temperature, T_0. This equation, which applies to both ideal and non-ideal regenerators, states that the acoustic energy gain is equal to the difference in the thermal energy carried by the ideal entropy flux in the regenerator. This is basically a statement of the first law of thermodynamics for an ideal regenerator, where the work produced in the regenerator is equal to its heat input minus its heat output.

Noting again that $\dot{S}_{re,ideal}$ is a constant in the regenerator, Eq. (4.56) can be differentiated with respect to x to yield:

$$\frac{d\dot{E}}{dx} \approx \frac{\dot{E}}{T_{re}}\frac{dT_{re}}{dx}. \tag{4.75}$$

This expression has been previously derived by other means [Swift (2002)], and is frequently used to approximate the acoustic energy gain in a regenerator with good solid-gas thermal contact in a traveling wave thermoacoustic device, although it does not

include losses from viscous effects. Note that the conductive loss and entropy flux loss terms have been retained in this analysis because they are functions of the local temperature gradient in the engine, and are needed for estimating the regenerator temperature profile and the acoustic energy output below. On the other hand, the viscous regenerator loss is not a function of the local temperature gradient, and is therefore neglected in this energy flux analysis.

4.2.7 The regenerator temperature profile

In the absence of any heat losses in the regenerator, the total energy flux in the regenerator is constant, and it follows that $d\dot{H}_{re}/dx = 0$. This criterion will change when reactant preheating is considered below, but for the time being, substitution of Eqs. (4.54) and (4.57) into this expression yields, upon rearrangement:

$$\frac{d^2 T_{re}}{dx^2} - \Xi \frac{dT_{re}}{dx} = 0, \tag{4.76}$$

where the parameter Ξ has been defined as:

$$\Xi \equiv \frac{\left(\dot{M} c_p\right)_{pr}}{\psi + Ak + A_s k_s}, \tag{4.77}$$

and the subscript *pr* is later used to denote the properties of the combustion products.

By specifying the temperatures at either end of the regenerator ($T_{re} = T_c$ at $x = 0$ and $T_{re} = T_{int}$ at $x = L$, as depicted in Figure 4.1), Eq. (4.76) can be solved for the mean temperature profile in the regenerator:

$$T_{re}(x) = T_c + (T_{int} - T_c)\frac{1 - e^{\Xi x}}{1 - e^{\Xi L}}. \tag{4.78}$$

In deriving this equation, it has been assumed that Ξ is a constant, an assumption that boils down to assuming that c_p, k, and k_s are independent of temperature in the regenerator, which is not entirely accurate. However, since these variables are not very strong functions of temperature, Eq. (4.78) provides a reasonable approximation for the temperature profile in the regenerator. Note that a similar derivation is given by Reid and Swift (2000), though it is only valid for standing wave thermoacoustic systems.

Knowing the regenerator's cold temperature and hot interface temperature, Eq. (4.78) allows one to calculate Ξ with just a single temperature measurement at any point within the regenerator. This can then be used to find $\dot{M}$ from Eq. (4.77), and is therefore a valuable means of evaluating the streaming mass flux in a closed cycle traveling wave thermoacoustic system. Such a procedure was suggested by Gedeon (1997), and was later employed by Job et. al. (2003) to determine the streaming mass flux passing through a quasi-adiabatic stack ($r_h \approx \delta_\kappa$) in a looped tube. While the theory Job et. al. (2003) developed to describe the temperature profile includes radial heat loss effects not modeled here, it suffers from a major shortcoming in that it also appears to neglect thermoacoustic heat pumping effects in the stack. In spite of this, their theory appears to agree qualitatively with their experimental data, though only one temperature measurement was made in the stack in the presence of an acoustic field, and there is no further experimental evidence to suggest that this agreement with theory is not merely coincidental.

Finally, also note that by differentiating Eq. (4.78) with respect to x to evaluate the temperature gradient at the regenerator's hot-side interface, the result can be

substituted into Eq. (4.71), along with Eq. (4.77), to yield a simplified expression for the hot-side acoustic energy flux:

$$\dot{E}_h = \dot{M} c_p \left(T_{int} - T_h - \frac{(T_c - T_{int}) e^{\Xi L}}{1 - e^{\Xi L}} \right), \tag{4.79}$$

where it has also been assumed that the quantity ($\psi + Ak + A_s k_s$) is independent of temperature.

4.2.8 Cold side energy fluxes

An energy balance for the cold heat exchanger can be written as:

$$\dot{H}_c = \dot{H}_{re,c} + \dot{Q}_c, \tag{4.80}$$

where $\dot{H}_c$ is the total energy flux in the open duct to the left of the cold heat exchanger, as shown in Figure 4.1. The total energy flux at the cold side of the regenerator, $\dot{H}_{re,c}$, can be found by setting $T_{re} = T_c$ in Eqs. (4.54) and (4.57), i.e.:

$$\dot{H}_{re,c} = \dot{M} c_p (T_c - T_0) - (\psi + Ak + A_s k_s) \left. \frac{dT_{re}}{dx} \right|_c . \tag{4.81}$$

The cold duct to the left of the regenerator can be assumed to be approximately isentropic with a negligible temperature gradient, so eliminating the appropriate terms from Eqs. (4.54) and (4.55) yields following equation for the total energy flux in the cold duct:

$$\dot{H}_c = \dot{M} c_p (T_c - T_0) + \dot{E}_c, \tag{4.82}$$

where it has also been assumed that the temperature in the cold duct is the same as the temperature of the cold heat exchanger, T_c. Substituting Eqs. (4.56), (4.81) and (4.82) into Eq. (4.80) yields:

$$\dot{Q}_c = -T_c \dot{S}_{re,ideal} + (\psi + Ak + A_s k_s) \left. \frac{dT_{re}}{dx} \right|_c . \tag{4.83}$$

This equation states that in addition to the normal heat rejection, $-T_c\dot{S}_{re,ideal}$, the heat transfer out of the cold heat exchanger, $\dot{Q}_c$, also includes the thermal energy losses at the cold end of the regenerator, as described in Eq. (4.81).

Finally, if the cold heat exchanger temperature is larger than the ambient temperature, then there is a second heat rejection, $\dot{Q}_0$, associated with the exhaust of combustion products at T_c to the environment at T_0. Assuming that the acoustic energy loss through the exhaust port is much smaller than the cold side acoustic energy, $\dot{E}_c$, and that all of the mean mass flux flows out the exhaust port, an energy balance around the exhaust port shows that this mean flow heat rejection can be written as:

$$\dot{Q}_0 = \dot{E}_c - \dot{H}_c = -\dot{M}c_p\left(T_c - T_0\right). \tag{4.84}$$

4.2.9 *Energy flux analysis*

A study of the above energy flux equations can provide some valuable insights into the processes that govern general open cycle traveling wave thermoacoustic engines. To facilitate this analysis, it is assumed that $T_c = T_0$, and the above equations are cast in a non-dimensional form by dividing energy flux terms by $-\dot{M}c_pT_0$, temperatures by the ambient temperature T_0, and lengths by the regenerator length, L. This non-dimensionalization is fairly straightforward and will not be performed here, although it is worth noting that all of the dimensionless energy fluxes in the region surrounding the regenerator only depend on three dimensionless parameters, T_h/T_0, T_{int}/T_0, and ΞL.

Solving the dimensionless forms of the above equations yields the temperature profile and various energy fluxes shown in Figure 4.3, for representative conditions in a basic open cycle traveling wave thermoacoustic engine. The temperature plotted in

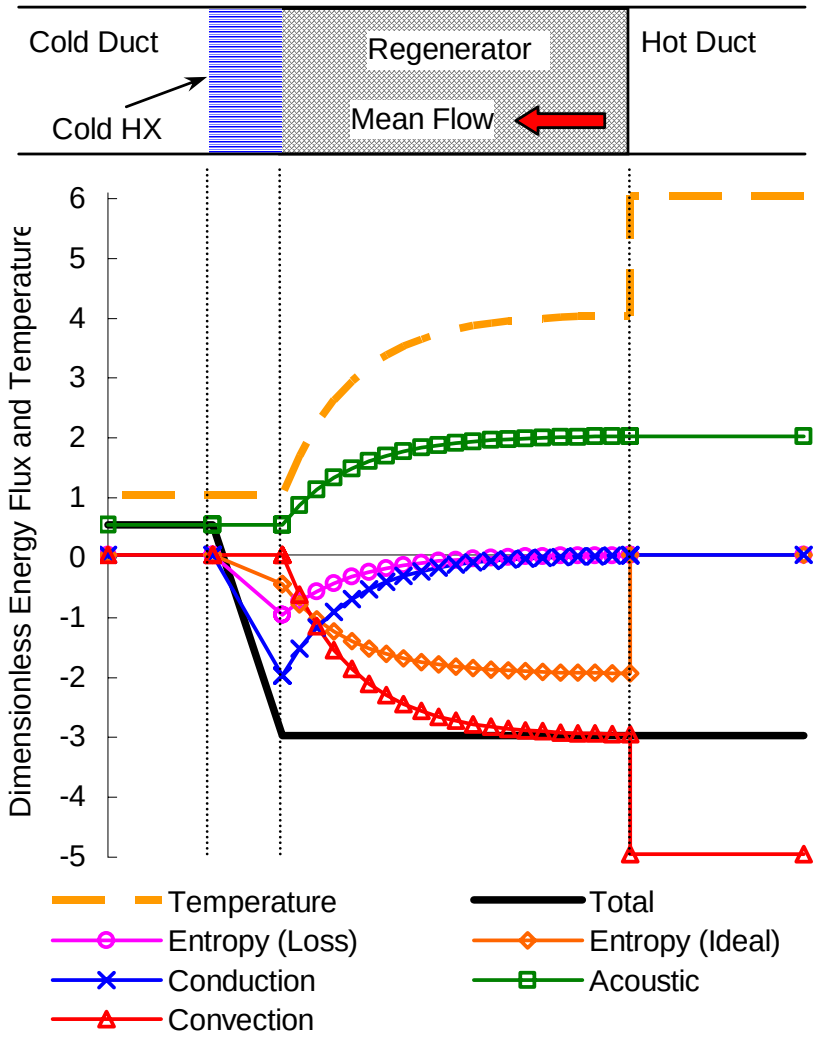

Figure 4.3: The spatial dependence of the dimensionless entropy fluxes and temperature in an open cycle thermoacoustic engine, for the representative conditions: $T_h/T_0 = 6$, $T_{int}/T_0 = 4$, and $\Xi L = -5$.

Figure 4.3 shows a significant temperature jump at the regenerator's interface with the hot duct, followed by an exponential temperature profile within the regenerator. The convective energy flux mirrors this profile, as it primarily depends on the local gas temperature.

Figure 4.3 shows that in the hot duct to the right of the regenerator, the total energy flux consists of the sum of the acoustic and convective energy fluxes, as described in Eq. (4.69), while just inside the regenerator, the total energy flux is equal to the sum of the convective energy flux and the regenerator's thermal energy losses, as expressed in Eq. (4.70). Note that in addition to these two energy fluxes in Figure 4.3, there is an acoustic energy flux within the regenerator that is "cancelled" by the thermal energy transport associated with the ideal second order entropy flux, as described in Eqs. (4.55) and (4.59).

In Figure 4.3, the second order entropy flux resulting from imperfect thermal contact in the regenerator, $\dot{S}_{re,loss}$, is shown along with the conductive energy flux, which are both proportional to the local temperature gradient in the regenerator. Since the convective energy flux decreases with the temperature in the regenerator, the conductive and imperfect entropy flux losses must increase as the temperature decreases to maintain a constant total energy flux in the regenerator. As a result, the temperature gradient is low at the regenerator's hot end, and high at its cold end, explaining the exponential shape of the regenerator's temperature profile, as expressed in Eq. (4.78). Since the details of the heat transfer out of the cold heat exchanger are not of interest in this study, the heat fluxes are simply depicted in Figure 4.3c as linearly decreasing to zero over the length of the cold heat exchanger.

The mechanism creating the exponential temperature profile in the regenerator turns out to be of great importance, since it implies that all of the convective thermal energy flux at the hot end of the regenerator, $\dot{M}c_p(T_{int} - T_0)$, is gradually converted into heat conduction and additional thermoacoustic entropy flux losses as it convects down the regenerator's temperature gradient. This energy, equal to the total energy flux of Eq. (4.81), is essentially wasted, and leaves the system through the cold heat exchanger, as described in Eq. (4.83). Consequently, the efficiency of a simple open cycle thermoacoustic engine will be very poor, since a substantial portion of the input thermal energy is exhausted to the atmosphere without performing any useful work.

4.3 Reactant Preheating Process

Recovery of this convective thermal energy loss could substantially improve the thermal efficiency of the thermoacoustic engine, without having significant effects on its operation. For this reason, the design of the TAPCE includes preheating of the combustion reactants by routing the reactant inlet pipes through the regenerator so that some of this waste heat is transferred to the reactants. Such preheating could increase the combustion process temperature, thereby increasing the input temperature, T_h, and the efficiency of the engine. Equivalently, the preheating could be used to reduce the amount of fuel required to reach a desired combustion temperature, T_h, thus increasing the fuel energy-to-acoustic energy conversion efficiency [Weinberg (1986)]. In either case, the transfer of waste heat from the regenerator into the combustion process reactants would result in a more linear temperature profile, thereby reducing the conductive and thermoacoustic entropy fluxes that leave the system through the cold heat exchanger. This reactant preheating process is analyzed in more detail below.

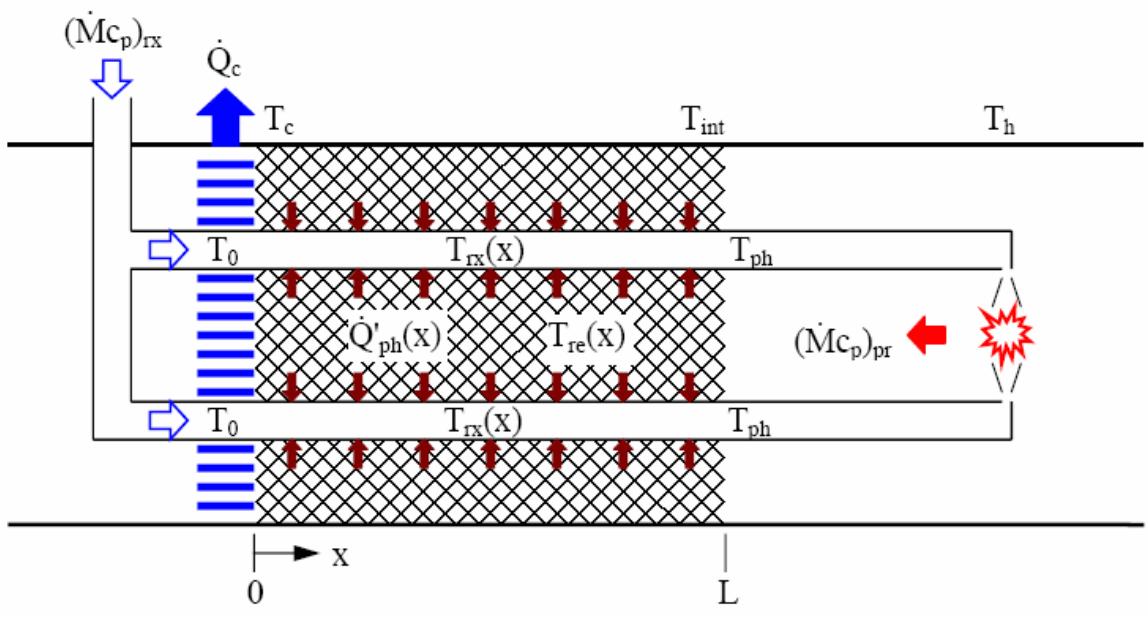

Figure 4.4: Diagram of the reactant preheating process

A schematic of the reactant preheating process used in the TAPCE is shown in Figure 4.4. Here, as with the more basic case of Figure 4.1, the regenerator's cold and hot sides are at temperatures T_c and T_{int}, respectively, with the mean mass flux of hot combustion products, $\dot{M}_{pr}$, flowing through the regenerator from right to left. The total mean mass flux of reactants, $\dot{M}_{rx}$, flows from left to right through the regenerator, and is evenly distributed between n individual reactant preheat pipes, each of inside diameter D_{ph}. The reactants enter the regenerator at ambient temperature, T_0, and exit at a preheat temperature, T_{ph}. A one-dimensional geometry is assumed in which the mean temperature at any axial location is denoted by T_{rx} for the reactants, and by T_{re} for the combustion products flowing through the regenerator.

4.3.1 *Heat transfer to the combustion reactants*

Assuming that the specific heat of the reactants is constant and that no other energy fluxes are important in the reactant preheat pipes, the heat transfer rate to the reactants can be expressed as:

$$\left(\dot{M}c_p\right)_{rx}\frac{dT_{rx}}{dx}=\dot{Q}'_{ph}, \tag{4.85}$$

where $\dot{Q}'_{ph}$ is the rate of heat transfer per unit length. In a global energy balance of the reactant preheating, Eq. (4.85) can be integrated across the length of the regenerator to yield:

$$\left(\dot{M}c_p\right)_{rx}\left(T_{ph}-T_0\right)=\dot{Q}_{ph}, \tag{4.86}$$

where $\dot{Q}_{ph}$ is the total rate of heat transfer to the reactants.

To determine the reactants' preheat temperature, T_{ph}, the details of the heat transfer process will need to be considered. Applying the above assumptions, the rate of heat transfer from the combustion products to the reactants can be expressed as [Incropera and DeWitt (1996)]:

$$\dot{Q}'_{ph}=n\pi D_{ph}h\left(T_{re}-T_{rx}\right), \tag{4.87}$$

where h is the convective heat transfer coefficient, and $n\pi D_{ph}$ is the total circumference of all of the individual preheat pipes across which heat is transferred. The convective heat transfer coefficient, h, is generally an empirical coefficient that is correlated to experimental data though the use of the Nusselt Number, $Nu = hD_{ph}/k$, which will be examined in more detail in Chapter 5 below. Substituting Eq. (4.87) into Eq. (4.85), applying the definition of the Nusselt Number and rearranging yields a differential equation for T_{rx}:

$$\frac{dT_{rx}}{dx} = N\left(T_{re} - T_{rx}\right), \tag{4.88}$$

where N is assumed to be a constant given by:

$$N \equiv \frac{n\pi kNu}{\left(\dot{M}c_p\right)_{rx}} = \frac{n\pi D_{ph} h}{\left(\dot{M}c_p\right)_{rx}}. \tag{4.89}$$

4.3.2 Heat transfer from the combustion products

The manner in which the total energy flux in the regenerator is affected by the rate of heat transfer to the reactants can be expressed as:

$$\frac{d\dot{H}_{re}}{dx} = -\dot{Q}'_{ph}. \tag{4.90}$$

Integrating this expression across the length of the regenerator yields:

$$\dot{H}_{re,h} - \dot{H}_{re,c} = -\dot{Q}_{ph}, \tag{4.91}$$

where the total energy fluxes at the hot and cold sides of the regenerator are still represented by Eqs. (4.70) and (4.81), respectively.

Since there is excellent thermal contact between the regenerator solid, the combustion products, and the walls of the reactant preheat pipes, these temperatures are all assumed to be equal to T_{re} at any axial location. Applying Eq. (4.87), and using Eqs. (4.54) and (4.57) yields:

$$\left(\dot{M}c_p\right)_{pr} \frac{dT_{re}}{dx} - \left(\psi + Ak + A_s k_s\right)\frac{d^2 T_{re}}{dx^2} = -n\pi D_{ph} h\left(T_{re} - T_{rx}\right). \tag{4.92}$$

Applying the definition

$$M \equiv \frac{\left(\dot{M}c_p\right)_{rx}}{\left(\dot{M}c_p\right)_{pr}}, \tag{4.93}$$

and Eqs. (4.77) and (4.89) to Eq. (4.92) results in a simple second order differential equation for T_{re}:

$$\frac{d^2T_{re}}{dx^2} - \Xi\frac{dT_{re}}{dx} = M\Xi N\left(T_{re} - T_{rx}\right). \tag{4.94}$$

4.3.3 General solution of the reactant preheating process

Equations (4.88) and (4.94) are two coupled differential equations for T_{rx} and T_{re}, respectively, which can be solved to determine the reactant preheat temperature, T_{ph}. The solution to this set of equations is greatly simplified by noting that the coefficients *M, N*, and Ξ are approximately independent of position and temperature within the regenerator. Using the property relationships in the following chapter to evaluate Eqs. (4.77), (4.89), and (4.93) for Ξ, *N,* and *M*, respectively, it can be shown that these parameters differ from their average values by 10% or less over the temperature range 300 K ≤ T ≤ 1000 K. At this level of error, it is reasonable to assume that these coefficients are constant in Eqs. (4.88) and (4.94), and that they can be represented by their average values within the regenerator or preheat pipes.

Assuming constant coefficients, solution of Eqs. (4.88) and (4.94) is most easily accomplished by forming a system of linear, coupled first order differential equations, where the second order Eq. (4.94) is expressed as a system of two first order equations:

$$\frac{dT_{re}}{dx} = T'_{re}, \tag{4.95}$$

$$\frac{dT'_{re}}{dx} = \Xi T'_{re} + M\Xi N\left(T_{re} - T_{rx}\right). \tag{4.96}$$

Employing some linear algebra, Eqs. (4.95), (4.96) and (4.88) can be cast in the form [Kreyszig (1993)]:

$$\mathbf{y}' = \mathbf{A}\mathbf{y}\,, \tag{4.97}$$

where

$$\mathbf{y} = \begin{bmatrix} T_{re} \\ T'_{re} \\ T_{rx} \end{bmatrix}, \tag{4.98}$$

$$\mathbf{A} = \begin{bmatrix} 0 & 1 & 0 \\ M\Xi N & \Xi & -M\Xi N \\ N & 0 & -N \end{bmatrix}. \tag{4.99}$$

Equation (4.97) is a classic eigenvalue problem that can be solved by assuming a solution of the form $\mathbf{y} = \mathbf{z}e^{\lambda x}$, where $\mathbf{z}$ is an eigenvector and λ is the corresponding eigenvalue [Kreyszig (1993)]. Substituting this solution form into Eq. (4.97) and using Eq. (4.99) yields:

$$(\mathbf{A} - \mathbf{I}\lambda)\mathbf{z} = \begin{bmatrix} -\lambda & 1 & 0 \\ M\Xi N & \Xi - \lambda & -M\Xi N \\ N & 0 & -N - \lambda \end{bmatrix}\mathbf{z} = 0\,. \tag{4.100}$$

Setting the determinant of $(\mathbf{A} - \mathbf{I}\lambda)$ equal to zero and solving yields three different eigenvalues:

$$\lambda_1 = 0; \quad \lambda_2 = \tfrac{1}{2}\left[\Xi - N + R\right]; \quad \lambda_3 = \tfrac{1}{2}\left[\Xi - N - R\right], \tag{4.101}$$

where

$$R \equiv \sqrt{(\Xi + N)^2 + 4M\Xi N}\,. \tag{4.102}$$

Solving Eq. (4.100) for each of the eigenvalues in Eqs. (4.101) gives the corresponding eigenvectors:

$$\mathbf{z}_1 = \begin{bmatrix} 1 \\ 0 \\ 1 \end{bmatrix}; \quad \mathbf{z}_2 = \begin{bmatrix} \tfrac{1}{2}(\Xi + N + R) \\ \tfrac{1}{4}(\Xi - N + R)(\Xi + N + R) \\ N \end{bmatrix}; \quad \mathbf{z}_3 = \begin{bmatrix} \tfrac{1}{2}(\Xi + N - R) \\ \tfrac{1}{4}(\Xi - N - R)(\Xi + N - R) \\ N \end{bmatrix}.$$

(4.103)

The general solution to Eq. (4.97) is a linear superposition of the three eigenvalue solutions, i.e. [Kreyszig (1993)]:

$$\mathbf{y} = c_1\mathbf{z}_1 e^{\lambda_1 x} + c_2\mathbf{z}_2 e^{\lambda_2 x} + c_3\mathbf{z}_3 e^{\lambda_3 x}, \tag{4.104}$$

where the constants c_1, c_2, and c_3 are determined by the boundary conditions. In this case, the boundary conditions $T_{rx}(x = 0) = T_0$, $T_{re}(x = 0) = T_c$, and $T_{re}(x = L) = T_{int}$, yield the following constants:

$$c_1 = T_0 + \frac{2R(T_{int} - T_0) + (T_c - T_0)\left[(\Xi + N - R)e^{\lambda_3 L} - (\Xi + N + R)e^{\lambda_2 L}\right]}{R\left(2 - e^{\lambda_2 L} - e^{\lambda_3 L}\right) + (\Xi + N + 2M\Xi)\left(e^{\lambda_3 L} - e^{\lambda_2 L}\right)}, \tag{4.105}$$

$$c_2 = \frac{(T_{int} - T_0)(\Xi - N - R) + (T_c - T_0)\left[2N - (\Xi + N - R)e^{\lambda_3 L}\right]}{NR\left(2 - e^{\lambda_2 L} - e^{\lambda_3 L}\right) + N(\Xi + N + 2M\Xi)\left(e^{\lambda_3 L} - e^{\lambda_2 L}\right)}, \tag{4.106}$$

$$c_3 = \frac{-(T_{int} - T_0)(\Xi - N + R) - (T_c - T_0)\left[2N - (\Xi + N + R)e^{\lambda_2 L}\right]}{NR\left(2 - e^{\lambda_2 L} - e^{\lambda_3 L}\right) + N(\Xi + N + 2M\Xi)\left(e^{\lambda_3 L} - e^{\lambda_2 L}\right)}. \tag{4.107}$$

Computing these coefficients and using Eqs. (4.98) and (4.101) - (4.107), the solution for the temperature profile of the combustion reactants can be determined from:

$$T_{rx}(x) = c_1 + c_2 N e^{\frac{1}{2}(\Xi - N + R)x} + c_3 N e^{\frac{1}{2}(\Xi - N - R)x}, \tag{4.108}$$

while the reactant preheat temperature, $T_{ph} = T_{rx}(x = L)$,can be computed from:

$$T_{ph} = c_1 + N(c_2 + c_3). \tag{4.109}$$

Likewise, the solution of the regenerator temperature profile is determined by:

$$T_{re}(x) = c_1 + c_2 \tfrac{1}{2}(\Xi + N + R)e^{\frac{1}{2}(\Xi - N + R)x} + c_3 \tfrac{1}{2}(\Xi + N - R)e^{\frac{1}{2}(\Xi - N - R)x}, \tag{4.110}$$

and its gradient is found with:

$$\begin{aligned} T'_{re}(x) = {} & c_2 \tfrac{1}{4}(\Xi + N + R)(\Xi - N + R)e^{\frac{1}{2}(\Xi - N + R)x} \\ & + c_3 \tfrac{1}{4}(\Xi + N - R)(\Xi - N - R)e^{\frac{1}{2}(\Xi - N - R)x}. \end{aligned} \tag{4.111}$$

4.3.4 Solution for M = -1

Note that the above solution does not apply in the special case where M = -1. As Figure 4.4 indicates, the mean mass flux of reactants flows in the positive x-direction, burns in the combustion zone, and the products flow back in the opposite direction such that $\dot{M}_{rx} = -\dot{M}_{pr}$. According to the definition of M in Eq. (4.93), the special case where M = -1 then applies when the specific heats of the reactants and products are assumed to be equal. This is a common assumption that is frequently made in combustion studies [Turns (1996)], and becomes more accurate for leaner combustion reactant mixtures, where the change in the chemical composition of the working fluid is not as pronounced. This situation also applies to the important case where the chemical composition of the working fluid does not change within the engine. In such a case, the working fluid is preheated in passing through the regenerator and is further heated in the "combustion zone," (e.g., with an electric heat exchanger) before flowing back into the regenerator.

Also, since it generally turns out that $M \approx$ -0.9 in the modeling studies below, the situation in which M = -1 serves as a good estimate of the more complicated general solution presented above, and allows for an easier interpretation of the results. To a reasonable degree of approximation, this estimation of the general solution is further simplified by assuming that $T_c = T_0$ in the following analysis.

Thus, in the case where M = -1, the eigenvalues of the characteristic Eq. (4.100) become:

$$\lambda_1 = 0; \quad \lambda_2 = 0; \quad \lambda_3 = \Xi - N . \tag{4.112}$$

Since the first two eigenvalues are equal, the general solution of Eq. (4.97) becomes [Kreyszig (1993)] :

$$\mathbf{y} = c_1\mathbf{z}_1 e^{\lambda_1 x} + c_2\left[\mathbf{z}_1 x e^{\lambda_1 x} + \mathbf{z}_2 e^{\lambda_2 x}\right] + c_3\mathbf{z}_3 e^{\lambda_3 x}, \tag{4.113}$$

where the eigenvectors can be shown to be:

$$\mathbf{z}_1 = \begin{bmatrix} 1 \\ 0 \\ 1 \end{bmatrix}; \quad \mathbf{z}_2 = \begin{bmatrix} 1/N \\ 1 \\ 0 \end{bmatrix}; \quad \mathbf{z}_3 = \begin{bmatrix} \Xi \\ \Xi(\Xi - N) \\ \Xi \end{bmatrix}. \tag{4.114}$$

Applying the new boundary conditions, where $T_c = T_0$, to the general solution for $M = -1$ in Eq. (4.113), the constants c_1, c_2 and c_3 become:

$$c_1 = T_0 - \frac{N(T_{int} - T_0)}{N^2 L - N\Xi L - \Xi\left(1 - e^{(\Xi - N)L}\right)}, \tag{4.115}$$

$$c_2 = \frac{N(N - \Xi)(T_{int} - T_0)}{N^2 L - N\Xi L - \Xi\left(1 - e^{(\Xi - N)L}\right)}, \tag{4.116}$$

$$c_3 = \frac{(T_{int} - T_0)}{N^2 L - N\Xi L - \Xi\left(1 - e^{(\Xi - N)L}\right)}. \tag{4.117}$$

Applying these constants to Eq. (4.113), the solution for the reactant temperature profile, in the case where $M = -1$, becomes:

$$T_{rx}(x) = T_0 + (T_{int} - T_0)\frac{N(N - \Xi)x - N\left(1 - e^{(\Xi - N)x}\right)}{N(N - \Xi)L - \Xi\left(1 - e^{(\Xi - N)L}\right)}, \tag{4.118}$$

while the regenerator temperature profile becomes:

$$T_{re}(x) = T_0 + (T_{int} - T_0)\frac{N(N - \Xi)x - \Xi\left(1 - e^{(\Xi - N)x}\right)}{N(N - \Xi)L - \Xi\left(1 - e^{(\Xi - N)L}\right)}. \tag{4.119}$$

Note from these equations that when there is no heat transfer to the reactants (i.e., $N = 0$), the reactants' temperature remains constant at T_0, while the combustion product temperature reduces to Eq. (4.78) above. In the case of very high heat transfer, where $|N| >> |\Xi|$ and $NL >> 1$, Eq. (4.119) yields a linear regenerator temperature profile, while Eq.

(4.118) predicts a mostly linear reactant temperature profile, with an exponential transitional component near $x = 0$, i.e.,

$$T_{rx}(x) \approx T_0 + (T_{int} - T_0)\left(\frac{x}{L} - \frac{1 - e^{(\Xi - N)x}}{NL}\right). \tag{4.120}$$

Such a case yields a constant temperature difference between the combustion reactants and products throughout most of the regenerator, resulting in a constant heat flux along most of the axial length of the regenerator as expressed by Eq. (4.87). This is the ideal situation that recovers nearly all of the "lost" convective thermal energy that enters the regenerator by preheating the combustion reactants, though the physical realization of this ideal is fairly difficult.

4.4 Engine Lost Work and Irreversibility

While the derived expressions for the energy fluxes in an open cycle traveling wave thermoacoustic engine tell us a great deal about the operation of such a device, consideration of the second law of thermoacoustics can tell us how the engine can be improved. In particular, the second law quantifies the various irreversibilities in the engine, which can be used to determine which loss mechanisms contribute the most to the inefficiency of the engine.

Several loss mechanisms have been identified in the TAPCE, including losses from axial conductive heat transfer, entropy flux due to imperfect thermal contact in the regenerator, viscous and thermal relaxation dissipation, and heat transfer across finite temperature differences, both in the reactant preheating process, as expressed in Eq. (4.87), and due to the mean temperature difference at the regenerator/hot duct interface. One valuable means of comparing these losses is to look at the amount of potential work

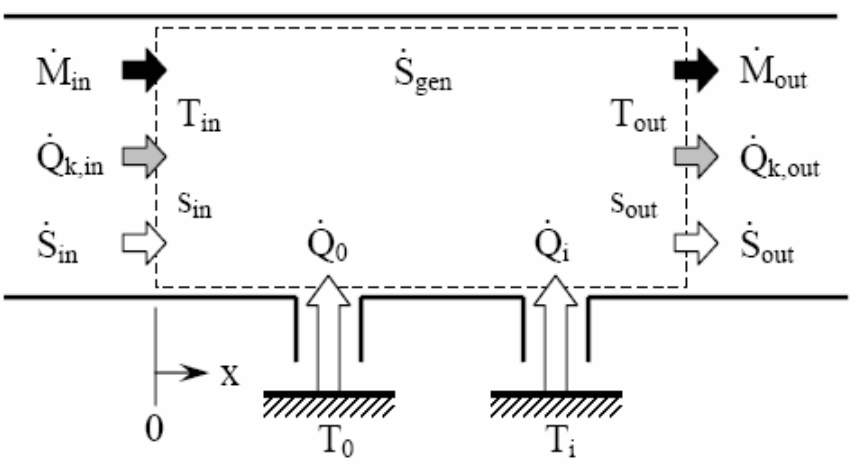

Figure 4.5: Generalized control volume for the second law thermodynamic analysis

that each of these irreversibilities dissipates. The amount of lost work, $\dot{W}_{lost}$, is linked to the entropy generated by the loss mechanism, $\dot{S}_{gen}$, through the Gouy-Stodola theorem, i.e. [Bejan (1997)]:

$$\dot{W}_{lost} = T_0 \dot{S}_{gen}, \tag{4.121}$$

where all entropy generation losses are referenced to the ambient temperature, T_0. To determine the amount of work lost due to each of the engine's irreversibilities, we must look at the second law of thermodynamics for each component.

4.4.1 The second law for thermoacoustic systems

To assist with the analysis of the engine's irreversibilities, we will consider a generalized section of a thermoacoustic device as shown in Figure 4.5, where total mass fluxes enter and leave the control volume, and heat is transferred in or out of the control volume at ambient temperature, T_0, and at other temperatures T_i. In addition, only steady

state processes will be considered in the following analyses, thus the total entropy in the control volume can be considered to be constant.

Neglecting transient effects, a statement of the second law of thermodynamics for the control volume of Figure 4.5 can be expressed as [Bejan (1997)]:

$$\dot{S}_{gen} = (\dot{m}s)_{out} - (\dot{m}s)_{in} - \sum_i \frac{\dot{Q}_i}{T_i}, \tag{4.122}$$

where $\dot{Q}_i$ are the individual heat transfers into the control volume at their respective temperatures, T_i. Expanding $(\dot{m}s)$ into its mean and acoustic components and time averaging yields, to second order:

$$(\dot{m}s) \approx \dot{M}s_m + \rho_m \tfrac{1}{2}\mathrm{Re}\left[s_1\tilde{U}_1\right] = \dot{M}s_m + \dot{S}, \tag{4.123}$$

where the definition of the second order entropy flux, $\dot{S}$, has been applied. Extracting the axial conduction heat fluxes from the general summation of heat fluxes in Eq. (4.122) yields:

$$\dot{S}_{gen} = \left(\dot{M}s_m + \dot{S} + \frac{\dot{Q}_k}{T_m}\right)_{out} - \left(\dot{M}s_m + \dot{S} + \frac{\dot{Q}_k}{T_m}\right)_{in} - \sum_i \frac{\dot{Q}_i}{T_i}, \tag{4.124}$$

where

$$\dot{Q}_k = -(Ak + A_s k_s)\frac{dT_m}{dx}. \tag{4.125}$$

By substituting Eq. (4.124) into Eq. (4.121), the work lost due to irreversible processes in the generalized control volume of Figure 4.5 can be written as:

$$\dot{W}_{lost} = T_0\left(\dot{M}s_m + \frac{\dot{Q}_k + T_m\dot{S}}{T_m}\right)_{out} - T_0\left(\dot{M}s_m + \frac{\dot{Q}_k + T_m\dot{S}}{T_m}\right)_{in} - \sum_i \frac{T_0\dot{Q}_i}{T_i}. \tag{4.126}$$

4.4.2 Lost work from irreversibilities in the TAPCE

Applying the appropriate control volumes, Eq. (4.126) above can be used to determine the amount of lost work attributed to each component of the TAPCE. The primary loss mechanisms that will be investigated in the TAPCE include the irreversibility of the combustion process, heat transfer across finite temperature differences at the regenerator/hot duct interface, in the reactant preheating process, and in the cold heat exchanger, viscous losses in the reactant inlet pipes and exhaust port, and by conduction and entropy flux losses in the regenerator.

4.4.2.1 Reactant inlet pipes

To simplify the analysis of the reactant inlet pipes, it can be assumed that acoustic effects are negligible in comparison with the mean flow effects, and that the axial conduction through the walls of the preheat pipes are included in the regenerator's conduction losses. The heat flux from the regenerator varies along the length of the preheat pipes according to Eq. (4.87), while the temperature from which this heat is transferred, T_i in Eq. (4.126), is the temperature of the wall of the preheat pipe, $T_{re}(x)$. Integrating this entropy flux due to heat transfer along the length of the regenerator and noting that the mass flux is constant, Eq. (4.126) for the reactant preheat pipes can be written as:

$$\dot{W}_{lost,rx} = \dot{M}T_0\left(s_{ph} - s_0\right) - T_0\int_0^L \frac{\dot{Q}'_{ph}(x)}{T_{rx}(x)}dx\,. \tag{4.127}$$

Assuming ideal gas behavior, the change in entropy can be represented as:

$$s_2 - s_1 = c_p \ln\left(\frac{T_2}{T_1}\right) - R\ln\left(\frac{p_2}{p_1}\right). \tag{4.128}$$

Using this expression and Eqs. (4.87) and (4.89) to describe the heat transfer, Eq. (4.127) becomes:

$$\dot{W}_{lost,rx} = \left(\dot{M}c_p\right)_{rx} T_0 \left[\ln\left(\frac{T_{ph}}{T_0}\right) + \frac{\gamma - 1}{\gamma} \ln\left(\frac{p_{m,s}}{p_m}\right) + N\left(L - \int_0^L \frac{T_{re}(x)}{T_{rx}(x)} dx \right) \right], \tag{4.129}$$

where $T_{rx}(x)$ and $T_{re}(x)$ are represented by Eqs. (4.108) and (4.110), respectively, $p_{m,s}$ is the mean reactant supply pressure, and p_m is the reference mean pressure in the combustion zone. This equation gives the lost work for two different loss mechanisms. The lost work due to the viscous pressure drop in the reactant header and preheat pipes is given by the second term in brackets in Eq. (4.129), while the lost work due to the heat transfer across a finite temperature difference is given by the sum of the remaining terms.

4.4.2.2 Combustion zone

The irreversibility of the combustion process alone can be determined by looking solely at the mean convective entropy fluxes of the preheated combustion reactants and the hot combustion products [Bejan (1997)]. Thus, neglecting the acoustic, conductive and heat transfer entropy fluxes, and applying Eq. (4.126) to the control volume of the combustion zone shown in Figure 4.1 yields:

$$\dot{W}_{lost,comb} = \dot{M}_{pr} T_0 \left(s_{ph} - s_h\right). \tag{4.130}$$

Note that since mass is not allowed to accumulate in the combustion zone, that $\dot{M}_{rx} = \dot{M}_{pr} < 0$ in this analysis, as depicted in Figure 4.1, although $\dot{W}_{lost,comb}$ is always positive since $s_h > s_{ph}$ for an exothermal combustion process [Bejan (1997)]. Also, since the preheated reactants and hot combustion products have different chemical compositions, simplifications such as Eq. (4.128) cannot be applied to this equation.

Finally, as will be seen in Chapter 6, the lost work associated with the irreversibility of the combustion process in some cases accounts for nearly half of the total lost work in the engine. Unfortunately this loss mechanism is unavoidable in combustion systems, though the modeling results of Chapter 6 show that the lost work associated with this process generally decreases for increasing combustion temperatures.

4.4.2.3 Regenerator/hot duct interface

At the interface between the hot side of the regenerator and its adjoining hot duct, the gas parcel temperature oscillations create a situation where heat is transferred across a finite temperature difference when the gas parcels enter the regenerator, as described in Figure 4.2 [Smith and Romm (1992), Bauwens (1998), Kittel (1998)]. The work lost in this situation can be determined with Eq. (4.126), where the hot duct can be approximately modeled as an isentropic environment with a negligible temperature gradient, so that $\left(\dot{Q}_k + T_m \dot{S}\right)_h \approx 0$. For a thin control volume surrounding the regenerator/hot duct interface in Figure 4.1, it can be assumed that no lateral heat transfer exits the control volume and that the pressure across it is constant. Consequently, Eq. (4.126) for the control volume can be written as:

$$\dot{W}_{lost,int} = \dot{M}_{pr} T_0 \left(s_h - s_{int}\right) - \frac{T_0}{T_{int}} \left(\dot{Q}_k + T_{int} \dot{S}_{re}\right). \tag{4.131}$$

For no lateral heat transfer across the control volume, the total energy fluxes across the control volume are equal, i.e., $\dot{H}_h = \dot{H}_{re,h}$. Using Eqs. (4.59), (4.69), (4.70) and (4.125), one can show that the heat flux at the hot side of the regenerator can be expressed as:

$$\dot{Q}_k + T_{int}\dot{S}_{re} = \left(\dot{M}c_p\right)_{pr}\left(T_h - T_{int}\right). \tag{4.132}$$

Applying Eqs. (4.128) and (4.132) to Eq. (4.131), the lost work at the regenerator/hot duct interface becomes:

$$\dot{W}_{lost,int} = \left(\dot{M}c_p\right)_{pr} T_0\left[1 - \frac{T_h}{T_{int}} + \ln\left(\frac{T_h}{T_{int}}\right)\right]. \tag{4.133}$$

Note that the sum of the terms in brackets in Eq. (4.133) is negative for $T_h > T_{int}$, but that the lost work is always positive, since $\dot{M}_{pr}$ is negative according to the sign convention in this analysis.

For no temperature difference across the interface (i.e., $T_h = T_{int}$), Eq. (4.133) states that there is no work lost in this location, but note from Eq. (4.71) that we require a temperature difference at the interface in order to produce acoustic power. The operation of the TAPCE is therefore dependent on the irreversible heat transfer at the regenerator/hot duct interface. Although this may seem to adversely affect the attractiveness of the TAPCE, the alternative is to use a hot heat exchanger, where the heat transfer into the engine is dependent on a difference between the heat exchanger's solid temperature and the temperature of the working fluid [Swift (1992)], which similar to the reactant preheating heat transfer described in Eq. (4.87). Since the work lost in each of these situations is very similar, the temperature difference that must be tolerated at the regenerator/hot duct interface does not significantly affect the viability of the TAPCE.

4.4.2.4 Regenerator

To determine the work lost in the regenerator, Eq. (4.126) can be written for a control volume enclosing the regenerator, but excluding the flow of combustion reactants through the preheat pipes, i.e.,

$$\dot{W}_{lost,re} = \dot{M}_{pr} T_0 \left(s_{int} - s_c\right) + T_0 \int_0^L \frac{\dot{Q}'_{ph}(x)}{T_{re}(x)} dx + \frac{T_0}{T_{int}} \left(\dot{Q}_k + T_{re}\dot{S}\right)_{int} - \frac{T_0}{T_c} \left(\dot{Q}_k + T_{re}\dot{S}\right)_c , \tag{4.134}$$

where, as was done for the reactant inlet pipes above, the heat transfer entropy flux per unit length is integrated over the length of the regenerator to give the total entropy flux due to the reactant preheating process. Using the definitions of $\dot{Q}_k$, $\dot{S}$, and $\dot{Q}'_{ph}$ in Eqs. (4.125), (4.59) and (4.87), respectively, Eq. (4.134) can be written as:

$$\dot{W}_{lost,re} = \dot{M}_{pr} T_0 \left(s_{int} - s_c\right) + \left(\psi + Ak + A_s k_s\right) \left(\frac{T_0}{T_c} \left. \frac{dT_{re}}{dx} \right|_c - \frac{T_0}{T_{int}} \left. \frac{dT_{re}}{dx} \right|_{int} \right) + T_0 \left(\frac{\dot{E}_c}{T_c} - \frac{\dot{E}_h}{T_{int}} \right) + T_0 \int_0^L \frac{n\pi D_i h \left(T_{re}(x) - T_{rx}(x)\right)}{T_{re}(x)} dx . \tag{4.135}$$

Finally, using Eq. (4.128) and making use of the definitions of Ξ, *N*, and *M* in Eqs. (4.77), (4.89) and (4.93), respectively, the work lost in the regenerator becomes:

$$\dot{W}_{lost,re} = \left(\dot{M}c_p\right)_{pr} T_0 \left[\ln\left(\frac{T_{int}}{T_c}\right) + \frac{\gamma - 1}{\gamma} \ln\left(\frac{p_{m,c}}{p_m}\right) \right] + T_0 \left(\frac{\dot{E}_c}{T_c} - \frac{\dot{E}_h}{T_{int}} \right) + \left(\dot{M}c_p\right)_{pr} T_0 \left[\frac{1}{\Xi} \left(\frac{T_0}{T_c} \left. \frac{dT_{re}}{dx} \right|_c - \frac{T_0}{T_{int}} \left. \frac{dT_{re}}{dx} \right|_{int} \right) + MN \left(L - \int_0^L \frac{T_{rx}}{T_{re}} dx \right) \right] . \tag{4.136}$$

Several types of irreversibility in the regenerator are explicitly accounted for in Eq. (4.136). The first term in brackets accounts for the convective heat fluxes entering and leaving the regenerator at its hot and cold ends, while the second term in brackets describes the work lost through viscous dissipation of the mean mass flux passing through the regenerator, where $p_{c,m}$ is the mean pressure at the cold side of the regenerator. This viscous term should be very small, as the mean pressure difference across the regenerator is a second order term, according to Eq. (4.19), indicating that

$p_{m,c}/p_m \approx 1$. The acoustic energy terms on the right side of Eq. (4.136) account for the viscous and thermal relaxation dissipation of acoustic energy in the regenerator. If dissipation in the regenerator is neglected, then these two terms cancel one another out, as an integration of Eq. (4.75) across the length of the regenerator would show. If dissipation is included, then $\dot{E}_h / T_{int} < \dot{E}_c / T_c$, and the lost work in the regenerator increases. The first term in brackets on the second line of Eq. (4.136) describes the change in conduction and imperfect entropy flux losses across the regenerator, where the temperature gradients at the cold and hot ends of the regenerator can be determined by substituting $x = 0$ and $x = L$, respectively, into Eq. (4.111) for the regenerator temperature gradient. The last term in Eq. (4.136) accounts for the irreversible heat transfer from the regenerator to the preheating reactants.

4.4.2.5 Cold heat exchanger

At the cold heat exchanger, there is a loss of work due to the transfer of heat across the finite temperature difference between T_c and ambient temperature, T_0. To be more specific, we assume that the temperature of the cooling fluid circulating through the cold heat exchanger is at ambient temperature, while the temperature of the combustion products on the thermoacoustic side of the heat exchanger is at the cold heat exchanger's temperature. If we also assume isentropic conditions in the cold duct to the left of the heat exchanger, the lost work expression of Eq. (4.126) can be applied to a control volume enclosing the cold heat exchanger and the cold side of the regenerator, yielding:

$$\dot{W}_{lost,chx} = \frac{T_0}{T_c}\left(\dot{Q}_k + T_c \dot{S}\right) + \dot{Q}_c , \tag{4.137}$$

where $\dot{Q}_c$ is evaluated at ambient temperature. Using the definitions of $\dot{Q}_k$, $\dot{S}$, and $\dot{Q}_c$ from Eqs. (4.125), (4.59) and (4.83), respectively, the work lost at the cold heat exchanger can be rewritten as:

$$\dot{W}_{lost,chx} = \left(1 - \frac{T_0}{T_c}\right)\dot{Q}_c = \left(1 - \frac{T_0}{T_c}\right)\left[\dot{E}_c + (\psi + Ak + A_s k_s)\left.\frac{dT_{re}}{dx}\right|_c\right]. \tag{4.138}$$

4.4.2.6 Combustion product exhaust

The combustion products passing through the cold heat exchanger are maintained at the temperature T_c in order to prevent the water vapor from condensing out of the gas mixture. These combustion products are exhausted to the atmosphere through the exhaust port, which also is a source of lost work since the combustion products still carry usable heat at the temperature T_c. Assuming that acoustic and conduction effects are negligible in the area surrounding the exhaust port, the lost work for the combustion exhaust process is simply equal to the flow availability of the combustion products [Bejan (1997)], i.e.:

$$\dot{W}_{lost,e} = \dot{M}_{pr}\left[h_c - h_0 + T_0(s_c - s_0)\right], \tag{4.139}$$

where h_c and s_c are evaluated at T_c and $p_{m,c}$. In this equation, the work lost in the combustion process is due to the thermal loss described above, in addition to the viscous pressure drop loss of the mean mass flux flowing through the exhaust port.

4.4.3 Efficiency of the TAPCE

Minimizing the entropy generation, and hence lost work, is equivalent to maximizing the power output of an engine [Bejan (1997)]. Thus, the combination of the above lost work computations for the primary components of the TAPCE can be used to

help optimize the geometry and operating conditions of the engine. To accomplish this, the sum of the lost work expressions above can be differentiated with respect to a particular geometric parameter or operating condition. Setting the result equal to zero and solving the equation yields an optimal value for the investigated parameter that generally minimizes the entropy generation. Note, however, that the second derivative must be taken to determine if the entropy generation is minimized (second derivative positive) or maximized (second derivative negative).

As an example, in the simple case with no reactant preheating, the sum of the work lost in the regenerator and the work lost at the regenerator/hot duct interface can be minimized with respect to the regenerator interface temperature, T_{int}. This can be shown to result in the same optimal interface temperature that yields the maximum acoustic power output for the engine, $T_{int,opt} \approx (T_h T_c)^{1/2}$, as derived by Weiland and Zinn (2004a). In a similar fashion, the above lost work expressions can be used to help maximize the power output of the engine with respect to a variety of variables, such as the regenerator length, L, interface temperature, T_{int}, preheat pipe diameter, D_{ph}, number of preheat pipes, n, etc. Although this can be done analytically, the forms of some of the expressions above suggest that numerical computation may work best for this sort of task.

Note, however, that the above expressions do not account for all of the loss mechanisms in the TAPCE. For instance, heat losses to the secondary cold heat exchanger and viscous dissipation in the inertance and resonator could represent a non-trivial fraction of the total losses in the system. Many of these loss mechanisms are accounted for in the model of the following chapter, although the lost work associated with each loss is not calculated.

Instead, we can measure the total losses modeled in the TAPCE by calculating the second law thermodynamic efficiency for the engine:

$$\eta_{II} = \frac{\dot{E}_L}{\dot{W}_{\max,fuel}}, \tag{4.140}$$

where $\dot{E}_L$ is the acoustic power output exiting the bottom of the TAPCE and entering the resonator, as shown in Figure 4.1, and $\dot{W}_{\max,fuel}$ is the maximum amount of work that can be derived from the incoming mass flux of fuel and air. This last quantity is attained by comparing the flow availabilities of the incoming reactants to the outgoing combustion products [Bejan (1997)].

Assuming that each flow enters and leaves the engine at ambient temperature, T_0, as depicted in Figure 4.4, the work that can be derived from the reactants is given by:

$$\dot{W}_{fuel} = \dot{M}\left[h_{rx} - h_{pr} - T_0\left(s_{rx} - s_{pr}\right)\right] - \sum T_0 \dot{S}_{gen}, \tag{4.141}$$

where the last term, in light of Eq. (4.121), is the sum of all of the work lost throughout the engine. The maximum amount of work is attained when this term is zero, i.e.:

$$\dot{W}_{\max,fuel} = \dot{M}\left[h_{rx} - h_{pr} - T_0\left(s_{rx} - s_{pr}\right)\right]. \tag{4.142}$$

The combination of Eqs. (4.140) and (4.142) will be the primary means of measuring the efficiency of the TAPCE in the following chapters.

CHAPTER 5

MODELING THE TAPCE

This chapter describes, in detail, the construction of a computational model of the TAPCE design. This model is used to help assess the efficiency and feasibility of the TAPCE, which is further discussed in Chapter 6.

Many of the computations in this numerical model are based on the equations derived in Chapter 4, which describes the theory of open cycle traveling wave thermoacoustic engines with combustion. The computer code that is based upon the model developed in this chapter can be found in Appendix A.

5.1 Engineering Equation Solver Program

The software program chosen for the modeling of the TAPCE is Engineering Equation Solver (EES) [F-Chart Software], as it is adept at iteratively solving problems with a large number of equations and unknowns. It is also capable of performing integration and differentiation, and can easily handle complex numbers.

As is shown below, the acoustic model of the TAPCE can be broken down into coupled sets of equations that describe the change in the complex acoustic pressure and volumetric velocity across various components of the engine. By linking the output of one component to the input of another, the entire engine can be acoustically modeled

using sets of equations describing each component in the engine, which are easily solved by EES to give the acoustic pressures and velocities throughout the engine.

In addition, EES is well-suited for the study of energy system designs, due to the large databases of fluid and solid properties that are built into the program. These are very helpful in allowing one to easily study the effects of varying the temperature, pressure, and fluid composition in the engine, and facilitate thermodynamic analyses of the engine's efficiency and losses.

5.2 Fluid Properties

The working fluids used in the TAPCE are generally either air, reactants, or combustion products. As noted in Chapter 3, it is assumed that air is present in all parts of the engine except for those components within the inner pipe, though trace amounts of combustion reactants or products may find their way into the remainder of the engine through the thermal buffer tube. For the purposes of this feasibility study, it can be assumed that the fluid in these parts of the engine is purely air, and that it behaves as an ideal gas.

Within the inner pipe portion of the engine, the reactants flow through the preheat pipes into the combustion zone, where they are converted into combustion products that flow through the regenerator and out the exhaust pipe. The compositions of the combustion reactants or products are primarily a function of the type of fuel used and the equivalence ratio, Φ, which expresses the ratio of the oxidizer required for complete combustion of the fuel to the total amount of oxidizer actually used. For the TAPCE model, we will choose methane (CH_4) as the fuel, because it is readily available as the primary component in natural gas, and would be used to fuel in the natural gas

liquefaction application of the TAPCE, as discussed in Chapter 3. A chemical equation describing the ideal combustion of a lean mixture of methane and air can be written as:

$$\Phi\,\mathrm{CH_4} + 2(\mathrm{O_2} + 3.76\mathrm{N_2}) \rightarrow \Phi\,\mathrm{CO_2} + 2\Phi\,\mathrm{H_2O} + 2(1-\Phi)\mathrm{O_2} + 7.52\,\mathrm{N_2}, \tag{5.1}$$

where it is assumed that the reaction progresses until the fuel is completely consumed, and that there is no dissociation of the combustion products.

The total number of moles of combustion reactants or products in Eq. (5.1) is equal to $N_{tot} = \Phi + 9.52$, thus the mole fraction of any particular species, i, in the reactant or combustion product mixtures is given by [Turns (1996)]:

$$\chi_i = \frac{N_i}{N_{tot}} = \frac{P_i}{P_{tot}}, \tag{5.2}$$

where P_i is the partial pressure of species i in a mixture with total pressure, P_{tot}. The total molecular weight of the mixture is [Turns (1996)]:

$$MW_{mix} = \sum_i MW_i \chi_i, \tag{5.3}$$

where MW is the molecular weight.

Since the total number of moles of reactants is equal to that of the combustion products in the ideal combustion of methane and air, Eq. (5.3) describes the molecular weight of both the reactants and the combustion products, though it should be noted that in general, this is not true of all fuels. As a result, the mean density of both the reactant and combustion product mixtures can be determined using the ideal gas equation of state:

$$\rho_m = \frac{p_m MW_{mix}}{R_u T_m} = \frac{p_m}{R T_m}, \tag{5.4}$$

where R_u is the universal gas constant.

The ratio of the total mass of a particular species in the mixture to the total mass of the mixture is known as the species mass fraction, Y_i, and can be expressed as [Turns (1996)]:

$$Y_i = \chi_i \frac{MW_i}{MW_{mix}}. \tag{5.5}$$

For a given equivalence ratio, the mole and mass fractions of each of the reactants' or products' species can be computed from Eqs. (5.2) and (5.5), respectively, which are then used to determine the fluid properties of the mixture of these components. For instance, the mass-specific enthalpies of the reactant and product mixtures can be represented, respectively, by [Turns (1996)]:

$$h_{rx} = \sum_i \left(Y_i h_i(T)\right)_{rx}; \quad h_{pr} = \sum_i \left(Y_i h_i(T)\right)_{pr}, \tag{5.6}$$

while the mass-specific entropies of the reactant and product mixtures are:

$$s_{rx} = \sum_i \left(Y_i s_i(T, P_i)\right)_{rx}; \quad s_{pr} = \sum_i \left(Y_i s_i(T, P_i)\right)_{pr}, \tag{5.7}$$

where the entropy is evaluated using the partial pressure defined in Eq. (5.2).

The change in enthalpy of the reactants or combustion products is often computed through the use of the constant pressure specific heat, i.e., $dh = c_p dT$. In these instances, the specific heat is most accurately computed by using Eq. (5.6) for the enthalpy. For example, for the temperature change across the regenerator, the mass-based specific heat of the combustion products is determined by:

$$c_{p,pr} = \frac{h_{pr}(T_{int}) - h_{pr}(T_c)}{T_{int} - T_c}, \tag{5.8}$$

and likewise for the reactants and other temperature differences. In other instances, the constant pressure specific heat at a particular temperature is needed, as in the

computation of δ_κ in Eq. (2.1). In this case, the specific heat is computed from [Belcher et. al. (1999)]:

$$c_p(T) = \frac{\bar{c}_p(T)}{MW_{mix}} = \frac{1}{MW_{mix}} \sum_i \chi_i \bar{c}_{p,i}(T), \tag{5.9}$$

where $\bar{c}_p$ is the molar constant pressure specific heat. Equation (5.9) can then be used to compute the ratio of specific heats, γ, from:

$$\gamma = \frac{\bar{c}_p}{\bar{c}_v} = \frac{\bar{c}_p}{\bar{c}_p - R_u} = \frac{c_p}{c_p - R}, \tag{5.10}$$

where $\bar{c}_v$ is the molar constant volume specific heat.

Finally, using the mole fractions of the reactants or combustion products, the dynamic viscosity and thermal conductivity coefficients of the reactant or product mixtures can be computed from [Belcher et. al. (1999)]:

$$\mu(T) = \sum_i \chi_i \mu_i(T), \tag{5.11}$$

$$k(T) = \sum_i \chi_i k_i(T). \tag{5.12}$$

5.3 Lumped Parameter Acoustic Models

As noted above, since the components of the TAPCE driver are all much smaller than an acoustic wavelength, they can be modeled acoustically as lumped parameter elements, such as resistances, inertances and compliances. By linking all of the lumped parameter components together, the acoustic pressures and volumetric velocities can be estimated at important points in the engine, thereby offering a very simple means of analyzing the feasibility of a thermoacoustic device.

5.3.1 General component models

The lumped parameter models for components in thermoacoustic devices have been derived by Backhaus and Swift (2000) and Swift (2002). These derivations are repeated below, as they are essential for understanding how the TAPCE is modeled.

5.3.1.1 Inertance and viscous resistance components

To begin, the momentum equation, Eq. (4.22), can be integrated over the length of a thermoacoustic component, Δx, to yield:

$$\Delta p_1 = \frac{-i\omega\rho_m \Delta x}{A(1-f_\nu)} U_1 . \tag{5.13}$$

This is the equation that is used to model the inertance components in the TAPCE lumped parameter model. The physical meaning of this equation can be ascertained by separating real and imaginary components of the thermoviscous function f_ν, i.e.

$$\Delta p_1 = -ZU_1 = -(i\omega L + R_\nu)U_1 , \tag{5.14}$$

where the inertance, L, and viscous resistance, R_ν, are represented by:

$$L = \frac{\rho_m \Delta x}{A} \frac{1 - \mathrm{Re}[f_\nu]}{|1-f_\nu|^2}, \tag{5.15}$$

$$R_\nu = \frac{\omega\rho_m \Delta x}{A} \frac{\mathrm{Im}[-f_\nu]}{|1-f_\nu|^2} . \tag{5.16}$$

In open ducts, thermoviscous functions can be accurately represented by their boundary layer approximations, i.e.:

$$f_{\nu,\kappa} = \frac{(1-i)\delta_{\nu,\kappa}}{2r_h} . \tag{5.17}$$

Noting that $r_h >> \delta_v$ in an open duct, f_v approaches zero according to Eq. (5.17), and the resistive term becomes small compared to the inertance term, which can be approximated as:

$$L \approx \frac{\Delta x \rho_m}{A}. \tag{5.18}$$

5.3.1.2 Compliance and thermal relaxation components

As was done above with the momentum equation, integrating the continuity equation, Eq. (4.34), over the length of an engine component yields:

$$\Delta U_1 = -\frac{i\omega A \Delta x\left[1 - f_\kappa(\gamma - 1)\right]}{\gamma p_m} p_1 + \int_0^{\Delta x} g_T U_1 dx + \int_0^{\Delta x} g_q \dot{q}_1 dx, \tag{5.19}$$

where g_T and g_q are defined by Eqs. (4.39) and (4.40), respectively.

In an open duct without pulse combustion or a mean temperature gradient, g_T and g_q are approximately zero, and the change in acoustic velocity across the component is expressed by the first term on the right side of Eq. (5.19), i.e.,

$$\Delta U_1 = -\frac{i\omega A \Delta x\left[1 - f_\kappa(\gamma - 1)\right]}{\gamma p_m} p_1. \tag{5.20}$$

This is the expression used in the modeling of the lumped parameter compliance elements in the TAPCE, and includes damping effects due to thermal relaxation of the acoustic temperature oscillations. This can be more readily seen by separating the real and imaginary parts of Eq. (5.20), i.e.:

$$\Delta U_1 = -\frac{1}{Z} p_1 = -\left(i\omega C + \frac{1}{R_\kappa}\right) p_1, \tag{5.21}$$

where the compliance, C, and thermal relaxation resistance, $1/R_\kappa$, are given by:

$$C = \frac{A\Delta x}{\gamma p_m}\left(1 + [\gamma - 1]\mathrm{Re}[f_\kappa]\right), \tag{5.22}$$

$$\frac{1}{R_\kappa} = \frac{\gamma - 1}{\gamma}\frac{\omega A \Delta x\, \mathrm{Im}[-f_\kappa]}{p_m}. \tag{5.23}$$

If it is further assumed that $r_h >> \delta_{v,\kappa}$ in the open duct geometry, then $f_\kappa \rightarrow 0$, according to Eq. (5.17), and the thermal relaxation term in Eq. (5.21) becomes much smaller than the compliance term, which can then be approximated as:

$$C = \frac{\Delta x A}{\gamma p_m} = \frac{V}{\gamma p_m}. \tag{5.24}$$

5.3.2 Regenerator model

Although most components in a traveling wave thermoacoustic engine can be modeled as open ducts, this is not true of the regenerator, where $r_{h,re} << \delta_{v,\kappa}$, $\mathrm{Re}[f_v, f_\kappa] \rightarrow 1$, and $\mathrm{Im}[f_v, f_\kappa] \rightarrow 0$. Also, since the thermal processes occurring in the regenerator are much more complex than those in an ordinary engine component, both the acoustic pressure and acoustic velocity vary throughout the regenerator. Consequently, it is not as easy to analytically integrate the thermoacoustic continuity and momentum equations across the regenerator to relate its input pressure and velocity to its output pressure and velocity. As a result, the TAPCE model includes a simultaneous integration of the thermoacoustic continuity and momentum equations across the regenerator. Since the EES program cannot perform integrations of complex numbers, these two equations are broken into their real and imaginary parts, and all four equations are integrated simultaneously across the regenerator.

To further complicate matters, the differential continuity and momentum equations derived above, Eqs. (4.34) and (4.22), respectively, are not easily employed for

these integrations since accurate thermoviscous functions f_v and f_κ do not exist for the irregular geometry of the stacked screen regenerator. To work around this problem, Swift and Ward (1996) derived a set of thermoacoustic conservation equations that use curve fits to experimentally determined friction factors and heat transfer coefficients for stacked screen regenerators. Some of these equations have already been used above in the determination of the parameter ψ_{ss} in Eq. (4.63) for stacked screen regenerators.

The thermoacoustic continuity equation of Swift and Ward (1996) is fairly complex and accounts for many different phenomena, though it can be reduced to a relatively compact expression by making a few reasonable assumptions about the environment within the regenerator. Specifically, if we assume ideal gas behavior, traveling wave acoustic phasing in the regenerator, a very large regenerator solid heat capacity compared to the gas, and that terms of order $(r_{h,re}/\delta_\kappa)^2$ can be neglected, then it can be shown that the thermoacoustic continuity equation for a stacked screen regenerator can be reduced to:

$$\frac{dU_1}{dx} \approx -\frac{i\omega C_{re}}{x_{re}} p_1 + \frac{1}{T_{re}} \frac{dT_{re}}{dx} U_1, \tag{5.25}$$

where the isothermal compliance of the regenerator is defined as:

$$C_{re} = \frac{\phi x_{re} A_{re}}{p_m}, \tag{5.26}$$

and $A_{re}\phi$ is the cross-sectional area of the gas in the regenerator. These equations are also used by Backhaus and Swift (2000) to evaluate the volumetric velocity change across the regenerator of the TASHE, and they are not very sensitive to the details of the regenerator geometry, since they can simply be derived by assuming that $f_v = 1$ and $f_\kappa = 1$ in Eqs. (4.34) and (5.22).

The thermoacoustic momentum equation for a stacked screen regenerator, as determined by Swift and Ward (1996), can be expressed as:

$$\frac{dp_1}{dx} = -\frac{i\omega\rho_{eff}}{A_{re}\phi}U_1 - \frac{\mu_m}{r_{h,re}^2 A_{re}\phi}\left[\frac{c_1(\phi)}{8} + \frac{c_2(\phi)Re_1}{3\pi}\right]U_1, \tag{5.27}$$

where μ_m is the local mean viscosity coefficient in the regenerator. The terms in brackets in Eq. (5.27) are Swift and Ward's curve fits to the experimental friction factors for stacked screen regenerators, as compiled by Kays and London (1984). The curve fit coefficients c_1 and c_2 are given by:

$$c_1(\phi) = 1268 - 3545\phi + 2544\phi^2, \tag{5.28}$$

$$c_2(\phi) = -2.82 + 10.7\phi - 8.6\phi^2. \tag{5.29}$$

Swift and Ward note that in most regenerators, the first term on the right side of Eq. (5.27), which accounts for the inertance of the regenerator, is usually less than 1% of the second term, which describes the viscous losses. Neglecting this term in Eq. (5.27), and substituting Eq. (4.65) for the acoustic Reynolds number, Re_1, yields:

$$\frac{dp_1}{dx} = -\frac{\mu_m}{r_{h,re}^2 A_{re}\phi}\frac{c_1(\phi)}{8}U_1 - \frac{4|\dot{m}_1|c_2(\phi)}{3\pi r_{h,re}(A_{re}\phi)^2}U_1. \tag{5.30}$$

Note that the coefficient of the second term on the right side of Eq. (5.30) is approximately independent of the temperature, since conservation of first order mass flux implies that $|\dot{m}_1|$ is approximately constant throughout the regenerator. The coefficient of the first term, on the other hand, is a function of temperature through the mean local viscosity coefficient, μ_m, which can be assumed to follow a power-law temperature dependence of the form [Backhaus and Swift (2000), Swift (2002)]:

$$\mu_m(T_m) = \mu_0(T_c)\left[\frac{T_m}{T_c}\right]^{b_\mu}, \tag{5.31}$$

where the power law exponent typically falls in the range $0.65 < b_\mu < 0.85$ for most common gases [Swift (2002)], and in the range $0.70 < b_\mu < 0.75$ for combustion products. Substituting Eq. (5.31) into Eq. (5.30) yields:

$$\frac{dp_1}{dx} = -\left[\frac{R_{c1}}{x_{re}}\left(\frac{T_m}{T_c}\right)^{b_\mu} + \frac{R_{c2}}{x_{re}}\right]U_1, \tag{5.32}$$

where the effective resistances due to each of the curve fit terms are defined as:

$$R_{c1} = \frac{\mu_0 x_{re} c_1(\phi)}{8 r_{h,re}^2 A_{re}\phi}, \tag{5.33}$$

$$R_{c2} = \frac{4 x_{re} c_2(\phi)|\dot{m}_1|}{3\pi r_{h,re}(A_{re}\phi)^2}, \tag{5.34}$$

where R_{c1} would be the resistance of the regenerator if only the first friction factor curve fit coefficient, c_1, were used, and the entire regenerator was assumed to be at the ambient temperature, T_0. For the purposes of the lumped parameter modeling, it is useful to define a total regenerator resistance that accounts for the variation of viscosity with temperature, i.e.:

$$R_{re} = R_{c2} + \frac{R_{c1}}{x_{re}}\int_0^{x_{re}}\left(\frac{T_{re}}{T_c}\right)^{b_\mu} dx, \tag{5.35}$$

where Eq. (4.110) can be used for $T_{re}(x)$.

Equations (5.25) and (5.32) are the thermoacoustic continuity and momentum equations that are simultaneously integrated across the regenerator in the numerical model of the TAPCE. Given the parameters that define the regenerator temperature

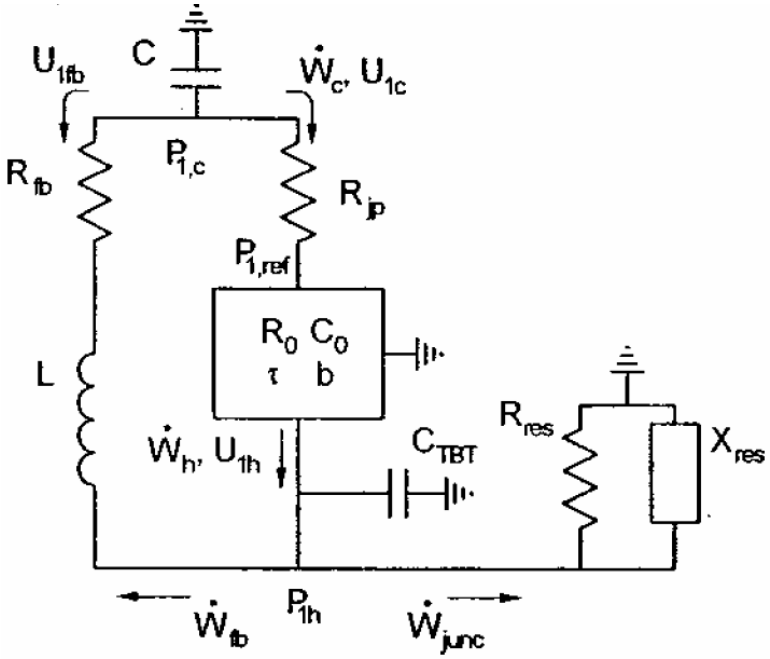

Figure 5.1: Detailed lumped parameter model used for the TASHE (reprinted with permission from [Backhaus and Swift (2000)])

profile, these integrations relate the cold side acoustic pressure and velocity to the pressure and velocity on the hot side of the regenerator.

5.3.3 Validation of the lumped parameter modeling method

Having developed lumped parameter acoustic models for the various components of a thermoacoustic engine, the degree of accuracy that these models can attain in capturing the true acoustic character of a thermoacoustic engine should be examined. Backhaus and Swift (2000) used various forms of the above equations to build two different models of the TASHE. The first model is a basic lumped parameter model, as shown in Figure 5.1. The lumped parameter components in this model are computed from the lumped parameter equations above, while the regenerator is assumed to have a linear temperature gradient, allowing simplified forms of Eqs. (5.25) and (5.32) above to

be integrated analytically. This model does a good job of describing the physics and operating principles of the TASHE, and provides good estimates of the acoustic pressures and velocities in the engine, though the accuracy of the basic lumped parameter model was not sufficient for comparing the models results with experimental data [Backhaus and Swift (2000)].

Therefore, a second model of the TASHE was built using the DeltaE program, which integrates the differential thermoacoustic continuity, momentum and energy equations throughout the entire device [Ward and Swift (1994)]. The DeltaE program is also able to incorporate many loss mechanisms present in the TASHE, and provides excellent agreement with experimental results [Backhaus and Swift (2000)].

The DeltaE inputs and outputs used for a particular operating point of the TASHE are available in the literature [Swift (2002)]. Using this data and the geometric dimensions of the resonator of the TASHE [Backhaus and Swift (2000)], a more detailed lumped parameter model of the TASHE was created, as shown in Figure 5.2. This model contains several components that are not a part of the basic model of Figure 5.1, including a detailed model of the resonator, the inertance of the thermal buffer tube, the compliance of the space between the jet pump and the regenerator, and the compliance of the feedback inertance. In addition, each of the inertance and compliance components of this model are calculated with Eqs. (5.13) and (5.19), respectively, to account for the viscous resistances of the inertance elements and thermal relaxation resistances of the compliances in the model, though they are not explicitly shown in Figure 5.2.

The regenerator in this detailed lumped parameter model is assumed to have a linear temperature profile, which is a good approximation in the TASHE, as long as any

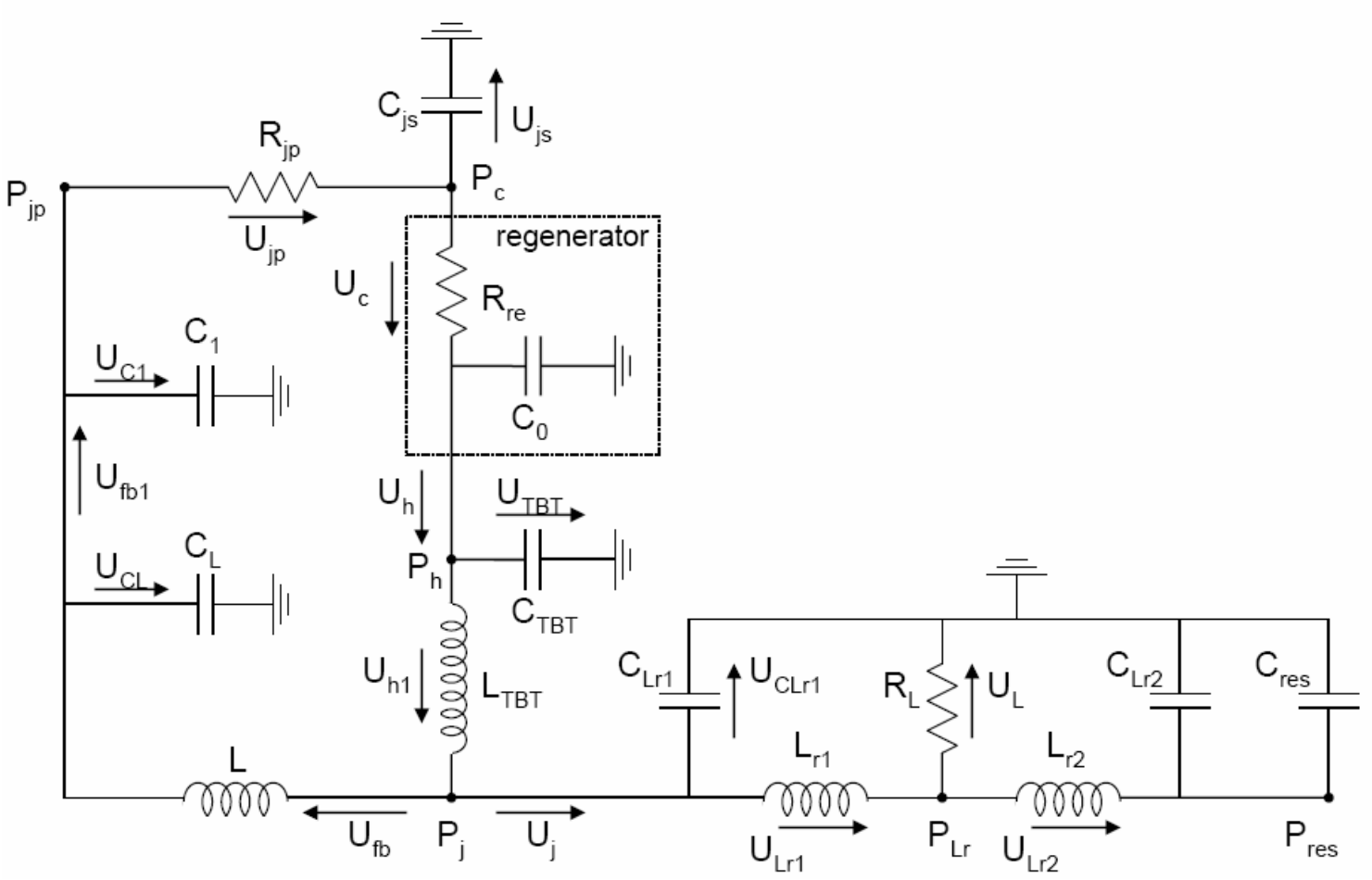

Figure 5.2: Extended lumped parameter model of the TASHE

streaming mass flux is suppressed with the jet pump. Using this linear temperature profile, the spatial distribution of the acoustic pressure and volumetric velocity in the regenerator are determined by simultaneously integrating Eqs. (5.32) and (5.25) across the regenerator. The resistance of the jet pump, R_{jp}, is determined from the appropriate equation cited by Backhaus and Swift (2000), and the acoustic load resistance, R_L, is simply adjusted to yield the desired temperature difference across the regenerator, which is it's primary function in the experimental TASHE setup.

The results of the detailed lumped parameter model match the DeltaE program outputs fairly well, and provide a good estimate of the true acoustic nature of the engine. The lumped parameter model of Figure 5.2 approximates the acoustic pressure outputs of TASHE's DeltaE model [Swift (2002)] within less than 2% error in magnitude, and to less than 2˚ in phase. Similarly, the acoustic volumetric velocities are approximated to within 7% or less in magnitude, and to about 5˚ in phase. The primary reason for these errors is that many of the smaller loss mechanisms that are included in the DeltaE model are not accounted for in the lumped parameter model, such as turbulence and viscous losses at heat exchangers, flow straighteners, pipe bends, and pipe junctions.

The detailed model also simulates the basic operation of the TASHE fairly well. For instance, increasing the resistance of the acoustic load has the effect of decreasing the temperature ratio across the regenerator of the TASHE, which is how the hot regenerator temperature is actually controlled in the TASHE. Also, increasing the heat input to the model increases its acoustic pressure amplitude, which also mimics the operation of the experimental TASHE device [Backhaus and Swift (2000)].

Having shown that the detailed lumped parameter model captures the acoustic character of the TASHE with a reasonable degree of accuracy, and that it can also mimic the engine's control mechanisms, we can begin to develop a detailed lumped parameter model of the TAPCE with a reasonable degree of confidence in the validity of this modeling strategy.

5.3.4 Determination of the TAPCE base geometry

For a simple feasibility analysis, it is sufficient to initially model the geometry of the TAPCE after that of the highly successful TASHE device [Backhaus and Swift (2000)]. This will serve as a good starting point for the base TAPCE geometry, which can then be optimized to better suit the particular strengths of the TAPCE design. As a result, the lumped parameter diagram of the TAPCE, as shown in Figure 5.3, is very similar to that of the TASHE in Figure 5.2. To use such a model, however, the basic geometry of the engine first needs to be determined. Then, Eqs. (5.13) and (5.19) can be applied to describe the various engine components in terms of their inertances and compliances as shown in the diagram, and Eqs. (5.25) and (5.32) can be used to describe the regenerator.

The toroidal geometry of the TASHE, as shown in Figure 2.4, is what allows the engine to attain such high thermal efficiencies, as it creates traveling wave acoustic phasing across the regenerator, and increases the acoustic impedance there to reduce the viscous dissipation in the regenerator [Backhaus and Swift (2000)]. A modified version of this geometry, as shown in the TAPCE design of Figure 3.2, uses two concentric pipes to help minimize several large thermal losses that appear in the TASHE. This change in

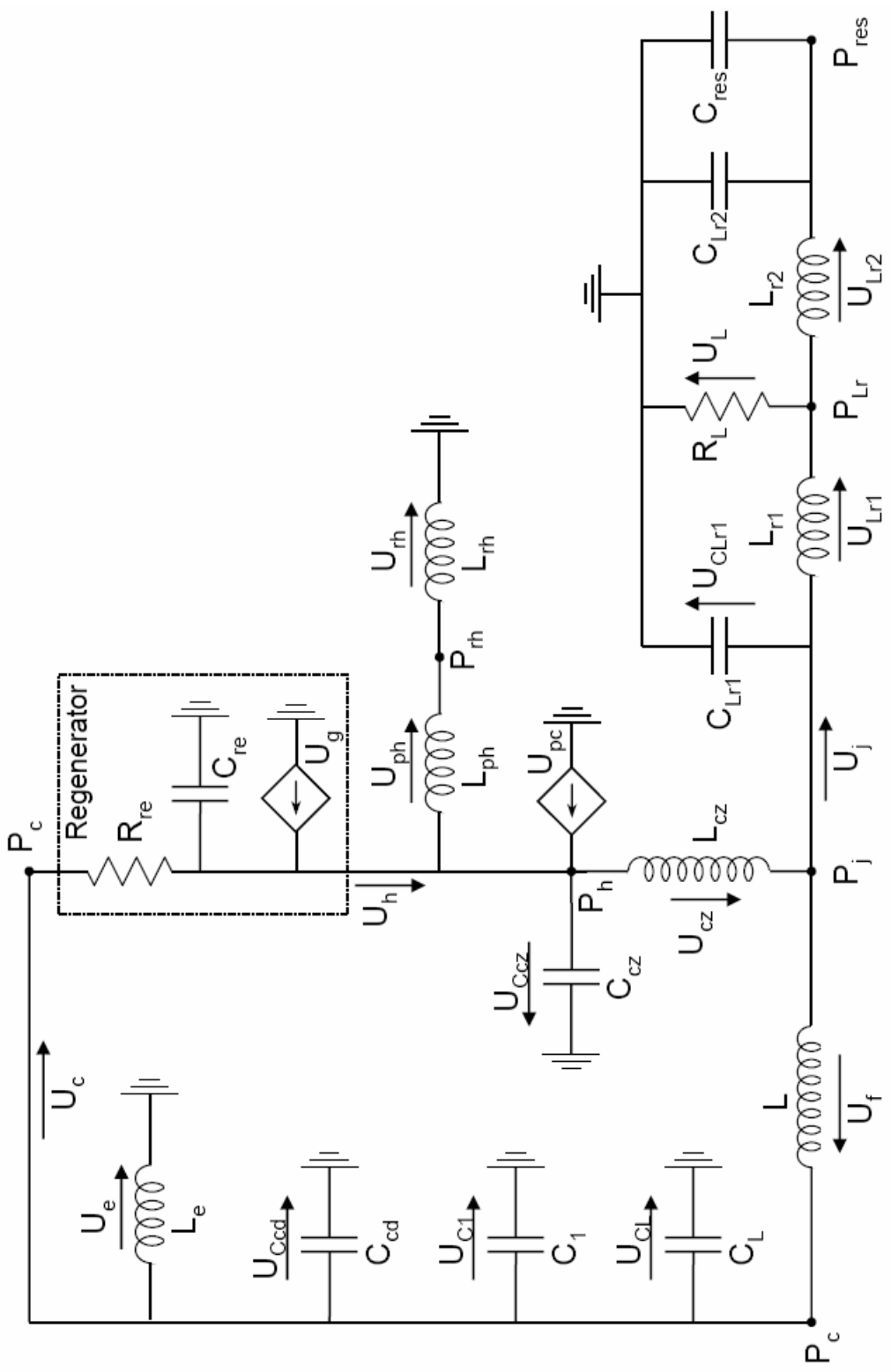

Figure 5.3: Lumped parameter model of the TAPCE

geometry must conserve the acoustical character of the TASHE, however, as its geometry dictates the acoustical magnitudes and phasing that allow the engine to operate so well.

In the TASHE, the relationships between the "mechanical" impedances of the lumped parameter elements determine the acoustical impedances in the engine. By equating the relative magnitudes of the lumped parameter impedances in the TAPCE to those in the TASHE, the acoustic character of the successful TASHE can be duplicated in the initial geometry of the TAPCE device. To accomplish this, ratios of various lumped parameter impedances in the TASHE will be used to determine the geometry of the TAPCE device. The details of this procedure are briefly outlined below.

The basic geometry of the TAPCE that will be considered in the computational model is shown in Figure 5.4. The main components of the driver can be identified as the compliance on the top, the inertance in the annulus between the concentric pipes, and the combustion zone, regenerator and cold duct in the inner pipe. All variables that describe these regions will bear the subscripts *c*, *l*, *cz*, *re*, and *cd*, respectively. For the purposes of this basic model, everything below the regenerator in the inner pipe of Figure 5.3 is assumed to represent a single component, the combustion zone. This includes the combustion zone, the thermal buffer tube, the flow straightener, and the cold heat exchanger, as depicted in Figure 3.2. The resonator, situated below the TAPCE driver, is composed of a compliance and an inertance with a side branch for an acoustic load, similar to that of the TASHE. The variables that describe these components are labeled with subscripts *Cr* and *Lr*, respectively. The geometric factors that need to be determined in the basic TAPCE model are the diameters and lengths of all of the pipes, as well as the length, porosity and "pore size" of the regenerator.

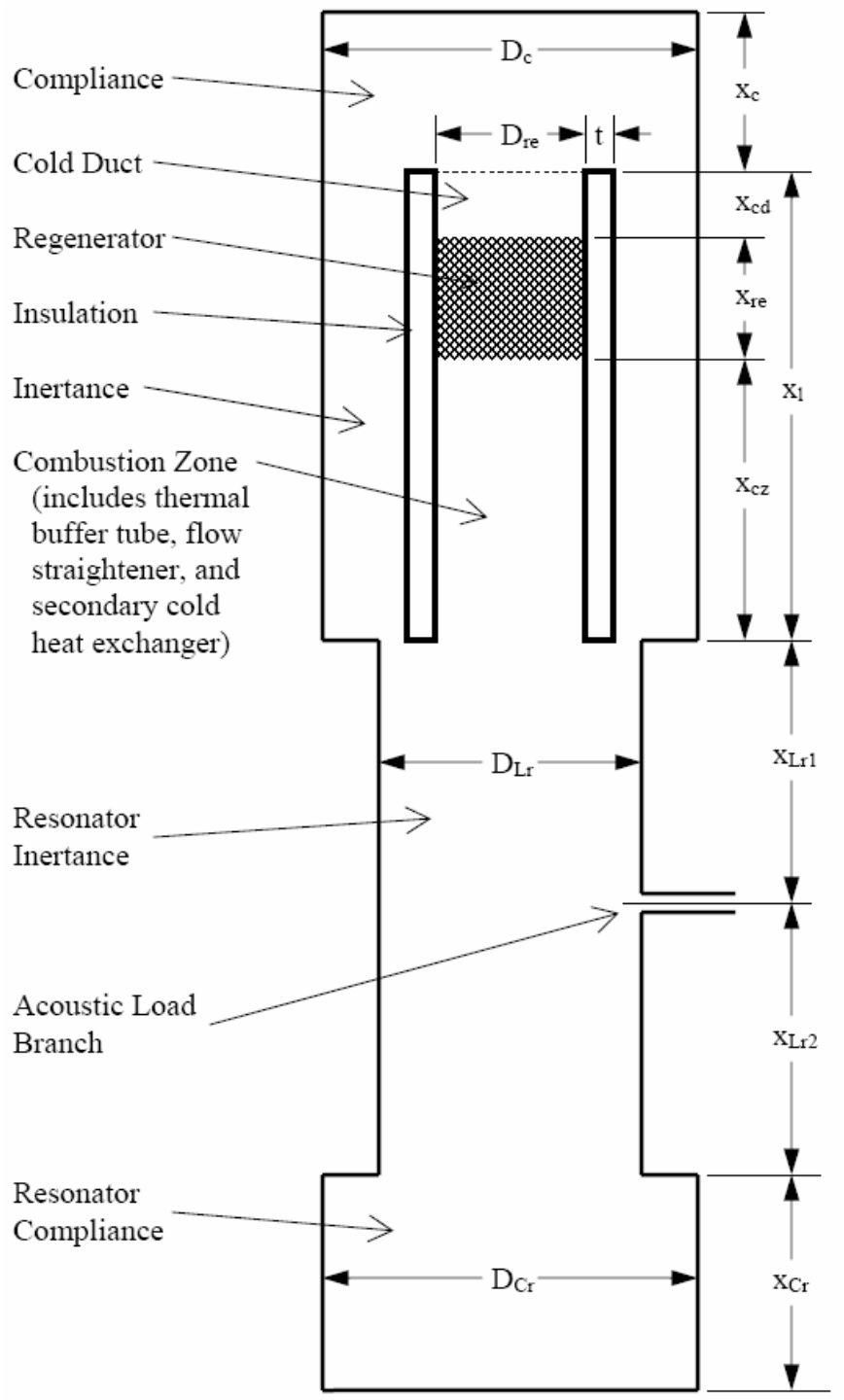

Figure 5.4: Schematic of the TAPCE Model Geometry

5.3.4.1 Choice of acoustic wavelength and engine diameter

Before proceeding, two basic choices need to be made concerning the overall scaling of the engine. First, the expected acoustic power output of the engine should be determined, which depends on the chosen application. Since acoustic power output is not really of primary importance in the development of an experimental device, the diameter of the outer shell of the engine is simply chosen to correspond to a readily available pipe diameter, somewhat arbitrarily chosen as 5" (0.128 m), in this case. Note that increasing the diameter of the TAPCE device would increase its acoustic power output and efficiency, as the acoustic power scales with the cross-sectional area, and viscous losses primarily scale with the diameter.

For an experimental device, the overall dimensions of the engine are a larger concern than its power output. The total height of the engine scales with the acoustic wavelength, λ, which is determined though the speed of sound of the working fluid, a, and the chosen frequency of acoustic oscillations, f, i.e.,

$$a = f\lambda = \frac{\omega\lambda}{2\pi}. \tag{5.36}$$

The speed of sound is a property of the working fluid, and is related to the fluid's state variables by:

$$a = \sqrt{\gamma R T_0} = \sqrt{\frac{\gamma p_0}{\rho_0}}. \tag{5.37}$$

The working fluid in the TAPCE is assumed to be primarily air at a temperature of 325 K, which is slightly elevated in anticipation of frictional heating and heat losses from the combustion zone that increase the overall temperature of the working fluid in

the device. Choosing an operating frequency of about 84 Hz (the same as that of the TASHE) results in an acoustic wavelength of $\lambda = 4.3$ meters. This yields an experimental setup that is 6-7 feet tall, which is appropriate for experimentation, if the device is roughly approximated as a half-wavelength resonator as shown in Figure 3.1.

5.3.4.2 Solution of basic engine dimensions

Most of the basic dimensions of the engine can be determined by solely examining the inertances and compliances of the various components, as approximated by Eqs. (5.18) and (5.24), respectively. The acoustic impedances of these components can be written as:

$$Z_{L,i} = i\omega L_i , \tag{5.38}$$

and

$$Z_{C,i} = \frac{1}{i\omega C_i} . \tag{5.39}$$

The ratio of a component's inertance to compliance impedances can be used to determine the length of the component's pipe. For instance, the length of the inner pipe, x_l, is determined by looking at the ratio of the impedances of the inertance and compliance of the annulus, i.e.:

$$\frac{\left|Z_{L_l}\right|}{\left|Z_{C_l}\right|} = \frac{\left|i\omega L_l\right|}{\left|1/i\omega C_l\right|} = \omega^2 L_l C_l = \omega^2 \frac{x_l \rho_m}{A_l} \frac{x_l A_l}{\gamma p_m}, \tag{5.40}$$

where Eqs. (5.18) and (5.24) have been used for the inertance and compliance of the annulus. Using Eqs. (5.36) and (5.37), Eq. (5.40) becomes:

$$\frac{\left|Z_{L_l}\right|}{\left|Z_{C_l}\right|} = \left(\frac{2\pi x_l}{\lambda}\right)^2 , \tag{5.41}$$

Table 5.1: TAPCE dimensions used in the detailed lumped parameter base model

Component	Length, x (cm)	Diameter, D (cm)	Area, A (cm^2)	Hydraulic Radius, r_h (cm)
Compliance	5.80	12.8	129.1	3.21
Inertance	19.26	--	38.14	0.515
Insulation	19.26	1.52 (thickness, t_{ins})	44.15	--
Inner Pipe Wall	19.26	0.05 (thickness, t_{wall})	1.21	--
Cold Duct	3.0	7.62	45.6	1.905
Regenerator	4.0	7.62	45.6	0.005267
Combustion Zone	12.26	7.62	45.6	1.905
First Resonator Inertance	35.7	8.34	54.63	2.085
Second Resonator Inertance	40.5	8.34	54.63	2.085
Resonator Compliance	34.5	20.3	324.3	5.08
Reactant Header	20	0.20	0.03142	0.05
Preheat Pipe (7 total)	10	0.05	0.00196	0.0125
Exhaust Pipe	10	0.10	0.00785	0.025

where this ratio is simply a function of the ratio of the pipe length to the acoustic wavelength. Given the value of this impedance ratio in the TASHE, 0.07943, we can then compute the inner pipe length since we have already determined the acoustic wavelength. Equation (5.41) can be used to determine many of the pipe lengths we seek for the basic TAPCE geometry, which can be found in Table 5.1.

Using these pipe lengths and the chosen diameter of the outer shell of the TAPCE driver, looking at ratios of compliances of various components can be used to determine their respective diameters. For example, the ratio of the compliance impedances of the inertance and the combustion zone can be used to determine the diameter of the inner pipe, D_{re}, i.e.:

$$\frac{\left|Z_{C_l}\right|}{\left|Z_{C_{cz}}\right|} = \frac{C_{cz}}{C_l} = \frac{x_{cz}A_{re}}{x_l A_l} = \frac{x_{cz}}{x_l}\frac{D_{re}^2}{D_c^2 - \left(D_{re} + 2\left[t_{wall} + t_{ins}\right]\right)^2}, \tag{5.42}$$

where we have accounted for the thickness of the inner pipe, t_{wall}, and its surrounding insulation, t_{ins}.

Another way to look at Eq. (5.42) is as a means for determining the insulation thickness surrounding the inner pipe in the TAPCE. This allows us to choose both the outer pipe diameter and the inner pipe diameter based on standard pipe sizes, and to make up the difference in Eq. (5.42) by altering the insulation thickness. It should be noted, however, that the thickness of the insulation will affect the radial heat losses out of the combustion zone, which are not modeled in this study. Choosing the inside diameters of the inner and outer pipes to be D_{re} = 0.0762 m (3 inches) and D_c = 0.128 m (5 inches), respectively, choosing an inner pipe wall thickness of t_{wall} = 0.5 mm, and determining the combustion zone and inner pipe lengths from Eq. (5.41), t_{ins} can be found from Eq. (5.42) and knowledge of the corresponding impedance ratio in the TASHE.

Finally, noting that the inertance of the resonator's compliance is negligible, only the volume of this compliance is of importance. As a result, the pipe diameter of this component was arbitrarily chosen to equal to D_{Cr} = 0.203 meters (about 8 inches), and its length chosen to yield the desired volume.

These special cases aside, the ratios of the lengths and areas found in Eq. (5.42) can be used to determine the diameters of the other pipes in the engine, which are listed in Table 5.1. It should be noted that by using the impedance ratios of the TASHE, the only parameters needed to determine the pipe lengths and diameters in the TAPCE thus far are the acoustic wavelength, λ, and the outer pipe diameter, D_c. The remaining

parameters to be found are the regenerator's length, x_{re}, hydraulic radius, $r_{h,re}$, and porosity, ϕ.

5.3.4.3 Determination of the regenerator base geometry

The purpose of the regenerator is to attain a high degree of gas-solid thermal contact, which will occur if the ratio of the regenerator hydraulic radius to the thermal penetration depth, $r_{h,re}/\delta_\kappa$, is much less than unity. Thus, changes in the device's working fluid, mean pressure, mean temperature, or operating frequency may necessitate a change in the regenerator's hydraulic radius because they change the thermal penetration depth.

As the temperature in the regenerator increases, the thermal penetration depth also increases, thus, for a constant regenerator hydraulic radius, the solid gas thermal contact improves (i.e., $r_{h,re}/\delta_\kappa$ decreases) for increasing temperature within the regenerator. The area of concern, then, is at the cold end of the regenerator, where low temperatures yield small thermal penetration depths, and the ratio $r_{h,re}/\delta_\kappa$ is the largest. Many thermoacoustic effects are a function of this ratio squared, and are generally considered low order effects in the regenerator. In order to ensure that this is the case, we'd like to make sure that $(r_{h,re}/\delta_\kappa)^2 \leq 0.10$. Consequently, knowing the mean pressure, operating frequency, working fluid, and ambient temperature, we'll set:

$$r_{h,re} = 0.316\delta_{\kappa,c}\,, \tag{5.43}$$

where $\delta_{\kappa,c}$ is the thermal penetration depth at the cold side of the regenerator. By comparison, the stacked screen regenerator in the TASHE has $r_{h,re}/\delta_{\kappa,c}$ = 42μm/140μm = 0.30 [Backhaus and Swift (2000)], while the parallel plate TASHE regenerator has $r_{h,re}/\delta_{\kappa,c}$ = 52μm/140μm = 0.37 [Backhaus and Swift (2001)].

Next, we'd like to set the total regenerator resistance. In order to achieve the high thermal efficiencies of engines like the TASHE, the acoustically compact network is designed to have the acoustic impedance of the inertance be much smaller than the acoustic impedance of the regenerator's resistance. Ideally, we'd like to match the impedance ratio $\omega L_l/R_{re}$ of the TASHE and the TAPCE, but unfortunately, determining R_{re} from Eq. (5.35) is a fairly complicated procedure.

As we're only looking for a starting point around which to build the TAPCE design, we will look at the regenerator resistance for the first curve fit coefficient, R_{c1}, instead of the total regenerator resistance, R_{re}. The impedance ratio between the inertance and regenerator resistance can then be written as:

$$\frac{\omega L_l}{R_{c1}} = \frac{\omega \rho_m x_l}{A_l} \frac{8 r_{h,re}^2 \phi A_{re}}{x_{re} \mu_0 c_1(\phi)}, \tag{5.44}$$

where use has been made of Eqs. (5.18) and (5.33). Substituting Eqs. (2.1) and (5.43) into this expression yields:

$$\frac{\omega L_l}{R_{c1}} = \frac{\omega \rho_m x_l}{A_l} \frac{8 \phi A_{re}}{x_{re} \mu_0 c_1(\phi)} 0.1 \left(\frac{2k_0}{\omega \rho_m c_p} \right) = \frac{1.6\phi}{c_1(\phi)\sigma_0} \frac{A_{re} x_l}{A_l x_{re}}, \tag{5.45}$$

where $\sigma_0 = \mu_0 c_p/k_0$, is the Prandtl number of the combustion gas from Eq. (2.3), evaluated at the regenerator's cold end temperature, T_c. Note that since the density and frequency dependencies have vanished, this ratio is only a function of the Prandtl number, which is generally known, and the geometries of the regenerator and the inertance.

Knowing the value of the impedance ratio in Eq. (5.45) from the detailed lumped parameter model of the TASHE would allow us to calculate either the porosity of the regenerator, ϕ, or its length, x_{re}, if the other parameter is known. The value of this impedance ratio in the TASHE is 0.2895, although using this number in Eq. (5.45) would

lead to some error in the determination of the regenerator length. Since the compliance of the jetting space, C_{js} in Figure 5.2, is very small, then the resistances of the regenerator, R_{re}, and the jet pump, R_{jp}, are essentially arranged in series. This means that the impedance of the inertance must be scaled with the sum of these two resistances, which are nearly equal according to the detailed lumped parameter model of the TASHE.

In the TAPCE, the jet pump is replaced by an acoustically transparent barrier, which can be a vibrating membrane, a rubber balloon, or a similar component as discussed in Chapter 3. Since the resistance of this acoustically transparent barrier should be very small in comparison to that of the jet pump, which relies on turbulent dissipation of jets to achieve the desired mean pressure difference [Backhaus and Swift (2003)], then the resistance of the acoustically transparent barrier can be neglected in the TAPCE model. Thus, as a result of the nearly equal resistances of the TASHE regenerator and jet pump, it is more appropriate to use half of the above mentioned TASHE impedance ratio, (i.e., 0.1448) in the determination of the TAPCE regenerator dimensions in Eq. (5.45).

Knowing this impedance ratio, the easiest parameter to specify in Eq. (5.45) would be the regenerator's porosity, ϕ, which we'll arbitrarily choose to be that of the TASHE, i.e., $\phi = 0.72$. This value can of course be changed later when the geometry of the TAPCE is optimized, though for now it allows us to calculate an appropriate regenerator length, which appears in Table 5.1.

Finally, note that for a stacked-screen regenerator, the porosity and hydraulic radius of the regenerator determine the diameter of the wire in the screens, D_{wire}, by the equation [Swift (2002)]:

$$D_{wire} = \frac{4 r_{h,re} (1 - \phi)}{\phi}, \tag{5.46}$$

and the "mesh number," n_{mesh}, of the screens (number of wires per unit length) by the equation:

$$n_{mesh} = \frac{4(1-\phi)}{\pi D_{wire}}. \tag{5.47}$$

Given these numbers, a regenerator with the appropriate porosity and hydraulic radius can be built, though some tinkering with the numbers may have to occur to obtain readily available wire mesh screens with the proper wire diameter and spacing.

5.4 Thermal and Mass Flux Modeling

Having determined a basic geometry for the TAPCE design, the acoustics of the TAPCE can then be modeled with the detailed lumped parameter model of Figure 5.3. This requires that some of the energy flux and mean mass flux effects be considered, however, as these effects determine the temperature profile across the regenerator, the temperature at the hot side regenerator interface, and the acoustic energy losses through the inlet and exhaust ports. The modeling of these effects is discussed below.

5.4.1 Reactant inlet pipes

The reactants' inlet is composed of two primary components as shown in Figure 3.2, the inlet header that brings the reactants from a plenum into the engine, and the reactants' inlet pipes, which branch off of the header, pass through the regenerator, and inject the preheated reactants into the combustion zone. As shown in Figure 3.3, we will consider an arrangement of 7 reactant inlet pipes that branch off of the header. The initial choices for the reactant inlet header and reactant inlet pipe dimensions are shown in Table 5.1.

Since the amount of acoustic energy that escapes the engine through these ports is roughly proportional to the cross-sectional area of the pipes, small pipe diameters are desired for these components. In addition, as we will see in the following chapter, reducing the diameter improves the preheating of the reactants, although at the cost of increasing the viscous flow losses through these pipes.

Since the lengths of the inlet pipes and header are much larger than their diameters, these pipes can be acoustically modeled as inertances, as shown in Figure 5.3. Thus, the acoustic impedances of the inlet pipes are given by Eq. (5.13), while the acoustic impedance of the reactant header also includes a radiation impedance at the interface between the header and the premixed reactant plenum [Kinsler et. al. (1982)],

$$Z_{rh} = \rho_{rx,0}\omega\left[\frac{ix_{rh}}{A_{rh}(1-f_v)} + \frac{\omega}{2\pi a_{rx,0}}\right], \tag{5.48}$$

where $\rho_{rx,0}$ and $a_{rx,0}$ are the reactant density and speed of sound at ambient temperature, respectively. To acoustically model these pipes, the fluid in the reactant header is assumed to be air at ambient temperature and average mean reactant header pressure, discussed below, while the inlet pipes' fluid is assumed to be air at the average temperature $(T_0 + T_{ph})/2$, and at the average mean pressure in the inlet pipes.

Since the diameters of the reactants' preheat pipes may be very small, we will compute the mean pressure drop across these pipes to permit determination of the work lost due to viscous forces in these pipes by Eq. (4.129). Thus, the mean pressure drop in a pipe can be expressed as [Fox and McDonald (1992)]:

$$\Delta p_m = F\frac{x}{D}\frac{\rho_m\langle u_m\rangle^2}{2} = \frac{F}{2\rho_m}\frac{x}{D_i}\left(\frac{\dot{M}}{nA_i}\right)^2, \tag{5.49}$$

where F is the friction factor, $\langle u_m \rangle$ is the spatial average of the mean velocity in the pipe, and the total mean mass flux, $\dot{M}$, is distributed equally through n individual pipes of diameter D_i and area A_i. This equation can be used to determine the difference between the mean supply pressure, $p_{m,s}$, and the reactant header mean pressure, $p_{m,rh}$, i.e.,

$$p_{m,s} - p_{m,rh} = \frac{F_{rh}}{2\rho_{rx,0}} \frac{x_{rh}}{D_{rh}} \left(\frac{\dot{M}}{A_{rh}} \right)^2 , \tag{5.50}$$

while the total pressure difference across the 7 identical preheat pipes can be written as:

$$p_{m,rh} - p_0 = \frac{F_{ph}}{2\rho_{rx}} \frac{x_{ph}}{D_{ph}} \left(\frac{\dot{M}}{7A_{ph}} \right)^2 . \tag{5.51}$$

Since the flow of combustion reactants through the inlet pipe system is assumed to be turbulent, with a Reynolds number of:

$$Re_i = \frac{\rho_m u_m D}{\mu_m} = \frac{4|\dot{M}|}{\pi \mu_m n D_i} , \tag{5.52}$$

assuming that the inner surfaces of the reactant header and inlet pipes are smooth and that $Re_{i,rx} \leq 10^5$, the Blasius correlation for turbulent flow can be used to determine the friction factor for each component, i.e. [Fox and McDonald (1992)]:

$$F_i = \frac{0.3164}{\left(Re_{i,rx}\right)^{0.25}} . \tag{5.53}$$

Equations (5.50) - (5.53) are used to determine the required reactant supply pressure, $p_{m,s}$, for a given reactant pipe configuration and mean engine pressure, p_m.

5.4.2 Reactant preheating

The reactant preheating heat transfer is fairly well described by Eqs. (4.85) - (4.89) above, although a Nusselt number correlation still needs to be chosen in order to

determine the coefficient N in Eq. (4.89). One common correlation for turbulent, fully developed gaseous flow in a pipe is given by [Kays and Crawford (1993)]:

$$Nu \approx 0.022 Re^{4/5} \sigma^{1/2}, \tag{5.54}$$

which is valid for $0.5 < \sigma < 1.0$ and $10^4 < Re < 10^5$, though this correlation must be modified somewhat to account for the possible presence of acoustic oscillations in the reactant preheat pipes of the TAPCE.

It is well documented that convective heat transfer rates increase, sometimes dramatically, in the presence of acoustic oscillations (see, e.g., Gopinath and Harder (2000)). One approach that has been used to approximate the effects of acoustic oscillations on the rate of convective heat transfer is to use a "Time Average Steady Flow Equivalent" (TASFE) mass flux in the computation of the Reynolds number in Eq. (5.52) [Mozurkewich (2001)]. While this method helps account for the increased convective heat transfer due to the presence of acoustic oscillations in the preheat pipes, it is over-simplified in that it does not account for the boundary layer disruptions that are generated by acoustic flow reversal.

To help determine the effect of the acoustic mass flux on the TASFE mass flux, we will define the total mass flux as [Weiland and Zinn (2003a)]:

$$\dot{m}_{tot} = \dot{M} + |\dot{m}_1| \sin(\omega t - \theta), \tag{5.55}$$

where θ is an arbitrary phase shift that will be determined below. The expression relating this total mass flux to the time average steady flow equivalent mass flux is:

$$\dot{M}_{tasfe} = \frac{\omega}{2\pi} \int_0^{2\pi/\omega} |\dot{m}_{tot}| dt . \tag{5.56}$$

In the case where $\dot{M} \geq |\dot{m}_1|$ and $\dot{M} > 0$, note that $\dot{m}_{tot} \geq 0$ for all times t in Eq. (5.55), indicating that there is no flow reversal due to acoustic gas motions. In this case, Eq. (5.56) can be expressed as:

$$\dot{M}_{tasfe} = \frac{\omega}{2\pi}\left[\int_0^{2\pi/\omega} \dot{M}dt + \int_0^{2\pi/\omega} |\dot{m}_1|\sin(\omega t - \theta)dt\right] = \dot{M}\,, \tag{5.57}$$

indicating that the TASFE mass flux and the mean mass flux are equivalent if no acoustic flow reversal is present.

In the instances where flow reversal occurs (i.e., $\dot{M} < |\dot{m}_1|$), the phase shift θ can be specified by letting $\dot{m}_{tot} = 0$ at $t = 0$, yielding:

$$\theta = \sin^{-1}\left(\frac{\dot{M}}{|\dot{m}_1|}\right). \tag{5.58}$$

Note that the total mass flux is zero at two different times during the acoustic cycle, once during each change in the direction of the fluid flow. Using Eqs. (5.55) and (5.58), and noting that the sine function has odd symmetry, the time at which the mass flux is zero midway through the acoustic cycle can be shown to be:

$$t_{mid} = \frac{\pi + 2\theta}{\omega}. \tag{5.59}$$

Assuming that $\dot{M} > 0$, the absolute value of the total mass flux can then be expressed as:

$$|\dot{m}_{tot}| = \begin{cases} \dot{M} + |\dot{m}_1|\sin(\omega t - \theta) & 0 \leq t \leq t_{mid} \\ -\dot{M} - |\dot{m}_1|\sin(\omega t - \theta) & t_{mid} \leq t \leq 2\pi \end{cases}. \tag{5.60}$$

Substituting Eqs. (5.59) and (5.60) into Eq. (5.56) for the time average steady flow equivalent mass flux yields:

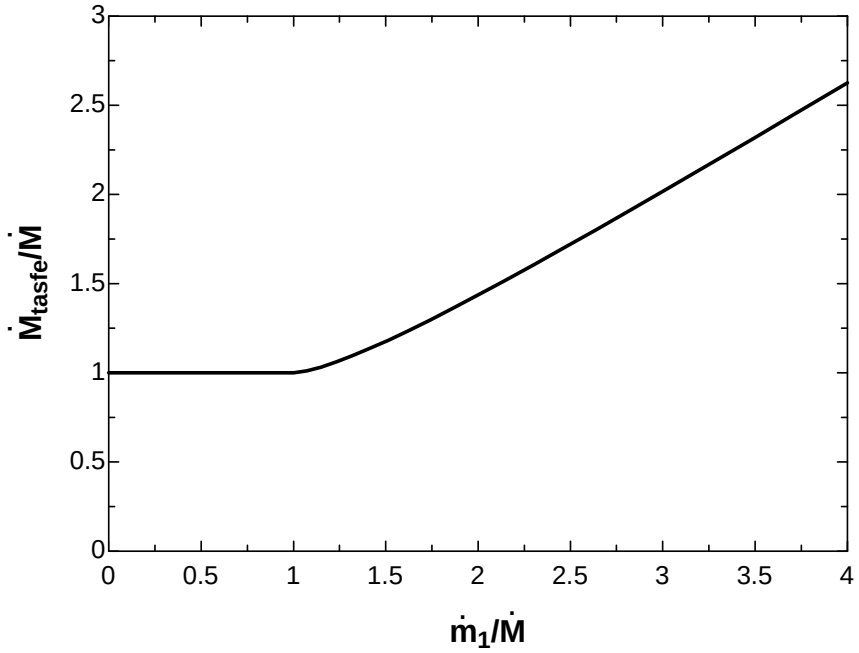

Figure 5.5: The dimensionless "Time Average Steady Flow Equivalent" mass flux versus the dimensionless acoustic mass flux.

$$\dot{M}_{tasfe} = \frac{\omega}{2\pi}\left[\int_{0}^{(\pi+2\theta)/\omega}\left(\dot{M}+|\dot{m}_1|\sin(\omega t-\theta)\right)dt - \int_{(\pi+2\theta)/\omega}^{2\pi/\omega}\left(\dot{M}+|\dot{m}_1|\sin(\omega t-\theta)\right)dt\right]. \quad (5.61)$$

By performing the suggested integrations and applying Eq. (5.58), the TASFE mass flux for the flow reversal case can be rearranged to produce a fairly simple expression. Combining this result with Eq. (5.56) yields:

$$\dot{M}_{tasfe} = \begin{cases} \dot{M} & \text{for } \dot{M} \geq |\dot{m}_1| \\ \dot{M}\,\dfrac{2[\cot(\theta)+\theta]}{\pi} & \text{for } \dot{M} < |\dot{m}_1| \end{cases}. \quad (5.62)$$

A basic plot of this function is shown in Figure 5.5, where it should be noted that $\dot{M}_{tasfe}$ is always greater than $\dot{M}$, and the effects of acoustic flow reversal can have a significant impact on the time averaged steady flow equivalent mass flux, $\dot{M}_{tasfe}$.

To approximate the effects of acoustic oscillations on the convective heat transfer to the reactant preheat pipes in the TAPCE model, Eq. (5.62) is used in place of $\dot{M}$ in the computation of the Reynolds number in Eq. (5.52), which is in turn used in the Nusselt number correlation of Eq. (5.54).

5.4.3 Combustion

Once the premixed combustion reactants are preheated in passing through the regenerator, they are injected from the preheat pipes into the combustion zone. Within the combustion zone, they react to produce hot combustion products. The combustion process can be separated into mean and oscillating components that act independently of one another. Each of these components is discussed in further detail below.

The details of the mean combustion process are assumed to be independent of the geometry of the combustion zone, and are unimportant for the purposes of the lumped parameter model of the TAPCE. In its simplest form, the combustion process can simply be modeled as a change in temperature from that of the reactants at T_{ph} to that of the combustion products, T_h. If it is assumed that the combustion reaction goes to completion, that there is no dissociation of the combustion products, and that no heat is transferred out of the combustion zone, except by convection of the reactants and products, then the problem of determining T_h is similar to finding the adiabatic flame temperature of a combustion process [Turns (1996)]. This is simply determined with the EES program by setting:

$$h_{rx}\left(T_{ph}\right) = h_{pr}\left(T_h\right), \tag{5.63}$$

where h_{rx} and h_{pr} are determined for their respective temperatures and compositions by Eq. (5.6). For a given fuel type, knowledge of any two of the quantities: T_{ph}, T_h, and Φ,

allows the EES program to calculate the third quantity by simple iteration of Eqs. (5.6) and (5.63).

To reconcile Eq. (5.63) with the expression for the change in mean energy flux across the combustion zone in Eq. (4.53), it should be noted that EES uses absolute enthalpies for all of the chemical species, which are referenced to a common thermodynamic state at T_{ref} = 298 K and P = 1 atm. In this regard, they also contain information on the enthalpy of formation of each chemical species, where, for ideal gases, the species absolute enthalpy in EES can be represented as [Turns (1996)]:

$$h_i(T) = h^{\circ}_{f,i} + c_{p,i}\left(T - T_{ref}\right). \tag{5.64}$$

Substituting this expression and Eq. (5.6) into Eq. (5.63) yields:

$$\sum_i \left(Y_i\left[h^{\circ}_{f,i} + c_{p,i}\left(T_{ph} - T_{ref}\right)\right]\right)_{rx} = \sum_i \left(Y_i\left[h^{\circ}_{f,i} + c_{p,i}\left(T_h - T_{ref}\right)\right]\right)_{pr}, \tag{5.65}$$

which can be rearranged to yield:

$$c_{p,pr}\left(T_h - T_{ref}\right) - c_{p,rx}\left(T_{ph} - T_{ref}\right) = \sum_i \left(Y_i h^{\circ}_{f,i}\right)_{rx} - \sum_i \left(Y_i h^{\circ}_{f,i}\right)_{pr} = \Delta h_c, \tag{5.66}$$

where Δh_c is the enthalpy of combustion, or the heat associated with the chemical energy stored in the fuel. The terms on the left side of this equation are generally referred to as the sensible enthalpy, which describe the thermal energy change due to the change in temperature [Turns (1996)]. Multiplied by the mass flux of reactants and products, $\dot{M} < 0$, Eq. (5.66) can be written as:

$$\dot{M}h_{h,s} - \dot{M}h_{ph,s} = -\dot{Q}_m, \tag{5.67}$$

where the subscript s denotes the sensible enthalpy, which is the enthalpy appearing in Eqs. (4.47) - (4.51) above, and the mean heat of combustion is shown to be $\dot{Q}_m = -\dot{M}\Delta h_c$ [Turns (1996)].

The change in acoustic energy across the combustion zone in the TAPCE is modeled with Eq. (4.52), where we still require an expression that describes the oscillating heat release, $\dot{Q}_1$. Recall from Chapter 3 that one possible mode of pulse combustion control is to externally modulate the inlet flow of preheated reactants into the combustion chamber. Since the oscillating mass flux from the preheat pipes is controlled by the acoustic pressure according to the lumped parameter inertance model of these pipes, an appropriate model for the oscillating heat release would be:

$$\dot{Q}_1 = \left(\alpha \frac{\dot{Q}_m}{|p_1|} \right) p_1 e^{i\theta_{pq}} = \alpha \dot{Q}_m e^{i(\omega t + \theta_{pq})}, \tag{5.68}$$

where α is the amplitude factor, $0 \le \alpha \le 1$, and $\dot{Q}_m$ is the maximum magnitude of the oscillating heat release, which is equal to the mean heat release as discussed in Chapter 4. Also, the phase shift between the oscillating pressure and oscillating heat release, θ_{pq}, is governed by the dynamics of the combustion process and the reactant supply system, and will most likely need to be determined experimentally.

In the TAPCE model, the effect of the oscillating heat release on the acoustics of the model is best described by integrating Eq. (4.34) across the length of the combustion zone and assuming that $f_\kappa \approx 0$, yielding:

$$U_{cz} - U_h = \frac{\gamma - 1}{\gamma p_m} \dot{Q}_1, \tag{5.69}$$

which shows that the oscillating heat release acts as a source of volumetric velocity [McManus et. al. (1993)].

5.4.4 *Regenerator interface*

The hot combustion products, at temperature T_h, are convected from the combustion zone, through the hot duct, to the hot side of the regenerator. At the regenerator/hot duct interface, the joining conditions between the approximately isentropic hot duct environment and the approximately isothermal regenerator cause a temperature drop from T_h to T_{int}, as discussed in the energy flux analysis of the previous chapter and in the detailed analysis of Weiland and Zinn (2003a).

Following the analysis above, the interface energy balance in the TAPCE lumped parameter model is described by Eq. (4.71), rewritten here with the help of Eq. (4.3) as:

$$\dot{M} c_p \left(T_{int} - T_h\right) = \tfrac{1}{2}\,\mathrm{Re}\left[p_{1,h}\widetilde{U}_{1,h}\right] + \left(\psi + Ak + A_s k_s\right)\left.\frac{dT_{re}}{dx}\right|_{int} . \tag{5.70}$$

As mentioned above, the temperature difference across the regenerator is typically determined by adjusting the acoustic load resistance, R_L, which effectively sets the regenerator's hot side volumetric velocity, $U_{1,h}$, according to Eq. (5.25). In the case where these parameters are fixed and the conductive and imperfect entropy flux losses are known, then increasing the mean mass flux, $\dot{M}$, would increase the acoustic pressure on the hot side of the regenerator, $p_{1,h}$. From this point of view, Eq. (5.70) then describes the mechanism for controlling the acoustic pressure in the TAPCE, a point of view that is verified in the demonstrations of following chapter. This control mechanism is analogous to the situation in the TASHE, where the input heating power of the hot heat exchanger determines the acoustic pressure magnitude in the engine [Backhaus and Swift (2000)].

Finally, in order to evaluate the last term of Eq. (5.70), we need to determine the parameter ψ and the thermal conductivity coefficients, k and k_s. The imperfect thermal

contact entropy flux coefficient, ψ, is computed using the stacked screen regenerator correlation of Eq. (4.63) and its supporting equations, all evaluated at the mean temperature of the regenerator. Since axial thermal conduction through the gas in the regenerator is much smaller than the conduction through the solid, the gaseous thermal conductivity, k, is neglected in Eq. (5.70). The solid axial conduction is composed of two terms, however, the contribution of the stacked screen regenerator, and the contribution of the pipe wall surrounding the regenerator. Any axial conduction through the insulation surrounding the inner pipe wall and through the walls of the reactant preheat pipes is neglected in this analysis, though slightly larger values of the inner pipe wall thickness, t_{wall}, can be chosen to help account for these losses.

It is assumed that the wire mesh screens of the regenerator are made of 304-stainless steel (as in the TASHE), having a temperature-dependent thermal conductivity of the form [Backhaus and Swift (2000)]:

$$k_{ss} = 13.2 + 0.112\left[T(°C)\right]^{0.68} \qquad W/m°C\,. \tag{5.71}$$

In addition, the intermittent contact between the stacked wire mesh screens in the regenerator serves to reduce the axial conduction down the regenerator by a factor of about $\varepsilon_k = 0.1$ [Swift (2002), Lewis et. al. (1998)].

Similarly, we will assume that the wall of the inner pipe is made of Inconel 625, with a temperature-dependent thermal conductivity which can be curve fit to [Backhaus and Swift (2000)]:

$$k_{wall} = 9.7 + 0.015\ T(°C) \qquad W/m°C\,. \tag{5.72}$$

Inconel 625 is used in the wall surrounding the regenerator in the TASHE, primarily because of its high tensile strength at high temperatures, but also because its thermal

conductivity is about 3 times lower than that of stainless steel [Backhaus and Swift (2000)]. As discussed above, this was an important design consideration in the TASHE, as the wall surrounding the regenerator had to be about 4 mm thick in order to safely contain the 30 atmospheres of mean pressure in the TASHE. Due to the concentric pipe design of the TAPCE, the burden of containing the elevated mean pressure in the engine is shifted from the regenerator pipe wall to the outer shell, thus allowing a very thin inner pipe wall and thus lower axial conduction losses through this pipe. For purposes of comparison to the TASHE, the inner pipe wall is still assumed to be composed of Inconel 625, though the pipe wall thickness, t_{wall}, is assumed to be much smaller, e.g., $t_{wall} \approx 0.50$ mm.

Accounting for all of these effects and the porosity of the regenerator, the thermal conductivity term of Eq. (5.70) can be written as:

$$A_s k_s \left.\frac{dT_{re}}{dx}\right|_{int} \approx \varepsilon_k (1-\phi) A_{re} k_{ss} \left.\frac{dT_{re}}{dx}\right|_{int} + t_{wall} D_{re} k_{wall} \left.\frac{dT_{re}}{dx}\right|_{int}, \tag{5.73}$$

where k_{ss} and k_{wall} are given by Eqs. (5.71) and (5.72), respectively.

5.4.5 Second order regenerator pressure difference

Recall from the previous chapter that the mean pressure difference across the regenerator is due to a combination of viscous and acoustic streaming effects, and can be written as [Waxler (2001)]:

$$\Delta p_{m,re} = -\frac{\alpha \mu_m L}{\rho_m} \dot{M} + \Delta p_{\dot{M}=0}, \tag{5.74}$$

where the first term on the right is due strictly to the viscous mean flow through the regenerator, and the second term is due to acoustic streaming effects. According to the

derivations of Waxler (2001), for a regenerator in which $(r_{h,re}/\delta_\kappa)^2 << 1$, this second pressure difference term is given by:

$$\Delta p_{\dot{M}=0} \approx -\frac{|p(L)|^2 - |p(0)|^2}{4p_0} = -\frac{|p_{1,h}|^2 - |p_{1,c}|^2}{4p_0}. \tag{5.75}$$

The first term on the right side of Eq. (5.74) can be expressed using a version of Eq. (5.49) that is adapted to the regenerator environment, i.e.:

$$\Delta p_{m,v} = -F\frac{x_{re}}{r_{h,re}}\frac{\rho_{re}\langle u_m\rangle^2}{2} = -F\frac{\mu_m \dot{M} Re_{re}}{8\rho_{re}\phi A_{re}}\frac{x_{re}}{r_{h,re}^2}, \tag{5.76}$$

where the regenerator Reynolds number, Re_{re}, is given by:

$$Re_{re} = \frac{4r_{h,re}\rho_{re}|\langle u_m\rangle|}{\mu_m} = \frac{4r_{h,re}|\dot{M}|}{\mu_m \phi A_{re}}, \tag{5.77}$$

and the friction factor, F, can be approximated with Swift and Ward's (1996) curve fits to the data of Kays and London (1984):

$$F = \frac{c_1(\phi)}{Re_{re}} + c_2(\phi), \tag{5.78}$$

where $c_1(\phi)$ and $c_1(\phi)$ are given by Eqs. (5.28) and (5.29), respectively.

Combined, the total mean pressure difference from the hot side of the regenerator, at mean pressure, p_m, to the cold side of the regenerator, at mean pressure $p_{m,c}$, can be determined from:

$$p_m - p_{m,c} = \Delta p_m = -\frac{\mu_m \dot{M}_{pr}}{8\rho_{re}\phi A_{re}}\frac{x_{re}}{r_{h,re}^2}\left[c_1(\phi) + c_2(\phi)Re_{re}\right] + \frac{|p_{1,c}|^2 - |p_{1,h}|^2}{4p_m}. \tag{5.79}$$

Since $\dot{M}_{pr}$ is negative according to our sign convention, note that both terms on the right side of Eq. (5.79) are positive, so that $p_m > p_{m,c}$.

5.4.6 *Exhaust port*

Once through the regenerator and the cold heat exchanger, the mean mass flux of cold combustion products flows out the exhaust pipe and into the environment. As in the reactant inlet pipes, the amount of acoustic energy escaping the TAPCE through this exhaust pipe is proportional to its area, thus the exhaust pipe diameter should be very small, e.g., D_e = 1.0 mm. Since the length of this pipe will be much larger than its diameter (see Table 5.1), it can be modeled acoustically as a lumped parameter inertance element as shown in Figure 5.3, with an added radiation impedance for a flanged exhaust pipe opening into the atmosphere, i.e. [Kinsler et. al. (1982)],

$$Z_e = \rho_{pr,0}\omega\left[\frac{ix_e}{A_e(1-f_v)} + \frac{\omega}{2\pi a_{pr,0}}\right], \tag{5.80}$$

where $\rho_{pr,0}$ and $a_{pr,0}$ are the combustion products' density and speed of sound at ambient temperature, respectively.

As with the reactants' inlet pipe system, the mean pressure difference across the exhaust pipe, between the cold side of the regenerator, $p_{m,c}$, and the environment, $p_{m,e}$, can be determined by the appropriate form of Eq. (5.49), i.e.:

$$p_{m,c} - p_{m,e} = \frac{F_e}{2\rho_{pr,0}}\frac{x_e}{D_e}\left(\frac{\dot{M}}{A_e}\right)^2, \tag{5.81}$$

where the friction factor can be found by using Eqs. (5.52) and (5.53) for cold combustion product properties.

CHAPTER 6

TAPCE PERFORMANCE AND OPTIMIZATION

Using the theory of Chapter 4 and the TAPCE model developed in Chapter 5, the performance characteristics of the engine are finally analyzed in this chapter. Recall from Chapter 5 that the base geometry of the TAPCE device was determined by duplicating various ratios of lumped parameter impedances in the TASHE, so that the resulting engine should reasonably approximate the acoustical character of the TASHE with the appropriate changes in working fluid, operating conditions, and concentric pipe geometry. The performance and operating characteristics of this base geometry will be analyzed in the following section.

Since many fundamental thermal and thermoacoustic processes are different in the TAPCE and the TASHE, this base configuration can be altered to better suit the strengths of the TAPCE design. Following the analysis of the base configuration performance, the theory and modeling of the previous chapters are used to guide an optimization of some of the geometric and operating parameters in the TAPCE design. This is followed by a parametric study of the pulse combustion performance, an analysis of the various loss mechanisms in the engine, and a comparison with existing thermoacoustic engine technologies.

6.1 TAPCE Base Configuration Performance

The geometry considered in the base TAPCE configuration is described in Table 5.1, though a few operating conditions still need to be chosen. First, the methane/air equivalence ratio is somewhat arbitrarily chosen to be $\Phi = 0.5$, while the cold heat exchanger temperature is set to $T_c = 325$ K, the same as that in the TASHE, and the ambient temperature is assumed to be $T_0 = 300$ K.

To avoid condensation of the water vapor in the combustion products, the maximum allowable pressure in the engine is determined by Eq. (3.3), which relates the partial pressure of the water vapor in the combustion products to the saturation pressure of water at the cold heat exchanger temperature. Since the maximum allowable pressure must include the acoustic pressure variations, a dimensionless pressure ratio of $|p_1|/p_m = 0.10$ is assumed in order to determine the mean pressure in the engine (i.e. $p_{max} = p_m + |p_1| = 1.10 p_m$), which turns out to be $p_m = 123.2$ kPa. This choice of the acoustic pressure ratio also allows the EES program to solve for the mean mass flux that is consistent with this acoustic pressure ratio.

Also, we'll choose to set the temperature of the hot side regenerator interface to be approximately that of the TASHE, i.e. $T_{int} = 841.7$ K, which is accomplished by allowing the EES program to solve for the value of the acoustic load resistance that results in this interface temperature. Finally, the magnitude of the heat release oscillations is set to zero so that the effect of the pulse combustion process on the overall engine performance can be investigated independently at a later point in the chapter.

Using these operating parameters, the geometry of Table 5.1 is used to compute the various lumped parameter impedances for the network of Figure 5.3. Using the

appropriate component model equations and flow balances discussed in Chapter 5, as well as other informational equations used in the engine analysis, the TAPCE model is then comprised of a set of 265 complex equations with 265 complex unknowns, without including several functions defined to handle the integrations, temperature profile solutions and reactant and combustion product gas properties. The EES program separates this system into its real and imaginary components, and iteratively solves the system of 530 equations and unknowns. The detailed computer code of the main program, subprograms, and resulting solution is presented in Appendix A.

Specifying the geometry of the TAPCE allows the EES program to calculate the operating frequency of the engine by matching the impedances between the driver and resonator sections of the engine. The operating frequency of the engine is about $f = 83.3$ Hz, which corresponds to a wavelength of $\lambda = 4.34$ meters, a little over 3 times the total length of the full engine at $x_{tot} = 1.36$ meters.

According to the model results, the reactants flow into the engine from a reservoir at a mean supply pressure of $p_{m,s} = 149.7$ kPa and the assumed temperature of $T_0 = 300$ K. In flowing through the regenerator, the reactants are preheated to a temperature $T_{ph} = 642$ K, at which point they enter the combustion zone at the mean pressure of $p_m = 123.2$ kPa and burn to produce hot combustion products at a temperature $T_h = 1759$ K. The total energy balance at the regenerator/open duct interface yields a regenerator interface temperature of $T_{int} = 842$ K, roughly the same as that of the TASHE. The temperature profiles of the reactants and combustion products as they flow through the regenerator are shown in Figure 6.1. These profiles were computed using Eqs. (4.108) and (4.110) above, with the calculated parameter values $M = -0.9078$, $N = 55.77$, and $\Xi = -19.96$.

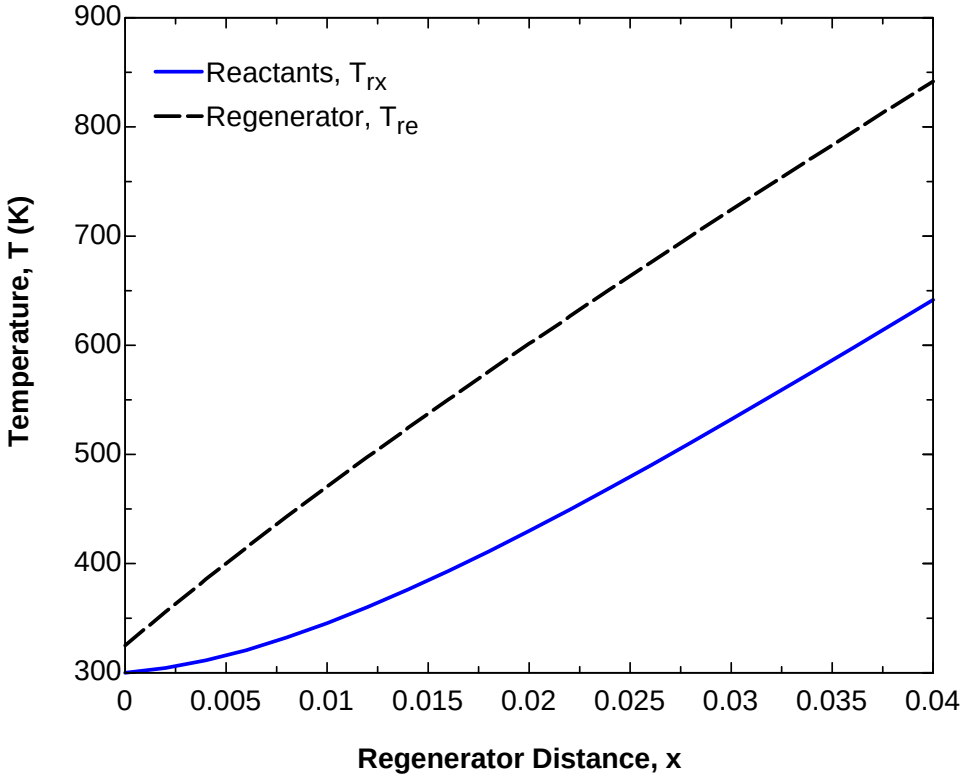

Figure 6.1: Reactant and regenerator temperature profiles for the base TAPCE configuration.

As the combustion products flow through the regenerator, they are cooled to the temperature of the cold heat exchanger, T_c = 325 K, and undergo a small change in mean pressure, to $p_{m,c}$ = 123.1 kPa. These combustion products are then exhausted to a reservoir at ambient temperature and a mean pressure of $p_{m,e}$ = 104.6 kPa. If it is desired that the combustion products exhaust to the ambient pressure, then a resistance valve can be added to the exhaust port in order to maintain control of the mean mass flux flowing through the engine. As it is, the mean mass flux flowing through the engine is very small, about $\dot{M}$ = 9.1 × 10^{-5} kg/s, which corresponds to a ratio of $\dot{M}/|\dot{m}_1|$ = 0.0177 in the engine, and a ratio of $\dot{M}/|\dot{m}_{1,rx}|$ = 0.706 in the reactant preheat pipes.

In general, the phases of the acoustic pressures and velocities in the TAPCE match those of the TASHE very well, though it should be noted that the reference phasor in the TAPCE is chosen to be the acoustic pressure at the hot side of the regenerator, $p_{1,h}$ (i.e., the phase of $p_{1,h}$ is set to zero), whereas the reference phasor for the TASHE is the cold side acoustic pressure, although the two generally vary in phase by less than 2˚. Most importantly, note that the phase of the cold side volumetric velocity, $U_{1,c}$, is about 26˚, while that of the hot side, $U_{1,h}$, is roughly -31˚. Since the phase of the acoustic pressure is roughly zero, this shows that traveling wave acoustic phasing does indeed exist within the regenerator. The volumetric velocity phase shift across the regenerator is due to the compliance of the regenerator [Backhaus and Swift (2000)], and can be controlled to some extent by changing the porosity or length of the regenerator.

The acoustic energy entering the cold side of the regenerator, $\dot{E}_c$ = 21.7 W, is amplified to $\dot{E}_h$ = 47.9 W across the regenerator, while the acoustic energy flowing into the resonator junction is $\dot{E}_L$ = 21.5 W. All analyses will focus on the acoustic energy

output at this location, since it is representative of the true output of the driving section of the TAPCE, and the physical configuration that exists below the driving section is dependent on the particular application of the engine. The heat addition by combustion is approximately $\dot{Q}_m$ = 129.2 W, while the total reactant preheating heat transfer is $\dot{Q}_{ph}$ = 31.9 W, and the heat rejection at the cold heat exchanger is $\dot{Q}_c$ = 102.5 W.

The total acoustic energy available from the fuel energy is $\dot{W}_{\max,fuel}$ = 133 W according to Eq. (4.142), yielding a second law efficiency of η_{II} = 16.2% from Eq. (4.140). This is a fairly low efficiency, especially when compared to the 42% second law efficiency of the TASHE [Backhaus and Swift (2000)]. Note, however, that the efficiency reported for the TASHE is for the conversion of electrical energy to acoustic energy, which is different from the situation studied in this work. A more detailed comparison of the efficiency of the TAPCE engine with other comparable technologies such as the TASHE will be presented at the end of the chapter.

The sources of irreversibility in the engine are computed with their lost work equations of Chapter 5, as shown in Table 6.1, and are dominated by the irreversibilities in the regenerator, followed closely by the irreversibility of the combustion process. These sources of lost work can be reduced by optimizing the geometry and operating conditions of the TAPCE, which will help increase its second law efficiency.

6.1.1 Acoustic load vs. regenerator temperature difference

Built into the lumped parameter TAPCE model are several mechanisms that illustrate how the actual TAPCE engine might be controlled. For instance, adjusting the resistance of the acoustic load, R_L, has the effect of changing the temperature at the hot

Table 6.1: Work lost in the TAPCE base configuration

Component	Work Lost or Gained (W)	Fraction of Available Work
Available Work from Fuel	133	1.000
Acoustic Power Output	21.5	0.162
Reactant Preheating Loss	1.57	0.012
Flow Availability	21.2	0.159
Heat Transfer from Regenerator	-21.2	-0.159
Viscous Pressure Drop	1.57	0.012
Combustion Process Loss	35.5	0.267
Regenerator/Hot Duct Interface Loss	12.4	0.093
Regenerator Loss	42.8	0.321
Flow Availability	-29.3	-0.220
Heat Transfer to Reactants	15.7	0.118
Conduction and Entropy Flux Loss	53.4	0.402
Viscous Acoustic Loss	2.95	0.022
Cold Heat Exchanger Loss	7.89	0.059
Flow Exhaust Loss	1.41	0.011
Other Losses	9.97	0.075

side of the regenerator, T_{int}, as illustrated in Figure 6.2. Here, we see that as the resistance of the acoustic load is decreased, the temperature at the hot side of the regenerator increases.

This is the same mechanism used to control the hot temperature in the TASHE, where the acoustic load is an orifice with a needle valve, whose resistance is adjusted by turning the valve's knob [Backhaus and Swift (2000)]. Opening the valve decreases the resistance to allow a larger acoustic velocity flow through the orifice. This increases the viscous dissipation in the valve, thus converting acoustic energy to heat [Fusco et. al. (1992)]. With an increase in acoustic power consumed at the acoustic load, the acoustic gain across the regenerator must increase, which is realized as an increase in the hot side regenerator temperature, as seen in Figure 6.2.

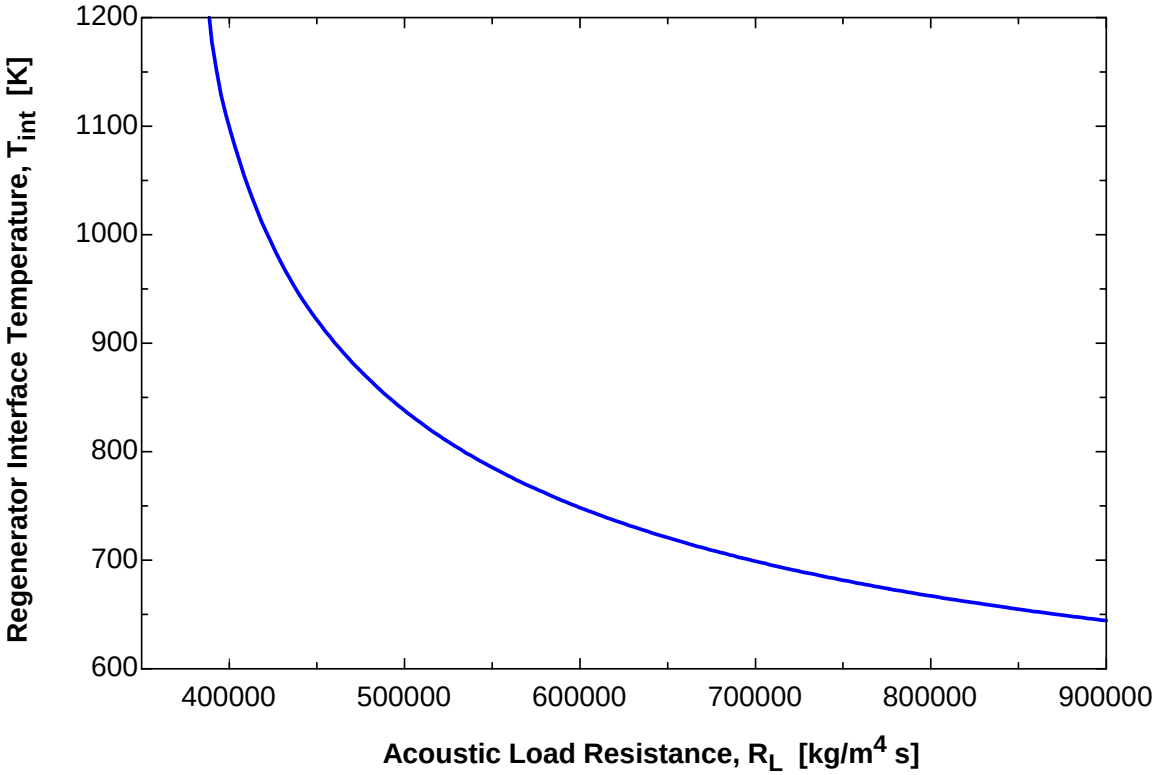

Figure 6.2: Adjustment of regenerator hot side temperature with acoustic load resistance for the TAPCE base configuration.

Finally, note that the efficiency of the engine has a maximum for some particular value of T_{int}, which is best explained in the case where there is no reactant preheating. In this instance, if the temperature difference across the interface is very small (i.e. $T_{int} \approx T_h$), then the acoustic energy flux leaving the hot side of the regenerator, $\dot{E}_h$, is approximately zero according to Eq. (4.71), but if there is a very small temperature difference across the regenerator (i.e. $T_{int} \approx T_c$), then the acoustic energy gain across the regenerator is approximately zero according to Eq. (4.74). Hence, a maximum acoustic power output must exist for some regenerator interface temperature between T_h and T_c. In the case of no reactant preheating, this optimal temperature can be shown to be slightly less than $T_{int,opt} = (T_h T_c)^{1/2}$ [Weiland and Zinn (2004a)].

For the interface temperature variations shown in Figure 6.2, the corresponding second law efficiencies are plotted in Figure 6.3, where we note that a maximum second law efficiency of $\eta_{II} = 16.4\%$ occurs at about $T_{int} = 765$ K. Unfortunately, since the hot combustion temperature is an unknown in the TAPCE (and is partially determined by T_{int} through the preheat temperature, T_{ph}), an expression for an approximate value of the optimal value of T_{int} cannot be obtained. As a result, the optimum T_{int} for each model configuration must be found numerically using the EES program.

6.1.2 Mean flow vs. acoustic pressure

As noted above, the TASHE used the hot heat exchanger input power to control the acoustic pressure magnitude. An analogous situation exists in the TAPCE, where the acoustic pressure is regulated through the total heat input to the engine, which is most easily controlled by adjusting the mean mass flux flowing through the engine. In practice, this mean mass flux is ultimately determined by the difference between the

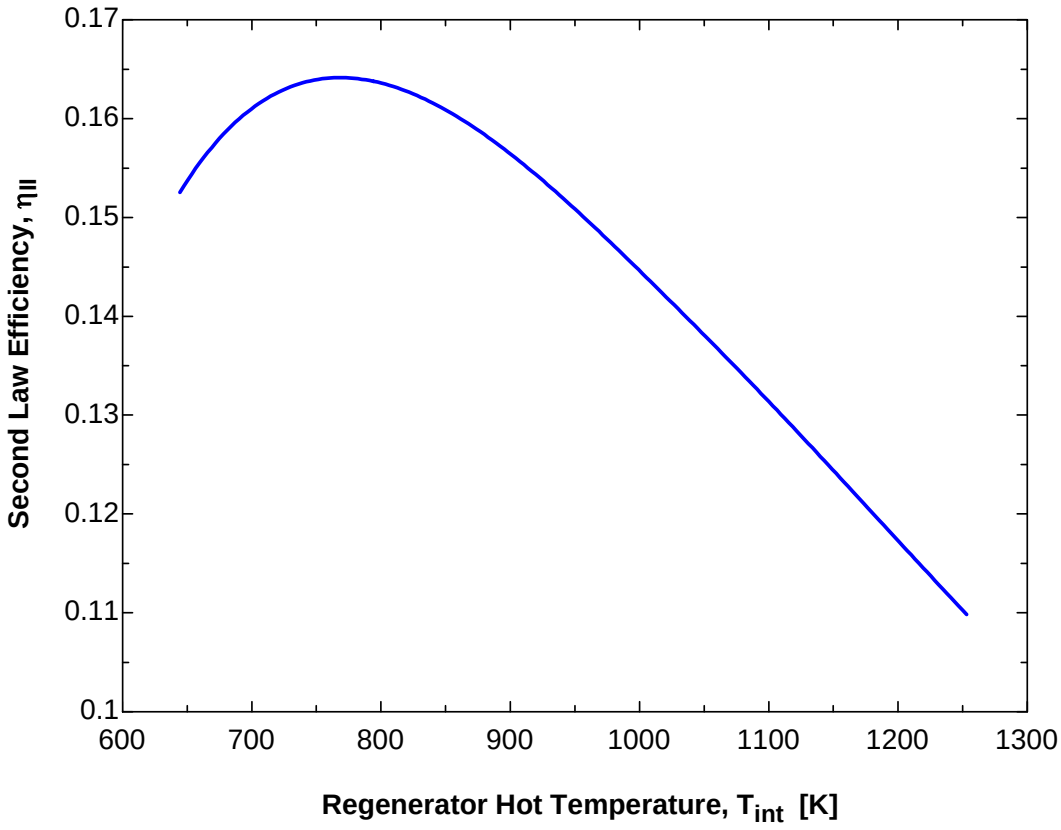

Figure 6.3: Optimal regenerator hot side temperature for the TAPCE base configuration.

mean pressures at the reactant supply reservoir and the exhaust, though these can be easily adjusted by adding valves to the inlet and exhaust piping.

As an example, Figure 6.4 shows the nearly linear dependence of the square of the dimensionless acoustic pressure magnitude at the cold end of the regenerator, $(|p_{1,c}|/p_m)^2$, which scales with the acoustic power, upon of the mean mass flux entering the reactant inlet header, $\dot{M}$. This relationship agrees with the predicted linear relationship between $(|p_{1,c}|/p_m)^2$ and the heat input from the hot heat exchanger in the TASHE [Backhaus and Swift (2000)]. Figure 6.4 also shows that the acoustic pressure magnitude is zero for a non-zero mean mass flux. This is analogous to the situation in other thermoacoustic engines, where a heat input threshold must be reached before acoustic oscillations spontaneously appear in the engine. At this threshold, the heat input essentially overcomes the thermal losses in the system, and any additional heat input is then used to generate acoustic energy. The same is true in the TAPCE, where a threshold mean mass flux (i.e., heat input) must be provided before the engine's thermal losses are overcome and acoustic oscillations appear.

The ability to change the acoustic pressure ratio in the engine affects its acoustic power output and efficiency as shown in Figure 6.5. As discussed above, this figure shows that the acoustic power output is proportional to the square of the acoustic pressure ratio, thus increasing the acoustic pressure ratio from 10% (i.e., $|p_{1,c}|/p_m = 0.1$) to 20% roughly quadruples the acoustic power output of the engine. Note, however, that the TAPCE model is only valid for acoustic pressure amplitudes up to about 10% of the mean pressure, as nonlinear loss mechanisms not included in the model begin to significantly affect the engine's performance for higher acoustic pressure amplitudes. As

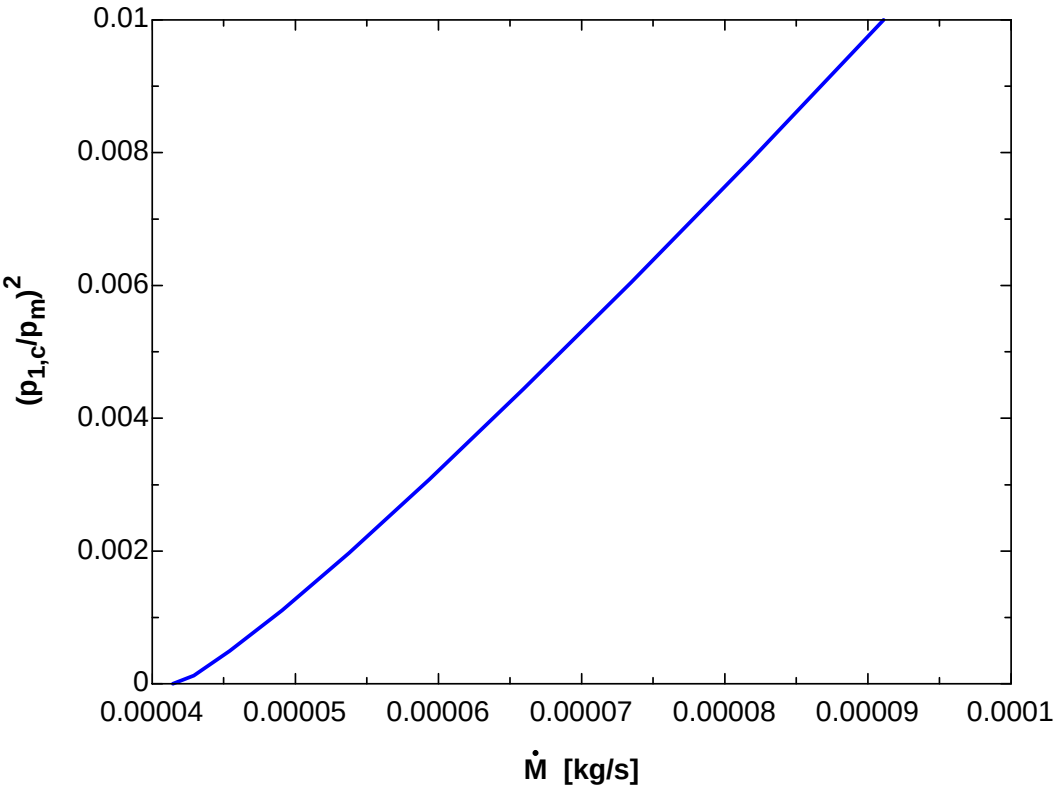

Figure 6.4: Adjustment of the acoustic pressure amplitude with the mean mass flux in the TAPCE base configuration.

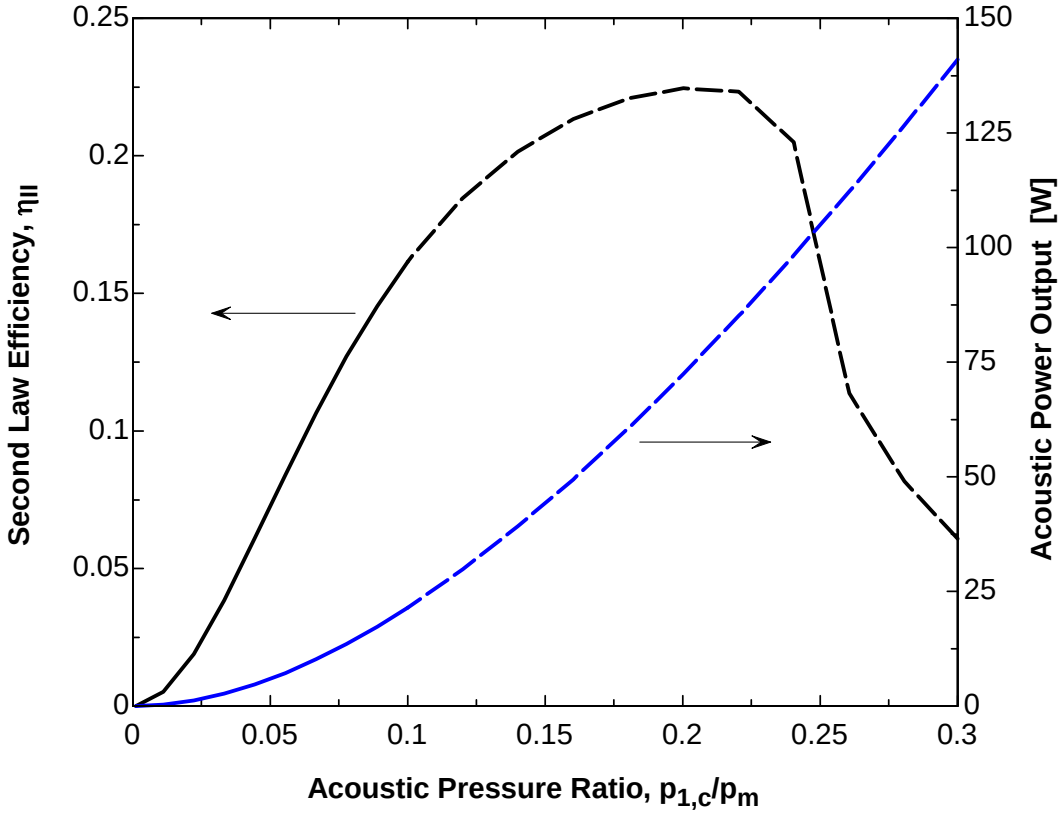

Figure 6.5: Efficiency and acoustic power output versus acoustic pressure ratio for the TAPCE base configuration.

a result, the dashed lines shown in Figure 6.5 are not quantitatively accurate, but may qualitatively show the general trends that result at higher acoustic pressure amplitudes.

Although the acoustic power output can always be increased by increasing the acoustic pressure amplitude, the efficiency of the engine may be adversely affected. As shown in Figure 6.5, the second law efficiency of the device begins to decrease for acoustic pressure amplitudes greater than 20%, since increasing mean flow rates reduce the reactant preheating efficiency and cause increased viscous losses in the inlet and exhaust pipes. In a practical device, nonlinear loss mechanisms will cause the maximum efficiency to shift towards lower acoustic pressure magnitudes. For example, the TASHE device achieves its highest thermal efficiency of 30% for an acoustic pressure amplitude of 6% and an acoustic power output of 710 W, while its most powerful operating point yields 890 W of acoustic power output and a thermal efficiency of 22% using an acoustic pressure ratio of 10% [Backhaus and Swift (2000)].

6.1.3 Equivalence ratio, cold heat exchanger temperature and mean pressure

As discussed in Chapter 3, we need to avoid condensation of the water vapor out of the cold combustion products, which could clog the pores in the regenerator. This requirement limits the mean pressure in the device to some maximum total pressure, which is a function of the equivalence ratio, Φ, and the cold heat exchanger temperature, T_c, as shown in Eq. (3.3). Furthermore, Figure 3.4 indicates that the maximum non-condensing mean pressure in the engine can be increased by either increasing T_c, or by decreasing Φ.

A few other operating conditions that may limit or affect the engine's performance must also be considered. For instance, a lower limit for the mean pressure

in the TAPCE can be determined by requiring that the mean exhaust pressure, $p_{m,e}$, be no lower than the ambient pressure, p_0. In this case, the primary factors influencing the minimum mean pressure in the engine are the geometry of the exhaust port and the mean mass flux and density of the gas passing through it, as described in Eq. (5.81). In addition, the lean flammability limit of the preheated reactant mixture must be considered, as it needs to be above that described in Eq. (3.4). This limit is primarily determined by the preheat temperature, T_{ph}, which is a function of many parameters, including T_c, $\dot{M}$, p_m, and the geometry of the regenerator and the reactant preheat pipes.

Using these limits, the range of allowable values of T_c and Φ is shown in Figure 6.6. To generate these limits, the acoustic pressure magnitude was maintained at $|p_{1,c}|/p_m = 0.10$, and the regenerator temperature ratio was held at $\tau = T_{int}/T_c = 2.59$ to keep the acoustic energy gain across the regenerator constant, while the mean mass flux and acoustic load resistance were allowed to vary. Note that these limits can be changed somewhat by altering the geometry of the engine, though for the base TAPCE configuration, they show that the engine should generally be operated at $\Phi \geq 0.4$, and $T_c \geq$ 325 – 335 K. Practical considerations also limit the TAPCE to $\Phi < 1$ to avoid fuel waste, and to some upper mean pressure limit at which safety and hardware complications must also be considered.

Keeping these limits in mind, the dependence of the second law efficiency and maximum mean pressure upon T_c is shown in Figure 6.7 for several values of Φ. The mean pressure, plotted using the right-hand axis, increases for increasing T_c and decreasing Φ, as mentioned above, and has a substantial effect on the second law efficiency of the engine, which is plotted using the left-hand axis in Figure 6.7. For

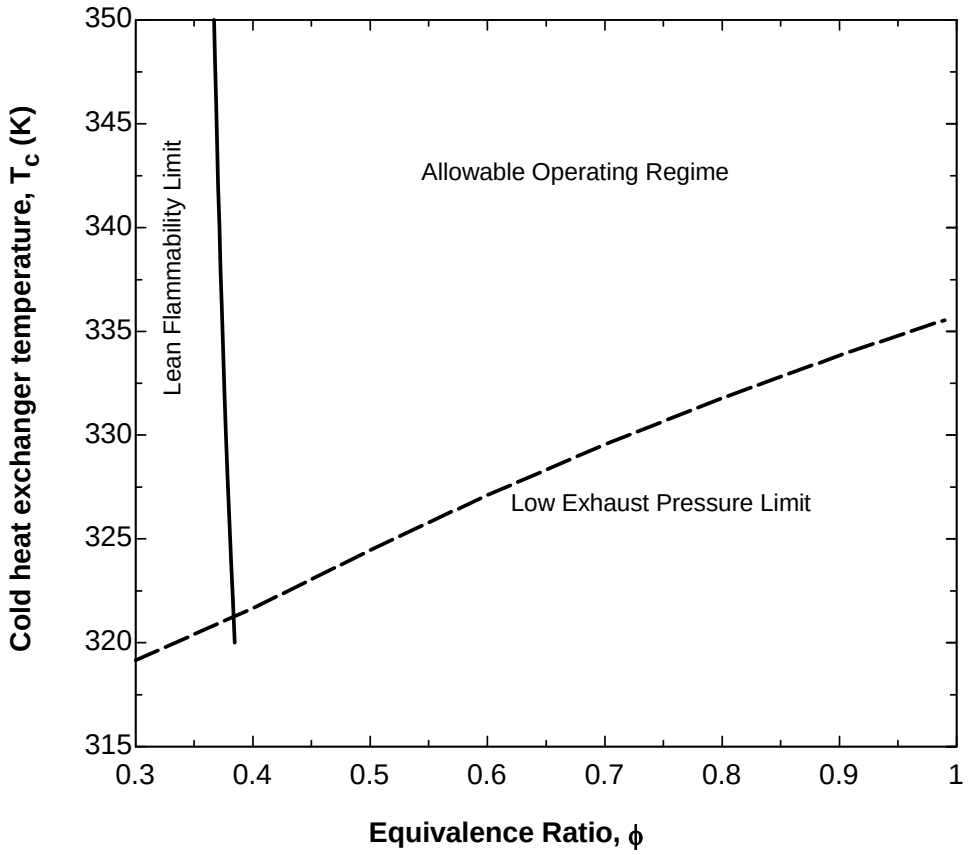

Figure 6.6: Allowable cold heat exchanger temperatures and equivalence ratios for the base TAPCE configuration.

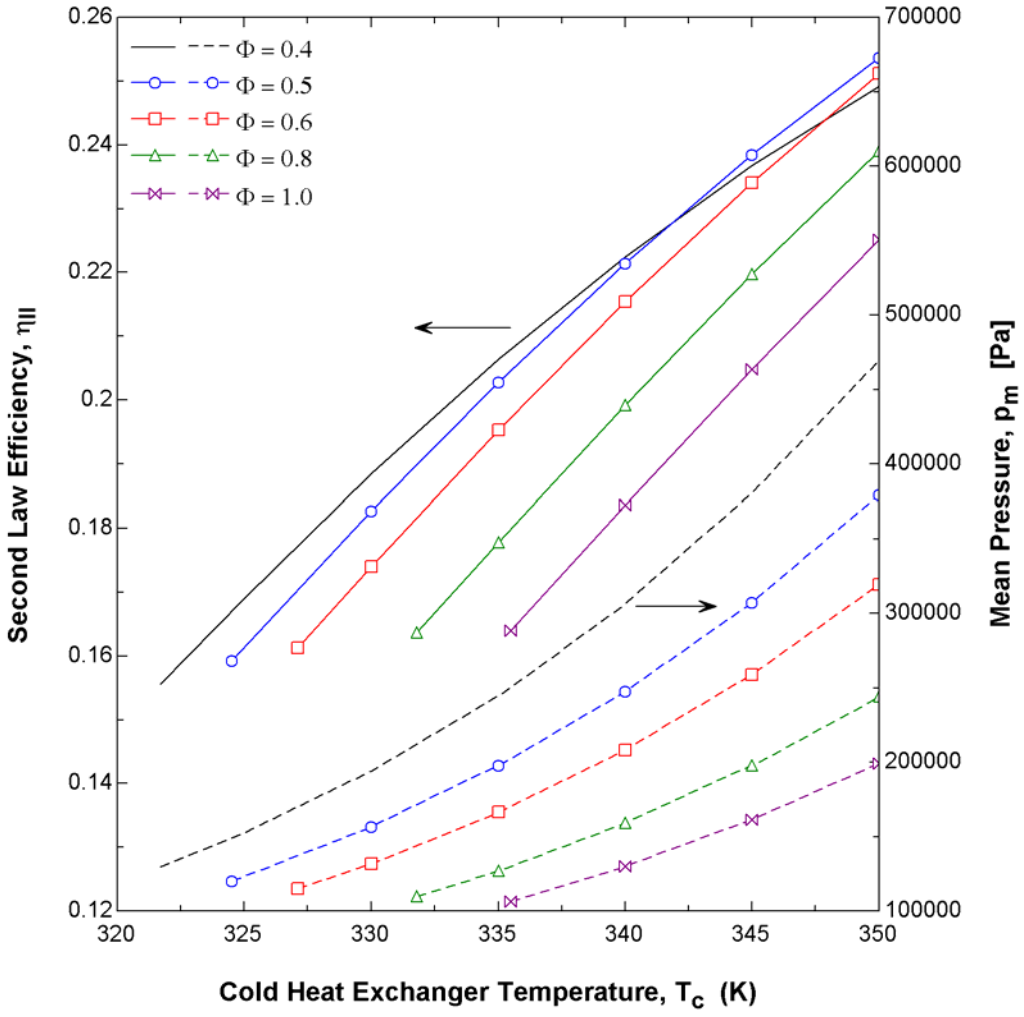

Figure 6.7: Second law efficiency and mean engine pressure versus cold heat exchanger temperature for several equivalence ratios in the base TAPCE configuration.

instance, for an equivalence ratio of $\Phi = 0.5$, the second law efficiency increases nearly 10% by changing T_c from 325 K to 350 K. There are several reasons for this increase in efficiency, though the increase in mean pressure is the primary cause, since it increases the acoustic power density in the engine while the thermal losses (primarily conduction) remain essentially constant. Note that increasing the mean pressure in the engine comes with additional complications not considered in the model, however, such as the power requirements for additional compression of the reactant supply and increasing the thickness of the outer shell of the device to conform to pressure vessel safety specifications.

Although the efficiency of the engine can be increased by decreasing the equivalence ratio or increasing the cold heat exchanger temperature in order to increase the non-condensing mean pressure, Figure 6.8 shows that these trends do not apply if the mean pressure is held constant. For a mean pressure of $p_m = 123$ kPa, Figure 6.8 indicates that higher efficiencies are possible for higher equivalence ratios, which is primarily due to the increased combustion temperatures that are possible for these equivalence ratios. In addition, lower cold heat exchanger temperatures result in higher efficiencies, as this increases the temperature difference across the regenerator, and results in lower thermal energy losses at the cold heat exchanger and exhaust.

6.2 Optimization of the TAPCE

In addition to increasing the mean pressure in the engine, there are several other ways in which the efficiency of the engine can be improved. Recall that the initial geometry of the TAPCE was obtained by requiring that the impedance ratios of various lumped parameter elements in the TASHE and TAPCE equal one another, thus

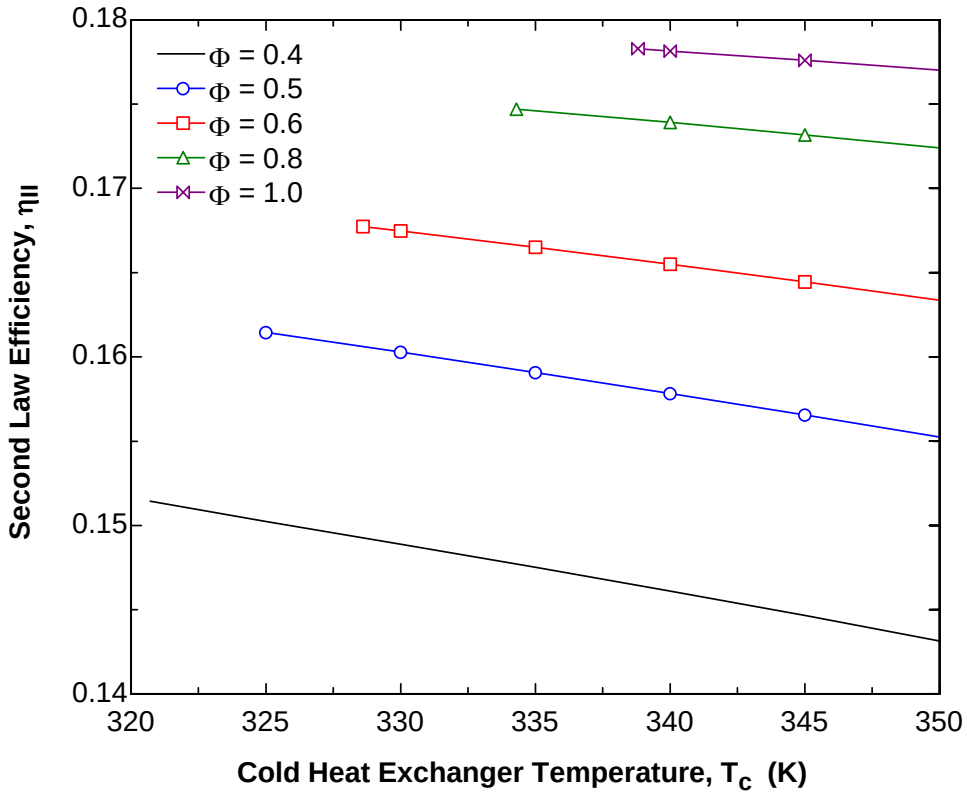

Figure 6.8: Second law efficiency versus cold heat exchanger temperature and equivalence ratio for a constant mean pressure of p_m = 123 kPa in the TAPCE base configuration.

duplicating the acoustical characteristics of the highly successful TASHE in the TAPCE design. This has been achieved in the base TAPCE configuration, where ratios of the various acoustic pressures and velocities at several points in the engine agree reasonably well with the respective ratios in the TASHE, both in magnitude and phase.

The thermal processes occurring in the TAPCE are much different than those in the TASHE, however, and few attempts have been made up to this point to take advantage of these differences. For example, the regenerator's hot temperature, T_{int}, was shown in Figure 6.3 to have an optimal value at which the second law efficiency of the engine was maximized. Many more optimizations that trade off various losses in order to improve the efficiency of the overall engine are possible in the TAPCE design, though only a few of these will be explored in depth in this work.

6.2.1 Identification of optimization parameters

A good place to begin the optimization process is with Table 6.1, as it delineates which loss mechanisms are responsible for most of the lost work in the engine. According to this table, the two components that account for most of the lost work in the engine are the regenerator and the combustion process, which consume 32.1% and 26.7% of the available energy in the fuel, respectively. Unfortunately, not much can be done about the combustion process irreversibilities, although these losses can be reduced somewhat by increasing the combustion temperature, T_h.

Therefore, one of the optimization goals will be to increase the reactant preheat temperature, T_{ph}, which both increases the combustion temperature and helps reduce the regenerator losses, as will be seen below. Note from Eq. (4.109) that T_{ph} is a strong function of the heat transfer parameter N, and will increase if N is increased, as will be

discussed below. Also note that T_{ph} will increase as the regenerator length increases, since the preheating heat transfer will then occur over a longer length in the reactant inlet pipes. This effect is described by Eq. (4.120) that approximates $T_{rx}(x)$ for $M = -1$, $T_c = T_0$, $|N| >> |\Xi|$ and $NL >> 1$, where it is shown that the temperature $T_{ph} = T_{rx}(L)$ increases for increasing L.

Since it accounts for most of the lost work in the engine, the regenerator should be the focus of the optimization efforts. In Table 6.1, the work lost in the regenerator is broken down into several constituent components. The dominant component is the conduction and entropy flux loss component, which is the first part of the third term on the right side of Eq. (4.136), i.e.:

$$\begin{aligned} \dot{W}_{lost,k} &= \left(\dot{M}c_p\right)_{pr} T_0 \frac{1}{\Xi}\left(\frac{1}{T_c}\frac{dT_{re}}{dx}\bigg|_c - \frac{1}{T_{int}}\frac{dT_{re}}{dx}\bigg|_{int}\right) \\ &= T_0\left(\psi + A_s k_s\right)\left(\frac{1}{T_c}\frac{dT_{re}}{dx}\bigg|_c - \frac{1}{T_{int}}\frac{dT_{re}}{dx}\bigg|_{int}\right) \end{aligned}, \tag{6.1}$$

where Eq. (4.77) has been applied in the last equality, and the contribution of the thermal conductivity through the gas, k, has been neglected in comparison with the thermal conductivity through the solid components, k_s.

With the exception of the ambient temperature, T_0, all of the terms in Eq. (6.1) can be manipulated in an attempt to reduce the work losses due to this mechanism. For instance, the area of the solid includes the regenerator screens, the wall of the pipe surrounding the regenerator and the walls of the reactant preheat pipes passing through the regenerator. Thus, the thickness of the inner pipe wall could be reduced to decrease the conduction losses through this component, but note that the lumped parameter model does not explicitly account for the axial conduction along the walls of the reactant preheat

pipes and through the insulation surrounding the inner pipe. Instead, these effects are lumped into the inner pipe wall conduction term by using a wall thickness, t_{wall} = 0.5 mm, that is thicker than what is actually required in the engine.

Since the wall thickness is already fairly small and accounts for other conduction effects in the engine, it will not be altered in the optimization process, although the conducting area of the solid in the regenerator can be decreased by increasing the porosity of the regenerator, ϕ, since $A_s = A_{re}(1-\phi)$. Increasing the porosity also reduces the parameter ψ, since, for a stacked screen regenerator, Eq. (4.63) gives:

$$\psi_{ss} = \frac{4\rho_m c_p}{\phi A_{re}\omega}\frac{(g_c - g_v)}{b(\phi)\sigma^{1/3}}\frac{r_{h,re}^2}{\delta_\kappa^2}|U_1|^2, \tag{6.2}$$

where $b(\phi)$ is given by Eq. (4.66). The ratio of the hydraulic radius to the thermal penetration depth has been set by Eq. (5.43) to be $r_{h,re}/\delta_\kappa$ = 0.316, though other values of this parameter could be considered. The other parameters affecting ψ are primarily determined by the gas properties (σ, ρ_m, and c_p), which are not easily manipulated, and the acoustic velocity in the regenerator (g_c, g_v, and U_1), which could be reduced to further decrease the work lost by the imperfect thermal contact entropy flux loss.

In addition to altering these terms, the work lost by conduction and imperfect entropy flux in Eq. (6.1) can be reduced by increasing T_c, reducing T_{int}, or increasing the length of the regenerator, L, which reduces both the hot and cold temperature gradients. Also recall from Chapter 4 that the addition of a mean mass flux creates a non-linear temperature profile in the regenerator that results in a larger temperature gradient at the cold end than at the hot end, thus increasing this factor in Eq. (6.1). However, as discussed in the analysis of the case where M = -1, excellent heat transfer from the

regenerator to the reactants occurs if N is large, which results in an approximately linear regenerator temperature profile.

Using the Nusselt number correlation from Eq. (5.54), and the definitions of the Reynolds number and the Prandtl number from Eqs. (4.142) and (2.3), respectively, Eq. (4.89) for N can be expressed as:

$$N = \frac{4Nu}{D_{ph} Re_{rx} \sigma} = \frac{0.088}{D_{ph} \sigma^{1/2}} \frac{Re_{tasfe}^{4/5}}{Re_{rx}} = \frac{0.084}{D_{ph}} \left(\frac{D_{ph} n \mu}{\dot{M}} \right)^{1/5} \left(\frac{\dot{M}_{tasfe}}{\dot{M}} \right)^{4/5} \left(\frac{k}{\mu c_p} \right)^{1/2}, \qquad (6.3)$$

where the mean mass flux, $\dot{M}$, had been distinguished from the time average steady flow equivalent mass flux, $\dot{M}_{tasfe}$ from Eq. (5.62), which is used in the Nusselt number correlation. In this form, it is evident that N is primarily increased by reducing the diameter of the individual reactant preheat pipes, D_{ph}, decreasing the mean mass flux, $\dot{M}$, and, to a lesser extent, by increasing the number of preheat pipes, n. Notice that decreasing D_{ph} will decrease the work lost in the regenerator, but will also increase the work lost due to the viscous pressure drop in the reactant preheat pipes, as expressed in Eqs. (4.129), (5.50) and (5.51), suggesting that an optimal preheat pipe diameter likely exists. As shown in Table 6.1, this viscous loss is currently fairly small, thus the preheat pipe diameters could be reduced below their current value of D_{ph} = 0.5 millimeters before an optimum is reached. Practical constraints will limit how small these pipes should be made, however, since this has a large effect on the reactant supply pressure, and thus, the power and size requirements of the compressor, which are not accounted for in this study.

The flow availability component of the regenerator loss in Table 6.1 is described by the first term on the right side of Eq. (4.136):

$$\dot{W}_{lost,flow} = \left(\dot{M}c_p\right)_{pr} T_0 \left[\ln\left(\frac{T_{int}}{T_c}\right) + \frac{\gamma - 1}{\gamma} \ln\left(\frac{p_{m,c}}{p_m}\right) \right] \approx \left(\dot{M}c_p\right)_{pr} T_0 \ln\left(\frac{T_{int}}{T_c}\right), \tag{6.4}$$

where the pressure term is very small compared to the temperature term. Note that this term is negative in Table 6.1, thus reducing the total work lost in the regenerator. To further reduce the regenerator's irreversibilities, the regenerator flow availability component could be increased by increasing T_{int}, which also generally decreases the lost work at the regenerator open duct interface, as expressed in Eq. (4.133). Balancing these two mechanisms against the loss mechanism of Eq. (6.1) results in an optimal regenerator interface temperature, as shown in Figure 6.3.

The other two terms of interest that comprise the regenerator lost work in Table 6.1 are the viscous acoustic loss and heat transfer components. The viscous loss component is described by the second term on the right side of Eq. (4.136), and is fairly small in comparison to the other terms. The preheating heat transfer component is slightly larger, and is a function of the finite temperature difference between the regenerator and the reactants, as described by the last term in Eq. (4.136). This component can be reduced by minimizing the difference between T_{re} and T_{rx}, which is essentially accomplished by increasing the heat transfer parameter, N, and/or increasing the length of the regenerator, L. Also note that this heat transfer component is coupled to the heat transfer component in the reactant preheating losses, which is the last term in Eq. (4.129). As shown in Table 6.1, this reactant preheating component is negative, and balances the flow availability component of the reactant preheating losses, which is the first term in Eq. (4.129).

The work lost at the cold heat exchanger and the exhaust port are both fairly small according to Table 6.1, and primarily increase with increasing T_c, as shown in Eqs.

(4.138) and (4.139). The last entry in Table 6.1 is a lump sum of all of the other loss mechanisms modeled in the TAPCE, and is simply the difference between the available work from the fuel and the sum of the acoustic power output and lost work terms in Table 6.1. These other losses include viscous and thermal relaxation losses to the solid surfaces throughout the TAPCE driver section, and acoustic losses out of the inlet and exhaust ports, which are each about 0.4 W in the base TAPCE configuration.

Finally, the acoustic power output, which is primarily adjusted through the volumetric acoustic velocity, U_1, must not to be overlooked in Table 6.1. The acoustically compact network is designed to reduce the volumetric velocity in the regenerator by making the acoustic impedance of the inertance much lower than that of the regenerator. As a result, the resistance of the regenerator and the geometry of the inertance can be adjusted to alter the fraction of U_1 that passes through the regenerator, which linearly scales with the acoustic power flowing through the regenerator. There is interest in reducing the acoustic velocity in the regenerator, however, as acoustic viscous losses and imperfect entropy flux losses are both functions of $|U_1|^2$, according to Eqs. (4.75) and (6.2), respectively. Since very small acoustic velocities result in little or no acoustic power output, an optimum volumetric velocity must exist that maximizes the acoustic power output for the engine.

Given the modeled TAPCE geometry shown in Figure 5.4, there are several convenient parameters that can be used to alter the acoustic velocity in the regenerator. One such parameter is the thickness of the insulation surrounding the inner pipe, t_{ins}, which effectively changes the impedance of the inertance by changing its cross-sectional area. In addition, the volume of the main compliance affects the total volumetric velocity

passing through the combination of the inertance and regenerator branches, thus changing the length of the compliance, x_c, can also be used to alter the acoustic velocity in the regenerator. Furthermore, since the magnitude and phase of the acoustic velocity changes appreciably across the length of the combustion zone, x_{cz}, depicted in Figure 5.4, changing this parameter will also alter the magnitude and phase of the acoustic velocity in the regenerator. Finally, the regenerator's acoustic velocity can also be easily controlled by altering its length or hydraulic radius, thus changing viscous resistance of the regenerator.

To summarize, the above analysis indicates that several key parameters are likely to influence the second law efficiency of the TAPCE: the regenerator interface temperature, T_{int}, the length of the regenerator, L, the porosity of the regenerator, ϕ, the thickness of the inner pipe insulation, t_{ins}, the length of the compliance, x_c, the length of the combustion zone, x_{cz}, and the regenerator's hydraulic radius, $r_{h,re}$,. These seven parameters will be used to optimize the geometry and operating conditions of the TAPCE in the following section. Other parameters mentioned above that are either already optimized or are limited by practical constraints include the preheat pipe diameter, D_{ph}, the number of preheat pipes, n, the thickness of the inner pipe wall, t_{wall}, and the gas properties.

6.2.2 Optimization process

First, note that the issue of the cold combustion product condensation is not considered during the optimization of the TAPCE geometry. To obtain some basis for comparison, the base TAPCE configuration settings of T_c = 325 K, Φ = 0.5, and p_m = 123.2 kPa are used, which should also yield exhaust pressures that are close to

atmospheric pressure in the cases studied. In addition, the acoustic pressure ratio is set to $|p_{1,c}|/p_m = 0.10$, while allowing the mean mass flux, $\dot{M}$, and the acoustic load resistance, R_L, to vary according to the needs of the optimization process.

The steps taken in optimizing the engine are shown in tabular form in Table 6.2, where w_{rx}, w_{comb}, w_{int}, w_{re}, w_{chx}, w_e, and w_{other} are the fractions of the available fuel work that are lost in the reactant inlet, combustion process, regenerator/open duct interface, regenerator, cold heat exchanger, exhaust, and other components, respectively, giving some indication of the effect of each of the parameter changes on the loss processes in the engine. The first row of data in this table corresponds to the base TAPCE configuration, while the last row is the optimized TAPCE configuration, for which a maximum second law efficiency of $\eta_{II} = 19.7\%$ is obtained.

In each step, one of the optimization parameters was varied until the second law efficiency reached a maximum, with one notable exception. Increasing the ratio of the regenerator's hydraulic radius to the cold side thermal penetration depth, $r_{h,re}/\delta_{\kappa,c}$, resulted in significant increases in the efficiency of the engine, as seen in Table 6.2, though the maximum efficiency was obtained for an unreasonably large value of $r_{h,re}/\delta_{\kappa,c}$. This ratio essentially describes the degree of solid/gas thermal contact in the regenerator, with larger values indicating decreased thermal contact. Initially, this parameter was chosen in Eq. (5.43) to satisfy $(r_{h,re}/\delta_{\kappa,c})^2 = 0.1$ to ensure that the square of this ratio is a small number, since terms of this order are frequently neglected in traveling wave thermoacoustics. Therefore, large values of $r_{h,re}/\delta_{\kappa,c}$ begin to push the limits of the assumptions made in important model equations such as Eq. (5.25) for dU_1/dx across the regenerator. As a result, a limit of $r_{h,re}/\delta_{\kappa,c} = 0.376$ was placed on this ratio, in part

Table 6.2: Optimizing steps in the TAPCE

T_{int} (K)	L (m)	t_{ins} (m)	ϕ	$r_{h,re}/\delta_{k,0}$	x_c (m)	x_{cz} (m)	η_{II}	*Acoustic Power* (W)	*Fuel Work Available* (W)	w_{rx}	w_{comb}	w_{int}	w_{re}	w_{chx}	w_e	w_{other}
842	0.04	0.0152	0.72	0.3162	0.058	0.1226	0.1615	21.5	133	0.0118	0.2672	0.0932	0.3214	0.0593	0.0106	0.0750
765	0.04	0.0152	0.72	0.3162	0.058	0.1226	0.1642	19.5	118.6	0.0096	0.2771	0.1171	0.2919	0.0589	0.0088	0.0725
765	0.04	0.0152	0.72	**0.376**	0.058	0.1226	0.1806	26.3	145.4	0.0127	0.2798	0.1133	0.2773	0.0576	0.0123	0.0663
765	0.04	0.0152	0.72	0.376	0.058	**0.095**	0.1816	28.2	155.5	0.0139	0.2808	0.1118	0.2763	0.0575	0.0138	0.0642
765	**0.05**	0.0152	0.72	0.376	0.058	0.095	0.1871	22.5	120.5	0.0101	0.2711	0.1210	0.2756	0.0573	0.0090	0.0689
820	0.05	0.0152	0.72	0.376	0.058	0.095	0.189	24.4	129.3	0.0116	0.2632	0.1037	0.2945	0.0573	0.0101	0.0706
820	0.05	0.0152	**0.75**	0.376	0.058	0.095	0.1924	23.1	120	0.0104	0.2622	0.1050	0.2913	0.0570	0.0089	0.0727
820	0.05	0.0152	0.75	0.376	**0.076**	0.095	0.1941	25.0	129	0.0115	0.2629	0.1039	0.2869	0.0566	0.0101	0.0739
840	0.05	0.0152	0.75	0.376	0.076	0.095	0.1944	25.7	132	0.0121	0.2602	0.0983	0.2933	0.0567	0.0105	0.0746
840	0.05	**0.014**	0.75	0.376	0.076	0.095	0.195	24.8	127.4	0.0115	0.2595	0.0991	0.2946	0.0568	0.0099	0.0736
840	0.05	0.014	0.75	0.376	0.076	**0.07**	0.1961	25.9	132.2	0.0121	0.2603	0.0982	0.2937	0.0567	0.0105	0.0725
840	0.05	**0.0125**	0.75	0.376	0.076	0.07	0.1967	25.1	127.6	0.0115	0.2596	0.0990	0.2950	0.0568	0.0099	0.0714

because other successful regenerators have been designed with similar values of $r_{h,re}/\delta_{\kappa,c}$ [Backhaus and Swift (2001)].

In addition to $r_{h,re}$, the parameter with the most influence on the efficiency of the engine is the regenerator length, as seen in Table 6.2. In changing the length of the regenerator or the combustion zone, the length of the inner pipe (i.e., the inertance) is held constant, while the length of the cold duct is allowed to vary. As the compliance of the cold duct has little influence on the acoustic character of the engine, the only concern, then, is that the cold duct is still long enough to house the cold heat exchanger and reactant inlet header, while still allowing enough room for the movement of the acoustically transparent barrier. Using the optimized dimensions in Table 6.2, the final cold duct length of 7.3 cm is more than adequate to house these components.

The data in Table 6.2 also indicates that changing the thickness of the insulation, t_{ins}, the length of the combustion zone, x_{cz}, or the length of the compliance, x_c, do not have a very large effect on the efficiency of the engine, probably because the initial values determined for the base configuration are already close to their optimal values, having been determined from the impedance ratios of the well-designed TASHE. The porosity of the regenerator, ϕ, does not have an appreciable influence on the engine efficiency either, though this can be used to our advantage in the construction of the TAPCE device. This allows us some flexibility in choosing commonly available wire mesh screens, where the hydraulic radius and porosity are approximately related to the wire diameters and mesh numbers of the screens by Eqs. (5.46) and (5.47), respectively.

Table 6.3: Work lost in the optimized TAPCE configuration

Component	Work Lost or Gained (W)	Fraction of Available Work	Fraction Change from Base Case
Available Work from Fuel	127.6	1.000	--
Acoustic Power Output	25.1	0.197	+0.035
Reactant Preheating Loss	1.47	0.011	-0.001
Flow Availability	21.9	0.172	+0.013
Heat Transfer from Regenerator	-21.9	-0.172	-0.013
Viscous Pressure Drop	1.47	0.011	-0.001
Combustion Process Loss	33.1	0.260	-0.007
Regenerator/Hot Duct Interface Loss	12.6	0.099	+0.006
Regenerator Loss	37.7	0.295	-0.026
Flow Availability	-28.1	-0.220	0.000
Heat Transfer to Reactants	16.9	0.133	+0.015
Conduction and Entropy Flux Loss	44.8	0.351	-0.051
Viscous Acoustic Loss	4.00	0.031	+0.009
Cold Heat Exchanger Loss	7.25	0.057	-0.002
Flow Exhaust Loss	1.26	0.010	-0.001
Other Losses	9.12	0.071	-0.004

6.2.3 Optimized TAPCE performance

The performance and loss mechanisms of the optimized TAPCE configuration are broken down into their various components in Table 6.3, where the last column gives the change in the fraction of work lost or gained by each loss mechanism between the base configuration and the optimized configuration.

In the optimizing the TAPCE configuration under constant acoustic pressure magnitude conditions, the mean mass flux is reduced from $\dot{m}_0 = 0.091$ g/s to $\dot{m}_0 = 0.087$ g/s, which effectively reduces the maximum work available from the input fuel stream from $\dot{W}_{\max,fuel} = 133.0$ W to $\dot{W}_{\max,fuel} = 127.6$ W. The acoustic power output increases, however, from $\dot{E}_L = 21.5$ W to $\dot{E}_L = 25.1$ W, thus increasing the second law efficiency from 16.2% to 19.7%. This increase in acoustic power is primarily a result of reducing

the regenerator's hydraulic radius, which has the effect of reducing the viscous resistance of the regenerator. As a result, the acoustic impedance of the regenerator is lowered in comparison to the impedance of the parallel inertance, thus allowing larger acoustic velocities, and hence larger acoustic power, to flow through the regenerator. This is countered by increased viscous acoustic losses in the regenerator due to the increased velocities, which increase by about 1% between the base and optimized configurations, as shown in Table 6.3.

Contributing to this 1% increase in the regenerator's viscous losses is the lengthening of the regenerator from 4 cm to 5 cm. This length change also has the effect of increasing the total surface area for reactant preheating in the inlet pipes, which increases the fraction of the work lost due to heat transfer across the regenerator/reactant temperature difference by 1.5%, according to Table 6.3. The primary benefit of lengthening the regenerator is to decrease its overall temperature gradient. The reactant and regenerator temperature profiles for both the base and optimized configurations are shown in Figure 6.9, where the reduction in the temperature gradients at either end of the regenerator is readily apparent. As indicated in Eq. (6.1), this leads to a reduction in the fraction of available work consumed by conduction and entropy flux losses in the regenerator, from 40.2% for the base configuration to 35.1% in the optimized configuration. In spite of this, Table 6.3 shows that this mode of irreversibility still accounts for the majority of lost work in the optimized TAPCE engine.

Finally, note from Figure 6.9 that the optimized engine configuration results in a higher reactant preheat temperature, T_{ph} = 677 K, compared to the base case, where T_{ph} = 642 K. This is due in part to the increased length of the regenerator, but can also be

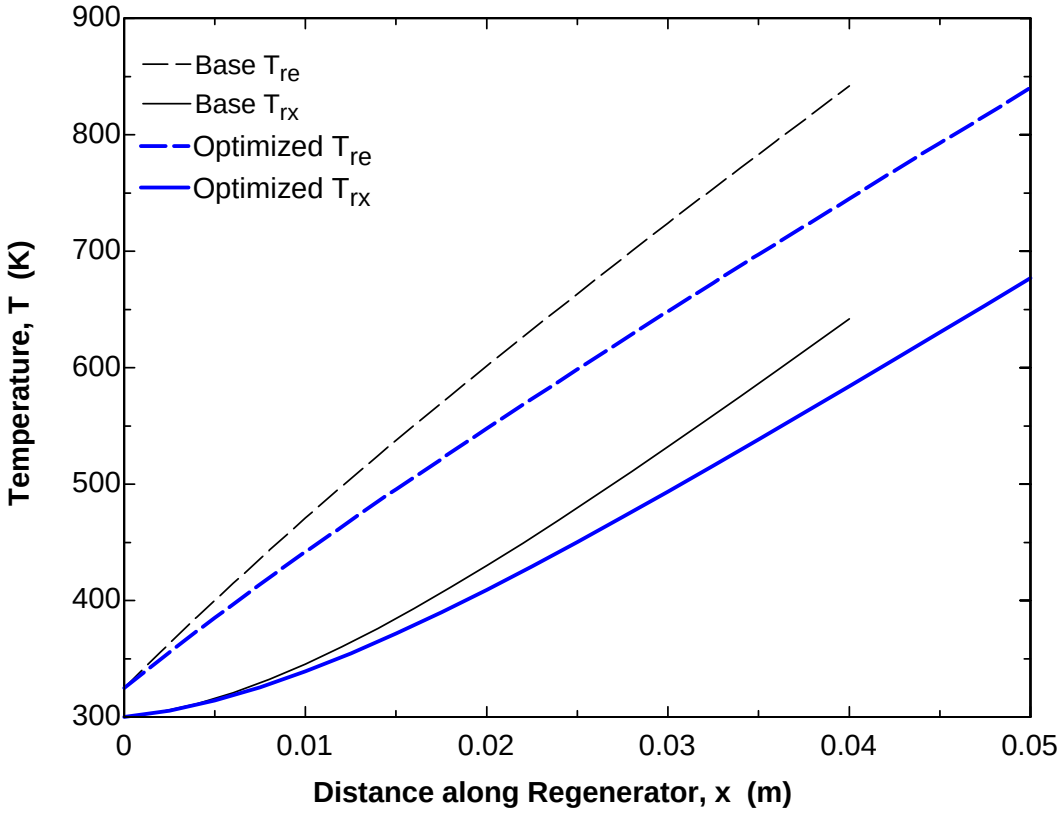

Figure 6.9: Temperature profile comparison for the base and optimized TAPCE configurations.

attributed to an increase value of the heat transfer parameter from $N = 55.8$ to $N = 57.1$, which results from a decrease in the mean mass flux, $\dot{M}$, as described by Eq. (6.3). The increased reactant preheat temperature results in a higher combustion temperature of T_h = 1788 K, though the resulting decrease in the fraction of available work consumed in the combustion process is only about 0.7% according to Table 6.3.

Overall, the results of the optimization process are not as good as we might have hoped, resulting in a second law efficiency of only 19.7% and a thermal efficiency, as defined by Eq. (4.2), of η_{th} = 20.2%. The thermal conduction and entropy flux losses are the primary contributor to this inefficiency, and still consume about 35% of the available work from the fuel in the optimized engine design. To illustrate this point, note that if the thermal conduction losses were reduced by half, the second law efficiency of the optimized TAPCE configuration becomes 24.3%, and could be further increased by additional optimization of the regenerator length and the regenerator interface temperature. Equivalently, the effects of the conduction heat losses can be reduced by increasing the mean pressure and acoustic power density of the engine.

As discussed above, the maximum mean pressure in the engine is limited to pressures at which the water vapor does not condense out of the cold combustion products, and is a function of the fuel type, equivalence ratio and cold heat exchanger temperature in the engine. Performing an analysis similar to that performed above for the base TAPCE configuration, Figure 6.10 shows the second law efficiency and maximum mean pressure of the optimized TAPCE configuration as a function of the cold heat exchanger temperature, T_c, and the equivalence ratio, Φ. Although the mean pressures in this case are approximately the same as those in Figure 6.7 for the base configuration, the

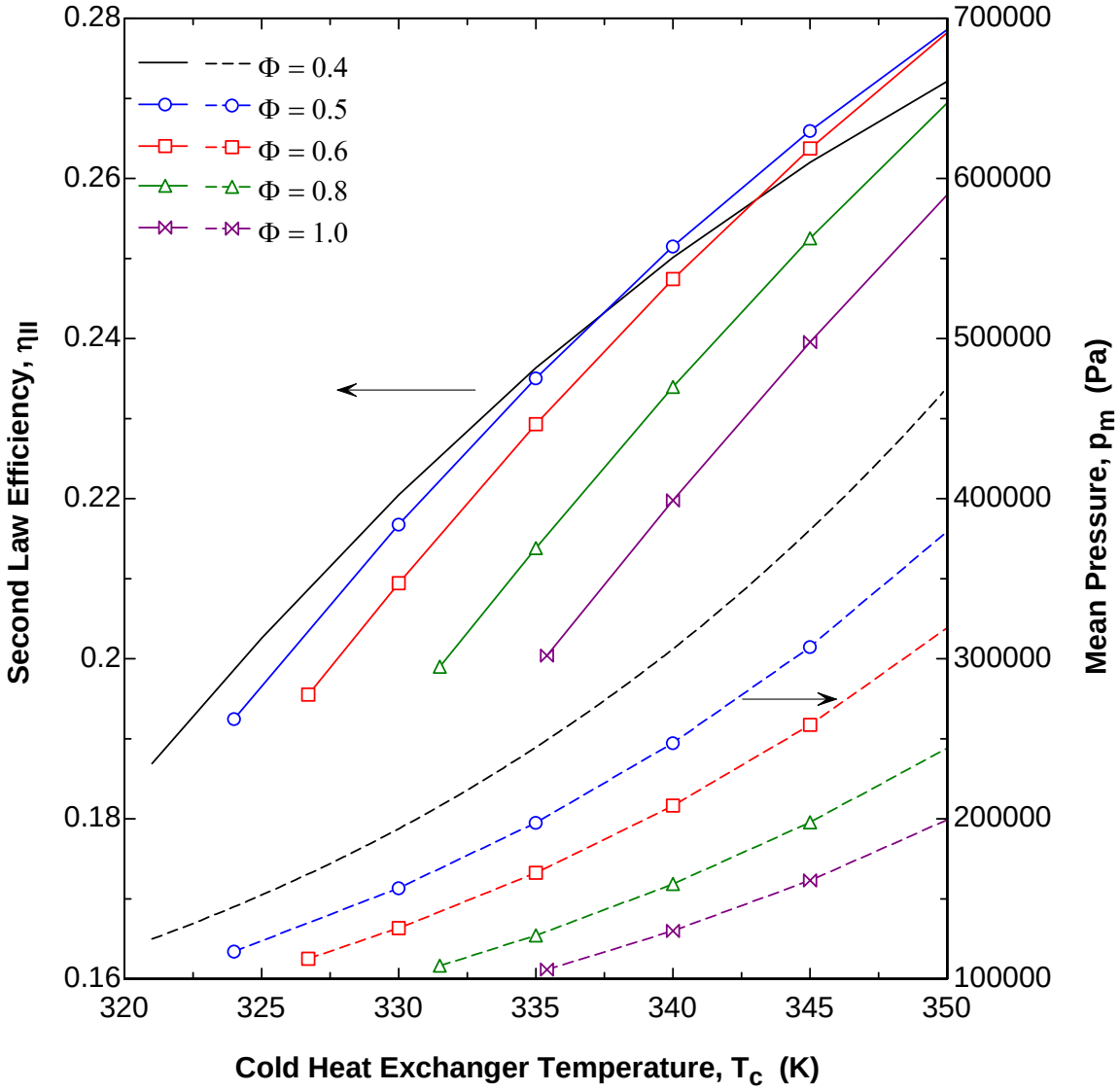

Figure 6.10: Second law efficiency and maximum mean pressure versus cold heat exchanger temperature for several equivalence ratios in the optimized TAPCE

second law efficiencies are, on average, over 3% higher for the optimized configuration. Note that the TAPCE configuration has been optimized for a relatively low pressure condition at T_c = 325 K and Φ = 0.5, and that the engine could be re-optimized to yield higher efficiencies than those shown in Figure 6.10 if operation at higher mean pressures is considered, since the balance between conduction losses and acoustic losses would then be altered. In addition, it should be pointed out that for the fuel chosen for this study, methane, that water vapor condenses out of the cold combustion product gases at lower pressures than any other hydrocarbon fuel, as shown in Figure 3.4. As a result, higher mean pressures and efficiencies could be attained by running the engine on other fuels such as propane, butane, or acetylene.

Note that if a solution can be devised for coping with the condensation problem, then the mean pressure in the device is only limited by the pressure vessel design restrictions. To investigate the full potential of the TAPCE device in this situation, the model was run using the geometry and operating conditions of the optimized TAPCE configuration, but with a mean pressure of 30 atmospheres, which is the mean pressure used in the TASHE. This change in mean pressure yields a second law efficiency of 37.7% and an acoustic power output of 444 W, which are both considerably higher than those attained for lower non-condensing mean pressures. Note that by simply changing the regenerator interface temperature from T_{int} = 840 K to T_{int} = 1120 K, the acoustic power output of the high pressure TAPCE increases to 550 W, corresponding to a second law efficiency of 41%. In addition, the power output and efficiency could be further increased by re-optimizing the geometry of the engine, since the geometry used in these calculations was optimized at 1.2 atmospheres mean pressure, where the relative

magnitudes of the gain and loss mechanisms are much different than those in the high pressure engine.

6.2.4 Unmodeled losses in the TAPCE

Although the above results are promising, it should be noted that the TAPCE model is just that, a computer model, and that an experimental TAPCE device is likely to have an appreciably lower efficiency than that of the model. Although this model incorporates many of the important loss mechanisms of the engine, many additional loss mechanisms exist that have not been accounted for in the model. For instance, the model does not currently account for thermal energy losses due to radial conduction, axial conduction to secondary cold heat exchanger, or radiation heat transfer away from the combustion zone. In addition, most thermoacoustic devices suffer from thermal energy losses due to Rayleigh streaming, a type of annular streaming can transport heat away from critical components of the engine and deposit them at the nearest cold heat exchanger [Bailliet et. al. (2001), Job et. al. (2003), Waxler (2001), Swift (2002)]. These losses are also unaccounted for in the TAPCE model, as are turbulence losses at either end of the inertance, transfer of acoustic energy out of the fundamental acoustic mode into higher frequency acoustic modes, and any acoustic transmission losses that may occur at the acoustically transparent barrier.

Furthermore, since the combustion processes in the engine have been assumed to be ideal, the model does not account for incomplete burning of the reactants, dissociation of the combustion product gases, or lower combustion temperatures due to heat losses [Turns (1996)]. Finally, if application of the TAPCE requires higher efficiencies or

acoustic power densities, then the reactant compression processes and associated losses must also be taken into account in determining the overall system efficiency.

6.3 Pulse Combustion Performance

One gain or loss mechanism that has not yet been accounted for is the pulse combustion process. The model of the pulse combustion process in Eq. (5.68) contains a simple amplitude factor, $\alpha = \left|\dot{Q}_1\right| / \dot{Q}_m$, where $0 \le \alpha \le 1$, and a phase shift parameter, θ_{pq}, which describes the phase shift between the acoustic pressure and unsteady heat release. This model essentially represents the combustion process as a simple volumetric velocity source as described in Eq. (5.69), which can increase or decrease the acoustic power flowing through the combustion zone.

For $\alpha = 1$ and $\theta_{pq} = 0$, almost all of the acoustic power gain by pulse combustion, $\dot{E}_{pc} = 1.45$ W, shows up as acoustic power output of the engine, which increases from $\dot{E}_L = 22.93$ W to $\dot{E}_L = 24.35$ W, and increases the second law efficiency from $\eta_{II} =$ 19.0% to $\eta_{II} = 20.2\%$. This agrees very well with the estimate of Eq. (4.46), using the value of the acoustic pressure ratio found in the combustion zone, $|p_{1,h}|/p_m = 0.0861$. Also, as expected, setting $\theta_{pq} = 180^\circ$ so that the acoustic pressure and heat release oscillations are out of phase reduces the acoustic power output to $\dot{E}_L = 21.5$ W and lowers the efficiency to $\eta_{II} = 17.8\%$.

As shown in Figure 6.11, the acoustic power output and second law efficiency each vary with the cosine of the phase shift, and linearly with the amplitude, α. This shows that the addition of the volumetric velocity source from pulse combustion does not

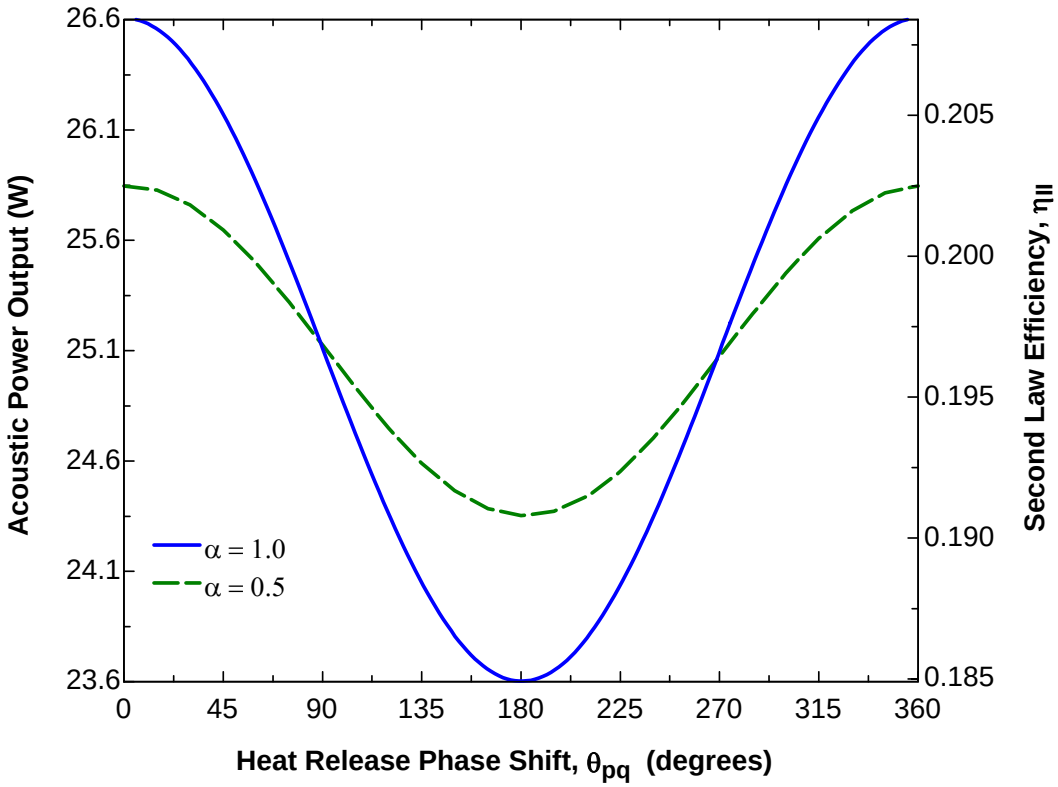

Figure 6.11: Influence of pulse combustion amplitude and phase shift on the acoustic power output and second law efficiency for the optimized TAPCE configuration.

affect the processes occurring in the remainder of the engine, with the exception of a slight increase in the viscous dissipation along the walls of the combustion zone.

Although the pulse combustion model used in this study is fairly simple, it qualitatively describes the primary effect of the pulse combustion process on the output of the thermoacoustic engine. Given the small (and very optimistic) power output gains that result, time spent doing more detailed models of the pulse combustion process would probably be better spent modeling the regenerator or other sources of loss in the engine.

6.4 Comparison with Competing Technologies

In order to evaluate the feasibility of the open cycle TAPCE design, its thermal efficiencies and acoustic power output should be compared to corresponding performance parameters in closed cycle thermoacoustic engines. Since the goal of the TAPCE is to convert fuel energy into acoustic energy, the closed cycle engines should also be evaluated based on the acoustic power output that they can derive from a similar input fuel stream.

There are two basic methods that can be used to transfer the chemical energy in the fuel into a closed cycle thermoacoustic engine. The first method involves the generation of electrical energy from the fuel, and then converting this electrical energy back into thermal energy in the closed cycle engine using, e.g., an electric resistance heater. While this method is certainly convenient from the end-user's standpoint, the conversion to electrical energy, transmission and conversion back to thermal energy is much less efficient than direct use of the thermal energy. The TASHE device created by Backhaus and Swift (2000) has achieved a thermal efficiency of 30%, which corresponds to a 42% second law efficiency. Since the TASHE uses an electric hot heat exchanger,

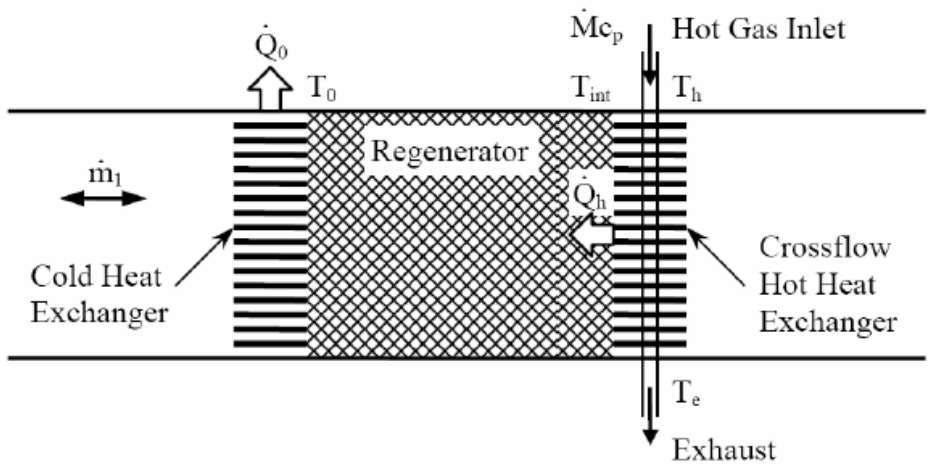

Figure 6.12: Schematic of a closed cycle traveling wave thermoacoustic engine using a crossflow hot heat exchanger.

these efficiency numbers are based on the conversion of electric power into acoustic power, and do not account for the efficiency of the generation of electric power from the fuel. As a result, the efficiency of the TASHE and other thermoacoustic engines utilizing electric hot heat exchangers cannot be directly compared to the efficiency of the TAPCE.

The second method for transferring fuel energy into a thermoacoustic engine involves the use of a combustion chamber and a hot heat exchanger to transfer the thermal energy in the hot combustion products into the thermoacoustic engine. The performance obtained with this method will be analyzed and compared to that provided by the TAPCE in the following sections.

6.4.1 Crossflow hot heat exchanger

A crossflow heat exchanger, as depicted in Figure 6.12, provides a practical means for transferring the heat from the hot stream of gas to a thermoacoustic engine because all of the heat transfer generally must occur over an acoustic displacement

length, which is normally much smaller than the diameter of the engine. However, the design of a crossflow heat exchanger will not allow all of the heat in the hot gas stream to be transferred into the engine, since the directionality of heat transfer requires that heat exchanger exhaust temperature be greater than the hot regenerator interface temperature, i.e. $T_e \geq T_{int}$.

Since high exhaust temperatures imply that a small fraction of the thermal energy in the hot gas is transferred to the engine, and low exhaust temperatures result in a low temperature difference and acoustic energy gain across the regenerator, it has been shown that an optimal temperature $T_{int} = (T_0 T_h)^{1/2}$ exists that maximizes the acoustic power output of a closed cycle thermoacoustic engine [Weiland and Zinn (2004a)]. In this case, the maximum power output differs from the maximum power output from an ideal open cycle thermoacoustic engine by a factor, ε, which is the effectiveness of the heat exchanger [Incropera and DeWitt (1996)], where the effectiveness is defined as the heat transfer of the heat exchanger divided by the maximum possible heat transfer for the temperatures and flow conditions involved. Since this maximum possible heat transfer is generally only possible in an infinitely long counterflow heat exchanger, it follows that $\varepsilon < 1$ for a practical crossflow heat exchanger configuration.

Consequently, an ideal open cycle thermoacoustic engine holds an advantage over the closed cycle thermoacoustic engine using a crossflow heat exchanger, as the ineffectiveness of the crossflow heat exchanger can be eliminated. In fact, a good analogy can be made between the two cases, where the heat transfer across the temperature difference at the regenerator/hot duct interface in an open cycle

thermoacoustic engine can be likened to the heat transfer across the temperature difference between the hot gas in the heat exchanger and the regenerator interface.

Recall from the energy flux analysis in Chapter 4 that the thermal energy convected into the regenerator at the temperature T_{int} in an open cycle thermoacoustic engine is essentially wasted, as it is converted to conduction and entropy flux losses in passing through the regenerator. To extend the analogy between the open cycle engine and the closed cycle engine with a crossflow heat exchanger, this convective energy loss is analogous to venting the exhaust gas leaving the crossflow heat exchanger to the atmosphere, as it still carries useful thermal energy at the temperature T_e. In each case, however, the efficiency of the overall cycle can be improved by recovering these thermal energy losses, generally by preheating the combustion reactants.

6.4.2 Reactant preheating efficiency

The reactant preheating process in the crossflow heat exchanger case can be very efficient, as there are no restrictions on the type of heat exchanger used to preheat the reactants, other than size and cost, and nearly all of the exhaust heat exiting the crossflow heat exchanger could be transferred to the reactants.

The reactant preheating case in the TAPCE is a similar situation, though the reactant preheating efficiency is now limited by the constraints of the regenerator and inlet piping system. The preheating efficiency of the TAPCE can be defined as:

$$\eta_{ph} = \frac{\left(\dot{M}c_p\right)_{rx}\left(T_{ph} - T_0\right)}{-\left(\dot{M}c_p\right)_{pr}\left(T_{int} - T_0\right)} = -M\,\frac{T_{ph} - T_0}{T_{int} - T_0}, \tag{6.5}$$

where M, as defined in Eq. (4.93), is negative according to the mass flux sign conventions in this study.

In the base TAPCE configuration, the preheating efficiency of Eq. (6.5) is about η_{ph} = 57.6%, and improves to η_{ph} = 64.0% in the optimized TAPCE configuration. However, this still falls well short of the efficiency that would be possible in, e.g., a counterflow heat exchanger, which could easily reach efficiencies in excess of 90% depending on the size and cost constraints of the heat exchanger [Incropera and DeWitt (1996)]. Therefore, in evaluating the overall efficiency of the TAPCE, the benefits of removing the ineffectiveness of the crossflow hot heat exchanger must then be weighed against the inefficiency of its reactant preheating process.

6.4.3 The Natural Gas Liquefier

To date, the only thermoacoustic system that approximates the architecture of the closed cycle thermoacoustic engine with a crossflow hot heat exchanger and a reactant preheating system is the 350 gallon per day natural gas liquefier, discussed in Chapter 3 [Arman et. al. (2004), Wollan et. al. (2002)]. In the latest version of this device, transfer of heat from the combustor to the engine is carried out with a separate, high pressure and temperature helium heat transfer loop, which is driven by a blower located on top of the device, as shown in Figure 3.6 [Arman et. al. (2004)].

The 350-gallon per day natural gas liquefier does not include a flue gas recuperator for preheating the combustion reactants, and much of the thermal energy in the fuel is exhausted to the atmosphere. As a result, the burner, heat transfer loop and thermoacoustic engine combine to convert fuel energy to acoustic energy with an approximate thermal efficiency of only 9%. Consequently, the system needs to burn about 55% of the input methane stream in order to generate the 34 kW of acoustic energy

needed to liquefy the remaining 45% in the thermoacoustic refrigerator [Arman et. al. (2004)].

If a recuperator were added to the system, it is estimated that about 85% of the fuel energy could be transferred into the thermoacoustic engine, yielding a combined fuel to acoustic conversion efficiency of about 25%. This scenario is expected to burn about 30% of the input methane stream to liquefy the remaining 70% [Arman et. al. (2004)].

If the fuel energy delivery system (combustor and heat transfer loop) to the thermoacoustic engine is about 85% efficient, then the thermal efficiency of the thermoacoustic engine alone is about 29%, which is consistent with the 30% thermal efficiencies reported for the TASHE [Backhaus and Swift (2000)]. Furthermore, a thermoacoustic efficiency of roughly 29% means that only about 30% of the input fuel energy is transferred into the thermoacoustic engine in the absence of a recuperator, which underscores the importance of using the crossflow heat exchanger exhaust to preheat the incoming reactants.

6.4.4 Efficiency and power output comparisons

Table 6.4 summarizes the results of this study by comparing the thermal efficiencies and acoustic power outputs of the TAPCE model to those of the TASHE and the natural gas liquefier engine. Overall, the lumped parameter modeling and optimization of the TAPCE device show that its predicted efficiency of about 20-25% for low mean pressures is roughly the same as that of the natural gas liquefier using a flue gas recuperator, which is about 25% efficient at converting fuel energy into acoustic energy [Arman et. al. (2004)]. Noting that the model developed in this study does not

Table 6.4: Thermal efficiency and acoustic power output comparisons

	TAPCE Model							Liquefier Engine		TASHE	
	Base configuration			Optimized configuration				With recuperator	Without recuperator	Most efficient	Most powerful
Working fluid	Air Φ=0.5	Air Φ=1.0	Air Φ=0.5	Air Φ=0.5	Air Φ=0.5	Air Φ=0.5	Air Φ=0.5	Helium	Helium	Helium	Helium
Acoustic pressure ratio	10%	10%	20%	10%	10%	10%	10%	7%	7%	6%	10%
Mean pressure (atm)	1.2	1.2	1.2	1.2	1.2	3.8	30	30	30	30	30
Condensation	No	No	No	No	No	No	Yes	--	--	--	--
Pulse combustion	None	None	None	None	$\alpha = 1$ $\theta_{pq} = 0$	$\alpha = 1$ $\theta_{pq} = 0$	None	--	--	--	--
Thermal efficiency	16.6%	18.3%	24.8%	20.2%	21.4%	28.8%	41%	25%	9%	30%	22%
Acoustic power output (W)	21.5	22.5	72.5	25.1	26.6	77.3	550	34,000	34,000	710	890

account for all of the loss mechanisms in the TAPCE, however, its actual thermal efficiencies should be somewhat lower than those shown in Table 6.4.

It is evident from Table 6.4 that the largest shortcoming of the TAPCE design is its acoustic power output. The power output of the TAPCE cannot be directly compared to that of the liquefier engine, since the scale of the liquefier engine, as shown in Figure 3.6, is much larger than that of the TAPCE. However, note that the physical size of the TAPCE is very similar to that of the TASHE, thus their acoustic power outputs can be readily compared.

As noted earlier, the low mean pressures used in the TAPCE are the primary reason for its lower acoustic power output, as they are limited by the need to keep the water vapor from condensing out of the combustion products and fouling the regenerator with liquid. The maximum non-condensing mean pressure in the TAPCE can be increased by increasing the cold heat exchanger temperature, decreasing the equivalence ratio, or changing the fuel type, though these adjustments still only allow for maximum pressures between 3 and 8 atmospheres according to Figures 3.4 and 3.5 . As shown in Table 6.4, the acoustic power output of the optimized TAPCE engine at $p_m \approx 1.2$ atm is about 27 W, while even at an elevated pressures of $p_m \approx 3.8$ atm (the maximum non-condensing pressure for methane at $\Phi = 0.5$ and $T_c = 350$ K), the power output of the TAPCE is only about 77 W. This pales in comparison to the TASHE, which generates a maximum acoustic power output of 890 W using helium at a mean pressure of 30 atm [Backhaus and Swift (2000)].

If the product condensation constraint on the TAPCE could be removed or eliminated, then the device could be more highly pressurized and could begin to approach

the power densities seen in the TASHE and similar devices. For instance, if some means is devised to keep water from condensing on the screens at the cold side of the regenerator, possibly by wicking it away or reorienting the regenerator to allow gravity to carry the liquid water away, then the TAPCE can operate at much higher mean pressures. As Table 6.4 shows, operation of the TAPCE at a mean pressure of 30 atmospheres can increase its power output to about 550 W, though this is still lower than the power outputs achieved by the TASHE. This is to be expected, however, since the acoustic power density in a thermoacoustic device is generally proportional to the speed of sound in its working fluid [Swift (2002)], and the speed of sound in air, which is the primary component in the working fluid of the TAPCE, is about 2.5 times lower than the speed of sound in helium, which is used in the TASHE.

Table 6.4 indicates that there are several strategies for further increasing the acoustic power output of the TAPCE. For example, calculations performed with the base configuration model show that increasing the equivalence ratio from $\Phi = 0.5$ to $\Phi = 1.0$ yields an increase in the acoustic power output, primarily due to an increase in the combustion temperature for higher equivalence ratios. Though the increase in acoustic power seems to be small in this case, optimization of the regenerator/open duct interface temperature should yield more significant power output gains for higher equivalence ratios.

In addition to the equivalence ratio effect, the pulse combustion process is shown to add about 6% to the engine's acoustic power output for an acoustic pressure amplitude of 10%, according to Table 6.4. Although this effect is not very large, it should be noted that an improperly phased pulse combustion process could act as an acoustic energy loss

mechanism, thus some attention must be paid to controlling the phasing of the pulse combustion process. It is noteworthy from Eq. (4.46), however, that the effect of pulse combustion scales linearly with the acoustic pressure ratio in the engine, thus the potential benefits of adding pulse combustion to a thermoacoustic engine increase as its design acoustic pressure amplitude increases.

Since the acoustic power is generally proportional to the square of the acoustic pressure ratio, increasing this pressure ratio can have a large impact on the acoustic power output in the engine, independent of the pulse combustion effects, as shown for the TAPCE base configuration in Table 6.4. These results show that increasing the acoustic pressure ratio from 10% to 20% can increase the power output from about 22 W to 72 W, though the values obtained for the latter case contain a large amount of error, since the TAPCE model does not account for loss mechanisms that are prevalent at these higher acoustic pressure ratios. Similar to the trend displayed in Table 6.4 for the TASHE device, the thermal efficiency is therefore expected to decrease for higher acoustic pressure ratios instead of increase, as predicted by the TAPCE model results.

One simple means for increasing the acoustic power output of the TAPCE that is not shown in Table 6.4, is to increase the engine's diameter, since the acoustic power that flows through a pipe is proportional to the pipe's cross-sectional area. In addition, reducing the effect of the conduction losses in the TAPCE would help increase the acoustic power output at both high and low pressures, since these losses are the primary contributor to the engine's inefficiency. For example, the axial thermal conduction through the regenerator could be reduced by altering its composition. The use of stacked wire mesh screens is already very useful in reducing the axial conduction due to the

intermittent contact between the screens, though this could easily be taken a step further by alternating wire mesh screens with screens of a lower thermal conductivity, such as fiberglass or plastic, depending on their melting points and availability in appropriate mesh sizes.

Given the number of options that exist for improving its acoustic power output, the TAPCE design should be able to produce comparable power outputs to the TASHE. If the product condensation, mean pressure and conduction loss issues are properly addressed, then a high-pressure TAPCE device would provide an efficient alternative to the traditional closed cycle thermoacoustic engine. Even if these issues are not addressed, the TAPCE does have several other noteworthy characteristics that enhance its attractiveness and viability. For instance, one nice feature of the TAPCE is that the burner and reactant preheating system are all integrated into the engine, thus reducing its overall size, complexity and cost. Consequently, the burner, crossflow hot heat exchanger, and flue gas recuperator in a closed cycle engine can be replaced by the combustion zone and the reactant preheating pipes in the TAPCE. This compact design also confines the heat addition process to the engine, thus minimizing heat losses that are more likely to occur whan external combustor and heat transfer apparatus are used. In addition, the removal of the hot heat exchanger from the engine eliminates the thermal stresses induced on the engine by this component, which is a significant maintenance and reliability issue in the 350 gallon per day natural gas liquefier [Wollan et. al. (2002)].

These reductions in complexity are particularly attractive when compared to the natural gas liquefier, where the heat transfer situation is further complicated by a separate, high pressure and temperature helium heat transfer loop that is used to transfer

heat from the combustor to the engine [Arman et. al. (2004)]. Depending on the configuration, this separate heat transfer loop adds at least one more heat exchanger to the system. As shown in a photo of the natural gas liquefier in Figure 3.6, the combustor and helium heat transfer loop add a significant amount of hardware to the top of the thermoacoustic engine, which is located within the machined cone at the top of the long vertical waveguide. Note that although this system was originally designed to also include a flue gas recuperator, it was not incorporated into the as-built system of Figure 3.6, meaning that the inclusion of this component will require additional hardware beyond what can already be seen in Figure 3.6 [Arman et. al. (2004)].

In addition to its compactness, the TAPCE is composed primarily of pipes, insulation, and wire mesh screens, with the acoustically transparent barrier being the only moving part inside the engine. Consequently, the TAPCE offers a very simple and compact means of driving a traveling wave thermoacoustic engine with a stream of gaseous fuel, thus the TAPCE would be well suited to applications where size, weight, cost, simplicity, or reliability are of prime importance.

In particular, the TAPCE would work well in light-weight portable electric power or portable cooling applications, where a small disposable or reusable canister of liquid fuel, such as propane or butane, could be used to power the device. To further simplify the TAPCE engine in such a device, flapper valves or asymmetric jet pumps could be added to the inlet and exhaust ports to create a self-breathing engine that operates at atmospheric pressure, similar to the operation of many pulse combustor devices [Zinn (1996)]. The modeling efforts above show that the thermal efficiency of the TAPCE at near-atmospheric pressures is about 20%, which is generally adequate for the types of

portable cooling and electric power devices that would be considered in these applications.

Furthermore, while the TAPCE may not be ideally suited to the high-power natural gas liquefaction application due to a lower acoustic power density, it does offer substantial simplifications in the hardware required, and therefore deserves some further consideration for this application. In addition, the TAPCE design should yield increased acoustic power densities and fuel to acoustic power conversion efficiencies when compared to the tunable pulse combustors used to enhance industrial processes by adding acoustic energy to a reaction chamber [Zinn (1996)]. As a result, the TAPCE could offer a reduction in both the fuel input and physical space required to drive acoustic oscillations of a certain magnitude in these reactors, thus the application of the TAPCE to industrial process applications deserves further consideration as well.

CHAPTER 7

CONCLUSIONS

This feasibility study shows that an open cycle thermoacoustic engine that incorporates an internal pulse combustion process is a viable concept, as it is fairly efficient at converting fuel energy to acoustic energy. In fact, the engine's feasibility and efficiency are enhanced by the use of internal combustion, since the reactant preheating mechanism employed in the TAPCE recovers much of the thermal energy input convected into the engine's regenerator, which would otherwise be converted into conduction and imperfect entropy flux losses in the regenerator [Weiland and Zinn (2004a)].

The design of the TAPCE is very simple and compact, which, in combination with its excellent thermal efficiency and respectable power output, makes the device very attractive for a variety of applications. Having established the feasibility and usefulness of the concept, the most obvious step in the continued development of the TAPCE is experimentation. In particular, the theories developed to describe the processes occurring within the regenerator and at the regenerator interface of an open cycle traveling wave thermoacoustic engine need to be verified. Additionally, the details of the mean and oscillating combustion processes that occur in the engine need to be resolved, where

issues related to the reactant injection configuration, ignition, flameholding and pulse combustion phase control need to be addressed.

The lumped parameter model developed in this study should provide a good starting point for the geometry of an experimental TAPCE device, while the theory and feasibility analysis presented here can guide the design and analysis of a practical, efficient open cycle thermoacoustic engine. In particular, this analysis shows that water vapor condensation from the combustion products poses a significant challenge to the design of a useful engine, since efficient operation of the regenerator requires that it remain free of liquid. Future experimental studies should concentrate on finding an acceptable solution to this problem, which would allow for the use of higher mean pressures and higher acoustic power densities in the engine. In addition, thermal conduction through the regenerator has been identified as a major source of irreversibility in the TAPCE device, therefore future studies should investigate the possibility of redesigning the regenerator to help reduce these losses. Finally, the acoustic power output of the engine and the ability of the pulse combustion process to contribute to this power output both increase as the acoustic pressure ratio increases. In order to produce more powerful and more efficient thermoacoustic engines that operate at these pressure ratios, future theoretical and experimental studies are required to better understand the nonlinear processes occurring in this high pressure amplitude regime.

APPENDIX A

This appendix contains the Engineering Equation Solver computer code for the base geometry lumped parameter model of the TAPCE, including the main program, its subprograms, and the base model solution.

```
{The Base TAPCE Model - Nate Weiland}


{! Important Control Parameter Sets}
"Mean mass flux ultimately controls the acoustic pressure ratio, among other things"
{Prat_c = 0.1            "Ratio of P_c to mean pressure (using P_c as reference phasor)"}
Prat_h = 0.0869          "Ratio of P_h to mean pressure (using P_h as reference phasor)"
{Prat_h_i = 0}
{m_dot_0 = 0.00009108       "[kg/s] - mean flow rate into regen hot side, with all losses"}
{m_dot_0_i = 0}

"Operating frequency is determined by coupling to resonator, tau is controlled by the acoustic
        load resistance"
tau = 2.59               "Temperature ratio across regenerator"
{T_reh = 765}
{T_reh_i = 0}
R_L_i = 0
{tau_i = 0}
{R_L = 496953            "Acoustic resistance (no load branch for R_L = infinity)" }
{omega = 528.5           "[rad/s] - angular frequency"}
omega_i = 0

"Determination of phi, T_c or P_0 to avoid combustion product condensation"
T_0 = 300                "[K] - ambient temperature"
{T_0_i = 0}
T_c = 325                "[K] - cold heat exchanger temperature"
{T_c_i = 0}
{P_0 = 3.103E+05         "[Pa] - TASHE Operating Pressure"}
{P_0_i = 0}
phi = 0.5                "equivalence ratio"
{phi_i = 0}
P_sat = pressure(STEAM, T=T_c, X = 1)
X_H2O = 2*phi/(phi+2*4.76)          "mole fraction of water vapor in combustion products"
X_H2O = P_sat/(P_0*1.1)

"!Calculation of Temperature Profile stats"
Call GenTProfiles(M, Xi, N, x_re, T_0, T_c, T_reh : T_ph, dTredx_0, dTredx_L)
T_ph_i = 0;  dTredx_0_i = 0;  dTredx_L_i = 0;

"! Energy Balance at hot-side regenerator interface"
m_dot_0*cp_reh*(T_h - T_reh) = P_h*U_h_r/2 - Q_dot_mesh_L - Q_dot_wall_L - Q_dot_psi_L
        "including conduction losses and imperfect heat transfer losses"

{! Acoustic Regenerator Integrations (from hot to cold)}
U_hr = real(U_h);   U_hi = -i*imag(U_h)
CALL PreheatIntBackT(M, Xi, N, x_re, T_0, T_c, T_reh, R_c1, R_c2, omegaC, b_mu, P_h, U_hr,
        U_hi : P_c, P_ci, U_c, U_ci)
P_ci_i = 0;  P_c_i = P_ci;  U_ci_i = 0;  U_c_i = U_ci

"! Pulse Combustion Source"
alpha = 0                "dimensionless magnitude factor,  0 <= alpha <= 1"
theta_pq = 0             "phase shift between P_h and Q_dot_1"
Q_dot_1 = alpha*Q_dot_fuel*exp(i*theta_pq)"oscillating heat release"
U_Q1 = (gamma - 1)/gamma/P_0*Q_dot_1 "volumetric velocity source of pulse combustion"
```

```
"! Air properties"
"Gas properties in the engine (except at the regenerator)"
T_air = 325                          "temperature of gas in remainder of the engine"
mu = viscosity(AIR,T=T_air)          "[kg/m s]"
k = conductivity(AIR,T=T_air)                "[W/m K]"
Cp = cp(AIR,T=T_air)                 "[J/kg K]"
gamma = Cp/cv(AIR,T=T_air)           "ratio of specific heats"
rho = density(AIR,T=T_air,P=P_0)     "[kg/m^3]"
a = soundspeed(AIR,T=T_air)          "[m/s] - speed of sound"
freq = omega/2/pi                    "[Hz] - Operating frequency"
lambda = a/freq                      "[m] - acoustic wavelength"

"Penetration depth calculations"
delta_v = (2*mu/omega/rho)^0.5               "[m] - viscous penetration depth"
delta_k = (2*k/omega/rho/Cp)^0.5             "[m] - thermal penetration depth"


"! Ambient Reactant Inlet gas properties"
rho_rx0 = density(AIR, T = T_0, P = (P_m_s + P_m_rh)/2)
delta_v_rx0 = (2*mu/omega/rho_rx0)^0.5    "viscous penetration depth at cold end of regen"

"Average Reactant Inlet gas properties"
T_rx_ave = (T_ph + T_0)/2
rho_rx = density(AIR, T = T_rx_ave, P = P_0)
cp_rx = cp(AIR, T = T_rx_ave)
mu_rx = viscosity(AIR, T = T_rx_ave)
Pr_rx = prandtl(AIR, T = T_rx_ave)
delta_v_ph = (2*mu_rx/omega/rho_rx)^0.5  "viscous penetration depth at cold end of regen"


"! Combustion Gas Properties"
Call MethaneT_ad(T_ph, T_h, phi, M_mix)  "returns T_h or phi, plus combustion gas molecular
        weight"
T_h_i = 0;  M_mix_i = 0
R = R#*1000/M_mix            "[J/kg K] - Gas constant"
rho_0 = P_0/T_c/R            "density of cold combustion products"

T_reh = T_c*tau              "[K] - temperature at hot end of regenerator"
T_ave = (T_reh + T_c)/2      "[K] - average regenerator temp for evaluating conductivity"

CALL ProductAveCp(T_c, T_reh, phi : cp_re)"ave. comb. gas cp within regenerator"
CALL ProductAveCp(T_reh, T_h, phi : cp_reh)"ave. comb. gas cp across regenerator interface"
CALL ProductAveCp(T_0, T_h, phi : cp_tot)"ave. comb. gas cp across total temperature range"
CALL ProductAveCp(T_0, T_reh, phi : cp_reh0)"ave. comb. gas cp between T_reh and T_0"
Call ProductAveCp(T_0, T_c, phi : cp_c0)   "ave. comb. gas cp between T_c and T_0"
CALL ProductCp(T_c, phi : cp_0)            "comb. gas cp at regen cold end"
cp_re_i = 0;  cp_reh_i = 0;  cp_tot_i = 0;  cp_reh0_i = 0;  cp_c0_i = 0;  cp_0_i = 0;

Call ProductViscFit(T_c, T_reh, phi : mu_0, b_mu) "combustion gas viscosity power law curve fit
        vs. T"
mu_0_i = 0;  b_mu_i = 0;
mu_m = mu_0*(T_ave/T_c)^b_mu          "viscosity of combustion gas in regenerator, at
        T_ave"
```

```
Call ProductCondFit(T_c, T_reh, phi : k_0, b_k)"combustion gas conductivity power law curve fit
      vs. T (only good to T_reh = 1400 K)"
k_0_i = 0;  b_k_i = 0;
k_m = k_0*(T_ave/T_c)^b_k          "thermal conductivity of combustion gas in regenerator, at
      T_ave"

Pr_m = cp_re*mu_m/k_m              "Prandtl Number of combustion gas in regenerator, at T_ave"
Pr_0 = cp_0*mu_0/k_0               "Prandtl Number of combustion gas in regenerator, at T_0"
delta_k_0 = (2*k_0/omega/rho_0/cp_0)^0.5 "thermal penetration depth at cold end of regen"
delta_k_L = delta_k_0*(T_reh/T_c)^((b_k + 1)/2)"thermal penetration depth at hot end of regen"
delta_v_0 = (2*mu_0/omega/rho_0)^0.5     "viscous penetration depth at cold end of regen"
c_0 = sqrt(cp_0*R*T_c/(cp_0 - R))        "speed of sound in cold combustion gas"


{Engine Components}

"! Regenerator"
"Geometry"
D_re = 0.0762                  "[m] - regenerator diameter (3 inches)"
A_re = pi*D_re^2/4             "[m^2] - regenerator area"
x_re = 0.040
{x_re_i = 0}
t_wall = 0.0005                    "[m] - inner pipe thickness"
t_pad = 0.0152                 "insulation thickness"
psi = 0.72                     "regenerator volume porosity (ratio of gas volume to total volume)"
D_wire = 4*r_h_re*(1-psi)/psi*1000  "[mm] - diameter of wire in regenerator wire mesh screens"
n_mesh = 4*(1-psi)/pi/D_wire               "[wire/mm] - wire mesh number"

"Check length scale ratios and viscosity correlations"
rh_dk0 = 0.3162                "r_h_re/delta_k_0, sets r_h_re for given operating
      conditions"
rh_dk0 = r_h_re/delta_k_0      "should be about 0.3 or less"
rh_dkL = r_h_re/delta_k_L      "should be about 0.1"
rh_x1 = r_h_re/magnitude(U_c)*A_re*psi*omega"checks that |x_1| >> r_h_re, OK if <<1"
c_psi_1 = 1268 - 3545*psi + 2544*psi^2     "1st regenerator viscosity coefficient curve fit (Swift &
      Ward Eq. A1)"
c_psi_2 = -2.82 + 10.7*psi - 8.6*psi^2     "2nd regenerator viscosity coefficient curve fit (S & W
      Eq. A2)"
Re_1 = 4*magnitude(m_dot_1)*r_h_re/A_re/psi/mu_m      "Acoustic Reynolds Number"

"Regen resistance and compliance"
R_c1 = x_re*mu_0/r_h_re^2/A_re*c_psi_1/psi/8"[kg/m^4 s] - cold regenerator resistance"
R_c2 = 4*x_re*magnitude(m_dot_1)*c_psi_2/3/pi/r_h_re/A_re^2/psi^2          "[kg/m^4 s] -
      Reynolds Number regenerator resistance"
R_0 = R_c1 + R_c2
C_re = psi*A_re*x_re/P_0               "[m^4 s^2/kg] - regenerator compliance"
omegaC = C_re*omega                    "used in pressure and velocity integrations"

"Mean pressure difference"
Re_re_m = 4*r_h_re*m_dot_0/mu_m/A_re/psi      "Reynolds number of mean mass flux in
      regen"
dP_M = mu_m*R*T_ave*x_re*m_dot_0/8/r_h_re^2/P_0/A_re/psi*(c_psi_1 + c_psi_2*Re_re_m)
      "pressure difference due to mean flow, from Swift and Ward"
dP_m0 = (magnitude(P_c)^2-magnitude(P_h)^2)/4/P_0    "pressure difference for m_dot_0 = 0,
      Waxler Eq. 33"
P_0 - P_m_c = dP_M + dP_m0      "total mean pressure drop across regenerator"
```

```
"! Combustion Zone"
x_cz = 0.1226                    "[m] - length of combustion zone"
r_h_cz = D_re/4                  "[m] - combustion zone hydraulic radius"

f_v_cz = (1-i)*delta_v/2/r_h_cz                  "viscosity thermoviscous function"
f_k_cz = (1-i)*delta_k/2/r_h_cz                  "thermal thermoviscous function"
Z_Lm = i*omega*x_cz*rho/A_re/(1 - f_v_cz)"inertance and visc. resistance"
1/Z_Cm = i*omega*x_cz*A_re/gamma/P_0*(1+(gamma-1)*f_k_cz)         "compliance & th.
        resistance"

"! Compliance"
D_c = 0.1282          "[m] - compliance diameter (5 inches)"
A_c = pi*D_c^2/4      "[m^2] - compliance area"
x_c = 0.0580          "[m] - compliance length"
r_h_c = D_c/4         "[m] - compliance hydraulic radius (could be lower, = V/A_surf)"

f_k_c = (1-i)*delta_k/2/r_h_c                    "thermal thermoviscous function"
1/Z_C1 = i*omega*x_c*A_c/gamma/P_0*(1+(gamma-1)*f_k_c)    "compliance and th. resistance"

"! Inertance"
x_l = 0.1926                                     "[m] - inertance length"
A_l = A_c - pi/4*(D_re + 2*(t_wall + t_pad))^2       "[m^2] - inertance area"
r_h_l = A_l/pi/(D_c + D_re + 2*(t_wall + t_pad))"[m] - inertance hydraulic radius"

f_v_l = (1-i)*delta_v/2/r_h_l                    "viscosity thermoviscous function"
f_k_l = (1-i)*delta_k/2/r_h_l                    "thermal thermoviscous function"
Z_LL = i*omega*x_l*rho/A_l/(1 - f_v_l)           "inertance and visc. resistance"
1/Z_CL = i*omega*A_l*x_l/gamma/P_0*(1+(gamma-1)*f_k_l)      "compliance & th. resistance"

"! Exhaust Port(s)"
x_e = 0.1             "[m] - pipe length"
D_e = 0.001           "[m] - pipe diameter"
A_e = pi*D_e^2/4      "[m^2] - pipe area"
r_h_e = D_e/4         "pipe hydraulic radius"
n_e = 1         "number of exhaust ports"

f_v_e = (1-i)*delta_v_0/2/r_h_e                  "viscosity thermoviscous function"
Z_e = omega*rho_0*(i*x_e/A_e/(1 - f_v_e) + i*3.4/pi/D_e + omega/2/pi/c_0)       "Exhaust port
        impedance"

Re_e = 4*m_dot_0/n_e/pi/mu_0/D_e         "Reynolds Number in an exhaust pipe"
f_M_e = 0.3164/Re_e^0.25                 "friction factor in a smooth exhaust pipe, valid for
        Re_e < 10^5"
P_m_c - P_m_e = f_M_e*x_e/2/D_e*(m_dot_0/n_e/A_e)^2/rho_0 "exhaust pipe mean pressure
        drop"
m_dot_e_rat = m_dot_0/n_e/rho_0/magnitude(U_e)         "ratio of mean to acoustic mass flux in
        exhaust pipe"

"! Inlet Preheat Ports"
x_ph = 0.10           "preheat pipe length"
D_ph = 0.0005              "individual preheat pipe diameter"
{D_ph_i = 0}
A_ph = pi*D_ph^2/4    "pipe area"
r_h_ph = D_ph/4       "pipe hydraulic radius"
n_ph = 7              "number of preheat pipes passing through the regenerator"
```

```
f_v_ph = (1-i)*delta_v_ph/2/r_h_ph            "viscosity thermoviscous function"
Z_ph = i*omega*rho_rx*x_ph/A_ph/(1 - f_v_ph)"single inlet port impedance"

Re_ph = 4*m_dot_0/pi/D_ph/n_ph/mu_rx    "Reynolds Number for an individual preheat pipe"
f_M_ph = 0.3164/Re_ph^0.25              "friction factor in a smooth preheat pipe, valid for
        Re_ph < 10^5"
P_m_rh - P_0 = f_M_ph*x_ph/2/D_ph*(m_dot_0/n_ph/A_ph)^2/rho_rx     "preheat pipe mean
        pressure drop"

"! Inlet Reactant Header"
x_rh = 0.200          "reactant header pipe length"
D_rh = 0.002          "header pipe diameter"
A_rh = pi*D_rh^2/4    "pipe area"
r_h_rh = D_rh/4       "pipe hydraulic radius"

f_v_rh = (1-i)*delta_v_rx0/2/r_h_rh           "viscosity thermoviscous function"
Z_rh = omega*rho_rx0*(i*x_rh/A_rh/(1 - f_v_rh) + omega/2/pi/a)   "reactant header impedance"

Re_rh = 4*m_dot_0/pi/D_rh/mu                  "Reynolds Number for reactant header pipe"
f_M_rh = 0.3164/Re_rh^0.25                    "friction factor in a smooth reactant header, valid for
        Re_rh < 10^5"
P_m_s - P_m_rh = f_M_rh*x_rh/2/D_rh*(m_dot_0/A_rh)^2/rho_rx0         "reactant header pipe
        mean pressure drop"

"! Resonator inertance"
D_Lr = 0.0834                 [m]     "diameter"
A_Lr = pi*D_Lr^2/4            "[m^2] - area"
r_h_Lr = D_Lr/4                       "[m] - hydraulic diameter"
f_v_Lr = (1-i)*delta_v/2/r_h_Lr               "boundary layer viscous thermoviscous function"
f_k_Lr = (1-i)*delta_k/2/r_h_Lr               "boundary layer thermal thermoviscous function"

{Pre-load Resonator Inertance}
x_Lr1 = 0.357                         "location of load branch in resonator inertance"
Z_Lr1 = i*omega*rho*x_Lr1/A_Lr/(1 - f_v_Lr)         "inertance and visc. resistance"
1/Z_CLr1 = i*omega*x_Lr1*A_Lr/gamma/P_0*(1+(gamma-1)*f_k_Lr)      "compliance and th.
        resistance"

{Post-load Resonator Inertance}
x_Lr2 = 0.405                         "length of resonator inertance after load branch"
Z_Lr2 = i*omega*rho*x_Lr2/A_Lr/(1-f_v_Lr) "inertance and visc. resistance"
1/Z_CLr2 = i*omega*x_Lr2*A_Lr/gamma/P_0*(1+(gamma-1)*f_k_Lr)      "compliance and th.
        resistance"

"! Resonator Compliance"
D_Cr = 0.203                  "diameter (8 inches)"
x_Cr = 0.345                  "[m] - length"
V_Cr = x_Cr*pi*D_Cr^2/4       "volume"
r_h_Cr = D_Cr/4               "[m] - hydraulic diameter"

f_k_Cr = (1-i)*delta_k/2/r_h_Cr                     "boundary layer thermoviscous function"
1/Z_Cres = i*omega*V_Cr/gamma/P_0*(1+(gamma-1)*f_k_Cr)    "compliance and th. resistance"

"Total length of engine and resonator"
x_tot = x_Cr + x_Lr2 + x_Lr1 + x_l + x_c
```

```
"!Engine Acoustics"
{Acoustic Amplitude}
P_h = Prat_h*P_0                    "[Pa] - Reference acoustic pressure"
Prat_c = magnitude(P_c)/P_0             "Acoustic pressure ratio"
Prat_c_sq = Prat_c^2

{Engine Component Models}
P_j = Z_LL*U_fb + P_c               "Main Inertance"
U_CL = P_c/Z_CL                     "Compliance of inertance"
U_C1 = P_c/Z_C1                     "Main compliance"
U_Cm = P_h/Z_Cm                     "combustion zone compliance"
P_h = Z_Lm*U_cz + P_j               "combustion zone inertance"
U_e = P_c/Z_e                       "Inertance and resistance of an exhaust port"
P_h = Z_ph*U_ph + P_ph              "Inertance and resistance of an inlet preheat pipe"
P_ph = Z_rh*U_rh                    "Inertance and resistance of the reactant header"

{Resonator Component Models}
U_CLr1 = P_j/Z_CLr1                 "Compliance of resonator inertance before load"
P_j = Z_Lr1*U_Lr1 + P_Lr            "Resonator inertance and visc. resistance before load"
P_Lr = U_L*R_L                      "Acoustic Load resistance"
P_Lr = Z_Lr2*U_Lr2 + P_res          "Resonator inertance and visc. resistance after load"
U_Lr2 = P_res*(1/Z_Cres + 1/Z_CLr2)"Resonator compliances and therm. resist."

{Flow Balances}
U_fb = U_CL + U_C1 + U_atb              "Continuity in main compliance and compliance of
        inertance"
U_atb = U_c + n_e*U_e               "Continuity at exhaust ports"
U_rh = n_ph*U_ph                    "Continuity at reactant header junction with preheat pipes"
{U_h = U_cz + U_Cm +n_ph*U_ph       "Continuity at combustion zone compliance and inlet preheat
        pipes"}
U_h = U_cz + U_Cm +n_ph*U_ph - U_Q1 "Continuity at combustion zone compliance and inlet
        preheat pipes"
U_cz = U_fb + U_j                   "Continuity at resonator-driver junction"
U_j = U_CLr1 + U_Lr1                    "Continuity in the resonator inertance before the load"
U_Lr1 = U_L + U_Lr2                 "Continuity between load and the rest of the resonator"

{! Acoustic Impedances}
Z_c = P_c/U_c               "[kg/m^4 s] - Acoustic impedance above regenerator"
Z_h = P_h/U_h               "[kg/m^4 s] - Acoustic impedance below regenerator"
Z_cz = P_j/U_cz             "[kg/m^4 s] - Acoustic impedance leaving combustion zone"
Z_j = P_j/U_j               "[kg/m^4 s] - Acoustic impedance entering load branch"
Z_fb = P_j/U_fb             "[kg/m^4 s] - Acoustic impedance entering feedback branch"

R_res = magnitude(Z_j)^2/real(Z_j)      "Load Resistance"
X_res = i*magnitude(Z_j)^2/imag(Z_j)    "Load Impedance"
Z_pl = rho_0*c_0/A_re                   "[kg/m^4 s] - Plane wave impedance at regenerator"
Z_ratio = magnitude(Z_c)/Z_pl           "Acoustic to characteristic impedance (higher is
        better)"

wL_Rre = -i*imag(Z_LL)/R_0          "omega*L/R_re, should be about 0.10"

{! Acoustic Power Calculations}
E_dot_c = real(P_c*conj(U_c))/2         "[W] - Acoustic power above regenerator"
E_dot_h = real(P_h*conj(U_h))/2         "[W] - Acoustic power below regenerator"
```

```
E_dot_cz = real(P_j*conj(U_cz))/2              "[W] - Acoustic power exiting combustion zone"
E_dot_j = real(P_j*conj(U_j))/2                "[W] - Acoustic power entering load branch"
E_dot_fb = real(P_j*conj(U_fb))/2              "[W] - Acoustic power entering feedback branch"

E_dot_v = real((P_j - P_c)*conj(U_fb))/2       "[W] - Viscous power dissipation in feedback branch"
E_dot_k = real(P_c*conj(U_CL))/2               "[W] - Thermal power dissipation in feedback branch"
E_dot_g = (tau-1)*E_dot_c                      "[W] - Thermal gain in regen"
{E_dot_v_re = R_re/2*tau*magnitude(U_c)^2      "[W] - Viscous power loss in regen"}
E_dot_vis = E_dot_g - (E_dot_h - E_dot_c) "Difference between ideal and actual gain (visc.
        regen loss)"
E_dot_e = n_e*real(P_c*conj(U_e))/2            "[W] - Acoustic energy lost out exhaust ports"
E_dot_ph = n_ph*real(P_h*conj(U_ph))/2         "[W] - Acoustic energy lost out inlet ports"
E_dot_Q1 = real(P_h*conj(U_Q1))/2              "[W] - Acoustic energy lost out inlet ports"

beta = E_dot_vis/(E_dot_h - E_dot_c)           "Regenerator Effectiveness (lower is better)"



"!Thermal Conduction Calculations"
k_wall = 9.7 + 0.015*(T_ave - 273.15)          "[W/m C] - regenerator wall conductivity (Inconel
        625)"
A_wall = pi*(D_re + 2*t_wall)^2/4 - A_re       "[m^2] - regenerator cross sectional area"
Q_dot_wall_L = -A_wall*k_wall*dTredx_L         "[W] - heat leak down the regenerator wall at hot
        side"
Q_dot_wall_0 = -A_wall*k_wall*dTredx_0         "[W] - heat leak down the regenerator wall at cold
        side"

k_mesh = 13.2 + 0.112/1.68*((T_reh - 273.15)^1.68 - (T_c - 273.15)^1.68)/(T_reh - T_c)
        "[W/m C] - regen mesh cond. (stainless 304)"
epsilon_s = 0.1                "Fudge factor to account for intermittent screen contact"
Q_dot_mesh_L = -(1-psi)*A_re*epsilon_s*k_mesh*dTredx_L       "[W] - heat leak down hot regen
        mesh"
Q_dot_mesh_0 = -(1-psi)*A_re*epsilon_s*k_mesh*dTredx_0       "[W] - heat leak down cold
        regen mesh"


"! Imperfect thermal contact entropy flux"
m_dot_1 = U_c*rho_0                                  "acoustic mass flux in regenerator"
m_dot_ratio = m_dot_0/magnitude(m_dot_1)"ratio of mean to acoustic mass fluxes at interface"
b_psi = 3.81 - 11.29*psi + 9.47*psi^2          "heat transfer curve fit factor (Swift & Ward Eq. A4)"
CALL gFits(Re_1 : g_c, g_v)          "Integrals of Swift & Ward's Eqs. 30 & 31"
g_c_i = 0;  g_v_i = 0;

psi_m = 2*(g_c - g_v)/b_psi/Pr_m^(1/3)*(cp_re*r_h_re*magnitude(m_dot_1))^2/A_re/psi/k_m
        "mesh regen"
Q_dot_psi_L = -psi_m*dTredx_L     "heat leak from imperfect solid/gas thermal contact in regen's
        hot side"
Q_dot_psi_0 = -psi_m*dTredx_0     "heat leak from imperfect solid/gas thermal contact in regen's
        cold side"


"! Preheat Calculations"
"Heat transfer parameters"
Xi = -m_dot_0*cp_re/(psi_m + (1-psi)*A_re*epsilon_s*k_mesh + A_wall*k_wall)  "regenerator
        side parameter"
XiL = Xi*x_re
```

```
M = -cp_rx/cp_re                "ratio:  (m_dot_0*cp)_rx/(m_dot_0*cp)_re, assuming m_dot_0's are
        equal"

"Time average steady flow equivalent approximation"
m_dot_ph_rat = m_dot_0/n_ph/rho_rx/magnitude(U_ph)    "ratio of mean to acoustic mass flux in
        preheat pipe"
theta = arcsin(m_dot_ph_rat_r)                        "theta, for m_0/m_1 <= 1"
m_dot_tasfe = m_dot_0*2/pi*(1/tan(theta) + theta)          "time average steady flow equivalent
        mass flux"
Re_tasfe = 4*m_dot_tasfe/pi/D_ph/n_ph/mu_rx      "TASFE preheat Reynolds Number"

Nus_rx = 0.022*Re_tasfe^0.8*Pr_rx^0.5                 "Nusselt Number correlation for gas heat
        transfer in an individual preheat pipe - from Kays & Crawford Eq. 14-7"
N = 4*Nus_rx/D_ph/Re_ph/Pr_rx                         "Heat transfer coefficient"

"Total Heat transferred to reactants"
Q_dot_ph = m_dot_0*(enthalpy(AIR, T = T_ph) - enthalpy(AIR, T = T_0))


"! Total Power Calculations"
Q_dot_mf = m_dot_0*cp_tot*(T_h - T_0)     "thermal energy in stream of hot combustion gas"
H_dot_h = E_dot_h - Q_dot_mf              "total power in hot duct"
H_dot_h_re = -m_dot_0*cp_reh0*(T_reh - T_0) + Q_dot_wall_L + Q_dot_mesh_L + Q_dot_psi_L"total power at re
H_dot_c_re = -m_dot_0*cp_c0*(T_c - T_0) + Q_dot_wall_0 + Q_dot_mesh_0 + Q_dot_psi_0
        "total power at regen cold side"
H_dot_c = -m_dot_0*cp_c0*(T_c - T_0) + E_dot_c "total power entering cold heat exchanger"
Q_dot_c = H_dot_c - H_dot_c_re            "heat transfer out of the cold heat exchanger"
Q_dot_0 = m_dot_0*cp_c0*(T_c - T_0)       "heat rejection of the mean flow to ambient"


"! Efficiency Calculations"
Q_dot_Mreh = m_dot_0*cp_reh0*(T_reh - T_0)"convection energy flux entering regenerator's hot
        end"
eta_ph = Q_dot_ph/Q_dot_Mreh              "preheating efficiency"

CALL MethaneRxHS(T_0, P_m_s, phi : h_rx_0, s_rx_0)    "reactant inlet supply enthalpy and
        entropy"
CALL MethanePrHS(T_0, P_m_e, phi : h_pr_0, s_pr_0)    "product exhaust enthalpy and
        entropy"
h_rx_0_i = 0;  s_rx_0_i = 0;  h_pr_0_i = 0;  s_pr_0_i = 0;

Q_dot_fuel = m_dot_0*(h_rx_0 - h_pr_0)    "Input fuel power"
eta_th = E_dot_j/Q_dot_fuel               "First law thermal efficiency"

E_dot_j_avail = m_dot_0*(h_rx_0 - h_pr_0 - T_0*(s_rx_0 - s_pr_0))       "Max work output via
        exergy analysis (Bejan Chs. 7.3 and 7.5)"
eta_2nd = E_dot_j/E_dot_j_avail           "Second law efficiency"


"! Work Lost Calculations"
CALL DeltaTint2(M, Xi, N, x_re, T_0, T_c, T_reh: dTrxint, dTreint)"Integrates T_re/T_rx over
        regenerator"
dTrxint_i = 0;  dTreint_i = 0;

"Reactant inlet pipes and header"
```

```
W_dot_lost_rx_dM = m_dot_0*cp_rx*T_0*ln(T_ph/T_0)              "difference in reactant flow
        entropy flux"
W_dot_lost_rx_dP = m_dot_0*T_0*R*ln(P_m_s/P_0)                 "reactant pipe viscous pressure
        drop"
W_dot_lost_rx_dT = m_dot_0*cp_rx*T_0*N*(x_re - dTrxint)                "preheat heat transfer"
W_dot_lost_rx = W_dot_lost_rx_dM + W_dot_lost_rx_dP + W_dot_lost_rx_dT   "total reactant
        lost work"
w_rx = W_dot_lost_rx/E_dot_j_avail          "fraction of available work lost to reactants"

"Combustion Process"
CALL MethaneRxHS(T_ph, P_0, phi : h_ph, s_ph)          "preheated reactant enthalpy and
        entropy"
CALL MethanePrHS(T_h, P_0, phi : h_h, s_h)       "hot combustion product enthalpy and
        entropy"
h_ph_i = 0;  s_ph_i = 0;  h_h_i = 0;  s_h_i = 0;
W_dot_lost_comb = -m_dot_0*T_0*(s_ph - s_h)    "work lost due to combustion process"
w_comb = W_dot_lost_comb/E_dot_j_avail "fraction of available work lost to combustion
        process"

"Regenerator/Hot Duct interface"
W_dot_lost_reh = m_dot_0*cp_reh*T_0*(T_h/T_reh - 1 - ln(T_h/T_reh))
w_reh = W_dot_lost_reh/E_dot_j_avail       "fraction of available work lost to hot regenerator
        interface"

"Regenerator"
W_dot_lost_re_dQ = -m_dot_0*cp_re*T_0*(dTredx_0/T_c - dTredx_L/T_reh)/Xi  "conduction and
        S_loss"
W_dot_lost_re_dT = -m_dot_0*cp_re*T_0*M*N*(x_re - dTreint)                "preheat heat
        transfer"
W_dot_lost_re_dM = -m_dot_0*T_0*(cp_re*ln(T_reh/T_c) + R*ln(P_m_c/P_0))   "mean flow"
W_dot_lost_re_dE = T_0*(E_dot_c/T_c - E_dot_h/T_reh)                      "acoustic
        viscous dissipation"
W_dot_lost_re = W_dot_lost_re_dQ + W_dot_lost_re_dT + W_dot_lost_re_dM +
        W_dot_lost_re_dE     "total"
w_re = W_dot_lost_re/E_dot_j_avail          "fraction of available work lost to regenerator"

"Cold heat exchanger"
W_dot_lost_chx = (1-T_0/T_c)*Q_dot_c
w_chx = W_dot_lost_chx/E_dot_j_avail       "fraction of available work lost to cold heat
        exchanger"

"Combustion Product Exhaust"
CALL MethanePrHS(T_c, P_m_c, phi : h_pr_c, s_pr_c)     "cold combustion product enthalpy and
        entropy"
h_pr_c_i = 0;  s_pr_c_i = 0;
W_dot_lost_e = m_dot_0*(h_pr_c - h_pr_0 - T_0*(s_pr_c - s_pr_0))
w_e = W_dot_lost_e/E_dot_j_avail           "fraction of available work lost to combustion product
        exhaust"

"Other losses:  viscous and thermal dissipation in pipes, inlet and exhaust losses"
W_dot_lost_other = E_dot_j_avail - W_dot_lost_rx - W_dot_lost_comb - W_dot_lost_reh -
        W_dot_lost_re - W_dot_lost_chx - W_dot_lost_e - E_dot_j
w_other = W_dot_lost_other/E_dot_j_avail  "fraction of available work lost to other processes"
```

```
{SUBPROGRAM PreheatIntBackT(M, Xi, N, L, T_0, T_c, T_reh, R_c1, R_c2, wC, b_mu, P_h,
        U_hr, U_hi : P_cr, P_ci, U_cr, U_ci)
Using the NEW solution of the regenerator preheating temperature profile, this program
        integrates the real and imaginary parts of the acoustic pressure and acoustic volumetric
        velocity from HOT to COLD across the regenerator.  Integration is done from hot to cold to
        take advantage of the fact that P_h is the reference phasor, and has no imaginary
        component
Inputs: M - ratio: (m_dot_0*c_p)_rx/(m_dot_0*c_p)_re
        Xi  - (m_dot_0*c_p)_re/(Psi_m + A*k)
        N - n*pi*D_i*h/(m_dot_0*c_p)_rx
        L - length of regenerator
        T_0 - ambient temperature
        T_c - cold heat exchanger temperature, reference temp for mu(T)
        T_reh - temperature at the hot end of the regenerator
        R_c1 - reference regenerator resistance for first curve fit coefficient
        R_c2 - regenerator resistance for second curve fit coefficient
        wC - regenerator compliance times the angular frequency, omega
        b_mu - exponent for viscosity temperature dependence
        P_h  - hot side regenerator acoustic pressure (purely real)
        U_hr - real part of hot side volumetric velocity
        U_hi - imaginary part of hot side volumetric velocity
Outputs:  P_cr - real component of cold side regenerator acoustic pressure
        P_ci  - imaginary component cold side regenerator acoustic pressure
        U_cr - real part of cold side volumetric velocity
        U_ci - imaginary part of cold side volumetric velocity
Created on 6/29/04 by Nate Weiland}


SUBPROGRAM PreheatIntBackT(M, Xi, N, L, T_0, T_c, T_reh, R_c1, R_c2, wC, b_mu, P_h,
        U_hr, U_hi : P_cr, P_ci, U_cr, U_ci)


{Solution of T_re(x) and T_re`(x)}
R = ((N+Xi)^2 + 4*M*Xi*N)^(0.5)
A = exp((Xi-N+R)*L/2)
B = exp((Xi-N-R)*L/2)
D_L = R*(2-A-B) + (Xi+N+2*M*Xi)*(B-A)
c1 = T_0 + (2*R*(T_reh-T_0) + (T_c-T_0)*((Xi+N-R)*B-(Xi+N+R)*A))/D_L
c2 = ((T_reh-T_0)*(Xi-N-R) + (T_c-T_0)*(2*N-(Xi+N-R)*B))/N/D_L
c3 = -((T_reh-T_0)*(Xi-N+R) + (T_c-T_0)*(2*N-(Xi+N+R)*A))/N/D_L
Ax = exp((Xi-N+R)*x/2)
Bx = exp((Xi-N-R)*x/2)

"Regenerator Temperature Solution"
T_re = c1 + c2*(Xi+N+R)/2*Ax + c3*(Xi+N-R)/2*Bx

"Regenerator Temperature Gradient Solution"
T_re` = c2*(Xi-N+R)*(Xi+N+R)/4*Ax + c3*(Xi-N-R)*(Xi+N-R)/4*Bx

{! Integrations with added resistance term, R_c2}
"Regenerator Pressure Integrals"
P_cr = P_h - integral((R_c1/L*(T_re/T_c)^b_mu + R_c2/L)*U_cr, x, L, 0)
P_ci = - integral((R_c1/L*(T_re/T_c)^b_mu + R_c2/L)*U_ci, x, L, 0)

"Regenerator Velocity Integrals"
U_cr = U_hr + integral((wC/L*P_ci + T_re`/T_re*U_cr), x, L, 0)
```

```
U_ci = U_hi + integral((-wC/L*P_cr + T_re`/T_re*U_ci), x, L, 0)

"Total Regenerator Resistance"
{R_re = R_c2 - R_c1/L*integral((T_re/T_c)^b_mu, x, L, 0)}

END
```

```
{SUBPROGRAM GenTProfiles (M, Xi, N, L, T_0, T_c, T_int: T_ph, dTredx_0, dTredx_L)}
{Program used to solve the following coupled ODEs for the regenerator's temperature and the
        preheating gas temperature:
        d^2T_re/dx^2 - Xi*dT_re/dx = M*Xi*N*(T_re - T_rx)
        dT_rx/dx = N*(T_re - T_rx)
This problem is broken down into three coupled first order linear differential equations, which are
        solved by finding the eigenvalues and eigenvectors of the set of equations and by applying
        the boundary conditions.  The solution procedure assumes that M is not equal to -1.
Inputs: M, the ratio of the reactant gas to the regenerator's (m_dot_0*c_p)
        Xi, regenerator convection to loss term ratio, (m_dot_0*c_p)_re/(Psi_m + A*k)
        N, reactant gas heat transfer coefficient, n*pi*D_i*h/(m_dot_0*c_p)_rx
        L, length of regenerator
        T_0, ambient temperature
        T_c, cold heat exchanger temperature
        T_int, temperature at the hot end of the regenerator
Output: T_ph, temperature of the preheated reactant gas leaving the regenerator
        dTredx_0, the regenerator temperature gradient at the cold end
        dTredx_L, the regenerator temperature gradient at the hot end
Created 6/29/04 - Nate Weiland}


SUBPROGRAM GenTProfiles (M, Xi, N, L, T_0, T_c, T_int: T_ph, dTredx_0, dTredx_L)


"! My solution of the eigenvalue problem"
R = ((N+Xi)^2 + 4*M*Xi*N)^(0.5)
A = exp((Xi-N+R)*L/2)
B = exp((Xi-N-R)*L/2)
D_L = R*(2-A-B) + (Xi+N+2*M*Xi)*(B-A)
D_2 = (Xi+N-R)*B
D_3 = (Xi+N+R)*A

"Preheat Temperature"
T_ph = T_0 + (T_int-T_0)*(R*(2-A-B) - (Xi-N)*(B-A))/D_L + (T_c-T_0)/D_L*(D_2-D_3+(2*N-
        D_2)*A-(2*N-D_3)*B)

"Cold side Regenerator Temperature Gradient"
dTredx_0 = (T_0-T_int)*2*R*Xi*(1+M)/D_L + (T_c-T_0)/4/N/D_L*((Xi-N+R)*(Xi+N+R)*(2*N-D_2) -
        (Xi-N-R)*(Xi+N-R)*(2*N-D_3))

"Hot side Regenerator Temperature Gradient"
dTredx_L = (T_int-T_0)*Xi*(1+M)*((Xi+N-R)*B - (Xi+N+R)*A)/D_L + (T_c-T_0)/4/N/D_L*((Xi-
        N+R)*(Xi+N+R)*(2*N-D_2)*A - (Xi-N-R)*(Xi+N-R)*(2*N-D_3)*B)

END
```

```
{SUBPROGRAM DeltaTint2(M, Xi, N, L, T_0, T_c, T_int: dTrxint, dTreint)}
{Program uses the NEW analytic solution to the reactant preheating problem to determine the
        integrals of T_rx/T_re and T_re/T_rx over the length of the regenerator, which are used in
        computing the entropy generated in the heat transfer.  The solution procedure assumes
        that M is not equal to -1.
Inputs: M, the ratio of the reactant gas to the regenerator's (m_dot_0*c_p)
        Xi, regenerator convection to loss term ratio, (m_dot_0*c_p)_re/(Psi_m + A*k)
        N, reactant gas heat transfer coefficient, n*pi*D_i*h/(m_dot_0*c_p)_rx
        L, length of regenerator
        T_0, ambient temperature
        T_c, cold heat exchanger temperature
        T_int, temperature at the hot end of the regenerator
Output: dTrxint, the integral of T_re/T_rx over the length of the regenerator
        dTreint, the integral of T_rx/T_re over the length of the regenerator
Created 6/29/04 - Nate Weiland}


SUBPROGRAM DeltaTint2(M, Xi, N, L, T_0, T_c, T_int: dTrxint, dTreint)


"! My solution of the eigenvalue problem"
R = ((N+Xi)^2 + 4*M*Xi*N)^(0.5)
A = exp((Xi-N+R)*L/2)
B = exp((Xi-N-R)*L/2)
D_L = R*(2-A-B) + (Xi+N+2*M*Xi)*(B-A)
D_2 = (Xi+N-R)*B
D_3 = (Xi+N+R)*A
Ax = exp((Xi-N+R)*x/2)
Bx = exp((Xi-N-R)*x/2)

"Reactant temperature profile"
T_rx = T_0 + (T_int-T_0)*(R*(2-Ax-Bx) - (Xi-N)*(Bx-Ax))/D_L + (T_c-T_0)*(D_2-D_3+(2*N-
        D_2)*Ax-(2*N-D_3)*Bx)/D_L

"Regenerator temperature profile"
T_re = T_0 +(T_int-T_0)*(R*(2-Ax-Bx) + (Xi+N+2*M*Xi)*(Bx-Ax))/D_L + (T_c-T_0)*(N*(D_2-D_3)
        + (Xi+N+R)*(2*N-D_2)*Ax/2 - (Xi+N-R)*(2*N-D_3)*Bx/2)/N/D_L

"Integrals"
dTrxint = integral(T_re/T_rx, x, 0, L, L/50)
dTreint = integral(T_rx/T_re, x, 0, L, L/50)

{x_step = L/20
$Integraltable x:x_step, T_re, T_rx}

END
```

```
{SUBPROGRAM gFits(Re_1 : g_c, g_v)
Program used to compute the curve fits to some integrals needed in the evaluation of psi_m
Inputs: Re_1 - the acoustic Reynolds Number, 4*|m_dot_1|*r_h_re/A_re/psi/mu_m
Outputs:  g_c - parameter from Swift and Ward, Eq. 30
          g_v - parameter from Swift and Ward, Eq. 31
Created by Nate Weiland - 6/30/04}


SUBPROGRAM gFits(Re_1 : g_c, g_v)


g_c_low = 1 - 0.73188*Re_1^0.6 + 0.59993*Re_1^1.2 - 0.52048*Re_1^1.8         "Swift and Ward
          Eq. B1"
g_c_hi = 1.2915*Re_1^(-0.55338)                                              "S & W Eq. B4"
g_c = g_c_hi/(1 + 2.9*Re_1^(-3)) + g_c_low/(1 + 0.33*Re_1^3)                 "S & W Eqs. B3 and B4"

g_v_low = 0.1689*Re_1^0.6 - 0.22604*Re_1^1.2 + 0.24654*Re_1^1.8 - 0.25379*Re_1^2.4 +
          0.25465*Re_1^3        "S&W Eq. B2"
g_v_mid = 0.0679 - 0.00685*(ln(Re_1) - 0.884)^2
g_v_hi = 0.405*Re_1^(-0.53)
g_v = g_v_hi/(1 + 715*Re_1^(-2)) + g_v_mid*(1 - 1/(1 + 715*Re_1^(-2)) - 1/(1 + 100*Re_1^5)) +
          g_v_low/(1 + 100*Re_1^5)

END
```

```
{Subprogram MethaneT_ad(T0, T_ad, phi, M_mix)
Function used to calculate the properties of a premixed methane-air flame.  Given two of the
      following inputs, the third is calculated:
      T0 - inlet temperature of premixed reactants
      T_ad - adiabatic flame temperature
      phi - equivalence ratio for the premixed fuel and air
Also, the molecular weight of the mixture is returned, M_mix, in units of (kg/kmol).  This is a
      function of phi, and is used to calculate other product gas properties in the calling program
Assume:  Complete, adiabatic combustion, lean premixed methane/air mixture, no dissociation
Created by Nate Weiland on 9/30/03
Modified on 12/22/03 to include M_mix output}

Subprogram MethaneT_ad(T0, T_ad, phi, M_mix)


"Molecular Weights"
M_CH4 = molarmass(CH4)
M_N2= molarmass(N2)
M_O2= molarmass(O2)
M_CO2= molarmass(CO2)
M_H2O= molarmass(H2O)
M_mix = phi/(phi+9.52)*M_CH4 + 2/(phi+9.52)*M_O2 + 7.52/(phi+9.52)*M_N2

"Reactant Mass Fractions"
Y_CH4 = phi/(phi+9.52)*M_CH4/M_mix      "[kg CH4/kg]"
Y_O2_1 = 2/(phi+9.52)*M_O2/M_mix        "[kg O2/kg] - O2 in reactants"
Y_N2 = 7.52/(phi+9.52)*M_N2/M_mix       "[kg N2/kg]"

"Enthalpy of inlet air"
h_N2_1 = enthalpy(N2, T=T0)             "[kJ/kg N2]"
h_O2_1 = enthalpy(O2, T=T0)             "[kJ/kg O2]"
h_CH4 = enthalpy(CH4, T=T0)             "[kJ/kg CH4]"
h_1 = Y_CH4*h_CH4 + Y_O2_1*h_O2_1 + Y_N2*h_N2_1"[kJ/kg] - total enthalpy of inlet air"

"Product Mass fractions"
Y_CO2 = phi/(phi+9.52)*M_CO2/M_mix
Y_H2O = 2*phi/(phi+9.52)*M_H2O/M_mix
Y_O2_2 = 2*(1-phi)/(phi+9.52)*M_O2/M_mix

"Product Enthalpies"
h_CO2_2 = enthalpy(CO2, T=T_ad)         "[kJ/kg CO2]"
h_H2O_2 = enthalpy(H2O, T=T_ad)         "[kJ/kg H2O]"
h_N2_2 = enthalpy(N2, T=T_ad)           "[kJ/kg N2]"
h_O2_2 = enthalpy(O2, T=T_ad)           "[kJ/kg O2]"

"Total enthalpy of products at regenerator's hot end"
h_2 = Y_CO2*h_CO2_2 + Y_H2O*h_H2O_2 + Y_N2*h_N2_2 + Y_O2_2*h_O2_2       "[kJ/kg]"
h_1 = h_2               "Energy Balance"

END
```

```
{Subprogram MethaneRxHS(T0, P0, phi : H, S)
Function used to calculate the absolute enthalpy and entropy of premixed methane and air
        reactants
Inputs: T0 - temperature of premixed reactants and combustion products
        P0 - mean pressure of both the reactants and products
        phi - equivalence ratio for the premixed fuel and air
Outputs:  H - absolute enthalpy of the reactants
        S - entropy of the reactants
Assume:  Complete, adiabatic combustion, lean premixed methane/air mixture, no dissociation
Created by Nate Weiland on 1/8/04}

Subprogram MethaneRxHS(T0, P0, phi : H, S)


"Reactant Gas Mole Fractions"
X_CH4 = phi/(phi+9.52)
X_O2 = 2/(phi+9.52)
X_N2 = 7.52/(phi+9.52)

"Molecular Weights"
M_CH4 = molarmass(CH4)
M_O2= molarmass(O2)
M_N2= molarmass(N2)
M_mix = X_CH4*M_CH4 + X_O2*M_O2 + X_N2*M_N2

"Reactant Mass Fractions"
Y_CH4 = X_CH4*M_CH4/M_mix     "[kg CH4/kg]"
Y_O2 = X_O2*M_O2/M_mix        "[kg O2/kg] - O2 in reactants"
Y_N2 = X_N2*M_N2/M_mix        "[kg N2/kg]"

"Enthalpy of inlet component mixture"
h_N2 = enthalpy(N2, T=T0)          "[kJ/kg N2]"
h_O2 = enthalpy(O2, T=T0)          "[kJ/kg O2]"
h_CH4 = enthalpy(CH4, T=T0)        "[kJ/kg CH4]"
H = Y_CH4*h_CH4 + Y_O2*h_O2 + Y_N2*h_N2    "[kJ/kg] - total enthalpy of inlet air"

"Entropy of the reactant mixture"
s_N2 = entropy(N2, T=T0, P = P0*X_N2)    "[kJ/kg K N2]"
s_O2 = entropy(O2, T=T0, P = P0*X_O2)    "[kJ/kg K O2]"
s_CH4 = entropy(CH4, T=T0, P = P0*X_CH4)"[kJ/kg K CH4]"
S = Y_CH4*s_CH4 + Y_O2*s_O2 + Y_N2*s_N2"[kJ/kg K] - total entropy of inlet flow"

END
```

```
{Subprogram MethanePrHS(T0, P0, phi : H, S)
Function used to calculate the absolute enthalpy and entropy of the combustion products of
        premixed methane/air mixture
Inputs: T0 - temperature of combustion products
        P0 - mean pressure of the products
        phi - equivalence ratio for the premixed fuel and air
Outputs:  H - absolute enthalpy of the combustion products
        S - total entropy of the combustion products
Assume:  Complete, adiabatic combustion, lean premixed methane/air mixture, no dissociation
Created by Nate Weiland on 1/8/04}

Subprogram MethanePrHS(T0, P0, phi : H, S)


"Product Gas Mole Fractions"
X_O2 = 2*(1-phi)/(phi+9.52)
X_N2 = 7.52/(phi+9.52)
X_CO2 = phi/(phi+9.52)
X_H2O = 2*phi/(phi+9.52)

"Molecular Weights"
M_O2= molarmass(O2)
M_N2= molarmass(N2)
M_CO2= molarmass(CO2)
M_H2O= molarmass(H2O)
M_mix = X_CO2*M_CO2 + X_H2O*M_H2O + X_O2*M_O2 + X_N2*M_N2

"Product Mass fractions"
Y_CO2 = X_CO2*M_CO2/M_mix
Y_H2O = X_H2O*M_H2O/M_mix
Y_O2 = X_O2*M_O2/M_mix
Y_N2 = X_N2*M_N2/M_mix

"Enthalpy of product gas mixture"
h_N2 = enthalpy(N2, T=T0)                    "[kJ/kg N2]"
h_O2 = enthalpy(O2, T=T0)                    "[kJ/kg O2]"
h_CO2 = enthalpy(CO2, T=T0)                  "[kJ/kg CO2]"
h_H2O = enthalpy(H2O, T=T0)                  "[kJ/kg H2O]"
H = Y_CO2*h_CO2 + Y_H2O*h_H2O + Y_N2*h_N2 + Y_O2*h_O2        "[kJ/kg]"

"Entropy of product gas components at the reference temperature"
s_CO2 = entropy(CO2, T=T0, P = P0*X_CO2)     "[kJ/kg K CO2]"
s_H2O = entropy(H2O, T=T0, P = P0*X_H2O)     "[kJ/kg K H2O]"
s_O2 = entropy(O2, T=T0, P = P0*X_O2)        "[kJ/kg K O2]"
s_N2 = entropy(N2, T=T0, P = P0*X_N2)        "[kJ/kg K N2]"
S = Y_CO2*s_CO2 + Y_H2O*s_H2O + Y_N2*s_N2 + Y_O2*s_O2        "[kJ/kg K]"

END
```

```
{Subprogram ProductAveCp(T0, T1, phi : cp)
Determines the average combustion product gas specific heat across a temperature difference,
      such that cp*(T1 - T0) yields the correct enthalpy difference
Inputs: T0 = reference temperature [K]
      T1 = second temperature of the temperature difference [K]
      phi = equivalence ratio of the reactants in the premixed methane-air flame
Outputs:  cp = const. pressure specific heat of the product gas across dT  (cp = dh/dT)
Assumes:  Complete, adiabatic combustion, lean premixed methane/air mixture, no dissociation,
      ideal gas
Created by Nate Weiland on 12/22/03}


Subprogram ProductAveCp(T0, T1, phi : cp)


"Product Gas Mole Fractions"
X_CO2 = phi/(phi+9.52)
X_H2O = 2*phi/(phi+9.52)
X_O2 = 2*(1-phi)/(phi+9.52)
X_N2 = 7.52/(phi+9.52)

"Molecular Weights"
M_CO2= molarmass(CO2)
M_H2O= molarmass(H2O)
M_O2= molarmass(O2)
M_N2= molarmass(N2)
M_mix = X_CO2*M_CO2 + X_H2O*M_H2O + X_O2*M_O2 + X_N2*M_N2

"Find Cp for the temperature difference"
h0_CO2 = enthalpy(CO2,T=T0)*M_CO2     "[kJ/kmol]"
h0_H2O = enthalpy(H2O,T=T0)*M_H2O     "[kJ/kmol]"
h0_O2 = enthalpy(O2,T=T0)*M_O2        "[kJ/kmol]"
h0_N2 = enthalpy(N2,T=T0)*M_N2        "[kJ/kmol]"
h0 = (X_CO2*h0_CO2 + X_H2O*h0_H2O + X_O2*h0_O2 + X_N2*h0_N2)/M_mix      "[kJ/kg]"

h1_CO2 = enthalpy(CO2,T=T1)*M_CO2     "[kJ/kmol]"
h1_H2O = enthalpy(H2O,T=T1)*M_H2O     "[kJ/kmol]"
h1_O2 = enthalpy(O2,T=T1)*M_O2        "[kJ/kmol]"
h1_N2 = enthalpy(N2,T=T1)*M_N2        "[kJ/kmol]"
h1 = (X_CO2*h1_CO2 + X_H2O*h1_H2O + X_O2*h1_O2 + X_N2*h1_N2)/M_mix      "[kJ/kg]"

cp = (h1 - h0)/(T1 - T0)              "[kJ/kg K]"

END
```

```
{Subprogram ProductCp(T0, phi : cp)
Determines the constant pressure specific heat of the products of premixed methane and air
      combustion
Inputs:  T0 = product gas temperature [K]
      phi = fuel/air equivalence ratio
Outputs: cp = mass-based const. pressure specific heat [kJ/kg K]
Assume:  Complete, adiabatic combustion, lean premixed methane/air mixture, no dissociation,
      ideal gas
Important:  uses the unit system of the calling program (J vs. kJ, etc.)!  The unit system must be
      mass-based for the specific heat calculation in this program to work.
Created by Nate Weiland on 2/2/04}


Subprogram ProductCp(T0, phi : cp)

{T0 = 325
phi = 0.5}

"Mole Fractions"
X_CO2 = phi/(phi+9.52)
X_H2O = 2*phi/(phi+9.52)
X_O2 = 2*(1-phi)/(phi+9.52)
X_N2 = 7.52/(phi+9.52)

"Molecular Weights"
M_CO2= molarmass(CO2)
M_H2O= molarmass(H2O)
M_O2= molarmass(O2)
M_N2= molarmass(N2)
M_mix = X_CO2*M_CO2 + X_H2O*M_H2O + X_O2*M_O2 + X_N2*M_N2

"Molar Const. Pressure Specific Heats"
cp_CO2 = cp(CO2,T=T0)*M_CO2          "[kJ/kmol K] - valid from 250 K to 3500 K"
cp_H2O = cp(H2O,T=T0)*M_H2O          "[kJ/kmol K] - valid from 250 K to 3500 K"
cp_O2 = cp(O2,T=T0)*M_O2             "[kJ/kmol K] - valid from 250 K to 3500 K"
cp_N2 = cp(N2,T=T0)*M_N2             "[kJ/kmol K] - valid from 250 K to 3500 K"
cp_mol = X_CO2*cp_CO2 + X_H2O*cp_H2O + X_O2*cp_O2 + X_N2*cp_N2     "[kJ/kmol K]"
cp = cp_mol/M_mix                    "[kJ/kg K]"

END
```

```
{Subprogram ProductViscFit(T0, T1, phi : mu0, b_mu)
Determines the power law exponent in a curve fit of combustion product gas viscosity
Inputs: T0 = reference temperature [K]
        T1 = maximum temperature in the curve fitting range [K]
        phi = equivalence ratio of the reactants in the premixed methane-air flame
Outputs:  mu0 = combustion product viscosity at T0
        b_mu = exponent for temperature dependence of viscosity (mu/mu0 = (T/T0)^b_mu)
Assumes:  Complete combustion, lean premixed methane/air mixture, no dissociation, ideal gas
Created by Nate Weiland on 12/22/03}

Subprogram ProductViscFit(T0, T1, phi : mu0, b_mu)


"Product Gas Mole Fractions"
X_CO2 = phi/(phi+9.52)
X_H2O = 2*phi/(phi+9.52)
X_O2 = 2*(1-phi)/(phi+9.52)
X_N2 = 7.52/(phi+9.52)

"!Curve Fitting for b_mu and b_k"
n = 10 "number of curve fitting points"
mu0 = mu[1]   "reference dynamic viscosity"

Duplicate j=1,n
        T[j] = T0 + (j-1)*(T1-T0)/(n-1)          "Create an array of temperatures"

        "Calculate an array of mu values, calculated mu values, and squared errors"
        mu_CO2[j] = viscosity(CO2,T=T[j])   "[kg/m s] - good to 2000 K"
        mu_H2O[j] = viscosity(H2O,T=T[j])   "[kg/m s] - good to 3500 K"
        mu_O2[j] = viscosity(O2,T=T[j])     "[kg/m s] - good to 3000 K"
        mu_N2[j] = viscosity(N2,T=T[j])     "[kg/m s] - good to 2500 K"
        mu[j] = X_CO2*mu_CO2[j] + X_H2O*mu_H2O[j] + X_O2*mu_O2[j] + X_N2*mu_N2[j]
        mu_calc[j] = mu0*(T[j]/T0)^b_mu
        sqerr_mu[j] = mu[j]^2 - mu_calc[j]^2
end

"This method of finding 'b_mu' is accurate to within about 0.5% of the full rms curve fitting"
error_mu = sum(sqerr_mu[1..n])
error_mu = 0

END
```

```
{Subprogram ProductCondFit(T0, T1, phi : k0, b_k)
Determines the combustion product gas thermal conductivity curve fit vs. temperature
Inputs: T0 = reference temperature [K]
        T1 = max temperature in the curve fit [K]
        phi = equivalence ratio of the reactants in the premixed methane-air flame
Outputs:  k0 = thermal conductivity of combustion product gas at T0
        b_k = exponent for temperature dependence of conductivity (k/k0 = (T/T0)^b_k)
Assumes:  Complete combustion, lean premixed methane/air mixture, no dissociation, ideal gas
Created by Nate Weiland on 12/22/03}


Subprogram ProductCondFit(T0, T1, phi : k0, b_k)


"Product Gas Mole Fractions"
X_CO2 = phi/(phi+9.52)
X_H2O = 2*phi/(phi+9.52)
X_O2 = 2*(1-phi)/(phi+9.52)
X_N2 = 7.52/(phi+9.52)

"!Curve Fitting for b_mu and b_k"
n = 10 "number of curve fitting points"
k0 = k[1]        "reference thermal conductivity"

Duplicate j=1,n
        T[j] = T0 + (j-1)*(T1-T0)/(n-1)          "Create an array of temperatures"

        "Calculate an array of k values, calculated k values, and squared errors"
        k_CO2[j] = conductivity(CO2,T=T[j]) "[W/m K] - good to 1400 K"
        k_H2O[j] = conductivity(H2O,T=T[j]) "[W/m K] - good to 3500 K"
        k_O2[j] = conductivity(O2,T=T[j])      "[W/m K] - good to 3000 K"
        k_N2[j] = conductivity(N2,T=T[j])      "[W/m K] - good to 1400 K"
        k[j] = X_CO2*k_CO2[j] + X_H2O*k_H2O[j] + X_O2*k_O2[j] + X_N2*k_N2[j]
        k_calc[j] = k0*(T[j]/T0)^b_k
        sqerr_k[j] = k[j]^2 - k_calc[j]^2
end

"This method of finding 'b_k' is accurate to within about 0.2% of the full rms curve fitting up to
        1400 K.  Above that it's much less accurate, as k_N2 and k_CO2 are only good to 1400
        K."
error_k = sum(sqerr_k[1..n])
error_k = 0

END
```

{Base Case Solution}

alpha_i=0
alpha_r=0
A_c_i=0 [m^2]
A_c_r=0.01291 [m^2]
A_e_i=0 [m^2]
A_e_r=7.854E-07 [m^2]
a_i=0 [m/s]
A_Lr_i=0 [m^2]
A_Lr_r=0.005463 [m^2]
A_l_i=0 [m^2]
A_l_r=0.003815 [m^2]
A_ph_i=0 [m^2]
A_ph_r=1.963E-07 [m^2]
a_r=361.2 [m/s]
A_re_i=0 [m^2]
A_re_r=0.00456 [m^2]
A_rh_i=0 [m^2]
A_rh_r=0.000003142 [m^2]
A_wall_i=0 [m^2]
A_wall_r=0.0001205 [m^2]
beta_i=0
beta_r=0.3161
b_k_i=0
b_k_r=0.8573
b_mu_i=0
b_mu_r=0.747
b_psi_i=0
b_psi_r=0.5904
cp_0_i=0
cp_0_r=1068
cp_c0_i=0
cp_c0_r=1067
Cp_i=0 [J/kg K]
Cp_r=1007 [J/kg K]
cp_reh0_i=0
cp_reh0_r=1123
cp_reh_i=0
cp_reh_r=1288
cp_re_i=0 [J/kg K]
cp_re_r=1126 [J/kg K]
cp_rx_i=0 [J/kg K]
cp_rx_r=1022 [J/kg K]
cp_tot_i=0 [J/kg K]
cp_tot_r=1227 [J/kg K]
c_0_i=0
c_0_r=363.7
c_psi_1_i=0
c_psi_1_r=34.41
c_psi_2_i=0
c_psi_2_r=0.4258
C_re_i=0
C_re_r=1.066E-09 [m^4 s^2/kg]
delta_k_0_i=0 [m]
delta_k_0_r=0.0002718 [m]
delta_k_i=0 [m]
delta_k_L_i=0 [m]
delta_k_L_r=0.0006578 [m]
delta_k_r=0.0002811 [m]
delta_v_0_i=0 [m]
delta_v_0_r=0.0002327 [m]
delta_v_i=0 [m]
delta_v_ph_i=0 [m]
delta_v_ph_r=0.0003282 [m]
delta_v_r=0.0002389 [m]
delta_v_rx0_i=0 [m]
delta_v_rx0_r=0.0002086 [m]
dP_m0_i=0 [Pa]
dP_m0_r=75.4 [Pa]
dP_M_i=0 [Pa]
dP_M_r=25.54 [Pa]
dTredx_0_i=0 [K/m]
dTredx_0_r=15740 [K/m]
dTredx_L_i=0 [K/m]
dTredx_L_r=11616 [K/m]
dTreint_i=0
dTreint_r=0.02992
dTrxint_i=0
dTrxint_r=0.05363
D_Cr_i=0 [m]
D_Cr_r=0.203 [m]
D_c_i=0 [m]
D_c_r=0.1282 [m]
D_e_i=0 [m]
D_e_r=0.001 [m]
D_Lr_i=0 [m]
D_Lr_r=0.0834 [m]
D_ph_i=0 [m]
D_ph_r=0.0005 [m]
D_re_i=0 [m]
D_re_r=0.0762 [m]
D_rh_i=0 [m]
D_rh_r=0.002 [m]
D_wire_i=0 [mm]
D_wire_r=0.1337 [mm]
epsilon_s_i=0
epsilon_s_r=0.1
eta_2nd_i=0
eta_2nd_r=0.1615
eta_ph_i=0
eta_ph_r=0.5762
eta_th_i=0
eta_th_r=0.1661
E_dot_cz_i=0 [W]
E_dot_cz_r=47.12 [W]
E_dot_c_i=0 [W]
E_dot_c_r=21.68 [W]
E_dot_e_i=0 [W]
E_dot_e_r=0.4083 [W]

E_dot_fb_i=0 [W]
E_dot_fb_r=25.65 [W]
E_dot_g_i=0 [W]
E_dot_g_r=34.48 [W]
E_dot_h_i=0 [W]
E_dot_h_r=47.88 [W]
E_dot_j_avail_i=0 [W]
E_dot_j_avail_r=133 [W]
E_dot_j_i=0 [W]
E_dot_j_r=21.47 [W]
E_dot_k_i=0 [W]
E_dot_k_r=1.842 [W]
E_dot_ph_i=0 [W]
E_dot_ph_r=0.4307 [W]
E_dot_Q1_i=0
E_dot_Q1_r=0
E_dot_vis_i=0 [W]
E_dot_vis_r=8.281 [W]
E_dot_v_i=0 [W]
E_dot_v_r=1.415 [W]
freq_i=0 [Hz]
freq_r=83.3 [Hz]
f_k_Cr_i=-0.002769
f_k_Cr_r=0.002769
f_k_cz_i=-0.007377
f_k_cz_r=0.007377
f_k_c_i=-0.004385
f_k_c_r=0.004385
f_k_Lr_i=-0.00674
f_k_Lr_r=0.00674
f_k_l_i=-0.02729
f_k_l_r=0.02729
f_M_e_i=0
f_M_e_r=0.03542
f_M_ph_i=0
f_M_ph_r=0.0528
f_M_rh_i=0
f_M_rh_r=0.04297
f_v_cz_i=-0.00627
f_v_cz_r=0.00627
f_v_e_i=-0.4654
f_v_e_r=0.4654
f_v_Lr_i=-0.005729
f_v_Lr_r=0.005729
f_v_l_i=-0.02319
f_v_l_r=0.02319
f_v_ph_i=-1.313
f_v_ph_r=1.313
f_v_rh_i=-0.2086
f_v_rh_r=0.2086
gamma_i=0
gamma_r=1.399
g_c_i=0
g_c_r=0.2144
g_v_i=0
g_v_r=0.0543
H_dot_c_i=0 [W]
H_dot_c_r=19.25 [W]
H_dot_c_re_i=0 [W]
H_dot_c_re_r=-83.28 [W]
H_dot_h_i=0 [W]
H_dot_h_r=-115.1 [W]
H_dot_h_re_i=0 [W]
H_dot_h_re_r=-115.1 [W]
h_h_i=0 [J/kg]
h_h_r=239876 [J/kg]
h_ph_i=0 [J/kg]
h_ph_r=239876 [J/kg]
h_pr_0_i=0 [J/kg]
h_pr_0_r=-1.550E+06 [J/kg]
h_pr_c_i=0
h_pr_c_r=-1.523E+06
h_rx_0_i=0 [J/kg]
h_rx_0_r=-130490 [J/kg]
k_0_i=0 [W/m K]
k_0_r=0.02656 [W/m K]
k_i=0 [W/m K]
k_mesh_i=0 [W/m C]
k_mesh_r=18.58 [W/m C]
k_m_i=0 [W/m K]
k_m_r=0.04386 [W/m K]
k_r=0.02749 [W/m K]
k_wall_i=0 [W/m C]
k_wall_r=14.35 [W/m C]
lambda_i=0 [m]
lambda_r=4.337 [m]
mu_0_i=0 [kg/m s]
mu_0_r=0.00001822 [kg/m s]
mu_i=0 [kg/m s]
mu_m_i=0 [kg/m s]
mu_m_r=0.00002821 [kg/m s]
mu_r=0.00001972 [kg/m s]
mu_rx_i=0 [kg/m s]
mu_rx_r=0.00002568 [kg/m s]
m_dot_0_i=0 [kg/s]
m_dot_0_r=0.00009107 [kg/s]
m_dot_1_i=0.002261 [kg/s]
m_dot_1_r=0.004608 [kg/s]
m_dot_e_rat_i=0
m_dot_e_rat_r=0.6982
m_dot_ph_rat_i=0
m_dot_ph_rat_r=0.7059
m_dot_ratio_i=0
m_dot_ratio_r=0.01774
m_dot_tasfe_i=0
m_dot_tasfe_r=0.0001036
M_i=0
M_mix_i=0 [kg/kmol]
M_mix_r=28.21 [kg/kmol]
M_r=-0.9078
Nus_rx_i=0
Nus_rx_r=6.273

n_e_i=0
n_e_r=1
N_i=0
n_mesh_i=0 [wire/mm]
n_mesh_r=2.666 [wire/mm]
n_ph_i=0
n_ph_r=7
N_r=55.77
omegaC_i=0
omegaC_r=5.580E-07
omega_i=0 [rad/s]
omega_r=523.4 [rad/s]
phi_i=0
phi_r=0.5
Prat_c_i=0
Prat_c_r=0.1
Prat_c_sq_i=0
Prat_c_sq_r=0.01
Prat_h_i=0
Prat_h_r=0.0869
Pr_0_i=0
Pr_0_r=0.7327
Pr_m_i=0
Pr_m_r=0.7242
Pr_rx_i=0
Pr_rx_r=0.6976
psi_i=0
psi_m_i=0 [W m/K]
psi_m_r=0.001035 [W m/K]
psi_r=0.72
P_0_i=0 [Pa]
P_0_r=123182 [Pa]
P_ci_i=0 [Pa]
P_ci_r=-421.5 [Pa]
P_c_i=-421.5 [Pa]
P_c_r=12311 [Pa]
P_h_i=0 [Pa]
P_h_r=10705 [Pa]
P_j_i=-162 [Pa]
P_j_r=10264 [Pa]
P_Lr_i=-205.7 [Pa]
P_Lr_r=3814 [Pa]
P_m_c_i=0 [Pa]
P_m_c_r=123081 [Pa]
P_m_e_i=0 [Pa]
P_m_e_r=104562 [Pa]
P_m_rh_i=0 [Pa]
P_m_rh_r=148614 [Pa]
P_m_s_i=1.000E-100 [Pa]
P_m_s_r=149656 [Pa]
P_ph_i=3393 [Pa]
P_ph_r=9385 [Pa]
P_res_i=140.1 [Pa]
P_res_r=-3479 [Pa]
P_sat_i=0
P_sat_r=13523
Q_dot_0_i=0
Q_dot_0_r=2.429
Q_dot_1_i=0
Q_dot_1_r=0
Q_dot_c_i=0 [W]
Q_dot_c_r=102.5 [W]
Q_dot_fuel_i=0 [W]
Q_dot_fuel_r=129.2 [W]
Q_dot_mesh_0_i=0 [W]
Q_dot_mesh_0_r=-37.34 [W]
Q_dot_mesh_L_i=0 [W]
Q_dot_mesh_L_r=-27.56 [W]
Q_dot_mf_i=0 [W]
Q_dot_mf_r=163 [W]
Q_dot_Mreh_i=0
Q_dot_Mreh_r=55.42
Q_dot_ph_i=0 [W]
Q_dot_ph_r=31.93 [W]
Q_dot_psi_0_i=0 [W]
Q_dot_psi_0_r=-16.29 [W]
Q_dot_psi_L_i=0 [W]
Q_dot_psi_L_r=-12.02 [W]
Q_dot_wall_0_i=0 [W]
Q_dot_wall_0_r=-27.22 [W]
Q_dot_wall_L_i=0 [W]
Q_dot_wall_L_r=-20.09 [W]
Re_1_i=0
Re_1_r=19.05
Re_e_i=0
Re_e_r=6364
Re_ph_i=0
Re_ph_r=1290
Re_re_m_i=0
Re_re_m_r=0.3381
Re_rh_i=0
Re_rh_r=2940
Re_tasfe_i=0
Re_tasfe_r=1468
rho_0_i=0 [kg/m^3]
rho_0_r=1.286 [kg/m^3]
rho_i=0 [kg/m^3]
rho_r=1.32 [kg/m^3]
rho_rx0_i=1.000E-100
rho_rx0_r=1.732
rho_rx_i=0
rho_rx_r=0.9115
rh_dk0_i=0
rh_dk0_r=0.3162
rh_dkL_i=0
rh_dkL_r=0.1307
rh_x1_i=0
rh_x1_r=0.03701
R_0_i=0 [kg/m^4 s]
R_0_r=169269 [kg/m^4 s]
R_c1_i=0 [kg/m^4 s]
R_c1_r=129234 [kg/m^4 s]

R_c2_i=0 [kg/m^4 s]
R_c2_r=40035 [kg/m^4 s]
r_h_Cr_i=0 [m]
r_h_Cr_r=0.05075 [m]
r_h_cz_i=0 [m]
r_h_cz_r=0.01905 [m]
r_h_c_i=0 [m]
r_h_c_r=0.03205 [m]
r_h_e_i=0 [m]
r_h_e_r=0.00025 [m]
r_h_Lr_i=0 [m]
r_h_Lr_r=0.02085 [m]
r_h_l_i=0 [m]
r_h_l_r=0.00515 [m]
r_h_ph_i=0 [m]
r_h_ph_r=0.000125 [m]
r_h_re_i=0 [m]
r_h_re_r=0.00008595 [m]
r_h_rh_i=0 [m]
r_h_rh_r=0.0005 [m]
R_i=0 [J/kg·K]
R_L_i=0 [kg/m^4 s]
R_L_r=496954 [kg/m^4 s]
R_r=294.7 [J/kg·K]
R_res_i=0 [kg/m^4 s]
R_res_r=2.454E+06 [kg/m^4 s]
s_h_i=0
s_h_r=9142
s_ph_i=0
s_ph_r=7842
s_pr_0_i=0
s_pr_0_r=7102
s_pr_c_i=0
s_pr_c_r=7139
s_rx_0_i=0
s_rx_0_r=6965
tau_i=0
tau_r=2.59
theta_i=0
theta_pq_i=0
theta_pq_r=0
theta_r=0.7837
T_0_i=0 [K]
T_0_r=300 [K]
T_air_i=0
T_air_r=325
T_ave_i=0 [K]
T_ave_r=583.4 [K]
T_c_i=0
T_c_r=325
T_h_i=0 [K]
T_h_r=1759 [K]
t_pad_i=0
t_pad_r=0.0152
T_ph_i=0 [K]
T_ph_r=641.7 [K]
T_reh_i=0 [K]
T_reh_r=841.8 [K]
T_rx_ave_i=0 [K]
T_rx_ave_r=470.8 [K]
t_wall_i=0 [m]
t_wall_r=0.0005 [m]
U_atb_i=0.001679 [m^3/s]
U_atb_r=0.003646 [m^3/s]
U_C1_i=0.02804 [m^3/s]
U_C1_r=0.001009 [m^3/s]
U_ci_i=0 [m^3/s]
U_ci_r=0.001758 [m^3/s]
U_CLr1_i=0.06096 [m^3/s]
U_CLr1_r=0.001125 [m^3/s]
U_CL_i=0.02777 [m^3/s]
U_CL_r=0.00125 [m^3/s]
U_Cm_i=0.01823 [m^3/s]
U_Cm_r=0.00005347 [m^3/s]
U_cz_i=-0.02353 [m^3/s]
U_cz_r=0.008811 [m^3/s]
U_c_i=0.001758 [m^3/s]
U_c_r=0.003583 [m^3/s]
U_e_i=-0.00007898 [m^3/s]
U_e_r=0.00006362 [m^3/s]
U_fb_i=0.05749 [m^3/s]
U_fb_r=0.005906 [m^3/s]
U_hi_i=0 [m^3/s]
U_hi_r=-0.005408 [m^3/s]
U_hr_i=0 [m^3/s]
U_hr_r=0.008945 [m^3/s]
U_h_i=-0.005408 [m^3/s]
U_h_r=0.008945 [m^3/s]
U_j_i=-0.08102 [m^3/s]
U_j_r=0.002906 [m^3/s]
U_Lr1_i=-0.142 [m^3/s]
U_Lr1_r=0.00178 [m^3/s]
U_Lr2_i=-0.1416 [m^3/s]
U_Lr2_r=-0.005895 [m^3/s]
U_L_i=-0.0004139 [m^3/s]
U_L_r=0.007675 [m^3/s]
U_ph_i=-0.00001664 [m^3/s]
U_ph_r=0.00001149 [m^3/s]
U_Q1_i=0
U_Q1_r=0
U_rh_i=-0.0001165 [m^3/s]
U_rh_r=0.00008046 [m^3/s]
V_Cr_i=0 [m^3]
V_Cr_r=0.01117 [m^3]
wL_Rre_i=0
wL_Rre_r=0.2109
w_chx_i=0
w_chx_r=0.05931
w_comb_i=0
w_comb_r=0.2672
W_dot_lost_chx_i=0
W_dot_lost_chx_r=7.887 [W]

W_dot_lost_comb_i=0 [W]
W_dot_lost_comb_r=35.53 [W]
W_dot_lost_e_i=0
W_dot_lost_e_r=1.409 [W]
W_dot_lost_other_i=-5.380E-105 [W]
W_dot_lost_other_r=9.967 [W]
W_dot_lost_reh_i=0 [W]
W_dot_lost_reh_r=12.4 [W]
W_dot_lost_re_dE_i=0 [W]
W_dot_lost_re_dE_r=2.951 [W]
W_dot_lost_re_dM_i=0
W_dot_lost_re_dM_r=-29.27 [W]
W_dot_lost_re_dQ_i=0
W_dot_lost_re_dQ_r=53.37 [W]
W_dot_lost_re_dT_i=0 [W]
W_dot_lost_re_dT_r=15.7 [W]
W_dot_lost_re_i=0 [W]
W_dot_lost_re_r=42.75 [W]
W_dot_lost_rx_dM_i=0 [W]
W_dot_lost_rx_dM_r=21.24 [W]
W_dot_lost_rx_dP_i=5.380E-105 [W]
W_dot_lost_rx_dP_r=1.568 [W]
W_dot_lost_rx_dT_i=0 [W]
W_dot_lost_rx_dT_r=-21.23 [W]
W_dot_lost_rx_i=5.380E-105 [W]
W_dot_lost_rx_r=1.572 [W]
w_e_i=0
w_e_r=0.01059
w_other_i=-4.046E-107
w_other_r=0.07494
w_reh_i=0
w_reh_r=0.09326
w_re_i=0
w_re_r=0.3214
w_rx_i=4.046E-107
w_rx_r=0.01182
XiL_i=0
XiL_r=-0.7986
Xi_i=0
Xi_r=-19.96
x_Cr_i=0 [m]
x_Cr_r=0.345 [m]
x_cz_i=0 [m]
x_cz_r=0.1226 [m]
x_c_i=0 [m]
x_c_r=0.058 [m]
x_e_i=0 [m]
x_e_r=0.1 [m]
X_H2O_i=0
X_H2O_r=0.0998
x_Lr1_i=0 [m]
x_Lr1_r=0.357 [m]
x_Lr2_i=0 [m]
x_Lr2_r=0.405 [m]
x_l_i=0 [m]
x_l_r=0.1926 [m]
x_ph_i=0 [m]
x_ph_r=0.1 [m]
X_res_i=0 [kg/m^4 s]
X_res_r=126789 [kg/m^4 s]
x_re_i=0 [m]
x_re_r=0.04 [m]
x_rh_i=0 [m]
x_rh_r=0.2 [m]
x_tot_i=0 [m]
x_tot_r=1.358 [m]
Z_C1_i=-438945 [kg/m^4 s]
Z_C1_r=766 [kg/m^4 s]
Z_CLr1_i=-168347 [kg/m^4 s]
Z_CLr1_r=451.2 [kg/m^4 s]
Z_CLr2_i=-148395 [kg/m^4 s]
Z_CLr2_r=397.7 [kg/m^4 s]
Z_CL_i=-443157 [kg/m^4 s]
Z_CL_r=4769 [kg/m^4 s]
Z_Cm_i=-587076 [kg/m^4 s]
Z_Cm_r=1722 [kg/m^4 s]
Z_Cres_i=-29450 [kg/m^4 s]
Z_Cres_r=32.48 [kg/m^4 s]
Z_cz_i=380344 [kg/m^4 s]
Z_cz_r=149340 [kg/m^4 s]
Z_c_i=-1.454E+06 [kg/m^4 s]
Z_c_r=2.723E+06 [kg/m^4 s]
Z_e_i=9.192E+07 [kg/m^4 s]
Z_e_r=7.938E+07 [kg/m^4 s]
Z_fb_i=-176949 [kg/m^4 s]
Z_fb_r=15359 [kg/m^4 s]
Z_h_i=529837 [kg/m^4 s]
Z_h_r=876322 [kg/m^4 s]
Z_j_i=126452 [kg/m^4 s]
Z_j_r=6535 [kg/m^4 s]
Z_LL_i=35698 [kg/m^4 s]
Z_LL_r=847.6 [kg/m^4 s]
Z_Lm_i=18696 [kg/m^4 s]
Z_Lm_r=118 [kg/m^4 s]
Z_Lr1_i=45422 [kg/m^4 s]
Z_Lr1_r=261.7 [kg/m^4 s]
Z_Lr2_i=51529 [kg/m^4 s]
Z_Lr2_r=296.9 [kg/m^4 s]
Z_ph_i=-4.172E+07 [kg/m^4 s]
Z_ph_r=1.752E+08 [kg/m^4 s]
Z_pl_i=0 [kg/m^4 s]
Z_pl_r=102567 [kg/m^4 s]
Z_ratio_i=0
Z_ratio_r=30.09
Z_rh_i=6.818E+07 [kg/m^4 s]
Z_rh_r=1.797E+07 [kg/m^4 s]

REFERENCES

Arman, B., Wollan, J., Kotsubo, V., Backhaus, S., and Swift, G., (2004). "Operation of thermoacoustic Stirling heat engine driven large multiple pulse tube refrigerators," submitted to the Proceedings of the 13th International Cryocooler Conference.

Backhaus, S. and Swift, G. W. (2000). "A thermoacoustic-Stirling heat engine: Detailed study," J. Acoust. Soc. Am., Vol. 107, pp. 3148-3166.

Backhaus, S. and Swift, G. W. (2001). "Fabrication and use of parallel plate regenerators in thermoacoustic engines," Proceedings of the 36th Intersociety Energy Conversion Engineering Conference, Savannah, GA, Vol. 1, pp. 453-458, Institute of Electrical and Electronics Engineers.

Backhaus, S. and Swift, G. W. (2003). "An acoustic streaming instability in thermoacoustic devices utilizing jet pumps," J. Acoust. Soc. Am., Vol. 113, pp. 1317-1324.

Bailliet, H., Gusev, V., Raspet, R., and Hiller, R. A., (2001). "Acoustic streaming in closed thermoacoustic devices," J. Acoust. Soc. Am., Vol. 110, pp. 1808-1821.

Bauwens, Luc, (1998), "Interface loss in the small amplitude orifice pulse tube model," Adv. Cryogenic Eng., Vol. 43, pp. 1933-1940.

Bejan, Adrian, (1997). *Advanced Engineering Thermodynamics*, 2nd edition (Wiley, New York).

Belcher, J. R., Slaton, W. V., Raspet, R., Bass, H. E., Lightfoot, J., (1999). "Working gases in thermoacoustic engines," J. Acoust. Soc. Am., Vol. 105, pp. 2677-2684.

Ceperley, Peter H., (1978). "Traveling Wave Heat Engine," U. S. Patent No. 4,114,380.

Ceperley, Peter H., (1979). "A pistonless Stirling engine – The traveling wave heat engine," J. Acoust. Soc. Am., Vol. 66, pp. 1508-1513.

Ceperley, Peter H., (1982). "Resonant Traveling Wave Heat Engine," U. S. Patent No. 4,355,517.

Ceperley, Peter H., (1985). "Gain and efficiency of a short traveling wave heat engine," J. Acoust. Soc. Am., Vol. 77, pp. 1239-1244.

Charles, I., Duband, L., and Ravex, A., (1999). "Permanent flow in low and high frequency pulse tube coolers – experimental results," Cryogenics, Vol. 39, pp. 777-782.

Chen, R. L., Chen, Y. C., Chen, C. L., Tsai, C., and DeNatale, J., (2002). "Development of Miniature Thermoacoustic Refrigerators," *40th AIAA Aerospace Sciences Meeting and Exhibit*, AIAA Paper No. 2002-0206.

De Blok, Cornelis Maria, Van Rijt, Nicolaas Adrianus Hendrikus Jozef, (2001). "Thermo-acoustic System," U. S. Patent No. 6,314,740.

F-Chart Software, Box 44042, Madison, WI, 53744.

Fox, Robert W., and McDonald, Alan T., (1992). *Introduction to Fluid Mechanics*, 4th edition, (Wiley, New York).

Fusco, A. M., Ward, W. C., and Swift, G. W., (1992). "Two-sensor power measurements in lossy ducts," J. Acoust. Soc. Am., Vol. 91, pp. 2229-2235.

Gardner, D. L., and Swift, G. W., (2003). "A cascade thermoacoustic engine," J. Acoust. Soc. Am., Vol. 114, pp. 1905-1919.

Gedeon, David, (1997). "DC gas flows in Stirling and pulse-tube cryocoolers," *Cryocoolers 9*, R. G. Ross, Ed., pp. 385-392, (Plenum, New York).

Gopinath, Ashok and Harder, Donald R., (2000). "An experimental study of heat transfer from a cylinder in low-amplitude zero-mean oscillatory flows," International Journal of Heat and Mass Transfer, Vol. 43, pp. 505-520.

Gusev, V., Job, S., Bailliet, H., Lotton. P. and Bruneau, M., (2000). "Acoustic streaming in annular thermoacoustic prime-movers," J. Acoust. Soc. Am., Vol. 108, pp. 934-945.

Hustad, Johan E., and Sonju, Otto K., (1988). "Experimental Studies of Lower Flammability Limits of Gases and Mixtures of Gases at Elevated Temperatures," Combustion and Flame, Vol. 71, pp. 283-294.

Incropera, Frank P. and DeWitt, David P., (1996). *Fundamentals of Heat and Mass Transfer*, 4th edition (Wiley, New York).

Job, S., Gusev, V., Lotton, P., and Bruneau, M., (2003). "Acoustic streaming measurements in annular thermoacoustic engines," J. Acoust. Soc. Am., Vol. 113, pp. 1892-1899.

Kays, W. M., and Crawford, M. E., (1993). *Convective Heat and Mass Transfer*, 3rd edition, (McGraw-Hill, New York).

Kays, W. M., and London, A. L., (1984). *Compact Heat Exchangers*, 3rd edition, (McGraw-Hill, New York).

Keolian, R., and Bastyr, K., (2004). Private communications.

Kinsler, L. E., Frey, A. R., Coppens, A. B., and Sanders, J. V., (1982). *Fundamentals of Acoustics*, 3rd edition, (Wiley, New York).

Kittel, Peter, (1998). "The temperature profile within pulse tubes," Adv. Cryogenic Eng., Vol. 43, pp. 1927-1932.

Kreyszig, Erwin, (1993). *Advanced Engineering Mathematics*, 7th edition, (John Wiley and Sons, Inc., New York).

Landau, L. D., and Lifshitz, E. M., (1987). *Fluid Mechanics*, 2nd edition, (Butterworth-Heinemann, Oxford).

Lewis, M. A., Kuriyama, T., Kuriyama, F., and Radebaugh, R., (1998). "Measurement of heat conduction through stacked screens," Adv. Cryogenic Eng., Vol. 43, pp. 1611-1618.

Lieuwen, T., and Zinn, B. T., (1998). "Role of equivalence ratio oscillations in driving combustion instabilities in low NOx gas turbines," *Proceedings of the 27th International Symposium on Combustion,* The Combustion Institute, pp. 1809-1816.

McManus, K. R., Poinsot, T., and Candel, S. M., (1993). "A review of active control of combustion instabilities," Progress in Energy Combustion Science, Vol. 19, pp. 1-29.

Mozurkewich, George, (2001). "Heat transfer from transverse tubes adjacent to a thermoacoustic stack," J. Acoust. Soc. Am., Vol.110, pp. 841-847.

Olson, J. R., and Swift, G. W., (1997). "Acoustic streaming in pulse tube refrigerators: Tapered pulse tubes," Cryogenics, Vol. 37, pp. 769-776.

Petach, M., Tward, E., and Backhaus, S., (2004). "Design Of A High Efficiency Power Source (HEPS) Based On Thermoacoustic Technology," Final report, NASA contract no. NAS3-01103, CDRL 3f.

Pierce, Allan D., (1989). *Acoustics, An Introduction to Its Physical Principles and Applications*, (Acoustical Society of America, Woodbury, NY).

Popescu, G., Radcenco, V., Gargalian, E., and Ramany Bala, P., (2001). "A critical review of pulse tube cryogenerator research," International Journal of Refrigeration, Vol. 24, pp. 230-237.

Radebaugh, R., (1990). "A review of pulse tube refrigeration," Advances in Cryogenic Engineering, Vol. 35, pp. 1191-1205.

Reid, R. S. and Swift, G. W. (2000). "Experiments with a flow-through thermoacoustic refrigerator," J. Acoust. Soc. Am., Vol. 108, pp. 2835-2842.

Reid, R. S., (1999). "Open cycle thermoacoustics," Ph.D. Thesis, Georgia Institute of Technology, School of Mechanical Engineering.

Reid, R. S., Ward, W. C., and Swift, G. W., (1998). "Cyclic Thermodynamics with Open Flow," Phys. Rev. Lett., Vol. 80, pp. 4617-4620.

Rott, Nikolaus, (1969). "Damped and thermally driven acoustic oscillations in wide and narrow tubes," Journal of Applied Mathematics and Physics, Vol. 20, pp. 230-243.

Rott, Nikolaus, (1975). "Thermally driven acoustic oscillations, Part III: Second order heat flux," Journal of Applied Mathematics and Physics, Vol. 26, pp. 43-49.

Schadow, K. C., and Gutmark, E., (1992). "Combustion instability related to vortex shedding in dump combustors and their passive control," Progress in Energy and Combustion Science, Vol. 18, pp. 117-132.

Smith, Joseph L. and Romm, Michael, (1992). "Thermodynamic Loss at Component Interfaces in Stirling Cycles," *Proceedings of the 27th Intersociety Energy Conversion Engineering Conference*, San Diego, CA, pp. 5.529-5.532, Society of Automotive Engineers.

Swift, G. W., (1988). "Thermoacoustic engines," J. Acoust. Soc. Am., Vol. 84, pp. 1145-1180.

Swift, G. W., (1992). "Analysis and performance of a large thermoacoustic engine," J. Acoust. Soc. Am., Vol. 92, pp. 1551-1563.

Swift, G. W., and Olson, J. R. (1999). "Tapered pulse tube for pulse tube refrigerators," U. S. Patent No. 5,953,920.

Swift, G. W., and Ward, W. C., (1996). "Simple Harmonic Analysis of Regenerators," Journal of Thermophysics and Heat Transfer, Vol. 10, pp. 652-662.

Swift, G. W., Gardner, D. L. and Backhaus, S., (1999). "Acoustic recovery of lost power in pulse tube refrigerators," J. Acoust. Soc. Am., Vol. 105, pp. 711-724.

Swift, Gregory W., (1995). "Thermoacoustic Natural Gas Liquefier," Natural Gas RD&D Contractor's Review Meeting, Baton Rouge, LA, April 4-6. Available at: http://www.lanl.gov/thermoacoustics/Pubs/index.html.

Swift, Gregory W., (2002). *Thermoacoustics: A unifying perspective for some engines and refrigerators* (Acoustical Society of America, Melville, NY).

Swift, Gregory W., Backhaus, Scott N., and Gardner, David L., (2000). "Traveling-wave Device with Mass Flux Suppression," U. S. Patent No. 6,032,464.

Turns, Stephen R., (1996). *An Introduction to Combustion, Concepts and Applications*, (McGraw-Hill, Inc., New York).

Ueda, Y., Biwa, T., Mizutani, U., and Yazaki, T., (2004). "Experimental studies of a thermoacoustic Stirling prime mover and its application to a cooler," J. Acoust. Soc. Am., Vol. 115, pp. 1134-1141.

Van Wijingaarden, W. C., (1999). "Therrnoacoustic refrigeration – A stirring concept for offshore associated gas liquefaction," *Monetizing Stranded Gas Reserves Conference*, Houston, December 7-9.

Waxler, Roger, (2001). "Stationary velocity and pressure gradients in a thermoacoustic stack," J. Acoust. Soc. Am., Vol. 109, pp. 2739-2750.

Ward, W. C., and Swift, G. W., (1994). "Design environment for low amplitude thermoacoustic engines (DeltaE)," J. Acoust. Soc. Am., Vol. 95, pp. 3671-3672.

Weiland, N. T. and Zinn, B. T., (2003a). "Open cycle traveling wave thermoacoustics: Mean temperature difference at the regenerator interface," J. Acoust. Soc. Am., Vol. 114, pp. 2791-2798.

Weiland, N. T. and Zinn, B. T., (2003b). "Traveling-wave thermoacoustic engines with internal combustion and associated methods," U. S. Patent Application No. 20030182939.

Weiland, N. T., Zinn, B. T., and Swift, G. W., (2004). "Traveling-wave thermoacoustic engines with internal combustion," U. S. Patent No. 6,732,515.

Weiland, N. T. and Zinn, B. T., (2004a). "Open cycle traveling wave thermoacoustics: Energy fluxes and thermodynamics," to appear in J. Acoust. Soc. Am., September 2004.

Weiland, N. T. and Zinn, B. T., (2004b). "Pulse combustion in a traveling wave thermoacoustic engine," to appear in the Proceedings of the ASME International Mechanical Engineering Conference, Anaheim, CA, November 13-19, Paper #: IMECE2004-61579.

Weinberg, Felix J., (1986). "Combustion in Heat-Recirculating Burners," in *Advanced Combustion Methods*, F. J. Weinberg, ed., (Academic Press, London), pp. 183-236.

Wollan, J. J., Swift, G. W., Backhaus, S., and Gardner, D. L., (2002). "Development of a Thermoacoustic Natural Gas Liquefier," AIChE Meeting, New Orleans, LA, March 11-14. Available at: http://www.lanl.gov/thermoacoustics/Pubs/index.html.

Xiao, J. H., (1992). "Thermoacoustic theory for cyclic flow regenerators. Part I: fundamentals," Cryogenics, Vol. 32, pp. 895-901.

Yarr, George A., and Corey, John A., (1995). "Linear Electrodynamic Machine," U. S. Patent No. 5,389,844.

Yazaki, T., Iwata, A., Maekawa, T., and Tominaga, A., (1998). "Traveling Wave Thermoacoustic Engine in a Looped Tube," Physical Review Letters, Vol. 81, pp. 3128-3131.

Zinn, B. T., (1986). "Pulsating Combustion," in *Advanced Combustion Methods*, F. J. Weinberg, ed., (Academic Press, London), pp. 113-181.

Zinn, B. T., (1996). "Pulse combustion applications: Past, present and future," *Unsteady Combustion*, F. Culick et. al., Ed., pp. 113-137, (Kluwer Academic Publishers, The Netherlands).